Ultrasonic Phased Array Techniques using Switched-Mode Excitation

Peter Raymond Smith

Submitted in accordance with the requirements

for the degree of Doctor of Philosophy

UNIVERSITY OF LEEDS

The University of Leeds

School of Electronic and Electrical Engineering

April 2013

The candidate confirms that the work submitted is his/her own, except where work which has formed part of jointly-authored publications has been included. The contribution of the candidate and the other authors to this work has been explicitly indicated below. The candidate confirms that appropriate credit has been given within the thesis where reference has been made to the work of others

- **Chapters 2 and 4 contain work published in:**

  Smith *et al.*, "A PLL-based phased array method to minimize phase quantization errors and reduce phasing-lobes", *Proceedings of IEEE International Ultrasonics Symposium, 2010*, pp. 1837-1840. [1]

  Smith *et al.*, "Ultrasound Array Transmitter Architecture With High Timing Resolution Using Embedded Phase-Locked Loops", *IEEE Transactions on Ultrasonics, Ferroelectrics, and Frequency Control*, vol. 59, no. 1, pp. 40-49, Jan. 2012. [2]

- **Chapters 3, 5, 6 and 7 contain work published or submitted for publication in:**

  Smith *et al.*, "Pre-Distorted Amplitude Modulated (PDAM) Chirps for Transducer Compensation in Harmonic Imaging", *Proceedings of IEEE International Ultrasonics Symposium, 2012*. [3]

  Smith *et al.*, University of Leeds, "Ultrasound Generation", UK Patent Application No. 122282.1, Dec. 2012.

  Smith *et al.*, "Width-Modulated Square-Wave Pulses for Ultrasound Applications", *Submitted to IEEE Transactions on Ultrasonics, Ferroelectrics, and Frequency Control*, Dec. 2012. *Accepted with Minor Revisions*, Apr. 2013, *In Press* [4]

  Cowell *et al.*, "Harmonic cancellation in switched mode Linear Frequency Modulated (LFM) excitation of ultrasound arrays", *Proceedings of IEEE International Ultrasonics Symposium, 2011*, pp. 454-457. [5]

  Smith *et al.*, "A Fractional Harmonic Excitation (FHE) Method for High Frequency Array Imaging", *Proceedings of IEEE International Ultrasonics Symposium, 2012*. [6]

Cowell *et al.*, “Phase Inversion based Selective Harmonic Elimination (PI-SHE) in Multi-level Switched-Mode Tone and Frequency Modulated Excitation”, *Submitted to IEEE Transactions on Ultrasonics, Ferroelectrics, and Frequency Control*, Dec. 2012. *Accepted with Minor Revisions*, Feb. 2013, *Accepted in Final Form*, Mar. 2013, *In Press* [7]

A full list of publications can be found in Chapter 1.

To my parents and Sarah

Acknowledgements

I would like to express my special thanks to my supervisor Dr. Steven Freear for encouraging me to pursue a Ph.D. and for his continued trust, support and friendship throughout my undergraduate and postgraduate studies.

I would also like to thank Dr. David Cowell for his advice, support and enthusiasm through my research.

I would also like to thank Prof. Mounir Ghogho and Dr. Andrew Kemp for supporting my Ph.D. application.

I would also like to extend my gratitude to members past and present of the Ultrasound Group who I have worked with and alongside including Mr. Benjamin Raiton, Dr. Sevan Harput, Mr. Stephen Ellwood, Dr. James McLaughlan, Mr. Gaël Léauté, Mr. Robert Ingham, Dr. David Charutz, Mr. Chau Vo Ky and Dr. Muhammad Arif.

I would also like to thank the many other students I have worked alongside and collaborated with on projects throughout my Ph.D. including, Mr. Omar Anwar, Mr. Bao Bui, Mr. Thinh Pham, Mr. Paul Thompson, Mr. Charles Winckler, Miss. Sara Qureshi and Mr. Rob James.

I am also grateful to the University of Leeds and the EPSRC for providing financial support by means of a Doctoral Training Grant throughout my research.

Lastly I would like to thank my close family and friends for their unwavering support throughout my studies.

Abstract

Ultrasound is predominantly an 'active' sensing modality, with information obtained by transmission of an acoustic wave, followed by analysis of received signals. Transmission occurs when electrical signals are converted to acoustic signals. This thesis covers the design and application of these electrical signals to an array transducer. As an introduction, the development of a bespoke ultrasound array research platform is discussed. This enabling technology is built around switched-mode excitation: a method of approximating an analogue waveform by selecting between discrete voltage levels. The use of switched-mode methods has led to three major topics of research.

Firstly, a transmit beamformer architecture that provides fine control of excitation sequence timing using embedded-phase locked loops is presented. This enables accurate implementation of firing sequences or phasing between transducer elements, thus minimizing time-quantization error, and providing an improved representation of the expected pressure field. An introduction to transmit beamforming is given, the impact of time-quantization is discussed, and the transmit beamformer's performance is demonstrated.

Secondly, a method of arbitrary waveform generation using switched-mode excitation is described. The method encodes width-modulated sequences of three or five discrete voltage levels, that, once passed through a transducer, give close approximation to the desired arbitrary waveform. Applications include: power control, pulse shaping, and array apodization. Each application is demonstrated by simulation and experimentation. An extension to the method is shown for 'chirp' coded imaging, demonstrating the capability for generation of frequency modulated waveforms. The improvement in image quality when compared with conventional square-wave, 'pseudo-chirp' excitation signals is shown.

Lastly, the performance of the width-modulated signals is further extended so as to remove unwanted third-harmonic content whilst still maintaining pulse amplitude control.

Removal of the third harmonic reduces harmonic distortion, has benefits in applications such as harmonic imaging, and extends the use of switched-mode operation with wide bandwidth transducers.

Table of Contents

List of Figures

List of Tables

List of Abbreviations

AWG	Arbitrary Waveform Generator
CT	Computerised Tomography
DAC	Digital to Analogue Converter
FET	Field Effect Transistor
FPGA	Field Programmable Gate Array
HIFU	High Intensity Focused Ultrasound
HRPWM	Harmonic Reduction Pulse-Width Modulation
IDR	Image Dynamic Range
IP	Intellectual Property
IVUS	Intra-Vascular UltraSound
LVDS	Low Voltage Differential Signalling
MOSFET	Metal Oxide Field Effect Transistor
MRI	Magnetic Resonance Imaging
NCO	Numerically Controlled Oscillator
NRMSD	Normalised Root Mean Squared Deviation
PCB	Printed Circuit Board
PLL	Phase-Locked Loop
PRF	Pulse Repetition Frequency
PVDF	PolyVinylidene DiFlouride
PWM	Pulse-Width Modulation
PZT	Lead Zirconate Titanate
RADAR	RAdio Detection And Ranging

RAM	Random Access Memory
RDR	Receive Dynamic Range
RF	Radio Frequency
RMSD	Root Mean Squared Deviation
SCR	Silicon Controlled Rectifier
SHE	Selective Harmonic Elimination
SONAR	SOund Navigation and Ranging
SPICE	Simulation Program with Integrated Circuit Emphasis
TDR	Transmit Dynamic Range
UARP	Ultrasound Array Research Platform
USB	Universal Serial Bus
VCO	Voltage Controlled Oscillator

List of Symbols

δ	Switching Angle
$\Delta\tau$	Minimum Time / Phase Resolution
δ_h	Harmonic Cancellation Switching Angle
ε_0	Permittivity of Free Space
ε_r	Material Dielectric Constant
Γ	Reflection Coefficient
λ	Wavelength
μ	Oversampling Factor
ω	Angular Frequency
ω'	LFM Angular Frequency
ω_0	Resonance Frequency
Φ	Maximum Phase Error
ρ	Density
τ_n	Element Delay
τ_n	Per-Element Delay
$\mathrm{PWM}(t)$	PWM Sequence
θ_δ	Switching Angle Separation
θ_G	Grating Lobe Angle
θ_s	Steering Angle
θ_{MAX}	Maximum Steering Angle
θ_{pq}	Worst Case Steering Angle
A	Area
a_n	Fourier Series Coefficient

B	Bandwidth
b_n	Fourier Series Coefficient
c	Speed of Sound
$c(t)$	Carrier Waveform
C_0	Clamped Capacitance
C_G	Gate Capacitance
$C_L(t)$	Low Carrier Base Waveform
$C_T(t)$	Top Carrier Base Waveform
$c_{\mathrm{NEG}}(t)$	Negative Carrier Waveform
$c_{\mathrm{POS}}(t)$	Positive Carrier Waveform
D	Aperture Width
d	Array Element Pitch
d_0	Capacitor Plate Separation
f	Frequency
$f(x)$	Function of x
f_s	Sampling Frequency
F_{IN}	PLL Input Frequency
F_{OUT}	PLL Output Frequency
F_{VCO}	PLL VCO Frequency
f_{sw}	Switching Frequency
$h(t)$	Transducer Impulse Response
I	Current
K	PLL Post-Scale Counter
k_t	Thickness Mode Electro-Mechanical Coupling Constant
L	Level Shift Scaling
M	PLL Feedback Counter
m	Integer Values
$m(t)$	Modulating Waveform
N	Number of Elements

n	Integer Value
n	Number of Cycles
n_L	Number of Levels
P	PLL Pre-Scale Counter
p	Number of Minimum Phase Quantization Periods
P_{LOSS}	Power Loss
Q	Charge
q	Number of Sub-Elements
QF	Q-Factor
R_a	Radiation Impedance
R_m	Radiation Impedance
R_{ss}	Auto-Correlation Output
$s(t)$	Analogue Signal
SL_{RMS}	Root Mean Square Sidelobe Level
T	Duration
t	Time
V	Voltage
w	Element Width
$y(t)$	Output Signal
Z	Acoustic Impedance
Z_c	Piezo-Electric Acoustic Impedance
z_{F}	Focal Distance
z_{rand}	Distance for Uncorrelated Lobes
z_{TR}	Transition Distance
l	Integer values

Chapter 1

Introduction

1.1 Motivation for Research

Ultrasound is predominately an 'active' sensing modality similar to RADAR and SONAR. Sensing is instigated by transmission of an acoustic wave of known form, operating typically in the tens of kHz to hundreds of MHz range, followed by acquisition of received signals. Information is obtained by analysing how the transmitted signal is influenced by the medium of propagation. Due to its active nature, the properties of the transmitted acoustic wave therefore has great influence on the results obtained.

Fundamental to the sensing modality is conversion between the electrical and acoustic domain. This conversion relies on the piezo-electric effect, as discovered by Pierre and Jacques Curie in 1880 [8], whereby application of an alternating electric field, or mechanical stress generates mechanical disturbance, or an electrical signal respectively. A transducer is a section of piezo-electric material packaged with electrodes and electrical interconnects. In its simplest form, a transducer will contain a single piezo-electric element. More complex transducer forms combine multiple elements together within one component. Such devices are called array transducers, and are now primarily used in a large number of medical and industrial applications.

Array transducers have revolutionised ultrasound as they offer much greater flexibility than their single element counterparts, enabling more complex beam and field patterns to be generated by control of collections of elements. Most notably, is the use of phased ar-

ray techniques such as beamforming and beamsteering that allow dynamic manipulation of the acoustic wave or beam in transmission using a fixed arrangement of sources, whilst in reception they enable increased sensitivity at a particular position. Beamsteering and focusing requires a system design that can add inter-element delays between firing of elements. In conjunction with techniques such as beamforming, other sophisticated methods such as signal coding can be applied in the acoustic domain. The principle of signal coding, requires transmission of a signal with a detectable embedded property, which can be distinguished by the receiver above interference and noise, thus improving the sensitivity of the system. Signal coding therefore requires a transmitter circuit that is capable of generating arbitrary waveforms that contain the desired code, e.g. frequency modulation.

Array transducers often contain hundreds of elements, each of which ideally requires a transmitter circuit for greatest flexibility, thus necessitating an array of transmitter circuits. The design of each element's ultrasound transmitter circuit is therefore not a trivial solution. For example, high voltages are necessary to provoke large mechanical disturbances (and acoustic pressures) capable of propagating through material to a desired depth, taking into account factors such as attenuation. High frequency 'Class A' RF power amplifiers are well-suited to the electrical requirements of an ultrasound transmitter, however are often large and expensive due to the requirement for heat sinks and cooling. Class A amplifiers are also inefficient in terms of power dissipation. An alternative transmitter solution to Class A amplifiers is the use of MOSFET semi-conductor pulser devices, similar to Class D amplifiers. These components use switched-mode excitation to select between several positive and negative voltage levels. Switching between discrete levels results in square-wave or staircase (stepped) pulses which approximate sinusoidal signals (often termed 'pseudo-sinusoidal'). MOSFETs are advantageous as they are capable of delivering high currents to piezo-electric loads, in small scale, low-cost, integrated packages. As a consequence, MOSFET switched-mode pulser devices have subsequently been the adopted standard within commercial machines for several years [9]. These devices are also well suited to future trends moving towards highly integrated portable, low-cost imaging systems [10, 11, 12].

The disadvantage of MOSFET switched-mode excitation is the inflexible nature of the transmitted output. Although convenient solutions, switched-mode circuits are limited by their switching between discrete levels, undesirable harmonic content, and lack of arbitrary waveform flexibility [13, 14].

The motivation of this research is to develop techniques that address these concerns, increasing the performance and flexibility of switched-mode circuits, so that optimal field profiles and signals can be transmitted for a range of applications. This research focuses on two key aspects of an ultrasound system, namely the transmit beamformer architecture, and the use of transmitter circuits at the system 'front-end'.

1.2 Objective of Research

The objective of this research is to improve the quality of the transmitted field and transmitted signal from an ultrasound array. This array is composed of many elements and is excited by an array of switched-mode circuits. These switched-mode circuits are commonly found through ultrasonic systems and are widely adopted, however have a reported limited functionality for advanced techniques. This research seeks to utilize these components differently, to attain performance similar to the use of a Class A linear amplifier device per channel.

Firstly, the transmitted field is directly affected by the firing sequence. Poor approximation of inter-element delays can result in pressure distributed by erroneous beams. Also, error can be introduced into the system, either by propagation in non-homogeneous materials, or by system components such as the transducer. The first objective of this research is to develop a flexible transmit beamforming architecture able to implement inter-element delays precisely, and dynamically, thus reducing error within the transmitted field.

A second objective is evaluate the pressure output generated by switched-mode circuits. The objective here is to develop methods of generating arbitrary waveform output. Arbitrary waveform capability enables techniques such as coded imaging. A key objective

is to enable accurate, and predictable pressure control during a pulse sequence without the need to adjust switching levels.

The third main objective is to evaluate the nature of harmonic content within the switched-mode signals, to reduce harmonic leakage and suppress undesired spectral content whilst maintaining amplitude control and arbitrary waveform functionality.

1.3 Achievements from the Research

- Contributed to the development of a flexible ultrasound array research platform used throughout the Ultrasound group at the University of Leeds.

- Design of an embedded transmit beamformer architecture to provide fine inter-channel timing resolution of switched-mode signals, thus improving the nature of the transmitted field.

- Development of an arbitrary waveform generation scheme using a fundamental-mode pulse-width modulation and switched-mode circuits.

- Extension for use with frequency modulated ‘chirp’ coded signals, showing benefits in coded imaging when compared with previously reported switched-mode methods.

- Development of a harmonic reduction pulse-width modulation method that permits arbitrary waveform control, with reduced third harmonic within the excitation signal.

- Contributed to two UK patent applications.

- Primary author of two journal publications and three conference proceedings.

- Co-authored and contributed to two journal publications and eight conference proceedings.

1.4 Journal Publications

As primary author:

- P. R. Smith, D. M. J. Cowell, B. Raiton, C. Vo Ky, and S. Freear, "Ultrasound Array Transmitter Architecture With High Timing Resolution Using Embedded Phase-Locked Loops", *IEEE Transactions on Ultrasonics, Ferroelectrics, and Frequency Control*, vol. 59, no. 1, pp. 40-49, Jan. 2012. [2]

- P. R. Smith, D. M. J. Cowell, and S. Freear, "Width-Modulated Square-Wave Pulses for Ultrasound Applications", *Submitted to IEEE Transactions on Ultrasonics, Ferroelectrics, and Frequency Control*, Dec. 2012. *Accepted with Minor Revisions*, Apr. 2013, *In Press* [4]

As sub-author:

- B. Raiton, J. R. McLaughlan, S. Harput, P. R. Smith, D. M. J. Cowell, and S. Freear, "The capture of flowing microbubbles with an ultrasonic tap using acoustic radiation force", *Applied Physics Letters*, vol. 101, no. 4, pp. 044102-044102-4, Jul. 2012 [15]

- D. M. J. Cowell, P. R. Smith, and S. Freear, "Phase Inversion based Selective Harmonic Elimination (PI-SHE) in Multi-level Switched-Mode Tone and Frequency Modulated Excitation", *Submitted to IEEE Transactions on Ultrasonics, Ferroelectrics, and Frequency Control*, Dec. 2012. *Accepted with Minor Revisions*, Feb. 2013, *Accepted in Final Form*, Mar. 2013, *In Press* [7]

1.5 Conference Publications

As primary author:

- P. R. Smith, D. M. J. Cowell, B. Raiton, C. Vo Ky, T. H. Pham, B. Q. Bui, and S. Freear, "A PLL-based phased array method to minimize phase quantization errors

and reduce phasing-lobes", *Proceedings of IEEE International Ultrasonics Symposium, 2010*, pp. 1837-1840. [1]

- P. R. Smith, D. M. J. Cowell, and S. Freear, "A Fractional Harmonic Excitation (FHE) Method for High Frequency Array Imaging", *Proceedings of IEEE International Ultrasonics Symposium, 2012*. [6]

- P. R. Smith, S. Harput, D. M. J. Cowell, J. R. McLaughlan, and S. Freear. "Pre-Distorted Amplitude Modulated (PDAM) Chirps for Transducer Compensation in Harmonic Imaging", *Proceedings of IEEE International Ultrasonics Symposium, 2012*. [3]

As sub-author:

- B. Raiton, J. R. McLaughlan, P. R. Smith, D. M. J. Cowell, S. Harput, and S. Freear, "Counter flow microbubble channelling using acoustic radiation force funnel", *Proceedings of IEEE International Ultrasonics Symposium, 2011*, pp. 2432-2435. [16]

- D. M. J. Cowell, P. R. Smith, and S. Freear, "Harmonic cancellation in switched mode Linear Frequency Modulated (LFM) excitation of ultrasound arrays", *Proceedings of IEEE International Ultrasonics Symposium, 2011*, pp. 454-457. [5]

- S. S. Qureshi, P. R. Smith, D. M. J. Cowell, K. M. Rajpoot, and S. Freear, "A Compact, Parameterized, Real-Time Beamformer, Benchmarked For Ultrasound Imaging", *Proceedings of IEEE International Ultrasonics Symposium, 2012*. [17]

- C. A. Winckler, P. R. Smith, D. M. J. Cowell, O. Olagunju and S. Freear, "The Design of a High Speed Receiver System for an Ultrasound Array Research Platform", *Proceedings of IEEE International Ultrasonics Symposium, 2012*. [18]

- B. Raiton, J. R. McLaughlan, P. R. Smith, S. Harput, D. M. J. Cowell, and S. Freear, "Non-invasive Cavitation Nuclei Trap for Histotripsy", *Proceedings of IEEE International Ultrasonics Symposium, 2012*. [19]

- J. R. McLaughlan, P. R. Smith, N. Ingram, L. Coletta, S. Evans, and S. Freear, "Chirp Excitation of Polydisperse Microbubble Populations for Increasing Sonoporatio Efficiency", *Proceedings of IEEE International Ultrasonics Symposium, 2012*. [20]

- O. Olagunju, P. R. Smith, D. M. J. Cowell, and S. Freear, "Randomized Excitation - A Novel Ultrasound Array Excitation Scheme", *Proceedings of IEEE International Ultrasonics Symposium, 2012*. [21]

- S. Harput, J. R. McLaughlan, P. R. Smith, D. M. J. Cowell, S. Evans, and S. Freear, "Separating the Second Harmonic Response of Tissue and Microbubbles using Bispectral Analysis", *Proceedings of IEEE International Ultrasonics Symposium, 2012*. [22]

1.6 Patent Applications

- P. R. Smith, D. M. J. Cowell, S. Freear, University of Leeds, "Ultrasound Generation", UK Patent Application No. 122282.1, Dec. 2012.

- B. Raiton, J. R. McLaughlan, S. Harput, P. R. Smith, D. M. J. Cowell, S. Freear, University of Leeds "Apparatus and Method for Manipulating Entrained Particles" UK Patent Application P138728GB. Mar. 2012

1.7 Thesis Structure

Chapter 1 outlines the motivations and objective of the research, summarises the achievements of the research and lists publications.

Chapter 2 sets a research context, describing clinical and research systems. This chapter provides an introduction to an ultrasound system architecture from a design perspective, describes the motivation for the development of a custom platform for research purposes, and provides an overview of the developed UARP system.

Chapter 3 discusses the transmitter stage of the UARP platform in more detail. An introduction to the use of switched-mode excitation to excite piezo-electric loads is presented, with the advantages and disadvantages of the technique when compared with other technologies explained. A review of the use of switched-mode technologies throughout previous ultrasound literature is provided. A summary of other amplifier technology is given in comparison with switched-mode signals. Lastly the UARP transmitter section is described from a hardware perspective.

Chapter 4 introduces array transducers and beamforming techniques. Issues are discussed such as non-ideal phasing or sequencing, and how errors introduced by the system or components can influence the radiated field. A transmit beamformer design that incorporates a method of applying precise and variable inter-element timings suited to switched-mode excitation is described. The applicability of using the beamformer to compensate for other random sources of error is also discussed.

Chapter 5 describes an arbitrary waveform generation method using switched-mode circuits and pulse-width modulation. Firstly, Fourier Series analysis of switched-mode sequences is presented, showing the variation in fundamental frequency output to a linear increase in pulse width. Using this analysis, an encoding scheme that considers the output pressure from the transducer in response to switched mode signals is discussed. This encoding scheme enables arbitrary waveform capability and pressure control. The performance of the scheme is demonstrated with simulation and experimental measurement.

Chapter 6 extends the width-modulation scheme for use with frequency modulated signals as used in signal coding, and experimentally demonstrates the applicability for coded imaging using a wire-phantom. Examples of arbitrary frequency modulated waveforms are also provided showing pre-distortion for transducer compensation.

Chapter 7 provides an introduction to selective harmonic elimination strategies previously proposed for switched-mode signals. The work discussed in Chapters 5 and 6, is then extended to provide a reduction of third harmonic content within the switched-mode signals whilst maintaining arbitrary waveform functionality. The third harmonic is the

greatest in terms of magnitude and therefore reducing it enables optimal performance with future wide-bandwidth devices for applications such as harmonic imaging.

Chapter 8 concludes with a summary of research to date, and suggests future research ideas.

Chapter 2

Research Platform Development

2.1 Introduction

A complete ultrasound system not only generates transmit signals, but also acquires signals, processes signals, receives user input and displays information in an output a user expects. For a simple single element system, an arbitrary waveform function generator can be used with a RF linear power amplifier to drive the transducer. Receive signals can be captured and displayed by an oscilloscope, or processed within software such as MATLAB (Mathworks, NA). This example system setup described is particularly suited to research and is shown in Figure 2.1. An arbitrary waveform generator can provide optimal performance with greater than 10, 12 or 14 bit amplitude resolution. A Class A power amplifier can provide wide-bandwidth, high gain and low harmonic distortion. Digital oscilloscopes enable real-time display and acquisition, GS/s sampling rates, MHz bandwidths, and automated mathematical measurement and/or processing on raw measurement data. For multiple elements however, this setup is not practical or cost-effective. Firstly, the size of such a setup across multiple channels would be large and inconvenient; Secondly, triggering, sequencing and control of independent channels is clumsy; Thirdly the 'cost-per-channel' is extremely high.

As transducer arrays are now the *de facto* standard for many ultrasound applications, and with the advantages arrays posses over single element solutions, there is a greater push towards developing research systems that can drive array transducers. Commercial

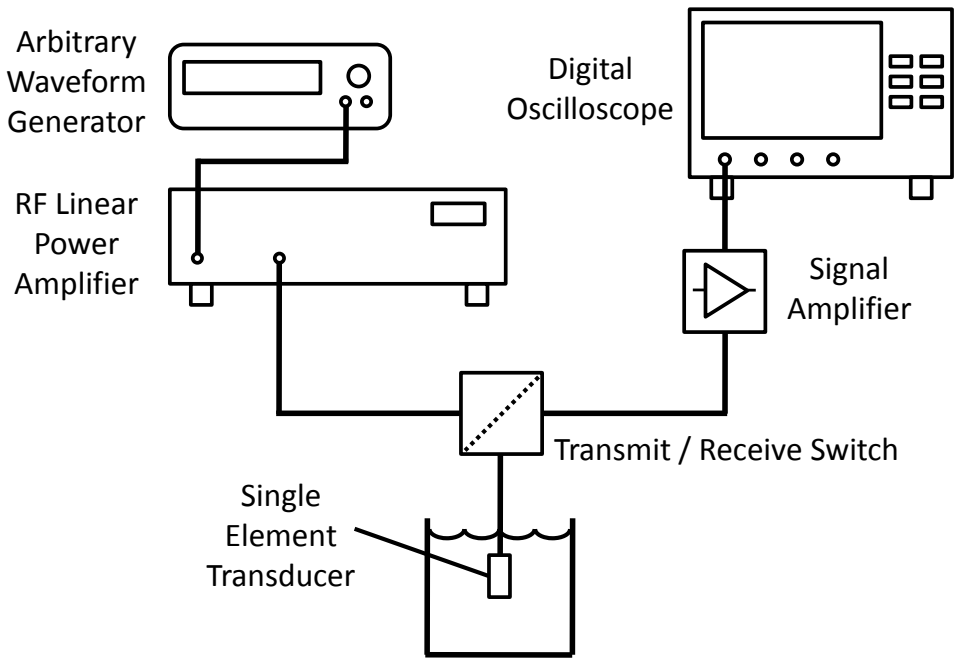

Figure 2.1: Single element transmit and receive ultrasound system with arbitrary waveform generator, power amplifier, transmit receive switch and digital oscilloscope

clinical systems are well equipped to drive array transducers, however these systems are not suited to research.

A commercial clinical system is designed to provide a medical professional with a diagnostic view of the patient in the clearest way. Clinical systems are therefore often mostly inflexible, with little access to raw data, or opportunity for quantitative or qualitative analysis of results. This is compounded by generation of a high-quality image or video file as the final output. A commercial clinical ultrasound imaging system for use with array transducers is a much more complex system than the single element example, consisting of many modules and subsystems. These are summarised in Figure 2.2

In a clinical system, many of these parameters such as transmit sequencing, and signal processing are fixed with defined functionality. Due to its nature, decisions have been made throughout the design of the system so that it is constrained within certain operative modes, with which a medical professional can be trained. In a multi-channel research system, the motivation differs. In this case, the system is required to have open functionality

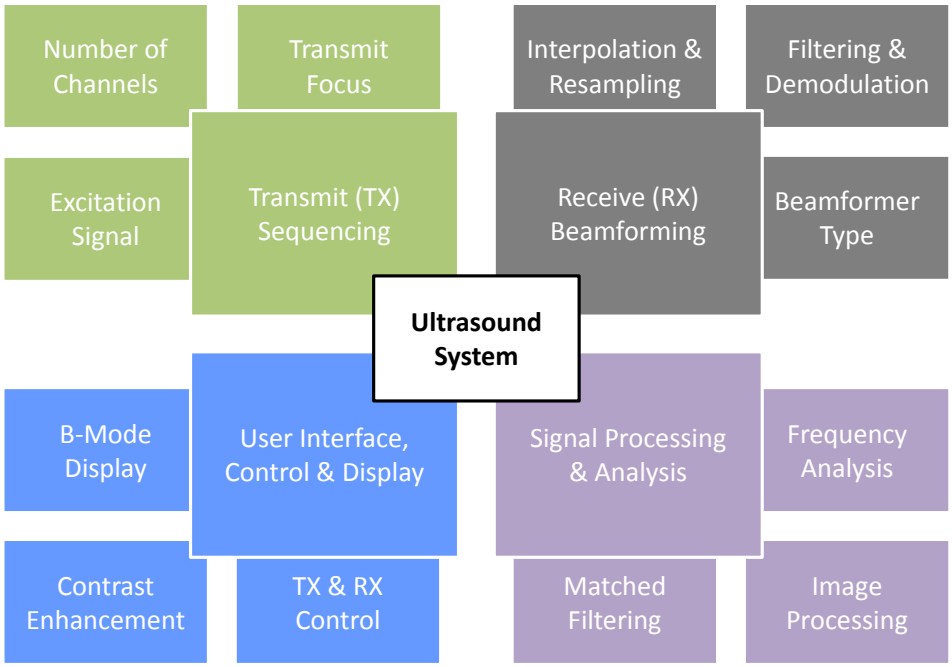

Figure 2.2: Modules defining an ultrasound system

not determined by modes or limited by user interface options. This level of flexibility is not provided to the researcher by a clinical system, therefore there is a requirement for a dedicated array platform to enable research.

In comparison with the single element research setup shown in Figure 2.1 the two systems differ widely. For example, many of the receive subsystems are built into the oscilloscope such as interpolation and filtering. However, aspects such as transmit sequencing, receive beamforming and B-Mode display require dedicated systems that can access and control multiple channels. This chapter discusses the development of an ultrasound array research platform, designed similar to commercial clinical systems, but offering the flexibility and access that a laboratory single element setup provides. An analysis of other existing research platforms and development groups are discussed, with arguments provided for the development of a bespoke research platform. Example opportunities for non-conventional operation are also discussed highlighting the impact a flexible platform can provide to the research community. Lastly, a discussion of the de-

veloped platform is provided, as well as a brief summary of other research facilitated by the platform.

2.2 Review of Existing and Current Technology

2.2.1 Single/Dual Channel Ultrasound Systems

The main issues of the setup shown in Figure 2.1 is the high cost and size per channel. Reducing the cost and size per channel whilst maintaining performance, and integrating aspects of the system such as transmit sequencing and receive storage is a desirable motivator for platform development. Single element research platforms also provide more portable solutions, requiring a single unit to be transported, as opposed to a collection of expensive equipment as shown in Figure 2.1. An example of this is a system developed by the University of Florence [23], [24] and [25] primarily for doppler processing of signals. This dual channel system was PC controlled, and used 8-bit, 64 MSPS DACs driving linear power amplifiers to generate 100 Vpp excitation signals. The reported system contained 64 MB of RAM for storage of received signals, and had dimensions of 18 x 20 x 5.5 cm.

A second example is reported in [26] of a high frame rate (130 fps) system for preclinical cardiac imaging in mice. This system used a commercial high-voltage monocycle transmitter (AVB2-TB-C, Avtech Electrosystems ltd), capable of 400 Vpp, from 50-100 MHz. This transmitter was coupled with 66 dB amplification and acquisition using a 14-bit ADC, and demonstrated cardiac imaging in mice using 40 MHz transducers. Note that the dimensions of the single channel transmitter alone are very large, at 10 cm x 43 cm x 37.5 cm.

Another example of a single-element system is discussed in [14]. This is an IVUS system, designed for flexibility, and based on FPGA technology. FPGAs are well-suited to research systems as they offer potential for continual upgrade and development. The system in [14] permitted multi-modal imaging by combining conventional IVUS imaging,

with photoacoustic imaging. To do this requires access to transmit and receive hardware, and also development and integration of a photo-acoustic transmitter within the system.

A further example is described in [27] of a flexible eight channel array system for micro ultrasound. This system used bipolar MOSFET excitation (Supertex TC6320) able to operate in the 20-80 MHz range. Received signals were sampled and interpolated using a fine-delay beamformer capable of 500 ps resolutions. The transmit beamformer had a resolution of 2.5 ns. The use of an annular array in [27] demonstrated the effectiveness of multiple elements for imaging, over single-element imaging using techniques such as dynamic beamforming. As the number of elements increases however so does the design complexity.

2.2.2 Multi-Channel Array Ultrasound Systems

Several groups have developed various multi-channel ultrasound systems suitable for use with array transducers. For example, the University of Florence have developed the ULtrasound Advanced Open Platform (ULA-OP), a highly portable array platform [28], [29], [30] based on a sigma-delta transmitter solution described in [31]. The platform has 64 channels, receive sampling of 50 MSPS with 12-bit resolution, provides access to pre-beamformed or raw RF data, is very compact at 34 x 14 x 23 cm, provides USB 2.0 connectivity to a laptop or PC and has a range of user selectable options. As a consequence, the system is very popular, and is used in collaboration with other research groups such as [32], [33]. The use of a sigma-delta transmitter stage is novel and provides high precision when representing analogue waveforms. Each channel has a sigma-delta bitstream generated by an FPGA, which is then filtered and amplified at the front end to generate high voltage output. A drawback to the system is however the excitation voltage, which is limited to 24 Vpp [28]. This limitation is presumably due to the requirement for linear power amplifiers required to amplify up to high voltage, with the sigma-delta approach replacing a high speed DAC in the system (as shown in their previous single channel platform [23], [24] and [25]). The authors themselves in [28] describe the lack of output voltage range as a potential limitation, and in a more recent paper, discuss future work to

develop a board capable of transmitting high-power square-pulses through each element when requested. The open ULA-OP research platform enables non-standard methods to be tested with ease as shown in [34], [32], [35] and [36].

A second example of a multi-channel research system has been developed at the University of Southern California. The motivation for this research group was to develop a system for high-frequency ultrasound applications ($>$ 20 MHz). Initial details of the system were provided by Hu *et al.* [37], in which a high-frequency beamformer architecture embedded on an FPGA was described. The system allowed for an aperture of 16 elements to be processed from a total of 64 channels in a linear-imaging scan. In conjunction with [37], an annular array system was also presented [38]. In 2007, Xu *et al.* [39] described the design of a bipolar pulse generator for use with the high frequency system using a Supertex TC6320 N- and P-Channel MOSFET pair transmitter circuit. The circuit operated in a switched-mode sense, with a tunable pulse-width to match to frequency. In the same year, details were published in [40] of a novel envelope detector design for use within the high frequency system.

The work in [40] also demonstrated the reprogrammable functionality of the FPGA components used. In 2010 details were published in [41] of an update to the system, which could now process 32 channels of data across 64 elements using channel multiplexing. The system had very high frame rates (reported at $>$ 400 fps) and an analogue beamformer to replace the digital design. Also included was a doppler processing unit presented in previous work [42]. In 2011 and 2012, the group published details of a high frequency AWG design suitable for high frequency coded and arbitrary transmission [43] and [44]. This deviated from the original bipolar pulse generator described in [39], and moved towards a more Class A/AB technology due to the need for very high frequency, arbitrary waveform capability.

The RASMUS and SARUS systems designed at the Technical University of Denmark are primarily targeted at synthetic array research. Details of the RASMUS system were first presented in [45], describing a system with 128 transmitter channels and 64 receiver channels, operating at 40 MHz (sampling rate) and with 12 bit precision. A key feature

of the system is the large amount of storage within the system, reported in this case as 24 GB of RAM. This enables approximately eight seconds of data to be captured, which can subsequently be analysed in post processing [45]. Further information about the RASMUS system emerged in [46], with more detailed explanation of the hardware, such as the use of 72 FPGAs. A predominant feature is the ability to capture large amount of data, and then process quickly, and has pushed the group forward in research into synthetic aperture imaging, blood flow imaging and other novel imaging modalities that demand the amount of resources available from this system. In 2007, new details emerged of a similar but expanded SARUS system, this time with 1024 channels. Sampling was at 70 MHz, with 12 bits using the latest device to device technology with 3.2 GBit/s 'Rocket' I/O links interconnects. Such is the large channel count, and high sampling rate, the system can generate 140 GB/s of data. Processing of the data is distributed across a separate Linux cluster of PCs. There are many benefits to the systems described. The processing power, storage capability and reprogrammable nature allow for novel methods and ideas to be tested easily. The large channel count of the SARUS system moves more towards 2-D array technology, and has potential for high frame rate 3-D or 4-D multi-modal imaging. The development of the system 'in-house' has enabled the group to target their specific goals, and design according to their wants and budget. Naturally this freedom does not come with an off-the-shelf solution. Such a system does comes at considerable cost however, and also complexity of both hardware and software design. Also, the large size is restrictive and a system such as this lacks portability. One of the many benefits of ultrasound is its portability when compared with other techniques such as CT or MRI scanning. Ultrasound systems are predominately portable systems that can be moved to the patients location (in a medical context) and/or around a test or inspection site. Whilst this system is in itself a research platform, large sizes may prevent ease of collaboration with other groups or departments due to the lack of portability. Another contributing factor to the system's size may be the choice of transmitter circuit (for which there exists little information in references [45] and [46]). However it is assumed based

on the literature that the system uses a DAC and amplifier solution due to use of 'linear amplifier' in several references.

A further example is a system developed by researchers in the University of Toledo, OH. [47]. This system has 128 linear transmitters, each capable of producing 144 Vpp voltage using 12 bit / 40 MHz DACs and linear power amplifiers. For the receiver side, the system has 128 12-bit / 40 MHz sampling channels, and 512 MB of memory buffer. The system has enabled the research group in [47] to investigate and demonstrate a novel limited diffraction transmit method, by enabling total control of transmit and receive parameters. The demonstrated approach seeks to remove the need for multiple linear RF transmitter circuits, that are physically large, have high power consumption and require good heat dissipation, by needing only one or two transmitter circuits. A solution such as this however limits overall system flexibility. The developed platform provides the research with access to pre-beamformed (raw-RF) data with which to perform signal processing. The hardware provides them the option to compare and contrast the proposed method with other methods known in the community.

In addition to the systems previously discussed, several commercial multi-channel systems exist. For example, the LeCoeur "Open" system by LeCoeur Electronique boasting up to 256 channels, variable sampling frequencies (10 to 80 MHz), and high voltage (120 Vpp) analogue output. Additional software options also provide control of parameters using a MATLAB scripting interface.

A second example includes the Verasonics ® system. This is a large channel-count (128 element transmit, 64 element receive) system employing tri-state (three level) pulsers with programmable waveform parameters. Other features of the system include frame averaging, and transmit apodization.

Other examples include systems by companies such as: Cephasonic (Santa Clara, CA) and their Firebird, and Griffin systems; and Peak NDT ltd. (Derby, UK) and their Micropulse MP5PA array controller system.

2.2.3 Research Interfaces

An alternative to the full development of an ultrasound system is to build a research interface to an existing system. Such interfaces are also being provided by commercial manufacturers. Research interfaces were reviewed in a paper by Hemmsen *et al.* [48]. Examples include: Hitachi's HiVision 5500 [49], the Ultrasonix 500 [50], Siemens SONOLINE Antares [51] and Visualsonics Research Interface. Research interfaces are a compromise between total system development and flexibility, however require good links with large companies, may have large cost associated with the package, and may only provide access to certain parameters as decided by the manufacturer. What is missing from research interfaces is the ability to upgrade software, re-sequence operations, or substitute existing hardware with new designs, without the backing of the commercial manufacturer. Indeed, what also may be missing is the opportunity for research at the hardware or software design stage.

2.3 Examples of Non-Standard Methods

The research systems described in the previous section have been used to research various non-standard methods. For example, development of the ULA-OP system has enabled simultaneous measurement of mechanical and haemodynamic properties of blood vessels [24], and also shown many other modes such as coded pulse-compression imaging, plane-wave imaging, combined imaging and doppler analysis, and elastography measurement [36].

The RASMUS system developed by Jensen *et al.* discussed potential for many standard and non-standard imaging methods such as linear and phased imaging, flow estimation, flow imaging, synthetic aperture imaging, synthetic aperture flow imaging and coded synthetic aperture imaging [46]. These examples show how invaluable a custom-built research system can be to a research group, and can also breed other areas of research with respect to implementation, design or methodology, imaging techniques, and signal processing.

2.4 Development of Enabling Technology

2.4.1 Motivation

Development of research systems provides a research group with greatest flexibility. Systems can be optimised for a particular research goal. Designing and developing the system in-house allows researchers access to all aspects of the design, and provides opportunity for both hardware and software development. For example, the majority of multi-channel systems described in Section 2.2.2 have opted to use DAC and power amplifier transmitter circuits in order to provide greatest flexibility in transmit, differing from commercial systems that have arbitrary waveform capability. The consequence of this is a reduction in maximum voltage output (as shown in the ULA-OP system), or the requirement for large systems with reduced portability. It is for these reasons that development of a research platform was undertaken by the Ultrasound group at the University of Leeds. As a consequence, novel aspects of implementation have been researched as part of the work discussed in later chapters. Most specifically the transmit beamformer, and switched-mode transmitter system components. To set a context for later chapters therefore, an overview of the generic UARP system is provided.

2.4.2 Overview: Ultrasound Array Research Platform

Work to develop the UARP (shown in Figure 2.3) started in 2007. The ultrasound group at the University of Leeds had previously developed single channel systems, using switched mode technology with MOSFETs as an alternative to linear RF power amplifiers as discussed by Cowell and Freear [52] and [53]. The work in [52] and [53] evaluated a multi-level transmit method suited for generating coded ‘chirp’ excitations using square-wave switched-mode approximations (or ‘pseudo-chirps’) and tapering using intermediate voltage levels. Work then started on developing an array platform incorporating the MOSFET based circuit, and based on switched-mode methods as opposed to linear power amplifiers seen in other research platforms. The MOSFET based excitation developed by [52] was then moved to a scalable platform design as described in [1]. [1] discusses the design of

an eight-channel transmitter board, with each channel capable of five-level excitation, this was then re-designed to incorporate an on-board Cyclone III FPGA (EP3C40Q240C8N, Altera). Each transmitter board was replicated to form a 96 channel transmit system. In conjunction with this, the group also designed backplane distribution boards [54], eight-channel receiver board designs [55], system software and firmware [56], [57], [58], as well as data distribution, power distribution and transducer connect boards. The current UARP system has 96 transmit and receive channels. An architectural system diagram is shown in Figure 2.4 with a summary of the UARP capability provided in Table 2.1.

Figure 2.3: Photograph of the UARP system developed at the University of Leeds

The UARP has supported publication of several journal and conference papers as well as supporting EPSRC grant and UK patent applications. As an example, a particular aspect of the technology close to the subject of this thesis is flexibility of the transmit architecture and generation of non-standard beam patterns. Work by Raiton *et al.* [16, 15, 59, 19] demonstrated manipulation and trapping of entrained particles under flow. In this

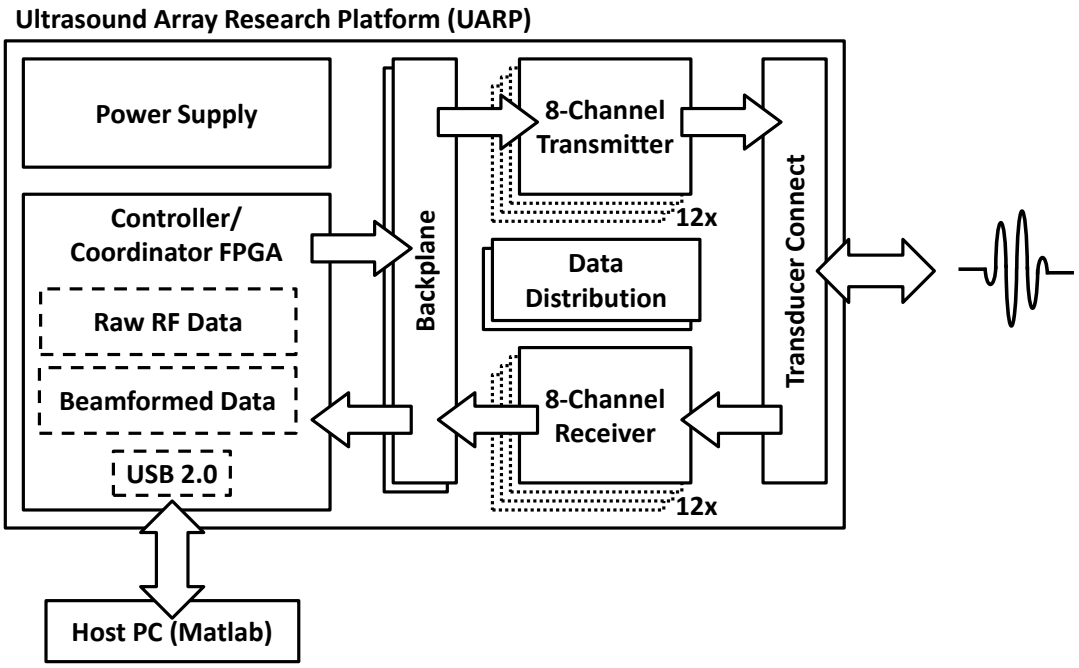

Figure 2.4: UARP system architecture

Table 2.1: Summary of UARP Features

UARP Features
96 Independent Transmit/Receive Channels
Maximum Output Voltage $\pm$ 100 V
Transmit Frequency: $<$ 20 MHz
Programmable Transmit Focusing and Steering
Receive Sampling: 50 MHz
Receive Sampling Resolution: 12 Bits
Receive Bandwidth: up to 15 MHz
Access to raw RF signals per element
Potential GPU Acceleration
Dimensions 37 cm x 34 cm x 31 cm

work, software and firmware was developed to program the UARP to generate a field for particle manipulation using travelling waves without the need for standing waves. The software enabled transmission of phase-inverted signals from half of the transducer to be transmitted by the array. An asymmetric field was produced to allow particles under flow

to be held stationary within a pressure null. The research has potential for histotripsy applications.

Similar use of the UARP technology included a randomized excitation scheme, [21], bi-spectral analysis of raw RF ultrasound data acquired using the UARP [22], and to demonstrate advances in therapeutic drug delivery mechanisms such as 'sonoporation' [20] .

2.5 Conclusions

This Chapter discussed the context for development of an enabling array research system. Examples and critique of other research platforms, including discussion of hardware architectures, and design choices has been provided, with examples of how valuable access to a research system is over a commercial system. A main conclusion is that many of the bespoke research systems have opted to use DAC and linear power amplifiers to produce more flexible excitation waveforms. This differs from the reported switched-mode technology found in commercial systems [9],[60],[61]. Previous research by Cowell and Freear [52] evaluated a multi-level switched-mode system for transmission of 'chirp' LFM signals. This technology was combined into a bespoke UARP that contains switched-mode circuits. An overview of the UARP has been presented, and provides a basis with which to explore other research areas. Development of the platform has provided the opportunity to research individual sub-components of the ultrasound system design. The following chapters of this thesis relate to research based on implementation of two major system components: the transmit beamformer architecture, and design of a transmitter scheme capable of arbitrary waveform generation using switched-mode excitation.

Chapter 3

Switched-Mode Excitation of Transducers

3.1 Introduction

Chapter 2 introduced single-channel and multi-channel ultrasound research systems developed to transmit, acquire, and process received signals. Signal transmission and reception is enabled using a transducer. This chapter discusses the properties of transducers in more detail, starting with a single element transducer as shown in the previous chapter, and then discussing multi-element array devices. Multi-element transducers are advantageous due to the ability to use beamforming techniques such as steering and focusing. These techniques will be discussed in Chapter 4. To utilise these techniques however, it is desirable to have an individual transmitter circuit per element, with the transmitter circuit able to generate large voltages and source large currents when driving a piezo-electric load.

This chapter provides an overview of the electrical properties of a transducer. A review of methods used to excite the transducer is given, followed by a discussion of other alternative amplifier technologies that may also be used. A comparison is made between the two types of amplifier circuits (analogue and digital), with the benefits of digital switched-mode amplifiers outweighing analogue types for multi-channel systems. The University

of Leeds UARP (as introduced in Chapter 2) is an example of a multi-channel system, and as such uses switched-mode technology. A more thorough description of the transmitter within the UARP is given and serves as a foundation for later chapters that describe technology control methods of switched-mode sequences within the UARP's 'front-end'.

3.2 Piezo-Electric Transducers

3.2.1 Single Element Transducers

The piezo-electric effect [8] is the fundamental principle which governs ultrasonic sensing and acoustics in general. A transducer is a component manufactured to harness the piezo-electric effect in an effective manner. A basic transducer consists of a section of piezo-electric material separating two electrodes. The thickness of the piezo-electric material is equal to half the wavelength of the desired centre frequency [62]. The most popular choice of piezo-electric material is a polycrystalline ferroelectric ceramic material, known as Lead Zirconate Titanate (PZT) [63] [64]. PZT is a man-made material which exibits a strong piezo-electric effect once 'poled', a process of heating whilst applying a large electric field (kV/cm) across the material to align magnetic dipoles within its structure along the direction of propagation. [63] [64]. The properties of PZT were first reported by Shirane and Suzuki in 1952 [65] and later by Jaffe *et al.* in 1954 [66], [67].

Application of an electric signal to the piezo-electric material causes structural deformation, and creates mechanical disturbance or vibration. This process can be described as electro-mechanical conversion. PZT is particularly popular due to its high electro-mechanical conversion factor when compared with other materials [62], and therefore is more efficient in converting electric signals to acoustic signals.

The mechanical disturbance generates a 'forward propagating' wave and a 'backward propagating' wave, of equal amplitudes but opposite polarity and direction. The forward propagating wave is primarily used for sensing within the system, and is therefore coupled into the medium. The backward propagating wave can internally reverberate within the component, generating additional unwanted pressure waves and lengthening the trans-

mission. It is therefore standard practice to attenuate or absorb the backward propagating wave using backing material [63]. Typical backing materials such as epoxy have a good acoustic impedance match to the piezo-electric material [63]. Providing a backing layer ensures that a short, damped pulse is transmitted when excited with an electrical impulse [62].

The forward propagating wave may also cause unwanted reverberation if coupled into material with a large difference in acoustic impedance. This reduces efficiency of transmission and sensitivity in reflection. Energy transfer between the piezo-electric material and the medium can be improved by using matching layers. Matching is often necessary for PZT, as it has a high acoustic impedance when compared with other materials such as tissue or water [62].

The amount of acoustic energy transmitted or reflected can be calculated using standard acoustic impedance equations for transmission and reflection coefficients [68, 67] Acoustic impedance is described as

$$Z = \rho c \tag{3.1}$$

where ρ is density of the medium, and c is the longitudinal speed of sound within the medium. The reflection coefficient, Γ, can be calculated using [69]

$$\Gamma = \left[\frac{Z_2 - Z_1}{Z_2 + Z_1}\right]^2 \tag{3.2}$$

and is a measure of the strength of reflection at a boundary between two materials with acoustic impedances Z_1 and Z_2. Ideally the transducer should minimise the value of Γ from the piezo-electric element to the medium, so that maximum transmission of acoustic energy is achieved. A final addition to the transducer may see the application of a plexiglass or polystyrene acoustic lens to focus (or de-focus) the forward propagating wave [63]. A diagram of a single-element transducer is shown in Figure 3.1.

Alternative piezo-electric materials to PZT exist such as Polyvinylidene Diflouride or PVDF, first described by Kawai in 1969 [70], [67]. PVDF is advantageous due to its low

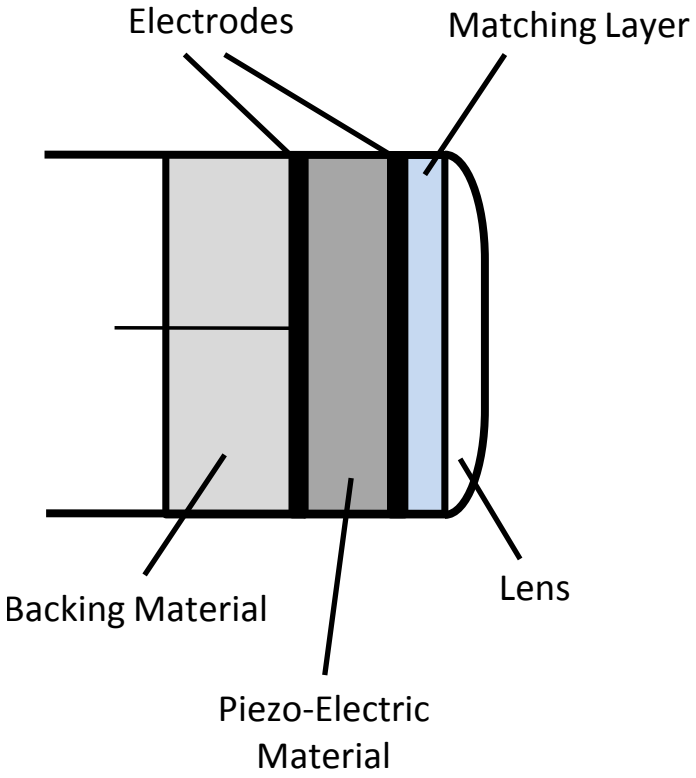

Figure 3.1: Diagram of a single element transducer

cost, low acoustic impedance, high bandwidth and flexible nature [63][67]. A drawback of PVDF however is its poor transmitting efficiency due to low mechanical coupling factor in acoustic-electro conversion [71]. As a consequence, PVDF is often used as a receiving component, in a hydrophone for example, requiring broadband response [63].

3.2.2 Array Transducers

Array transducers package multiple independent piezo-electric elements within a single assembly [63]. Multiple elements are advantageous as they provide a higher level of flexibility in both transmit and receive modes when compared with single element equivalents. Manufacture of array transducers involves a similar process of applying electrodes, acoustic lenses, acoustic backing and matching layers to each element. The piezo-electric material is ‘diced’ to form gaps between elements referred to as ‘kerfs’. Kerfs are usually filled with a highly isolating material such as air in order to reduce inter-element crosstalk [63]. At high frequencies however, the ability to dice elements for high-frequency arrays

can be problematic due to the small kerf widths required [62]. As frequencies and channel count increases, these manufacturing issues such as dicing, and interconnection increase the cost of transducer components. Figure 3.2 shows a diagram of an array transducer.

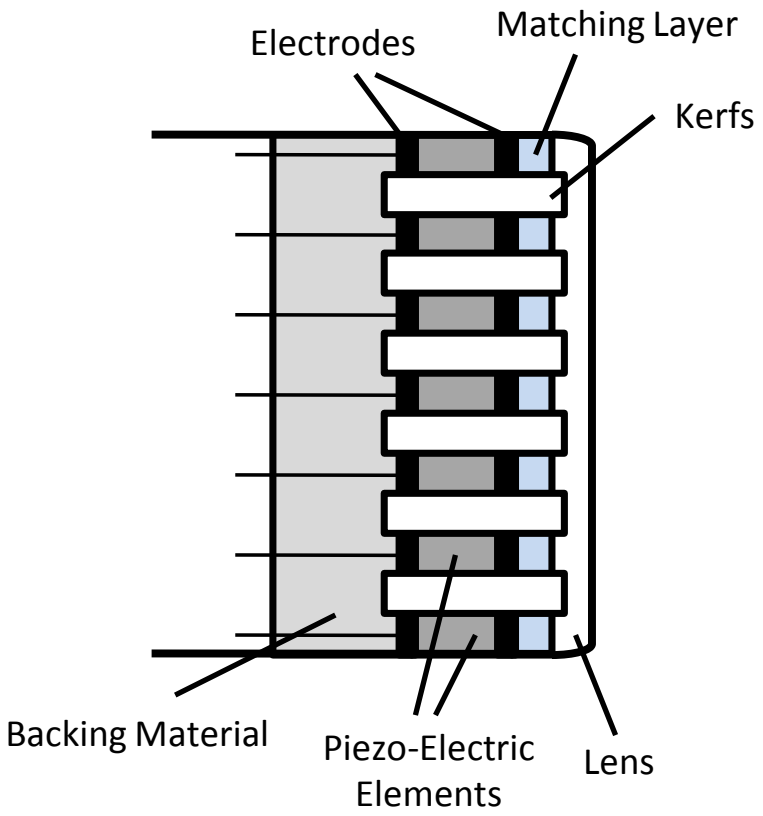

Figure 3.2: Diagram of a multi-element array transducer

3.3 Electrical Properties of Transducers

Electrically, a transducer element can be considered as a section of isotropic material sandwiched between a pair of conductive plates [67] as can be seen in Figures 3.1 and 3.2. A transducer can therefore have a capacitance, C_0, defined by

$$C_0 = \frac{\varepsilon_r \varepsilon_0 A}{d_0} = \frac{Q}{V} \tag{3.3}$$

where ε_r is the dielectric constant of the material, ε_0 is the permittivity of free space, A is the material area, d_0 is material width, Q is charge stored, and V is potential. It is known that a capacitive load causes a large inrush current from the source in response to a step

input. This can also be seen for the equation relating current to voltage for a capacitor

$$I = C_0 \frac{dV}{dt}. \tag{3.4}$$

This large inrush current can be problematic, and the capacitance of the piezoelectric element can be "tuned" by selecting a shunt inductor of value $1/(\omega_0^2 C_0)$ [63]. This tuning inductor ideally converts the impedance of the load to be purely resistive.

A transducer can also be considered as a resonant circuit due to its crystal property. The circuit shown in Figure 3.3 describes series and shunt equivalent circuits of a trans-

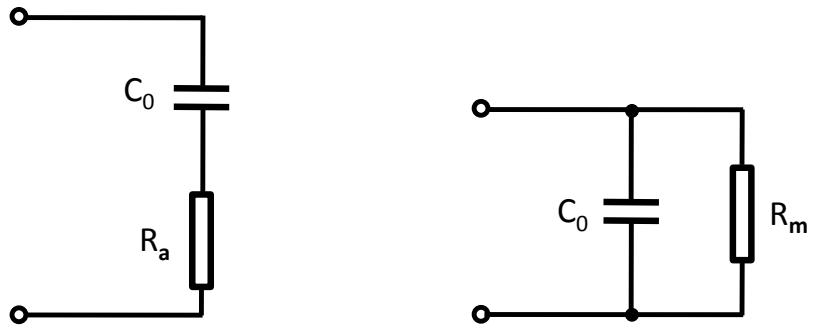

Figure 3.3: Series and shunt transducer equivalent circuits at resonance

mitting transducer at resonance [63]. Radiation resistances R_a and R_m can be calculated using

$$R_a = \frac{4k_t^2 Z_c}{\pi \omega_0 C_0 (Z_1 + Z_2)} \tag{3.5}$$

and

$$R_m = \frac{\pi (Z_1 + Z_2)}{4k_t^2 \omega_1 C_0 Z_c} \tag{3.6}$$

where C_0 is defined according to (3.3), k_t is the thickness mode electro-mechanical coupling coefficient, $Z_c = AZ$ where Z is the acoustic impedance of the piezoelectric element, ω_0 is the parallel resonance frequency at which the input electrical impedance is maximum, ω_1 is the series resonance frequency at which input electrical impedance is minimal and Z_1 and Z_2 are the acoustic impedances of the medium and transducer backing respectively. A variety of more complex models exist that define electro-acoustic interaction in greater detail. Such models can be used to simulate different transducer configurations,

and also medium propagation in programs such as SPICE. These models include the Mason model [72], Redwood's model [73], the KLM model [74], and other variations such as Leach's model [75].

Equivalent circuits permit analysis of excitation in both the electrical and acoustic domains. It can be seen from the equivalent circuit models shown in Figure 3.3, that a transducer can be classed as a resonant circuit, as discussed in other literature [76, 63, 68, 69]. The choice of materials used during transducer manufacture have great influence on the resonant properties of the transducer, including damping, impedance matching, and electro-mechanical conversion. A resonant circuit has an associate Q factor, QF, described by [62]

$$QF = \frac{f_2 - f_1}{f} \tag{3.7}$$

where f_1 and f_2 are the half-power frequencies. The Q factor describes the bandwidth of the transducer, which can therefore be thought of as a form of bandpass filter that filters electrical signals whilst converting them to the acoustic domain. Any filter will have a impulse response determined by its bandwidth and Q factor. A high Q factor indicates low damping, and longer duration impulse response. A low Q factor indicates high damping, and very short duration impulse response. The choice of materials used in manufacture alter the impulse response. For greatest axial resolution, it is best to use a low Q factor, and a very short 'shock' type electrical impulse.

Section 3.4 will now review strategies used to excite transducers effectively, to first produce short-duration impulses, and then driving transducers with longer 'coded' sequences.

3.4 Review of Excitation Circuits

Historically, two methods of pulsed transducer excitation existed. Firstly, shock excitation by discharge of a capacitor and secondly tone-burst excitation using a gated sinusoidal waveform at RF frequency [77] [78] [79]. Tone-burst excitation of the transducer was considered more complex to implement, and less effective than shock excitation,

especially as shock excitation could switch hundreds of volts quickly to create larger mechanical disturbances. For propagation in an attenuating material this is advantageous so as to increase penetration depth. As well as generating large voltages, shock excitation has potential to produce very wide-bandwidth, short-duration signals suitable for optimal axial resolution. Early examples of shock excitation circuits include the use of Thyristors and Silicon Controlled Rectifiers (SCRs), as discussed in [78], [79], [80]. Thyristors and SCRs are components that are non-conducting until a trigger voltage is applied to its gate terminal. Typical circuits using SCRs accumulate charge on a capacitor, before quickly discharging it through the SCR device, by triggering its gate. After the charge stored in the capacitor has dissipated, the SCR stops conducting. The process can be repeated once the capacitor has been charged sufficiently. An example circuit is shown in Figure 3.4, consisting of a charge storage capacitor, C, a SCR device and resistors R_1 and R_2. Note

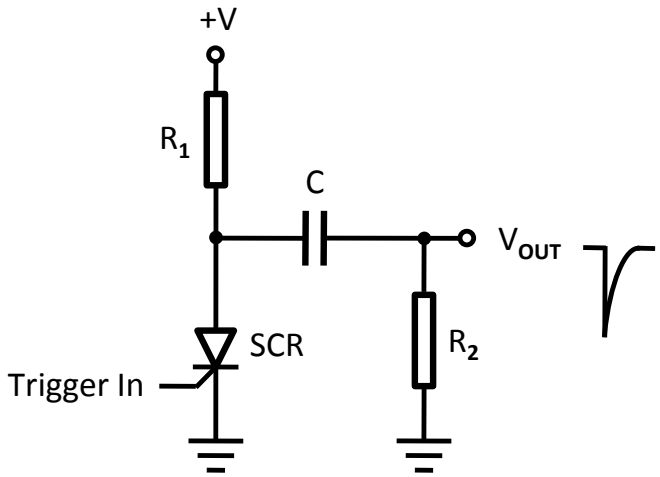

Figure 3.4: Shock excitation pulser circuit using a charging capacitor and Silicon Controlled Rectifier

that the time constant R_1C defines how quickly charge accumulates on the capacitor, and should be minimised for increased Pulse Repetition Frequency (PRF) [78]. C however should be maximized so as to accumulate most charge [81] without exceeding the capabilities of the SCR [78]. As a consequence R_1 (most often the source impedance) should have a low value. Resistor R_2 is used as a discharge resistor, and should be kept small in

order to dissipate energy quickly. A practical example of this circuit was demonstrated by Okyere and Cousin [78] capable of switching 1000 V in 100 ns with a PRF of 1000 Hz.

In the 1980's SRCs were being replaced by high power Field Effect Transistors (FETs) as shown in Figure 3.5. This substitution was necessary, as although SCRs could turn on

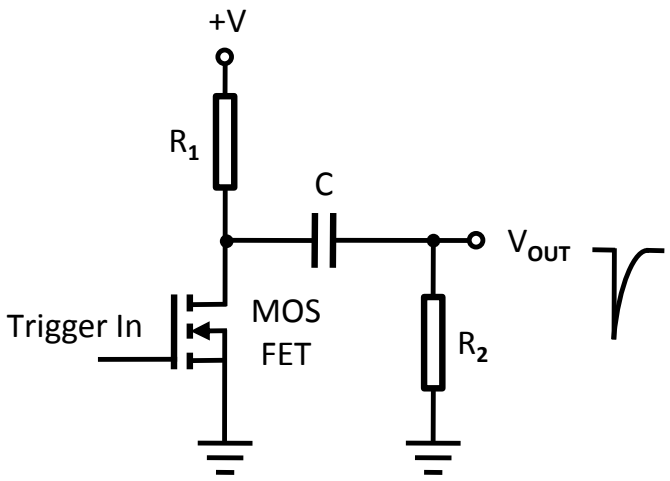

Figure 3.5: Shock excitation pulser circuit using a charging capacitor, and N-channel MOSFET in-place of a SCR

and dissipate charge quickly, turning the devices off again was more problematic. Mattila discussed this issue in [79] showing the decrease in rise time for a negative unipolar pulse, after direct substitution of a power MOSFET for the SCR. This improved rise time enabled shorter duration, wider bandwidth pulses to be produced without sacrificing switching voltage. A paper by Persson [82] used a collection of different MOSFET transmitter configurations to investigate how the shape of the electrical excitation signal altered the pulse-echo response of the transducer. Persson [82] demonstrated that using rectangular pulses generated greater pressure response than 'impulse' or 'spike' excitation, and that the use of bipolar excitation generated larger pressure amplitude as a consequence of a sharp leading and trailing edge. During this period, Hayward described that the majority of ultrasound systems had now adopted some form of switching circuit for transducer excitation [81]. [83] continued pursuing the use of MOSFET excitation circuits, discussing a link between the need for independent control of multi-element devices. In the same

year Martin [80] also demonstrated how variation of pulse width could produce ultrasonic pulses optimised for resolution or maximum amplitude.

In the 1990s, led by work in RADAR techniques describing frequency modulated square wave excitations by Johnston [84], several authors such as O'Donnell [85], and Pollakowski [86] explored the use of switched-mode circuits to generate similar, frequency modulated waveforms for ultrasound coded imaging. O'Donnell in 1992 described the use of a 'pseudo-chirp', showing a switched-mode binary approximation of a sinusoidal coded waveform, generated using discrete voltage levels [85] similar to those shown by Johnston [84]. Pollakowski in 1994 also discussed the advantage of switched-mode pseudo-chirp excitations for coded imaging over DACs and broadband amplifiers [86] and potential for non-linear chirp generation that differed from use in RADAR. In 1999, two switched-mode d.c.-to-RF power inverter designs (single-ended and full-bridge) were used to successfully drive a 1 MHz transducer for ultrasonic cleaning [87]. In a comparable paper [88], the use of a Class D inverter was also shown to be beneficial for a similar application. The choice of Class D in [88] over other analogue amplifier technologies was due to cost and efficiency. These designs showed the potential of switching-mode circuits for use in very high power applications such as ultrasonic cleaning, acoustic cavitation or therapeutic high intensity focused ultrasound (HIFU). In 2002 Brown and Lockwood [89] described the design of a low-cost pulse generator capable of 10 kW pulses ranging from 10 to 500 ns. A push-pull switching circuit was used to generate a unipolar, negative shock excitation, with very low ripple and short duration. In 2006 Haider, working for General Electric, described bipolar and multi-level switching circuits now commonly used in ultrasound technology [9]. In [9] Haider described, unipolar, bipolar and three level circuits, whereby the transducer is charged to a potential and then discharged either through a resistor, or by a return to ground (return to zero) switch. In 2007 Xu *et al.* extended the work in [89], designing a circuit capable of generating bipolar switched-mode excitations, for use with very high frequency (> 50 MHz) array transducers. Up to the present day many other examples exist of switched-mode techniques for high voltage excitation as described in literature such as [52], [13], [90], [14], [12], and

in patents such as [91, 61, 60]. However, recent authors such as [14] and [92] have discussed the use of different amplifier classes to describe more arbitrary waveforms, due to a limitation in arbitrary pressure output from switched-mode excitation using three or five levels [92]. The recent literature included designs of high voltage analogue amplifiers for transducer excitation. For example, Gao and Gui described the use of a Class A/B amplifier design with a pre-distortion technique to account for non-linearity, over high voltage switched-mode pulsers [92]. Qui *et al.* described the design of a multi-purpose pulse generator incorporating high voltage switched pulsers, and also the use of a three stage amplifier chain, required due to the lack of control over pulse characteristics provided by switched-mode pulser circuits. Later chapters of this thesis investigate this limitation. For now however, it is important to discuss alternative amplifier technologies, and compare them against the switched-mode methods discussed in this section.

3.5 Summary of Amplifier Technology

Amplifiers can be categorised into classes such as A, B, C, D, E, and F [93] and further classified as switching or non-switching. An analogue, non-switching amplifier takes a continuous signal and increases its power or voltage according to a gain (the ratio of input to output) [94]. A switching amplifier class will generate a switched-mode output, which is a modulated representation of the input. Analogue amplifier classes are Classes A to C. Switching amplifier classes are Classes D to F.

The simplest amplifier is a Class A amplifier, which usually consists of a single biased transistor device, operating in a linear mode, that conducts in proportion to the input signal. A Class A amplifier can be described as having a conduction angle of 360°or 2π [93]. The term conduction angle describes the period with which the output stage is conducting in response to an input of a single sinusoidal cycle. A conduction angle of 360°means that the the output stage conducts throughout the whole cycle. A Class A amplifier consequently has a large quiescent current and dissipates power in the form of heat, with or without an input signal [95]. Power dissipated as heat raises the temperature of the output stage, increases the temperature of surrounding components causing them greater stress,

and can result in accelerated failure [93]. To deal with the large amount of power dissipation, Class A amplifiers require heat sinks, and/or circulating air to assist cooling. Heat sinks are heavy, bulky and expensive [93] however are almost always necessary for high power Class A designs.

A Class B amplifier amplifies a single positive or negative cycle, and is therefore non-conducting for half a period, or has a conduction angle of 180°[93]. Class B amplifiers are rarely found in isolation (as they reject half of the signal) but are usually found in a push-pull configuration, with each device conducting according to the positive or negative half cycle applied. Note that a Class A amplifier can be push-pull also, using two devices, with the input signal to one device phase-inverted. In a Class A push-pull configuration both devices are still conducting, therefore both angles of conduction are 360°. Class B (push-pull) amplifiers suffer from crossover distortion when the input signal is lower than the bias voltage of either of the devices [95]. This creates a 'deadzone' around zero volts, equal to twice the voltage drop of the device used.

A Class A/B design biases each of the push-pull transistors so that at low input signals the amplifier operates as Class A, and at zero input both devices are conducting, but at high input signals operation resembles Class B [93]. Class A/B systems provide best compromise between the continuous conduction from Class A, and the crossover distortion from Class B designs. The conduction angle of a Class A/B amplifier is dependent on how much each device is conducting in its usual Class B stage.

Amplifiers classes such as Class D operate differently. A Class D amplifier converts an analogue input signal into a set of switching states by means of modulation. The most common form of modulation is to alter pulse width by comparison with a triangular carrier [93]. The modulated representation of the waveform is then amplified using a switching output stage (usually some sort of FET device) that selects a voltage level. In its simplest form, a Class D amplifier will only switch between two levels, often a ground state, and another voltage in a push-pull configuration. Most applications require a filter to reconstruct or demodulate the switched output signal from the input signal. The output transistors draw no current when not conducting, and have very low V_{DS} drop when

they are conducting [94]. As a consequence Class D amplifiers are highly efficient when compared with other analogue classes.

Class D amplifiers rely on switching at a rate quicker than the reconstruction filter can respond, thus providing a time-averaged output. Inefficiency of Class D amplifiers however, comes with high switching rates, where multiple high frequency commutations cause power loss. Switching loss is attributed to continual charging of MOSFET gate capacitance at frequency [93] [94], C_G, where

$$P_{Loss} = C_G V^2 f_{sw}. \tag{3.8}$$

Minimizing the switching frequency f_{sw} reduce switching losses, at a risk of output waveform degradation.

Class D amplifiers operating with pulse-width modulation are seen as the future of amplifier technology due to their high efficiency, small size and power capability. Alternative switching amplifiers such as sigma-delta modulators, have also been widely adopted that use other modulation types, such as pulse-density modulation (PDM). Switched-mode class D amplifiers save on cost, and also require less heatsinking due to lower power dissipation than analogue amplifier technologies [93]. As a consequence, switched-mode circuits that can switch high currents at high speed are advantageous for piezo-electric excitation. The next section details how Class D switching technology has been incorporated into the UARP, due to its benefits over analogue solutions for multi-channel excitation.

3.6 Enabling Technology: Ultrasound Array Research Platform (UARP)

Section 3.5 described the advantages and disadvantageous of many of the amplifier technologies briefly covered in Chapter 2 when describing bespoke research platforms. Chapter 2 also briefly discussed the development of the UARP system. This will now be discussed in greater detail.

The UARP transmitter consists of a multi-level MOSFET circuit as discussed in [52]. Section 3.4 described the development of switched-mode circuits for ultrasound from SCR controlled capacitor discharge, to the multi-level MOSFET circuits in the design of the UARP. Indeed commercial manufacturers such as Supertex, Texas Instruments and Maxim IC have developed integrated circuits packaging multiple power MOSFETs, MOSFET drivers, and level translation circuits for multi-level switched-mode excitation of transducers. In the case of the UARP, six MOSFETs are packaged within a single MAXIM 4811 (MAXIM Integrated Technologies), [96] device, with one device providing quinary-level excitation signals per channel. A portion of the circuit is shown in Figure 3.6 and can be explained as follows. T1, T3, and T5 are P-channel, enhancement mode MOSFETs, whilst T2, T4, and T6 are N-channel enhancement mode MOSFETs. Enhancement mode means that conduction (of electrons or holes) increases with increasing input signal. T5 and T6 are included to return the output to ground in order to truncate the pulse as discussed by Haider [9] and [52]. Each switching-device is controlled by a MOSFET driver (not shown in Figure 3.6) internal to the MAX4811 device. The MOSFET driver enables CMOS-logic level input (0 to 3.3 V) to control each MOSFET. A single UARP transmitter board houses eight MAX4811, with each device's MOSFET CMOS inputs controlled by an Altera Cyclone III (EP3C40Q240C8N) FPGA. Figure 3.7 shows an annotated photo of the transmitter board. The role of the FPGA is to control incoming instructions within the system, and directs the switching of each channel's device. The use of an FPGA enables controlled switching of each channel in parallel. Consequently, the work described in later chapters is dependent on the flexibility and individual control of each channel using the on-board FPGA.

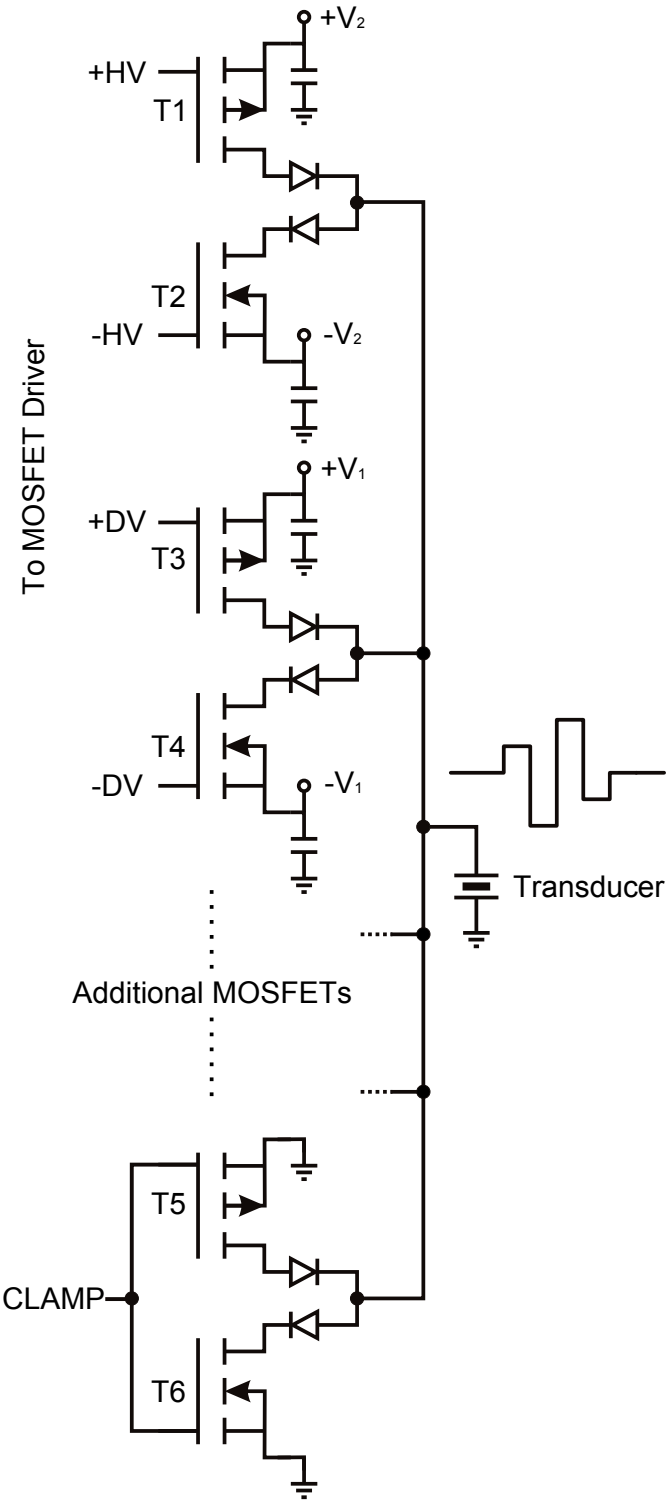

Figure 3.6: Multi-level MOSFET circuit (five levels shown with return to zero)

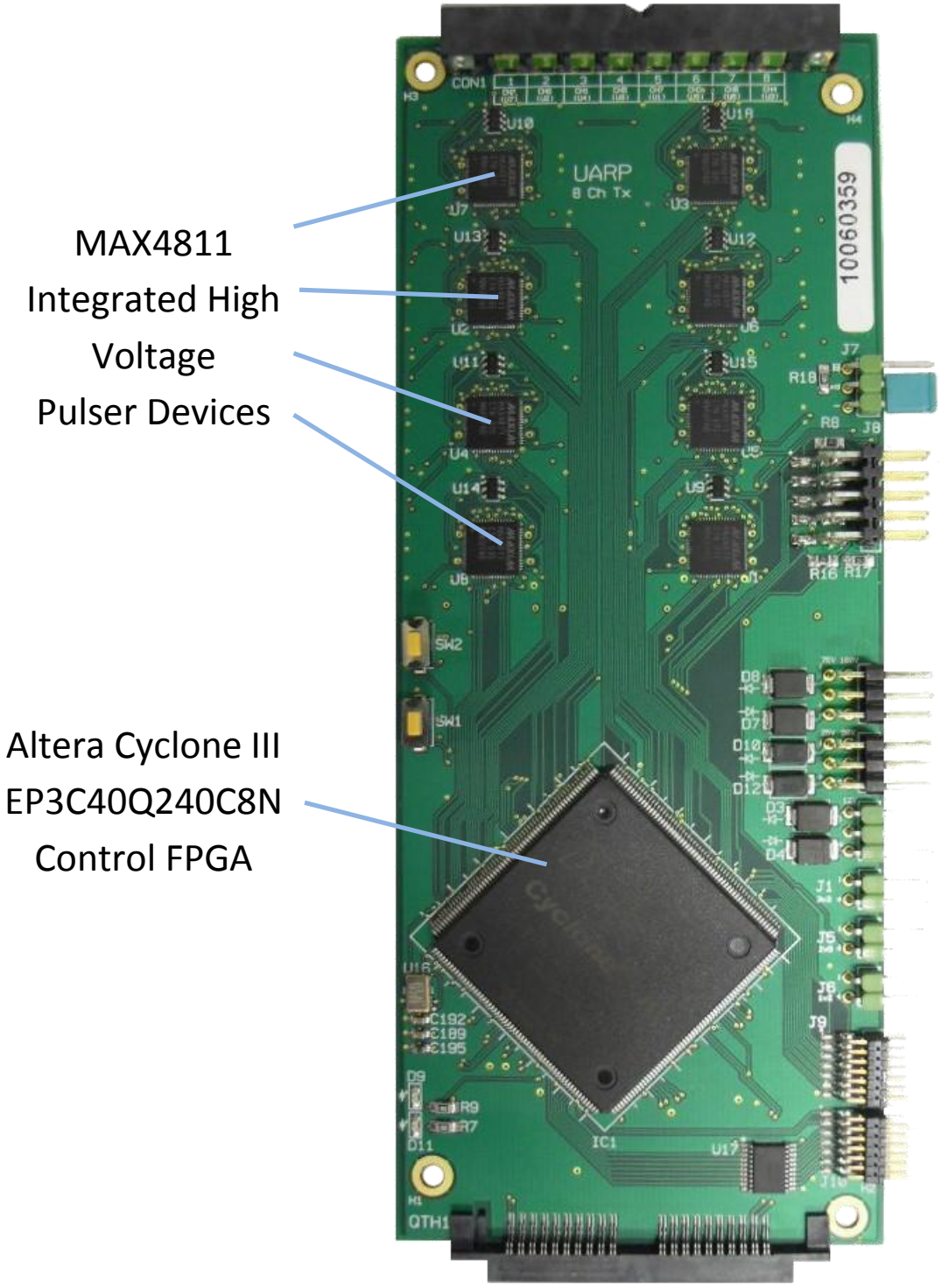

Figure 3.7: Eight-channel UARP transmitter board

3.7 Conclusions

This chapter discussed the properties and composition of single element and array transducers, giving explanation as to how a transducer can be modelled and the requirements for excitation. The advantages of 'shock' excitation over sinusoidal tone burst signals were discussed, particularly with respect to the ability to quickly switch-large voltages using switching circuits such as SCRs and MOSFET devices. The evolution of switched-mode circuits for piezo-electric excitation were also introduced as discussed in Brown and Lockwood [89], Haider [9], Xu [39] and Cowell and Freear [52]. These switched-mode circuits are used as an alternative to analogue amplifier technologies such as Class A, B and A/B devices. In terms of cost, size, and power consumption, Class D amplifiers operating in a switched-mode are more suited than other analogue amplifier technologies for use with array transducers, where multiple elements require multiple transmitters. There are however recent examples such as [92, 14] that discuss a lack of flexibility of switched-mode circuits, instead opting to favour analogue designs for transmitter circuits.

The latter part of the chapter, presents the UARP transmitter design. This design uses multi-level MOSFET high voltage pulser integrated circuits, co-ordinated by a local FPGA, and operated in a switched-mode. The following chapters of this thesis describe how each pulser chip is controlled by the FPGA. Future chapters examine encoding of switching signals, with pulse-width modulation, i.e. controlling the time with which a particular MOSFET is conducting in response to a desired input, and with consideration of the resonant nature of a transducer element as described in this chapter. Chapter 4 discusses how inter-element sequencing of excitation, i.e. delaying the MOSFET switching control signals sent from the FPGA to each pulser device can alter the nature of the transmitted field profile.

Chapter 4

Switched-Mode Timing Control

4.1 Introduction

Chapter 3 described how piezo-electric material is packaged with electrodes and other auxiliary components to form single element and multi-element array transducers. Multi-element arrays ideally require an dedicated transmitter circuit per element, for maximum flexibility. Also discussed within Chapter 3 was the use of switched-mode circuits to excite transducer elements. These switched-mode circuits may be unipolar, bipolar or multi-level switching configurations that provide 'shock' excitation, or stepped or square-wave approximations to analogue excitations. There is a distinct advantage of switched-mode methods over analogue amplifier technologies especially for large channel-count systems, and permits the use of different waveforms per element, and also enables control of inter-element sequencing. Excitation sequencing control can be used to form acoustic beams of pressure by combining contributions from multiple elements (known as beamforming). Beamforming is achieved by applying electronic delays to signals. This technique is known as array phasing [97] due to continuous wave signals requiring a phase difference between signals for beam manipulation. Such beamforming methods rely on the ability to manipulate inter-element timing of excitation signals - specifically in the context of the UARP, switched-mode trigger signals that excite the transducer and generate the desired beam profile. These switched-mode signals are generated, and delayed by each transmitter board's FPGA. Using beamforming techniques, beams of pressure can be focused to

a point and/or steered ‘off-axis’ providing greater directivity and sensitivity for identifying targets. The use of different waveforms per element alongside beamforming can alter the characteristics of the beam and reduce pressure levels in regions outside of the main beam, and is known as apodization.

The most prevalent effect on the characteristics of the radiated beam however is determined by the position and arrangement of sources within the array transducer. Position of sources, excitation sequencing and per-element excitation are the main topics discussed in this chapter, and are addressed as follows. Firstly, a description of common physical arrangement of elements within transducers is provided. The position of elements impacts on beamforming techniques which in turn relies on accurate sequencing of excitation signals. Poor sequencing accuracy introduces phase quantization error (as opposed to amplitude quantization error), which can adversely alter the radiated beam profile, as can other forms of random error. A discussion of the types of phase quantization error is provided as well as examples shown in simulation. To combat poor sequencing accuracy, the latter part of the chapter describes the design of an embedded hardware architecture for a transmit beamformer, as used within the UARP. The design is able to dynamically adjust switched-mode trigger signals to give high timing precision and reduce phase quantization error in sequencing. The method described can also be used to correct other sources of error such as phase aberration effects caused by a non-homogeneous medium. Firstly however, the physical aspects of array transducers are discussed.

4.2 Array Transducers

Transducers are application specific components due to different sensing modalities requiring ultrasound to be transmitted and received from different positions. The performance of the transducer when used with steering and focusing is directly affected by the distribution of elements. Naturally, the arrangement of elements affects the coverage of the radiated ultrasound, as well as the ‘field of view’ with which the transducer encompasses.

The most common arrangements are shown in Figure 4.1 [98], [62] [99]. These in-

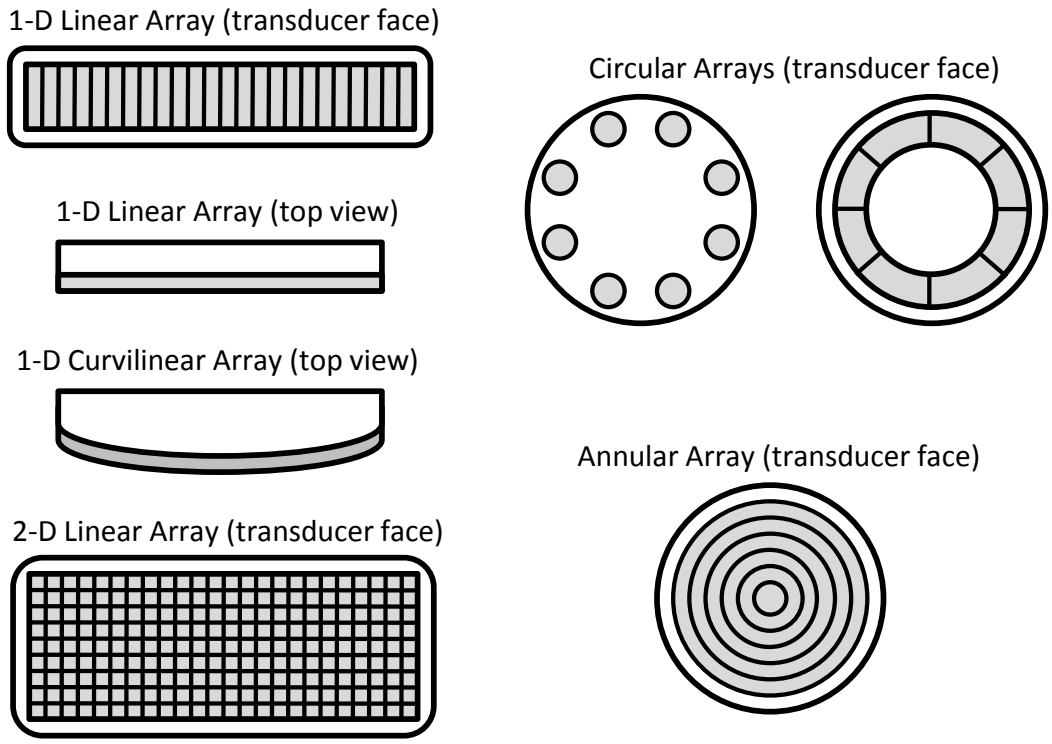

Figure 4.1: Common transducer types

clude linear, curvilinear, annular and 2-D array patterns [98] [62] [99]. The most common of which is the 1-D linear array.

4.2.1 Linear Arrays

Linear 1-D arrays as shown in Figure 4.1 are the most common and simple transducer arrangements, and are composed of a row of elements enabling both focusing and steering in the x,z plane. Focusing in the elevation y,z plane can be achieved with a suitable acoustic lens [63].

Linear arrays enable two of the most popular types of imaging to be conducted; linear-phased and phased-linear [69]. These terms are often shortened to linear-array and phased-array imaging. The term phased-array is potentially misleading however, as both linear and sector imaging rely on phased-array techniques such as focusing, with sector imaging utilising steering and focusing. Other more advanced imaging methods such as compound plane wave imaging, utilise steering only. In all these examples the use of signal phasing or phased array techniques to steer or focus beams is required. In

this case, the imaging types have been defined as linear imaging and sector imaging as shown in Figure 4.2.

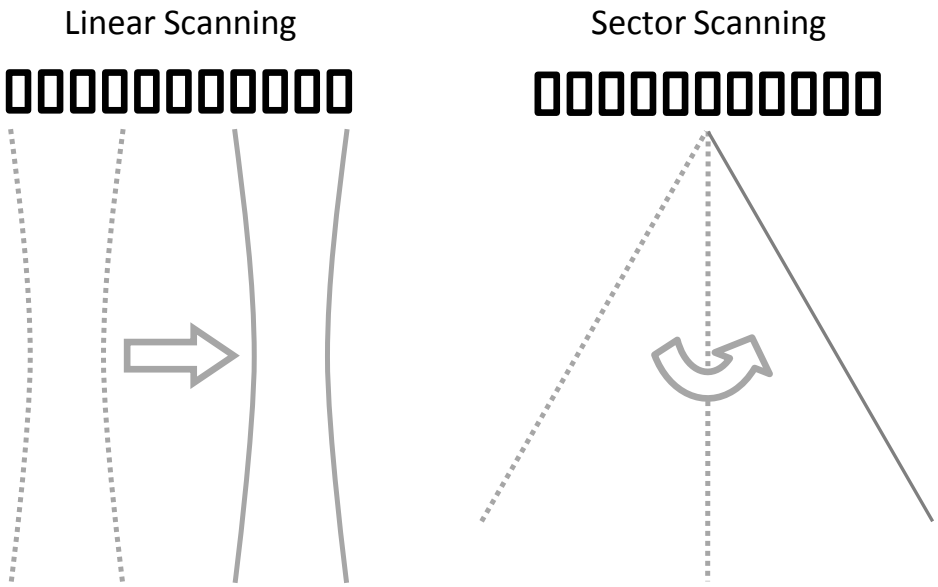

Figure 4.2: Example 1-D linear array transducer imaging modes

Linear imaging with a 1-D linear array uses a subset or collection of elements transmitted towards a focal point. The same subset of elements is used to receive the reflected ultrasound, with each element's contribution coherently summed to form a single image line. A full image is formed by moving the subset of elements or 'aperture' along the face of the transducer by a single element, and transmitting and receiving another line. As a result, the image formed is rectangular and does not extend beyond the width of the transducer.

Sector imaging with a 1-D linear array typically uses all elements to transmit at a particular focal depth and at a defined angle. All elements are also used in receive, with beamforming techniques used to steer to an angle and focus to a point along the scan-line. Additional image lines are acquired by moving to different angles. As a consequence, the image formed is 'fan' shaped potentially allowing for regions greater than the width of the transducer to be imaged.

4.2.2 Additional Array Types

Table 4.1 provides a summary of the other array types shown in Figure 4.1. Note that some of the transducer types shown have different modes of operation, most will use phased-array techniques for optimum results.

Array Type	Description	Comments
Curvilinear	Elements arranged on a curved surface.	Generates an approximately trapezoidal image.
	Linear imaging is applied.	Little use of phased-array techniques.
Annular	Coaxially aligned concentric rings of piezo-electric material	Enables spherical focusing but not steering, which requires mechanical translation.
Circular	Composed of elements in a ring structure.	Enables spherical focusing but not steering
2-D Linear	Grid like arrangement of elements.	May operate in linear or sector scanning mode.
	High flexibility in beam manipulation.	Permit 3-D and 4-D imaging.

Table 4.1: Overview of different array types

4.2.3 Definition of Array Geometry

The transducer types discussed in Figure 4.1 and Table 4.1 are different physical arrangements of multiple elements, however many of these conform to the generalised geometry of a linear 1-D array, as shown in Figure 4.3. A linear 1-D array is the most common

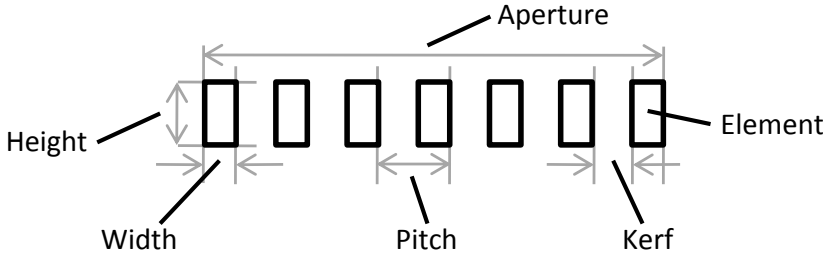

Figure 4.3: Generalised transducer array geometry

of array types and is also used mostly throughout the rest of this work. It can be seen that each of the elements in the linear array has a defined height, width, and kerf between elements as a described in Chapter 3. The total distance between elements (taking into account element width and kerf) is known as the pitch, d, where

$$d = \text{kerf} + w \tag{4.1}$$

where w is the element width.

A subset of N elements is defined as an aperture as described in the linear imaging case. An aperture has a size D defined by [100]

$$D = Nd \tag{4.2}$$

4.3 Beamforming

A single piezo-electric element excited by an electrical impulse will vibrate and produce a pressure wave. The properties of this pressure wave can be described by the element's impulse response as discussed in Chapter 3. In the simplest case, if the element is considered a point source then a spherical wavefront will be produced. A linear 1-D array of point sources generates an array of wavefronts that can sum coherently to generate a plane wavefront, travelling perpendicularly away from the row of point sources. This summation is in accordance with Christian Huyghens theory of constructive and destructive interference. The principle of constructive interference can be used to form and steer beams by controlling the sequencing of firing. Note that also in the real case, array transducers are not composed of point sources, but of elements with width and height as shown in Figure 4.3. These physical characteristics can have impact on the direction and directivity of the wavefront as discussed in various literature such as [101, 98].

4.3.1 Steering

Steering or deflection of the plane wave as shown in Figure 4.4 can be achieved by applying a linearly increasing delay profile across the linearly spaced aperture.

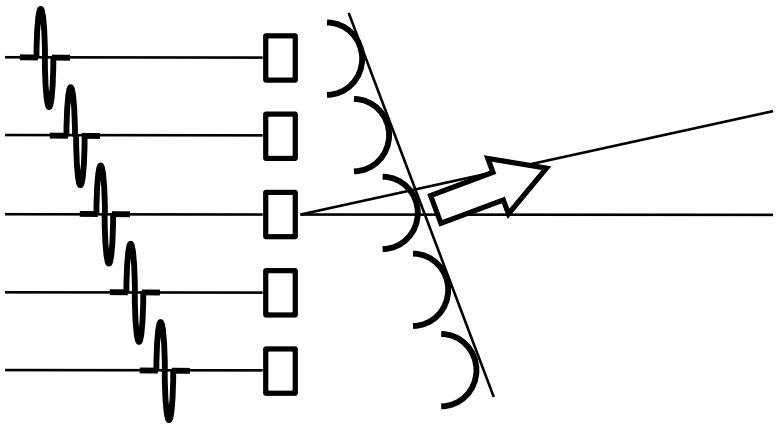

Figure 4.4: Steering of a beam with a linear array of elements

The delay between adjacent elements τ_n, to deflect the plane wave at an angle θ_s, is equal to [102] [103]

$$\tau_n = \frac{d \sin \theta_s}{c} \tag{4.3}$$

Steering of a beam electronically, removes the need for physical or mechanical manipulation of the transducer device (as is necessary for single-element transducers), and enables a beam to sweep across a region by electronic control of excitation timing.

4.3.2 Focusing

An unfocused wave radiated from a transducer of N elements at an angle θ_s will insonate an area approximately the same width as the aperture. This unfocused wave will eventually start to diverge after the natural transition distance z_{TR}. The region before the transition distance is known as the near field or Fresnel region. The region from the transition distance and beyond is known as the far field or Fraunhofer region. Definitions of these regions are shown in Figure 4.5.

An unfocussed wave has low lateral resolution. Resolution can be increased for a particular depth by focusing the beam towards a point as shown in Figure 4.6. Focusing

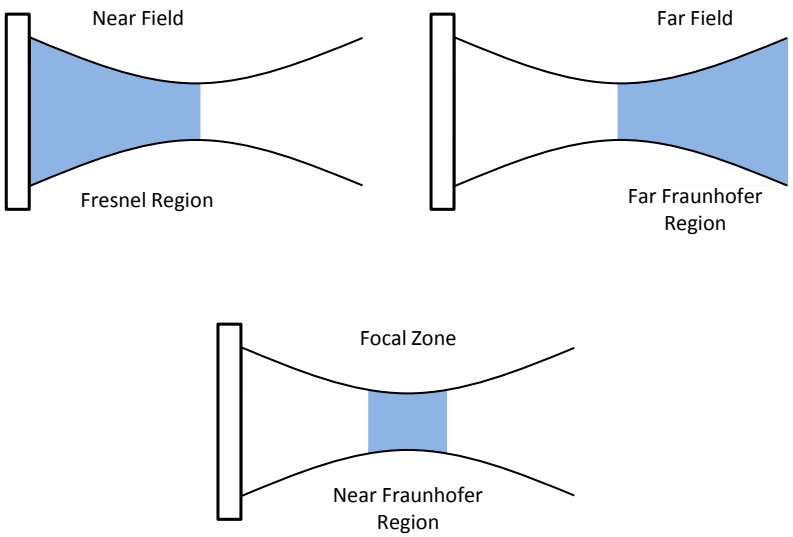

Figure 4.5: Definition of near field and far field as well as Fresnel and Fraunhofer regions

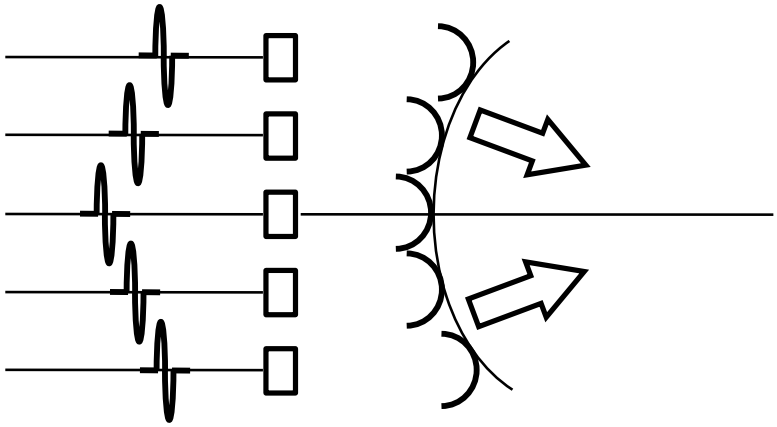

Figure 4.6: Focusing of a beam with a linear array of elements

deposits energy to a focal region in transmit, and increases sensitivity at a particular point in receive. Focusing brings the crossover point between the near field and far field shown in Figure 4.5 closer to the transducer face. Targets within the focal region are subjected to larger acoustic pressures, as the energy from all elements is directed towards the focal region. This results in stronger reflections from targets within the focused beam as a result of larger input pressure. Targets outside of the beam are subject to less energy, and consequently exhibit lower reflections. The ability to focus an array is determined by the physical size of the array, and is restricted by the transition distance z_{TR} [103] where

$$z_{\mathrm{TR}} = \frac{D^2}{4\lambda}. \tag{4.4}$$

Arrays can only be focused in the region between z_{TR} and the transducer's face. Beyond z_{TR}, focusing has no effect. Focusing to a distance z_{F} can be achieved by applying a parabolic delay profile as described by [69]

$$\tau_n = \frac{1}{c}\left[\left(z_{\mathrm{F}}^2 + (N-1)^2\, d^2 / 4\right)^{1/2} - \left(z_{\mathrm{F}}^2 + (n\,d)^2\right)^{1/2}\right] \tag{4.5}$$

where τ_n is the per element delay, and

$$-\frac{(N-1)}{2} \leq n \leq \frac{(N-1)}{2}.$$

This focusing formula can be defined in a variety of ways, for example as in [103]. The work in [103] discussed the applicability of (4.5) compared to other derivations taking into account element number, and the use of negative time such as those described in [104], [68] [69].

4.3.3 Combined Steering and Focusing

Combining steering and focusing gives greatest manipulation of an ultrasound beam as shown in Figure 4.7. This is achieved by combining the parabolic focal delay profile with

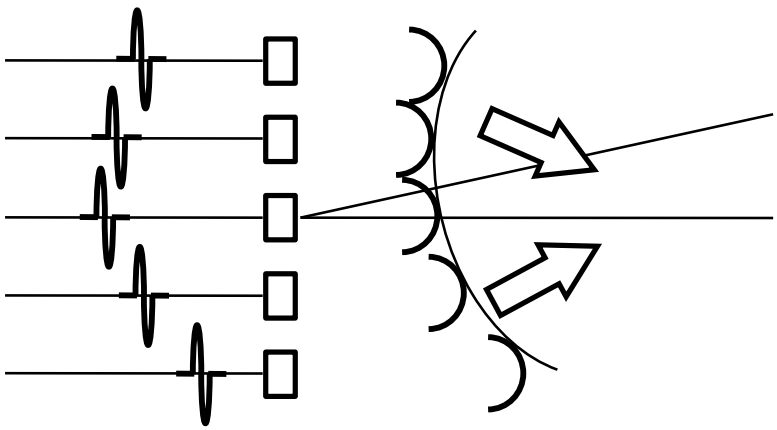

Figure 4.7: Combined steering and focusing of a beam with a linear array of elements

the linear steering profile, with per-element time delays calculated using [69]

$$\tau_n = \frac{1}{c}\left[\left(z_{\mathrm{F}}^2 + (N-1)^2 d^2/4 + (N-1)\, z_{\mathrm{F}} d \sin|\theta_s|\right)^{1/2} - \left(z_{\mathrm{F}}^2 + (nd)^2 - 2n z_{\mathrm{F}} d \sin\theta_s\right)^{1/2}\right] \quad (4.6)$$

where $-\pi/2 \leq \theta_s \leq \pi/2$ and $-N \leq n \leq N$.

4.4 Grating Lobes

For linear imaging it is desirable for the transducer to cover a wide scan area. Consequently, the field of view is maximised by increasing d, and reducing N (in this case the number of elements in the sub aperture). Increasing d enables the transducer scan a wider area, whilst reducing N increases the number of lines within the image.

For sector imaging it is desirable to sweep across the largest range of angles. For this modality, a large value of d limits the angular region that can be scanned due to the presence of grating lobes. Grating lobes are unwanted replicas of the main beam located within the field, caused by periodically spaced sources that are simultaneously excited, constructively interfering in the transmitted field. For an unsteered array, grating lobes occur at angles defined by [63]

$$\theta_G = \sin^{-1}\left(\frac{l\lambda}{d}\right) \quad (4.7)$$

where l is an integer in the range $-2, -1, 1, 2$ etc. During steering, grating lobes can cause reflections from targets in the field of view of the transducer, but outside of the main beam, thus causing interference. The angle of these grating lobes considering steering angle is defined by [102]

$$\theta_G = \sin^{-1}\left(\sin\theta_s - \frac{l\lambda}{d}\right). \quad (4.8)$$

The maximum steering angle without grating lobe interference, θ_{MAX}, can be calculated using [102]

$$\theta_{\mathrm{MAX}} = \sin^{-1}\left(\frac{\lambda\,(N-1)}{dN} - 1\right) \tag{4.9}$$

Several strategies exist to alter the position, and reduce the magnitude of grating lobes. For example, in phased-array probes used for sector scanning, transducers fabricated with $d < \lambda/2$ moves the position of grating lobes to beyond 90°, positioning them behind the transducer face. Arrays with $d < \lambda/2$ are said to be 'fully sampled' according to Nyquist criterion [63]. However, if $d > \lambda/2$ and grating lobes are within the field of view, the magnitude of the grating lobe can be reduced by increasing the width of transducer elements, and through the use of short, broadband pulses as discussed by Drinkwater and Wilcox [98].

Grating lobes are an example of pressure being distributed at undesirable locations away from the main beam. Any excess pressure throughout the field reduces the sensitivity of the main beam and can cause distortion during image reconstruction. A second example of undesired pressure distribution can occur due to inaccuracies in transmit or receive beamforming. This is known as phase quantization error, and can give rise to effects similar to grating lobes depending on the type and magnitude of the error.

4.5 Phase Quantization

Phase or time quantization is the rounding or sampling of theoretical inter-element delays τ_n such as those calculated with (4.3) (4.5) or (4.6) to delays of defined precision. The level of precision is determined by the hardware architecture and the minimum achievable delay between elements. A delay profile rounded or quantized to a minimum discrete time interval results in deviation or rounding error. The deviation from the ideal phase delay profile is described as phase quantization error [100]. Errors introduced as a result of coarse phase quantization have a detrimental effect on the beam pattern, and applies to both the transmit and receive cases.

Phase deviation or error can be classed as either correlated (periodic) or uncorrelated (random) [100]. Correlated phase quantization error is error that repeats over the length of the aperture, whilst uncorrelated error has no defined periodicity.

Correlated error occurs as a result of beams being steered off axis with a linear delay profile as described by (4.3). Quantization of a linear delay profile produces a staircase quantized delay profile, whereby multiple elements undergo the same phase excitation. [97]. The worst cases of correlated error occur when the minimum time increment (or integer multiple of) extends over two elements or more [105]. Uncorrelated phase quantization error describes deviations with no defined periodicity across the aperture, such as when beams are focused. Additional uncorrelated or random phase errors can be introduced into the field pattern by other means such as element inhomogeneity as described by Duxbury *et al.* [106], Zhang *et al.* [107] or non-homogeneous materials [108].

4.5.1 Phase Quantization Literature Review

The impact of correlated and uncorrelated phase quantization error within array applications has been discussed in previous literature; A summary of which is given here. Early discussion of quantization error primarily considered the continuous wave case for correlated lobes in the far field. Beaver [109] for example discussed the presence of additional lobes due to correlated phase errors in a steered (non-focused) ultrasound system. In this analysis it was shown that additional lobes appeared when a regular phase error occurred across the array with continuous wave excitation. With respect to the pulsed case, it was postulated that additional lobes would still be present, however would be decreased in amplitude, similar to the effect of pulse duration on grating lobe patterns.

The effect of correlated error was also discussed in [97] with the authors describing element phase grouping (i.e. a number of adjacent elements transmitting or receiving together as a result of coarse quantization). The authors determined that the correlated error associated with phase grouping caused limitations in the near field and when combined with focusing (uncorrelated error) produced larger sidelobes and non-ideal beam profiles.

Magnin *et al.* [110] demonstrated the emergence of quantization-induced lobes in pulsed excitation ultrasound systems as opposed to previous continuous wave discussions ([109] and [97]). These quantization lobes increased sidelobe amplitude, thereby limiting the dynamic range of the ultrasound system, and potential for spurious reflections that may degrade resolution. Correlated error and uncorrelated error cases were discussed corresponding to steering and focusing, with the authors establishing that the amplitude of spurious quantization lobes decreased not only with pulse duration but also as a result of uncorrelated error introduced with focusing.

Hoen [111] discussed a more practical case using pulsed excitation, criticising [112] for continuous wave analysis. Whilst this criticism may be fair with reference for imaging, it must be noted that continuous wave ultrasound is often used for therapeutic applications (e.g. [113]), and as such, the analysis is still valid and useful. Also discussed was the effect that delay discretisation had on sidelobe levels, but not the mainlobe.

Von Ramm and Smith [104] analyzed the effect of phase quantization on image dynamic range, considering the transmitted beam profile and the received (synthetic) beam profile. The authors defined image dynamic range as the ratio of the on-axis response to the maximum undesired off-axis response [104], and can be calculated by consideration of transmit dynamic range (TDR) and receive dynamic range (RDR). TDR can be defined as the difference between the mainlobe and a peak sidelobe in the transmitted field and is defined in dB as shown in (22) of [104]

$$\mathrm{TDR} = 20\log\frac{N}{2n}\sqrt{\frac{1+\cos\Phi}{1-\cos\Phi}} \tag{4.10}$$

where n is the number of cycles within the excitation pulse and the maximum phase error per element Φ is defined as [104]

$$\Phi = 2\pi f \Delta\tau \tag{4.11}$$

where $0 < \Phi < \pi$ and $\Delta\tau$ is the minimum time resolution of the system.

Von Ramm and Smith [104] defined IDR as the summation of TDR and RDR

$$\text{IDR} = \text{TDR} + \text{RDR}. \tag{4.12}$$

As a consequence, an increase in either TDR or RDR as a result of reduced quantization effects corresponds to an overall increase in IDR, and hence improved image quality. RDR can be increased by oversampling and/or using signal processing techniques such as interpolation [37]. TDR however is limited by the $\Delta\tau$ of the transmit beamformer.

Von Ramm and Smith concluded their analysis by suggesting a maximum tolerable phase error of $\lambda/8$ for apertures of greater than $N = 16$ elements, and excitation signals of $n = 5$ cycles or less. Note that whilst the maximum tolerable phase error is expressed as a path length or phase difference, where λ is the wavelength of the centre frequency of the excitation pulse in the medium, it can also be represented using the following relationships as derived from [104], [114] and [100]. The maximum phase difference Φ is most often expressed in terms of the wavelength λ and an oversampling factor μ

$$\Phi = \frac{\lambda}{\mu}. \tag{4.13}$$

This oversampling factor can be calculated by considering the frequency of interest f sampled by a sampling frequency f_s

$$\mu = \frac{f_s}{f}. \tag{4.14}$$

This sampling frequency is effectively equal to the inverse of the minimum time resolution of the system $\Delta\tau$

$$f_s = \frac{1}{\Delta\tau}. \tag{4.15}$$

Peterson and Kino [114] pursued the concept of a maximum tolerable phase error considering the effect of uncorrelated error within the focused but non-steered case. This analysis was extremely thorough, and is seen as the dominant reference on quantization error. Their discussion of uncorrelated error described two effects in the beam pattern;

subsidiary foci in the near field and distinct quantization lobes in the far field. As a result of their analysis, a suggested estimation of RMS sidelobe level was described with

$$SL_{RMS} \approx 20\log\frac{\pi}{\mu\sqrt{6N}} \quad \text{for } \mu >> 1 \tag{4.16}$$

Equation (4.16) is often used when describing appropriate quantization resolution in transmit and or receive. Several authors suggests a minimum value of $\Phi = \lambda/32(\mu = 32)$ as described in [69], [115] and [116]. Figure 4.8 plots estimations of RMS sidelobe level for different sizes of arrays using (4.16). It can be shown that for a 96 element array (N

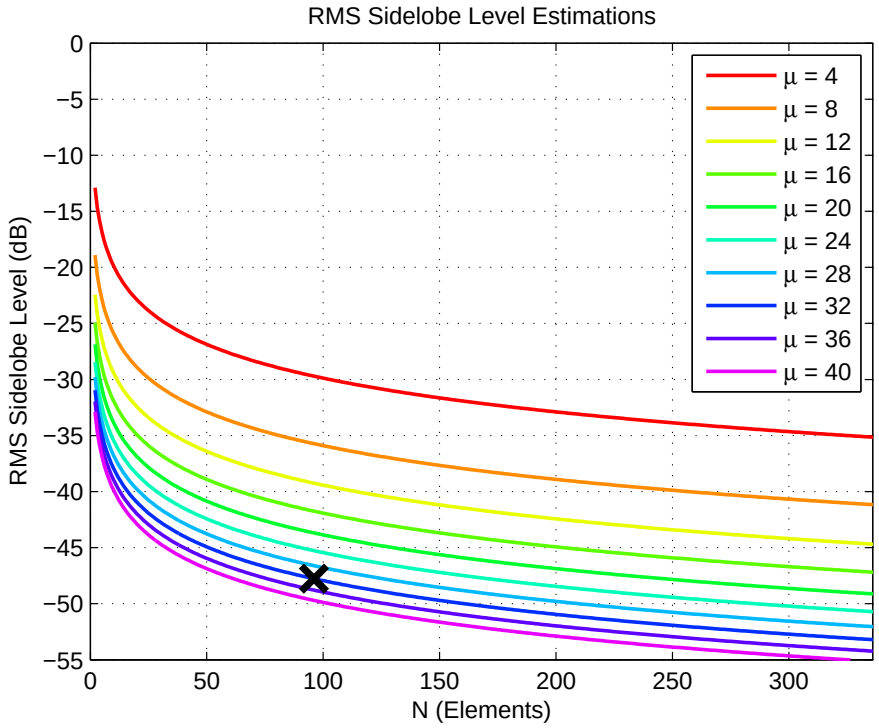

Figure 4.8: Estimations of RMS sidelobe level for combinations of N and different levels of μ. The cross depicts -48 dB for a 96 element array at $\mu = 32$

= 96) and with μ = 32, the estimated RMS sidelobe level approaches -48 dB (as shown by a cross in Figure 4.8). When the number of elements N is altered at μ = 32, SL_{RMS} values are still within the -40 dB to -50 dB range e.g. 64 elements: SL_{RMS} = -46 dB, or 128 elements: SL_{RMS} = -49 dB.

Following Kino's analysis, Lancee *et al.* [117] studied the effect of phase errors in transmission only, and discussed the validity of modelling phase error using probabil-

ity distributions. Two extreme error distributions were simulated to show that whilst the probability distributions of phase error were the same analytically, the effect in the radiated field was noticeably different. One conclusion from the work in [117] was that phase quantization error must be minimised to avoid distortions, and the effect of the error could be simulated for particular worst cases.

Wang *et al.* [113] described the effect of phase errors on the field pattern for a continuous wave therapeutic application. Also discussed were errors in the field occurring due to low resolution of phase shifter electronics, non-homogenous media, or imperfect array fabrication. In [113] a novel example of quantizing the relative phases (difference between elements) as opposed to quantizing the computed phases difference was proposed. Wang's main conclusions echoed the previous literature stating that with an increase in phase quantization error sidelobes are increased, and mainlobe intensity is reduced.

Holm and Kristoffersen [100] combined the effect of steering with the focused case as described in [114] in order to evaluate a 'worst case' where quantization effects were most severe. It was shown that the worst case with respect to ultrasound applications would be the use of continuous wave excitation and a combination of maximum correlated error (i.e. steering in a direction where a minimum delay increment covers two elements) and uncorrelated error (introduced as a result of focusing). Worst case steering angles can be calculated by rearranging (4.3) to give

$$\theta_s = \sin^{-1}\left(\frac{\tau_n c}{d}\right) \tag{4.17}$$

and then substituting τ_n for $\Delta\tau/2$

$$\theta_{pq}|_{p=1,q=2} = \sin^{-1}\left(\frac{\Delta\tau c}{2d}\right) \tag{4.18}$$

for p integer numbers of $\Delta\tau$ extending over q sub-elements [100]. An example of $p = 1, q = 2$ is shown in Figure 4.9. Prediction of this angle of quantization lobe can be

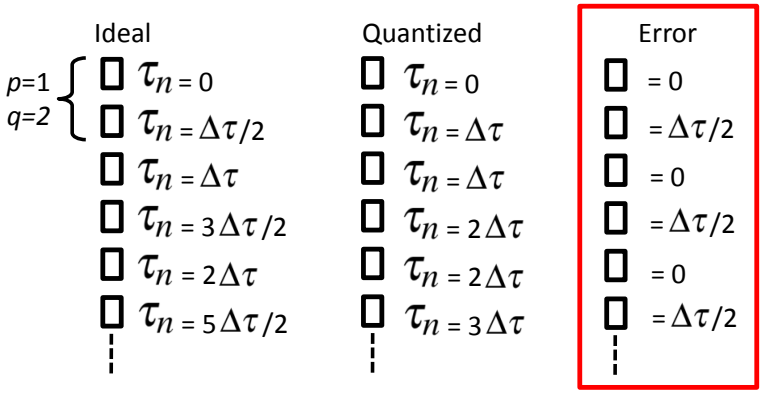

Figure 4.9: Definition of worst case correlated error showing periodic error across the array

calculated as described in [100] using

$$\theta_k|_{p=1,q=2} = \sin^{-1}\left(\frac{\lambda}{2d}\left(\frac{1}{m}-1\right)\right) \tag{4.19}$$

for the worst case described in [100] using $m = -1$. Estimations for peak sidelobe levels were derived for a continuous wave excitation, however as previous authors discuss, continuous wave calculations tend to over-estimate the severity of quantization lobes with respect to imaging applications [110], [111]. Holm and Kristoffersen also commented that in the near field, transmit dynamic range is mostly limited by uncorrelated error and not correlated error. The limit at which correlated lobes, have greater interference than uncorrelated (random) lobes is defined by the distance z_{rand}, beyond which correlated lobes have greater impact on the field. For rectangularly weighted apertures,

$$z_{\text{rand}} = \frac{4.6\pi^2}{12}\frac{(D\cos\theta_s)^2}{\lambda}\frac{\mu}{N} \tag{4.20}$$

which is a more specific version of the generalised (24) in [100]. For most arrays, according to (4.20), the uncorrelated lobes will dominate for ranges beyond z_{TR}. An example is shown in Figure 4.10 for a 5 MHz array with $d = \lambda$ spacing. With respect to Figure 4.10, for all lines that are below the black line z_{TR}, correlated lobes will impact. For all cases above z_{TR}, only uncorrelated lobes will impact. The Figures show as described in

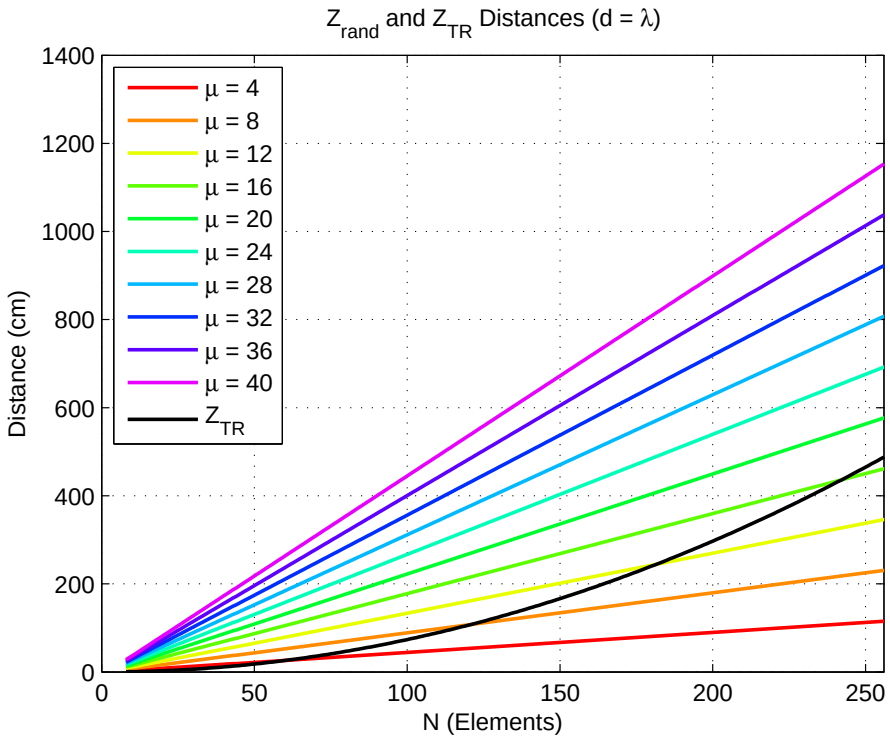

Figure 4.10: z_{rand} vs. z_{TR} for different N and different quantization values

Holm and Kristoffersen's discussion [100] that uncorrelated (random) sidelobes are of most important over the correlated case, unless using a large array and low value of μ.

4.5.2 Summary of Literature Review

It is well established that poor quantization of phase causes anomalous effects in the radiated beam profile. For continuous wave excitation these effects are more distinct than for the pulsed case. Steering causes correlated quantization lobes due to a periodic error repeating across the array. Focusing causes uncorrelated quantization lobes due to random error across the array caused by the parabolic delay profile. Evaluation of the necessary minimum quantization value for an expected RMS sidelobe level was defined by Peterson and Kino in 1984 [114] [76], with $\mu = 32$ being the accepted value for receive and transmit beamformers [69],[115],[116]. Holm and Kristoffersen [100] discussed the likelihood of a worst case: steering to an angle of maximum correlated error and also focusing. Their analysis however showed that for most cases correlated lobes would not interfere with ultrasound imaging and it was the uncorrelated error caused by focusing

that was of most concern. The next section demonstrates some of these effects previously discussed in the literature.

4.6 Demonstration of Phase Quantization Effects

Field profiles from ultrasound transducers can be simulated using the well-referenced Field II package [118], [119]. Field II is a MATLAB toolbox developed by the Technical University of Denmark (DTU) by Jensen *et al.* and simulates a radiated beam profile by calculating the field at each point using the spatial impulse response. Quantization can be introduced to a simulation by using the 'xdc_quantization' or 'ele_delay' functions.

4.6.1 Correlated Error

Figures 4.11 to 4.18 demonstrate several cases of correlated periodic error in the far field as a result of steering to worst case angles for $\mu = 4$ to $\mu = 32$. Worst case angles are calculated by taking the minimum time period corresponding to each μ value, and using (4.17) to calculate the steered angle. The upper plot (a) in each Figure shows the ideal case (steered to the same angle defined in (4.17), but with ideal delays used (i.e. no time delay quantization). The lower plot (b) in each Figure shows the quantized case. Note the emergence of a phase quantization lobe of high level present in the field, in each of the lower Figure plots, e.g. in Figure 4.11. In these simulations an aperture of $N = 32$ elements spaced at $\lambda/2$ was used with continuous wave excitation. Continuous wave excitation provides the worst case, as narrowband signals coherently sum, and quantization lobes are more distinct.

Figures 4.19 to 4.26 show the same data, but are plotted in an angular fashion intersecting the radial transition distance of the aperture (19.2 mm). Plotting through the pressure field permits direct comparison of the difference between the ideal, and quantized representations. For reference it can be seen that Figure 4.19 is very similar to one of the cases of extreme quantization discussed in [100], although with different simulation parameters and simulated using different methods.

Table 4.2 presents data showing the angle steered, location of quantization lobe, and value of peak sidelobe from the mainlobe for the cases of correlated error shown. It can be seen that as accuracy of delays increases, quantization lobes are reduced to between -18 and -20 dB. sidelobe will also be further reduced in the pulsed, broadband case [63]. Note that other combinations of p and q exist that provide far field lobes, such as when $p = 3$, as reported in the literature [100]. Such angles will produce far field correlated lobes at angles predicted by [100], but with lower levels of side lobe than the $p = 1, q = 2$ case.

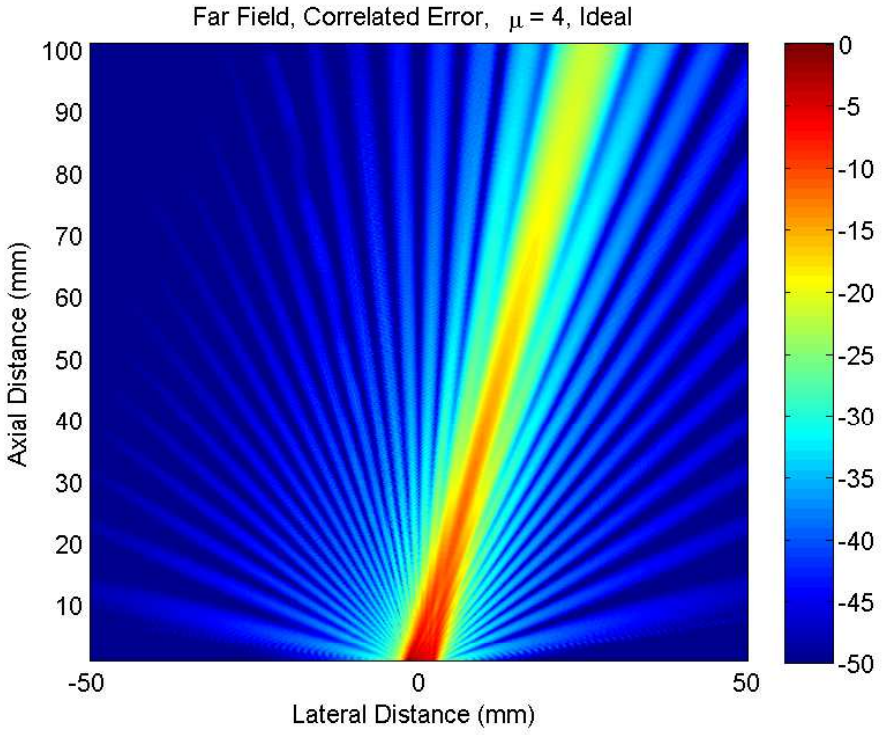

(a)

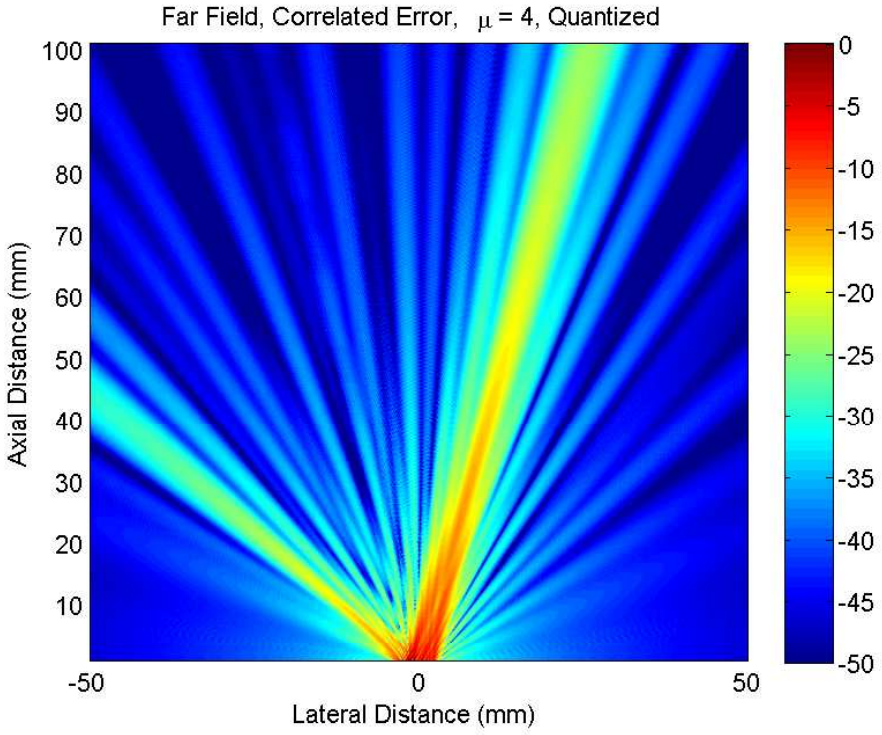

(b)

Figure 4.11: Comparison of simulated field profiles showing correlated error using continuous wave excitation. Ideal time delays (a) vs. quantized delays (b). Quantization at $\mu = 4$ and steered to worst case angle of 14.48°

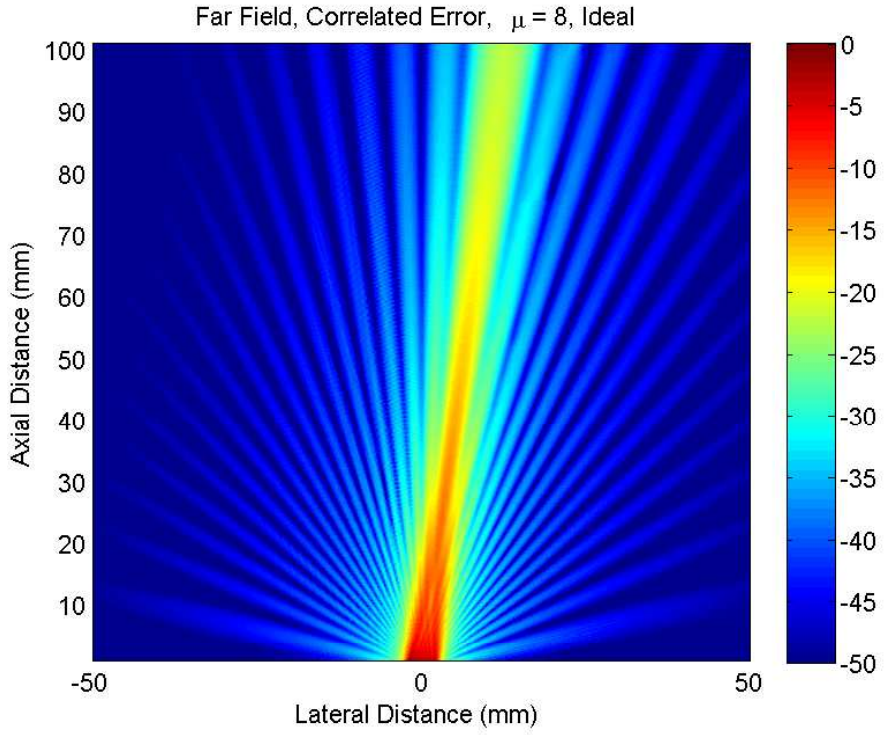

(a)

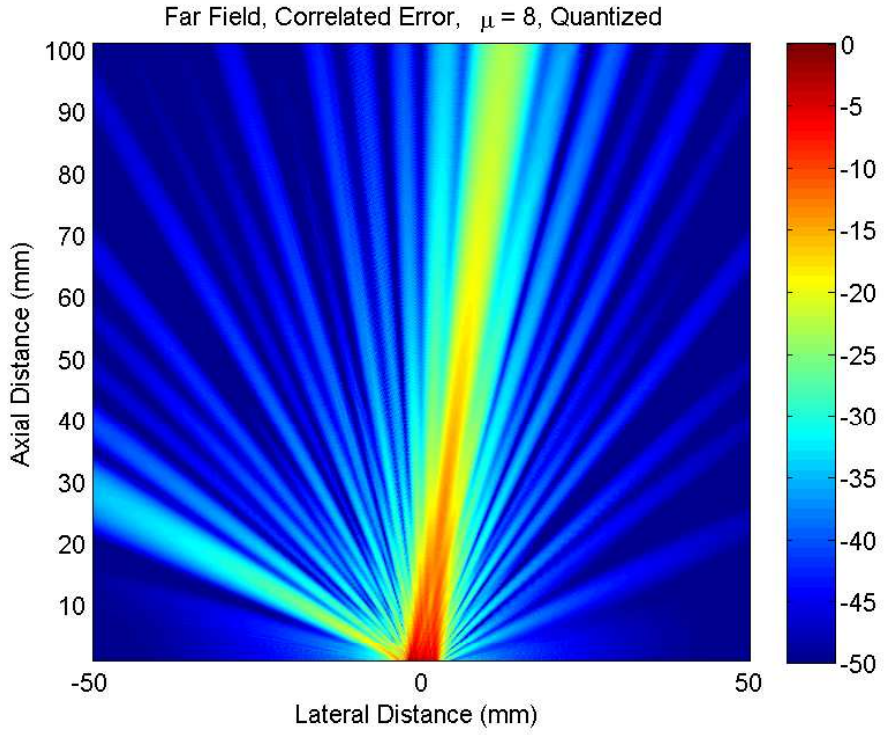

(b)

Figure 4.12: Comparison of simulated field profiles showing correlated error using continuous wave excitation. Ideal time delays (a) vs. quantized delays (b). Quantization at $\mu = 8$ and steered to worst case angle of 7.18°

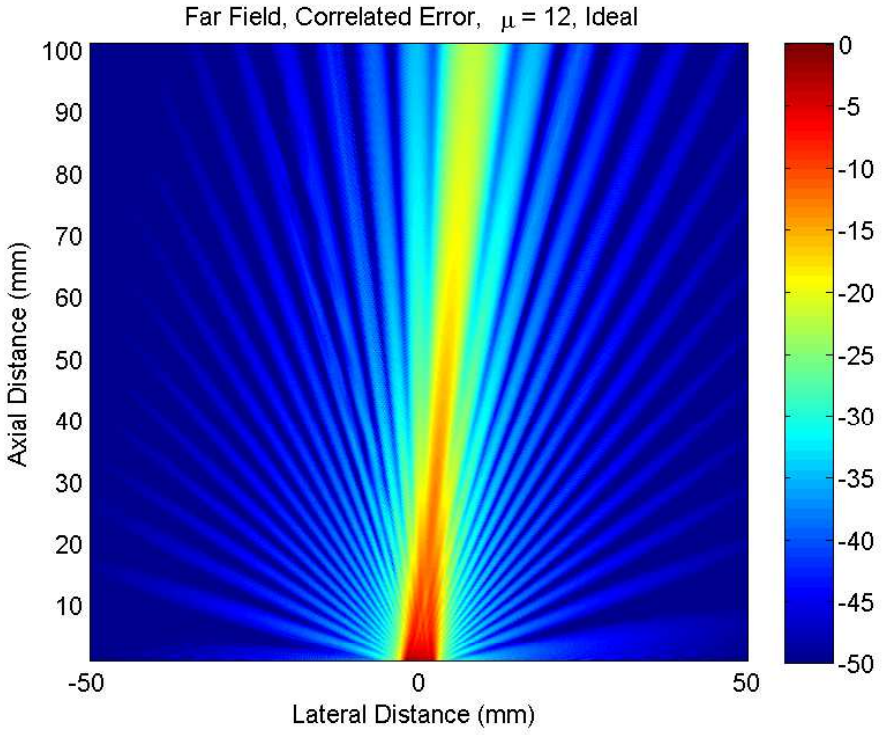

(a)

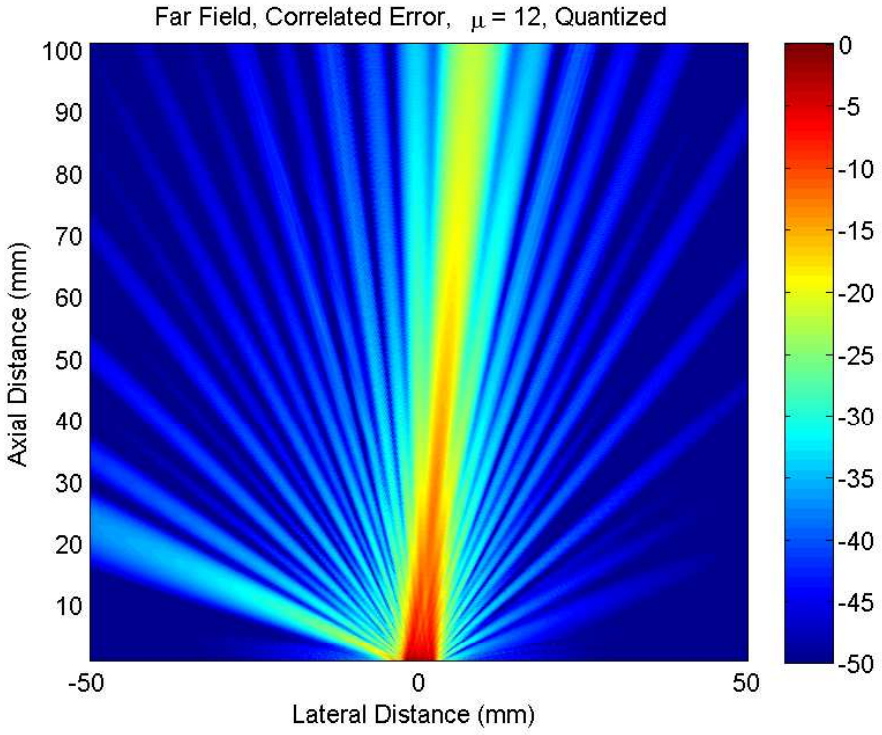

(b)

Figure 4.13: Comparison of simulated field profiles showing correlated error using continuous wave excitation. Ideal time delays (a) vs. quantized delays (b). Quantization at $\mu = 12$ and steered to worst case angle of 4.78°

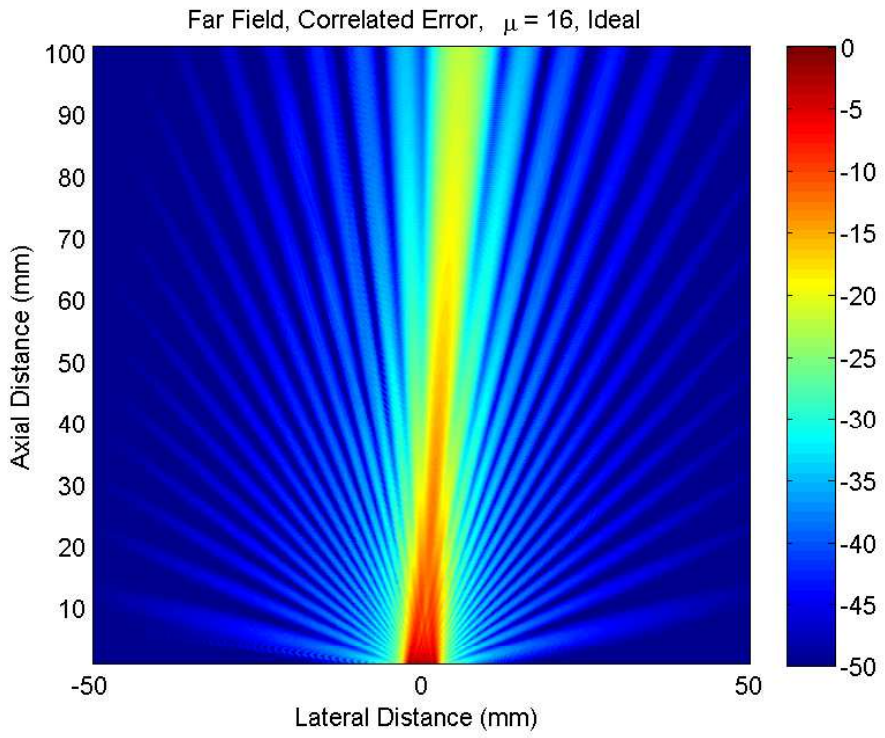

(a)

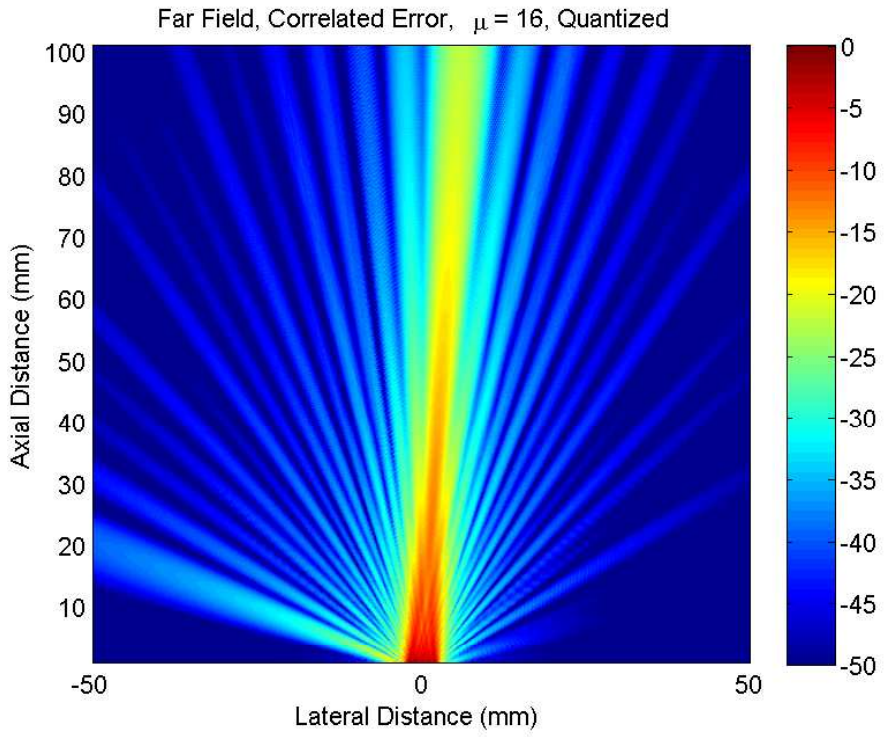

(b)

Figure 4.14: Comparison of simulated field profiles showing correlated error using continuous wave excitation. Ideal time delays (a) vs. quantized delays (b). Quantization at $\mu = 16$ and steered to worst case angle of 3.58°

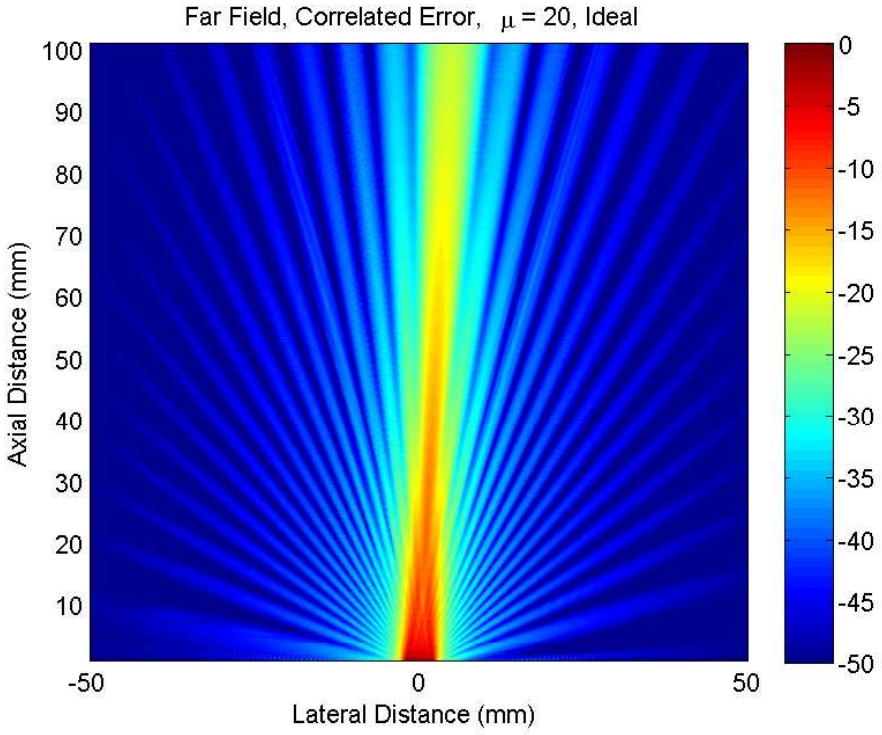

(a)

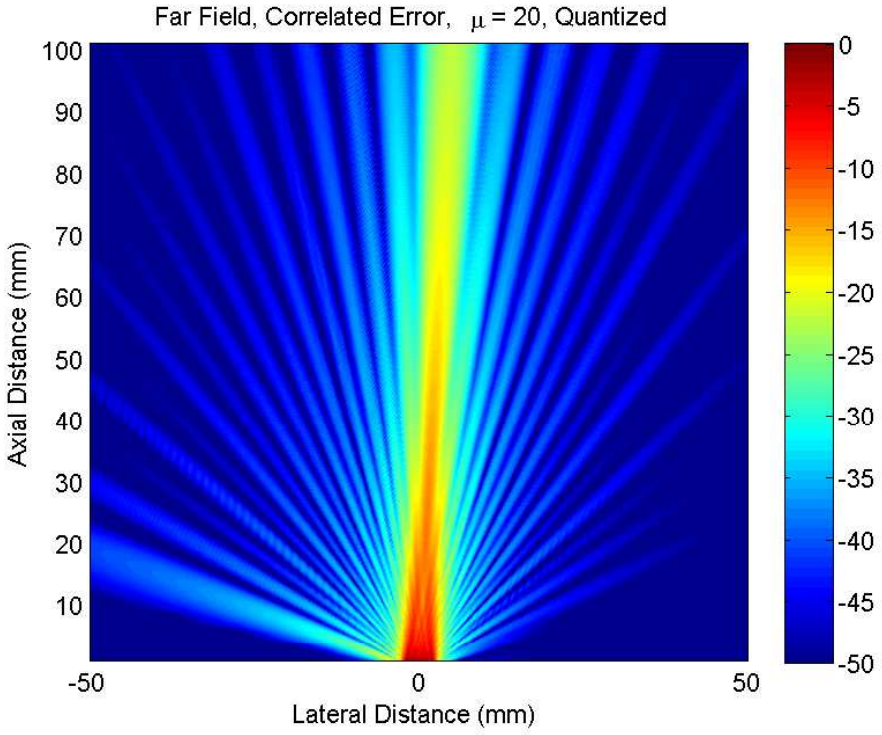

(b)

Figure 4.15: Comparison of simulated field profiles showing correlated error using continuous wave excitation. Ideal time delays (a) vs. quantized delays (b). Quantization at $\mu = 20$ and steered to worst case angle of 2.87°

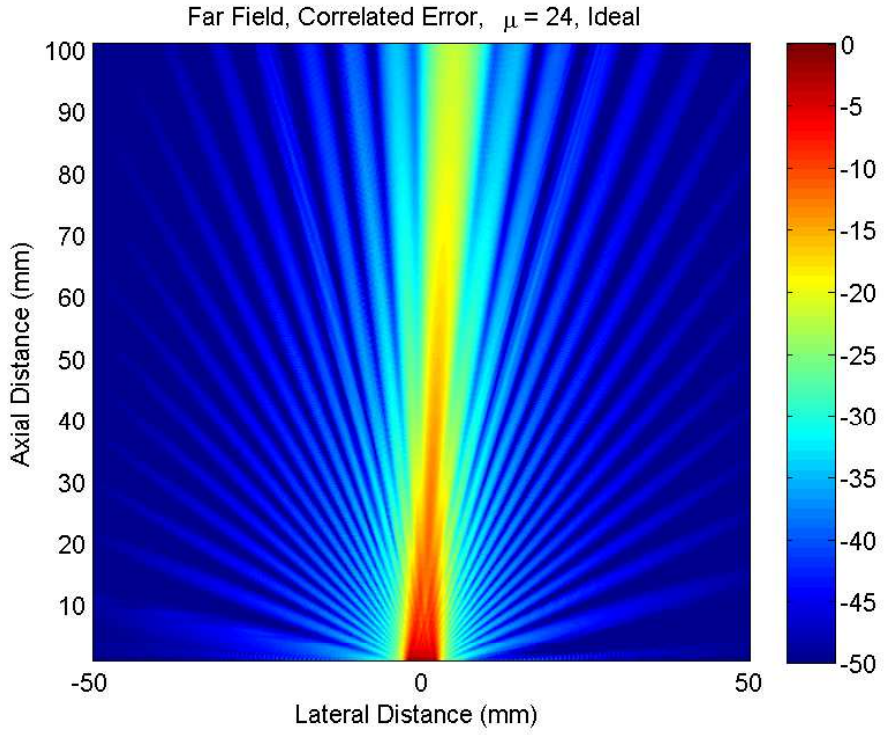

(a)

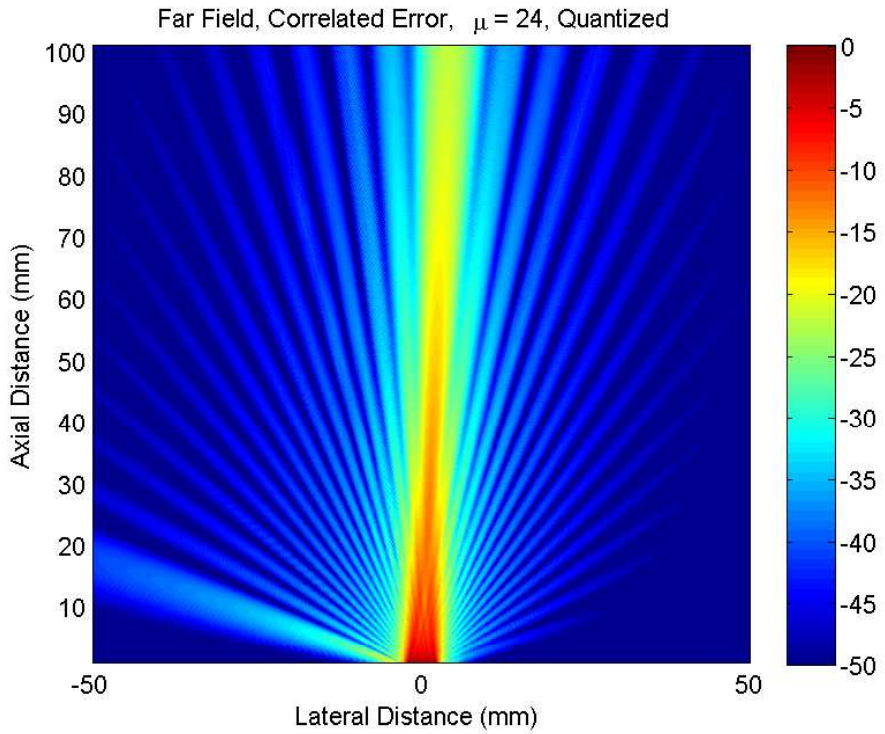

(b)

Figure 4.16: Comparison of simulated field profiles showing correlated error using continuous wave excitation. Ideal time delays (a) vs. quantized delays (b). Quantization at $\mu = 24$ and steered to worst case angle of 2.39°

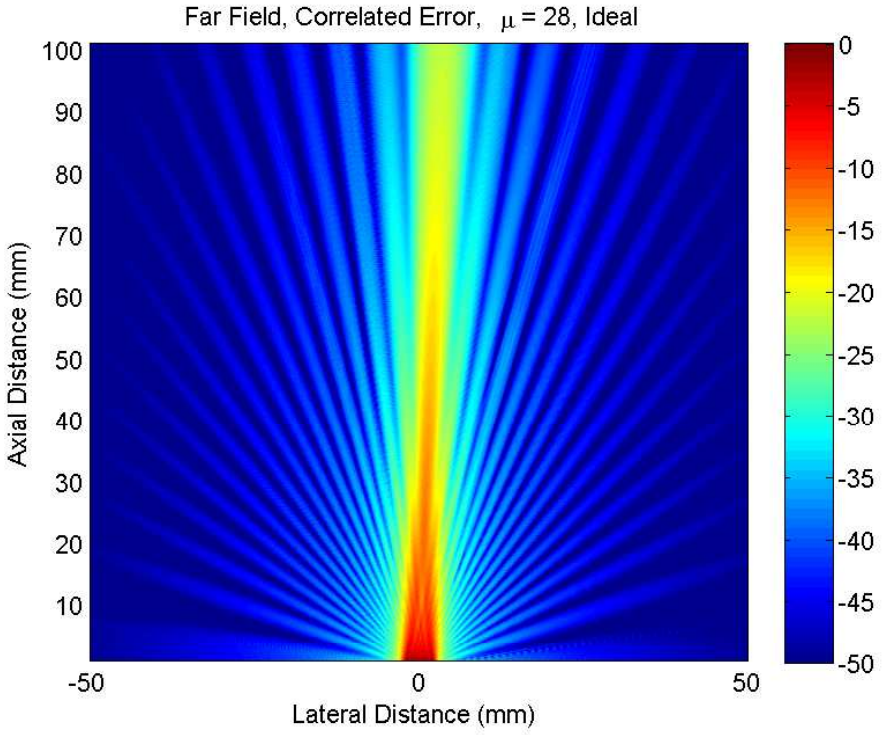

(a)

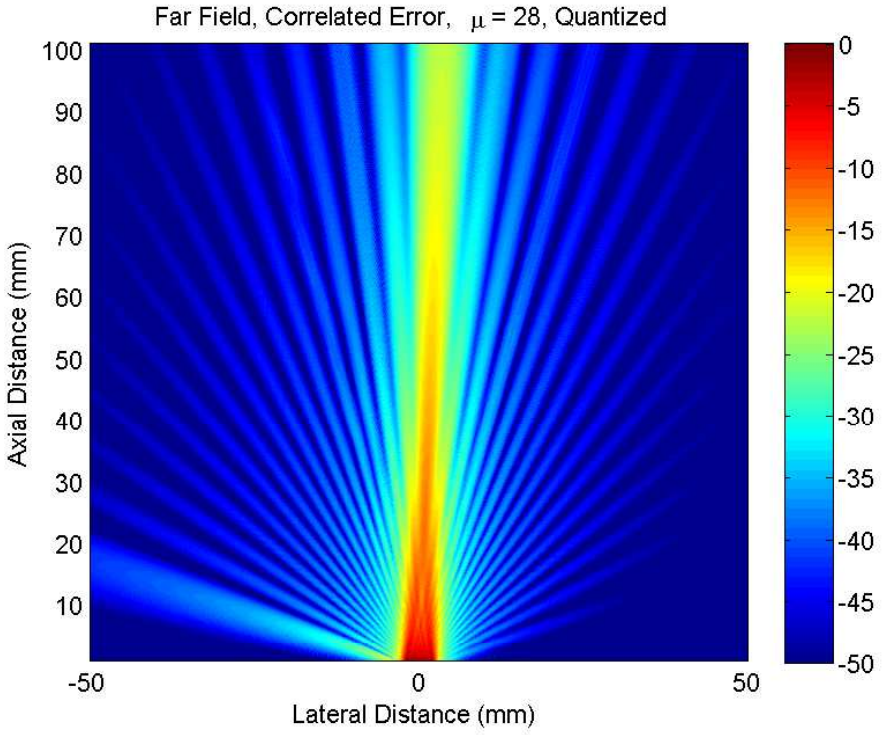

(b)

Figure 4.17: Comparison of simulated field profiles showing correlated error using continuous wave excitation. Ideal time delays (a) vs. quantized delays (b). Quantization at $\mu = 28$ and steered to worst case angle of 2.05°

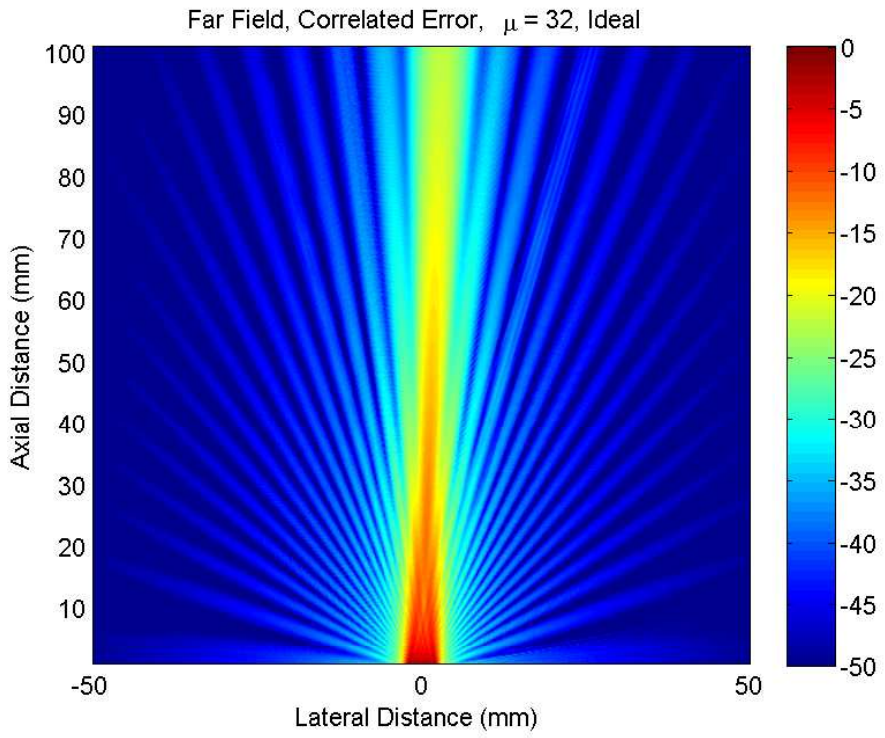

(a)

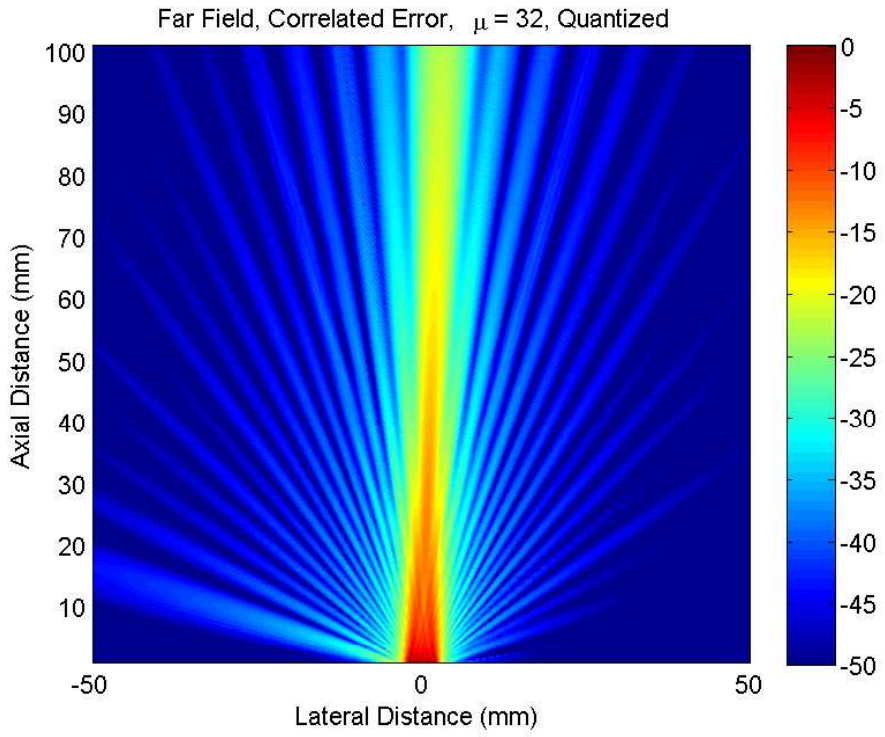

(b)

Figure 4.18: Comparison of simulated field profiles showing correlated error using continuous wave excitation. Ideal time delays (a) vs. quantized delays (b). Quantization at $\mu = 32$ and steered to worst case angle of 1.79°

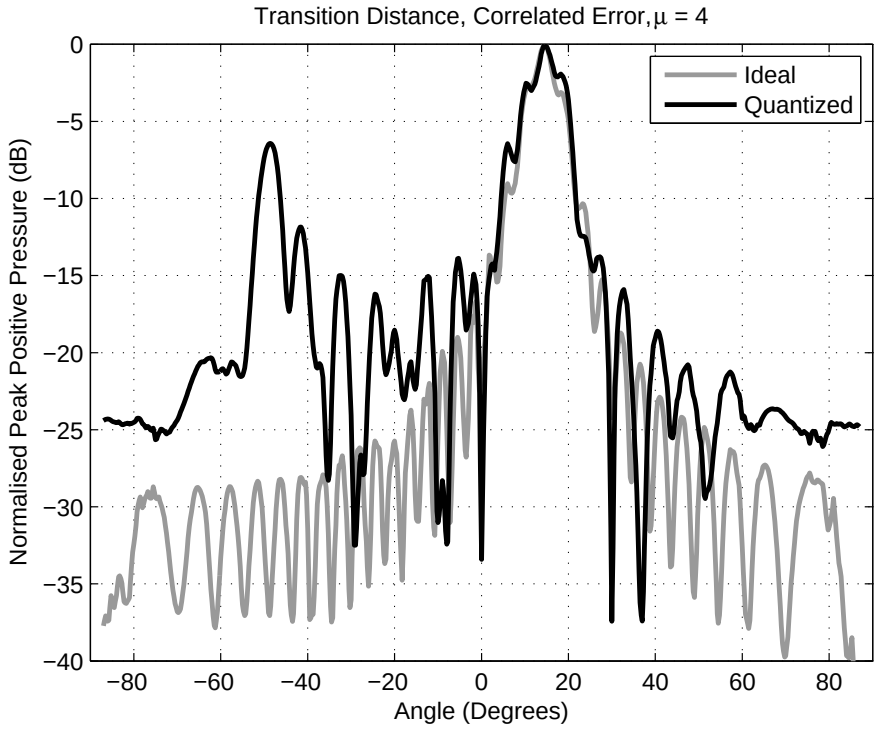

Figure 4.19: Radial field profile at the transition distance showing correlated error using continuous wave excitation. Ideal time delays vs. quantized delays. Quantization at $\mu = 4$ and steered to worst case angle of 14.48°

μ	Steered Angle	Correlated Quantization Lobe (k = -1) Angle °	Peak Quantization Lobe Level (dB)
4	14.48	-48.60	-6.4
8	7.18	-61.04	-12.7
12	4.78	-66.44	-16.0
16	3.58	-69.64	-18.2
20	2.87	-71.81	-19.9
24	2.39	-73.40	-20.0
28	2.05	-74.64	-20.9
32	1.79	-75.64	-22.4

Table 4.2: Position of 'worst case' quantization lobes for far field, correlated errors.

Correlated error lobes are caused by a phase quantization error that occurs periodically across the array. It can be seen that reducing $\Delta\tau$ lessens the impact of correlated error, as the magnitude of the error between elements is reduced. Notice also that the steering equation in (4.3) does not depend on N, the number of elements. The location of

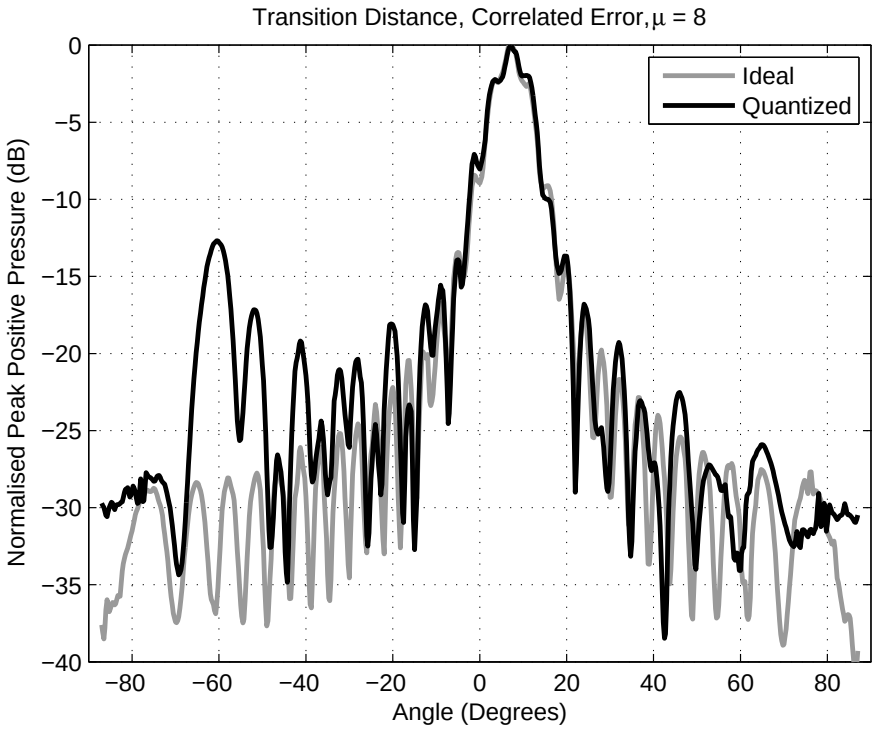

Figure 4.20: Radial field profile at the transition distance showing correlated error using continuous wave excitation. Ideal time delays vs. quantized delays. Quantization at $\mu = 8$ and steered to worst case angle of 7.18°

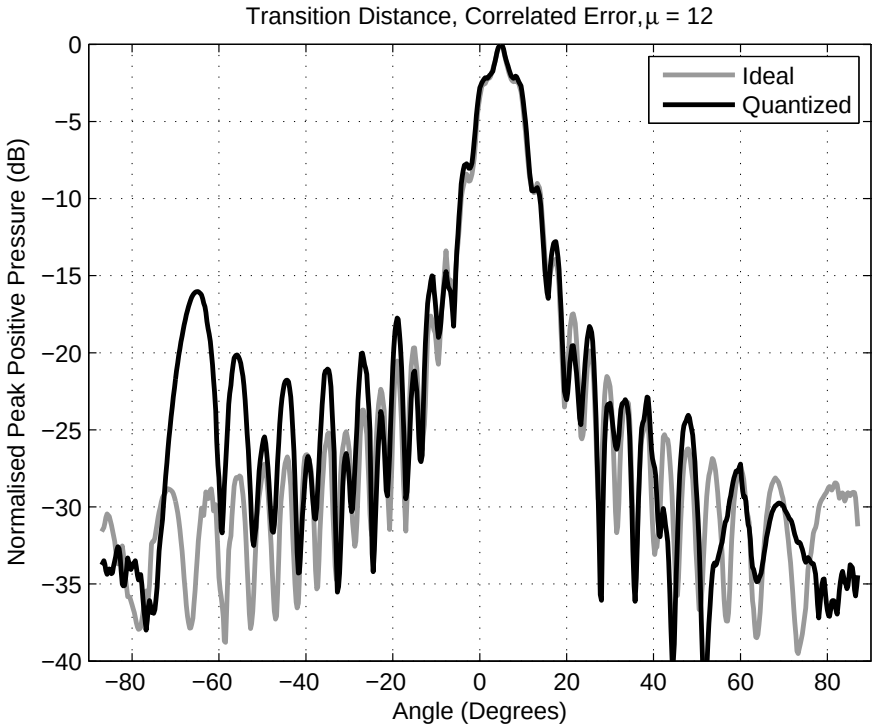

Figure 4.21: Radial field profile at the transition distance showing correlated error using continuous wave excitation. Ideal time delays vs. quantized delays. Quantization at $\mu = 12$ and steered to worst case angle of 4.78°

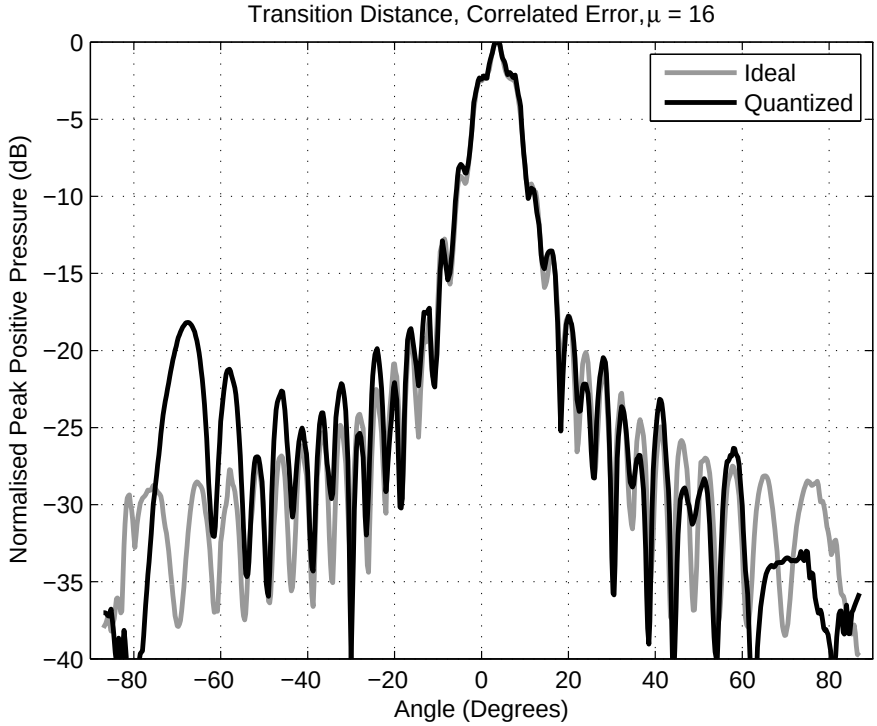

Figure 4.22: Radial field profile at the transition distance showing correlated error using continuous wave excitation. Ideal time delays vs. quantized delays. Quantization at $\mu = 16$ and steered to worst case angle of 3.58°

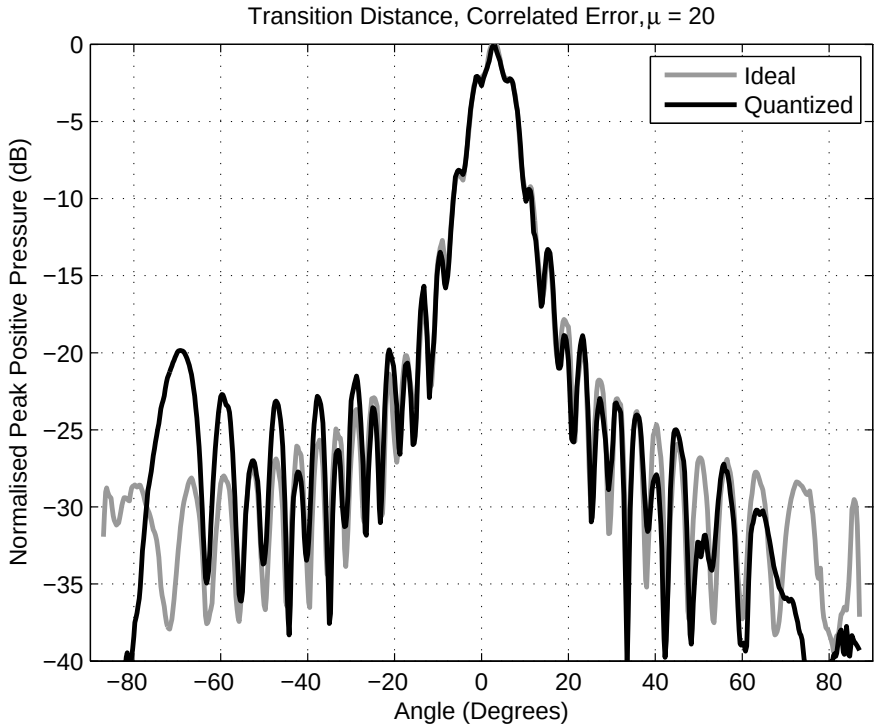

Figure 4.23: Radial field profile at the transition distance showing correlated error using continuous wave excitation. Ideal time delays vs. quantized delays. Quantization at $\mu = 20$ and steered to worst case angle of 2.87°

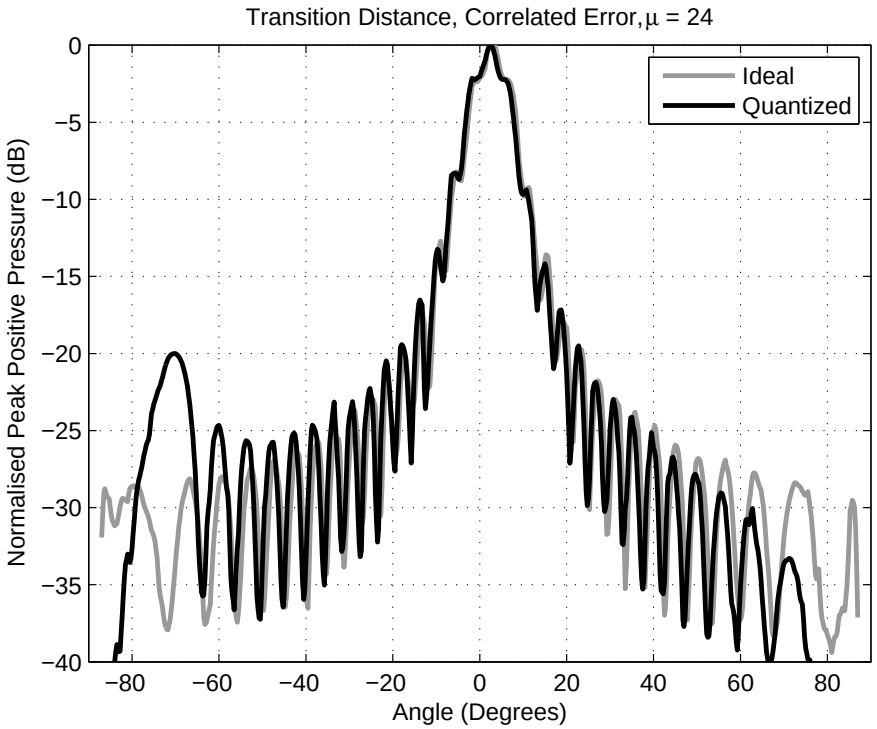

Figure 4.24: Radial field profile at the transition distance showing correlated error using continuous wave excitation. Ideal time delays vs. quantized delays. Quantization at $\mu = 24$ and steered to worst case angle of 2.39°

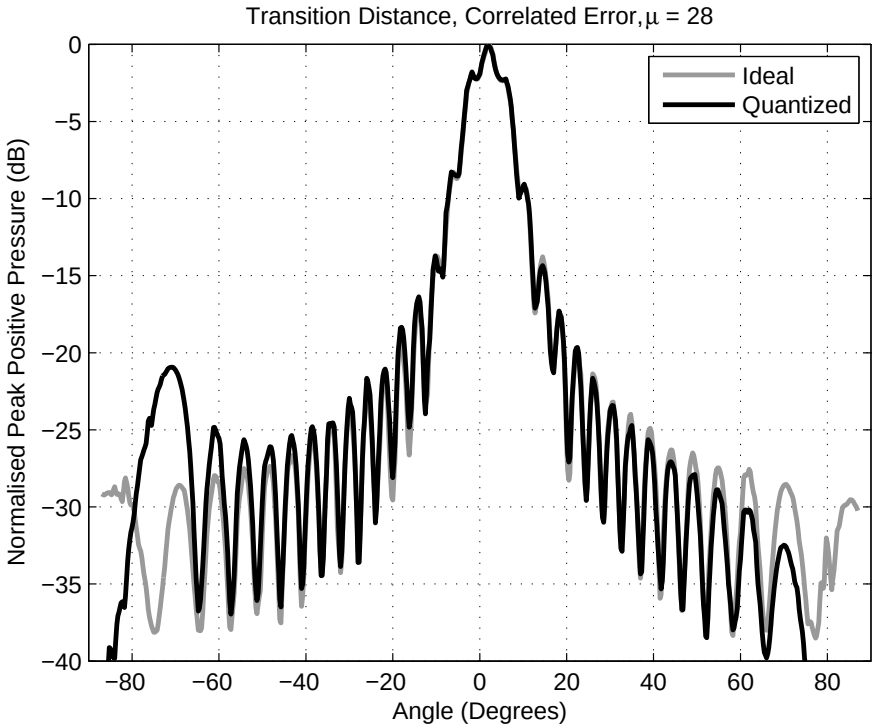

Figure 4.25: Radial field profile at the transition distance showing correlated error using continuous wave excitation. Ideal time delays vs. quantized delays. Quantization at $\mu = 28$ and steered to worst case angle of 2.05°

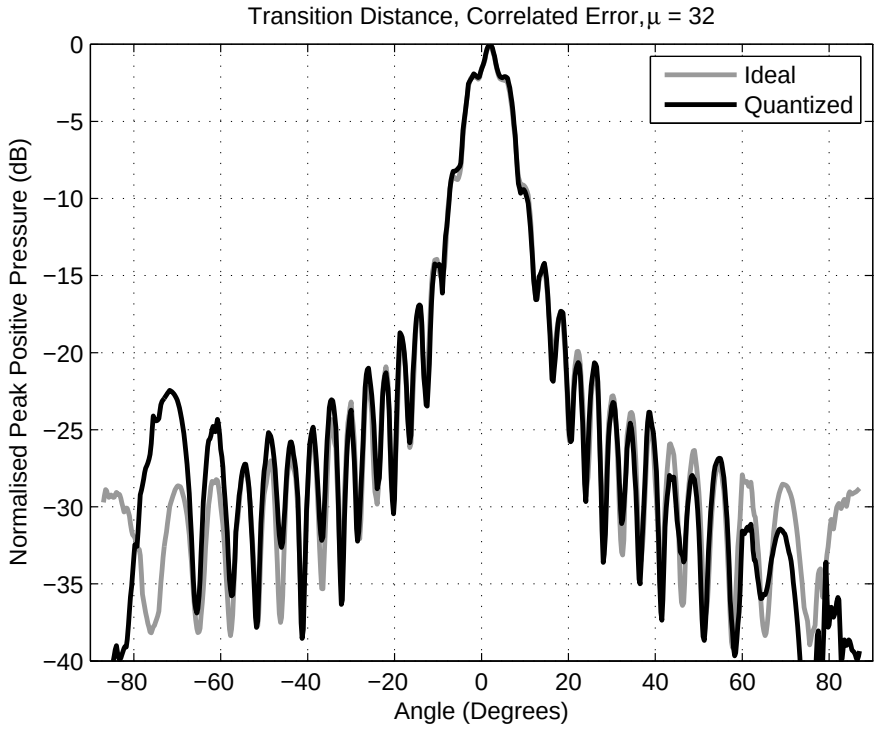

Figure 4.26: Radial field profile at the transition distance showing correlated error using continuous wave excitation. Ideal time delays vs. quantized delays. Quantization at $\mu = 32$ and steered to worst case angle of 1.79°

correlated or periodic quantization lobes is therefore not altered by increasing N from the $N = 32$ case shown previously, up to $N = 128$ as discussed in [100]. As a consequence, steering angles that provide correlated error can be accurately calculated by using the physical properties of the transducer, and $\Delta\tau$. This is not the case for uncorrelated error.

4.6.2 Uncorrelated Error

Uncorrelated error occurs due to differences in time-delays or phase that are non-periodic. This is most often as a result of focusing in the near field, which requires a parabolic delay profile, as shown in Figure 4.6. This section demonstrates how uncorrelated error, introduced by poor phase quantization of focusing delays can cause quantization lobes in the far field, and subsidiary foci in the near field as described in [114]. Figure 4.27 defines these terms. Quantization lobes in the far field are caused by two methods: firstly, due to beams focused at subsidiary foci between the transducer face and the desired focal point, and secondly as a result of virtual foci (representations of quantization foci that originate behind the transducer). Far field quantization lobes deposit energy away from the main beam, and can reduce sensitivity of the main beam. Subsidiary near field foci are shown by the green and red lines. These foci deposit energy before the focal point, and can lead to clutter around and beyond the focal point into the far field. This phenomenon was initially presented by Peterson and Kino [114] [76].

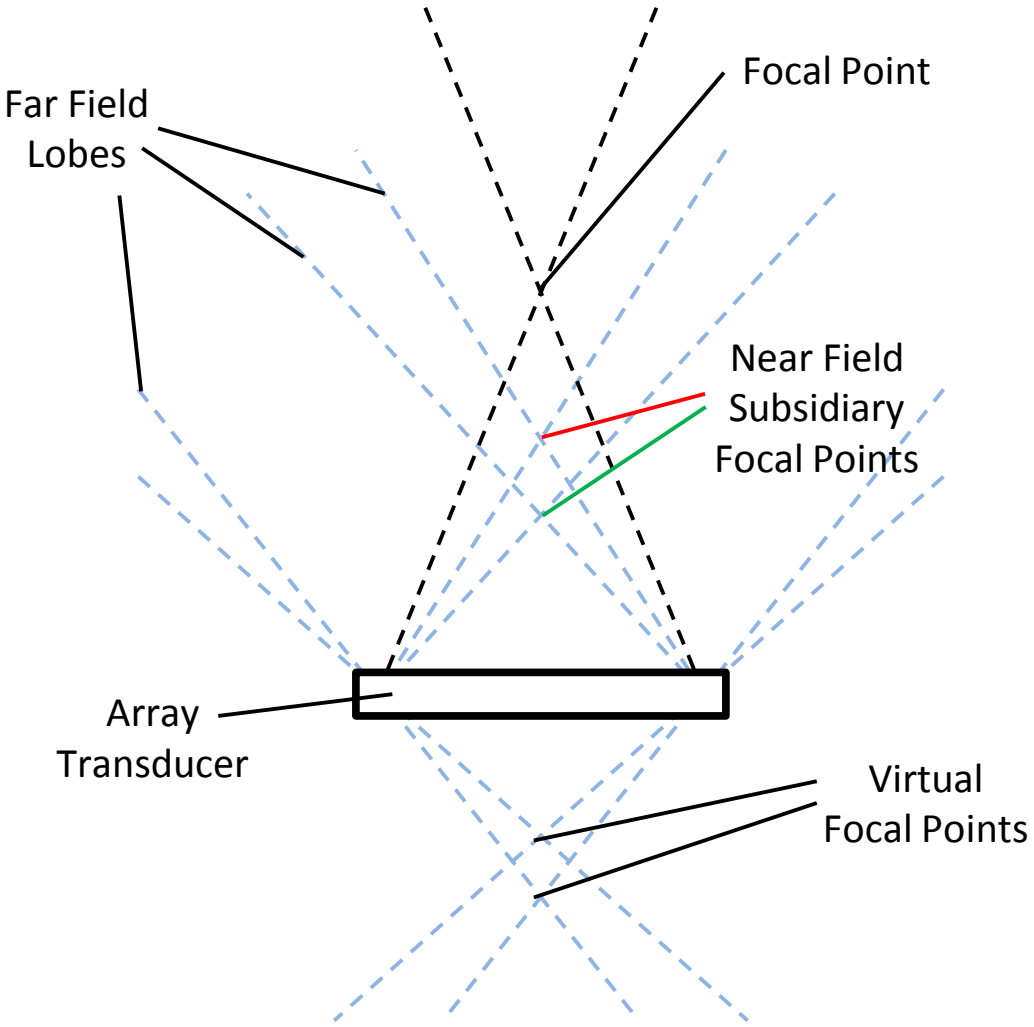

Figure 4.27: Diagram of the effect of uncorrelated error caused by focusing on the beam profile, showing quantization lobes in the far field and subsidiary foci in the near field

Figures 4.28 to 4.43 show simulation of a typical phased array probe used for sector imaging ($N = 64$, $d = \lambda/2$). In each case the focal distance is half the transition distance $z_{TR}/2$ which is equivalent to 38.4 mm at 5 MHz. Quantization values ranging from $\mu = 4$ to $\mu = 32$ have been plotted showing the peak positive pressure profile, and a radial sector. In order to fully demonstrate the presence of uncorrelated lobes, a narrowband continuous wave excitation has been used. For reference, Figure 4.28 shows the ideal case, where no time quantization is used and delays are implemented as calculated. The radial profiles, taken at the focal length are plotted to allow a comparison between the quantized, and ideal case. It can be seen that the uncorrelated lobes are much different to the correlated case. For the correlated case, the peak magnitude decreased in accordance with an increase in μ. For the uncorrelated case this is not true. Inspection of the field plots in Figures 4.29 to 4.44 show that both the position and peak of the lobes moves with every case.

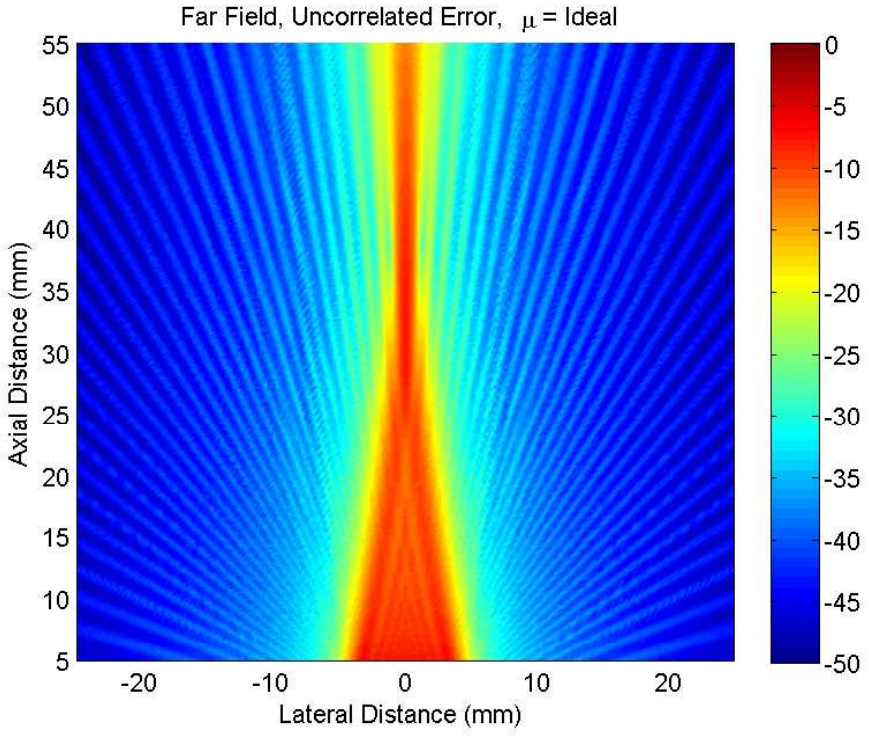

Figure 4.28: Simulated beam profile, 64 element $\lambda/2$ array, focused to 38.4 mm ($z_{TR}/2$), with ideal delays (no delay quantization) (narrowband simulation)

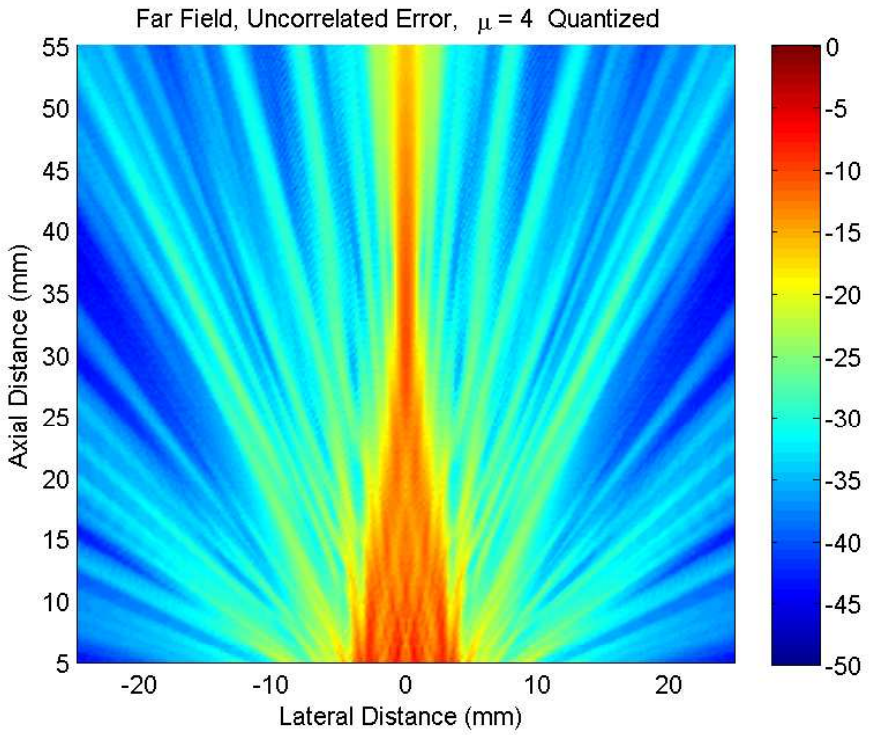

Figure 4.29: Simulated beam profile, 64 element $\lambda/2$ array, focused to 38.4 mm ($z_{\mathrm{TR}}/2$), with delays quantized to $\mu = 4$ (narrowband simulation)

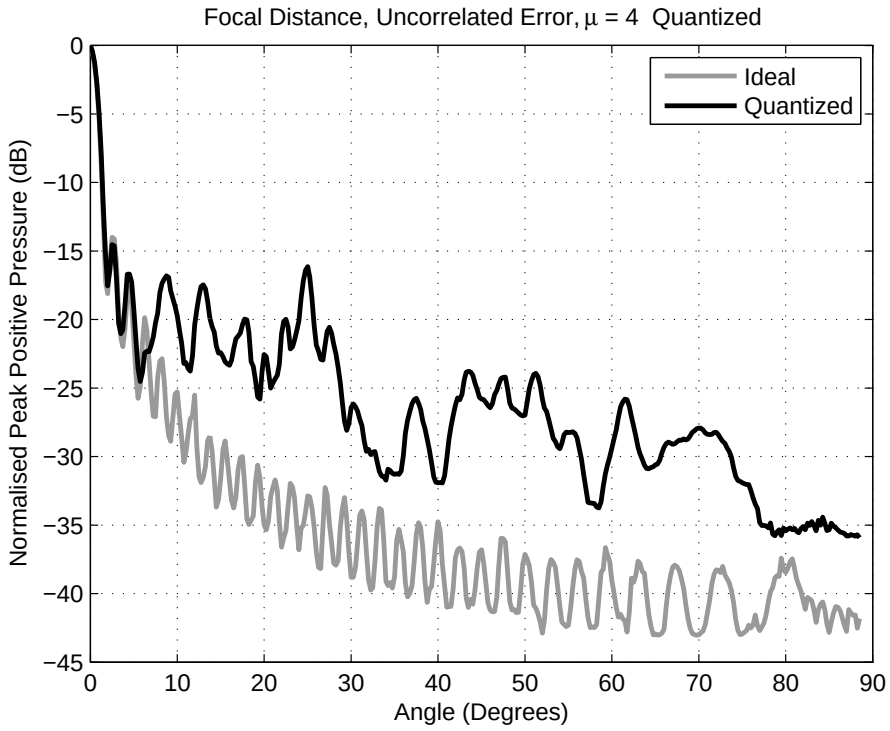

Figure 4.30: Simulated radial field profile, 64 element $\lambda/2$ array, focused to 38.4 mm ($z_{\mathrm{TR}}/2$), with delays quantized to $\mu = 4$ (narrowband simulation)

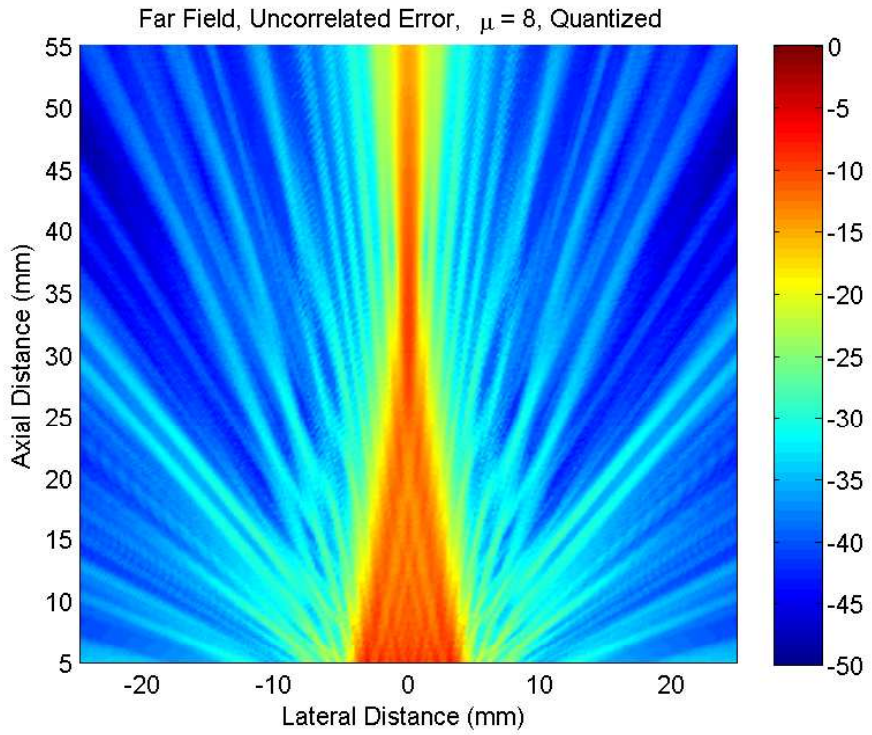

Figure 4.31: Simulated beam profile, 64 element $\lambda/2$ array, focused to 38.4 mm ($z_{\mathrm{TR}}/2$) with delays quantized to $\mu = 8$ (narrowband simulation)

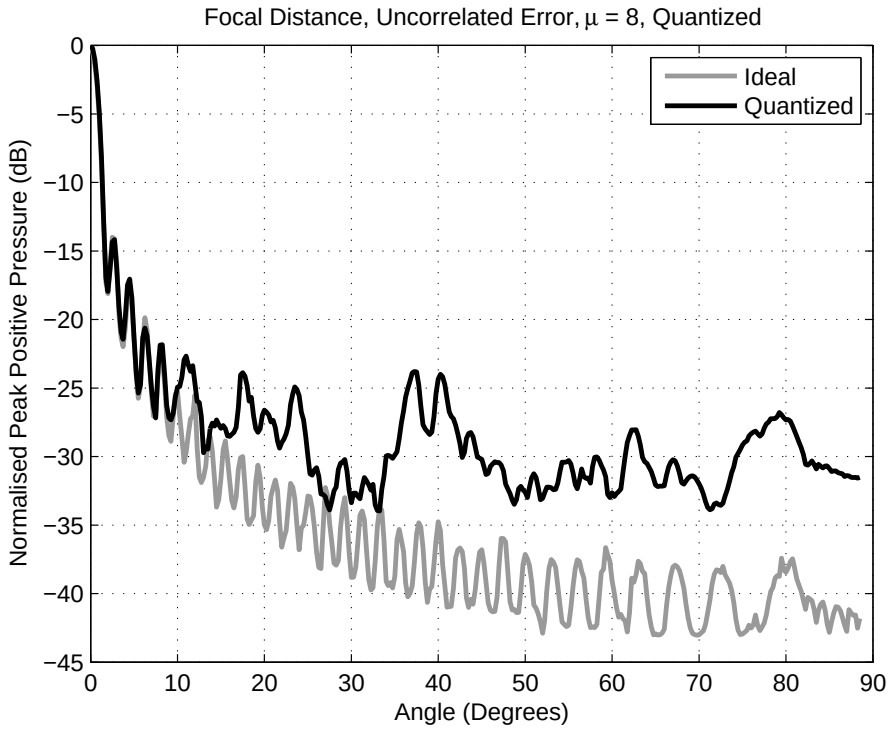

Figure 4.32: Simulated radial field profile, 64 element $\lambda/2$ array, focused to 38.4 mm ($z_{\mathrm{TR}}/2$), with delays quantized to $\mu = 8$ (narrowband simulation)

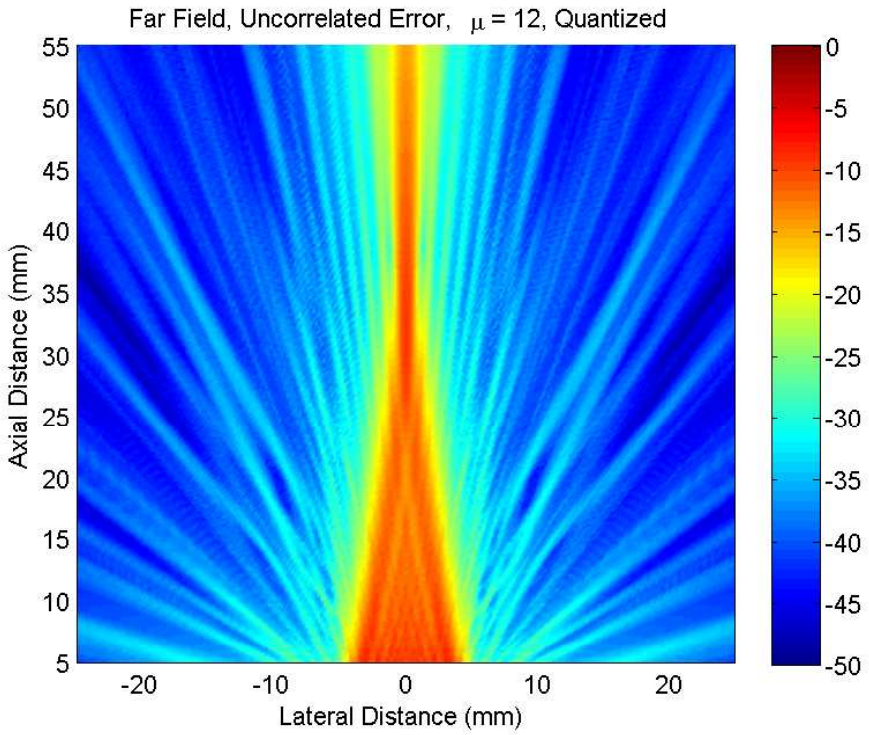

Figure 4.33: Simulated beam profile, 64 element $\lambda/2$ array, focused to 38.4 mm ($z_{\mathrm{TR}}/2$), with delays quantized to $\mu = 12$ (narrowband simulation)

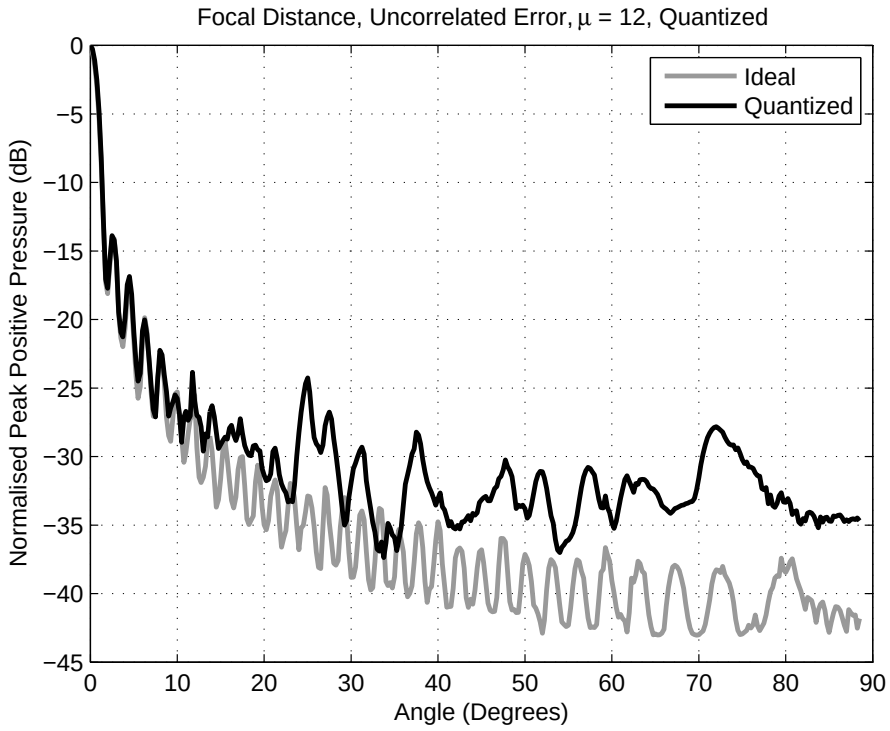

Figure 4.34: Simulated radial field profile, 64 element $\lambda/2$ array, focused to 38.4 mm ($z_{\mathrm{TR}}/2$), with delays quantized to $\mu = 12$ (narrowband simulation)

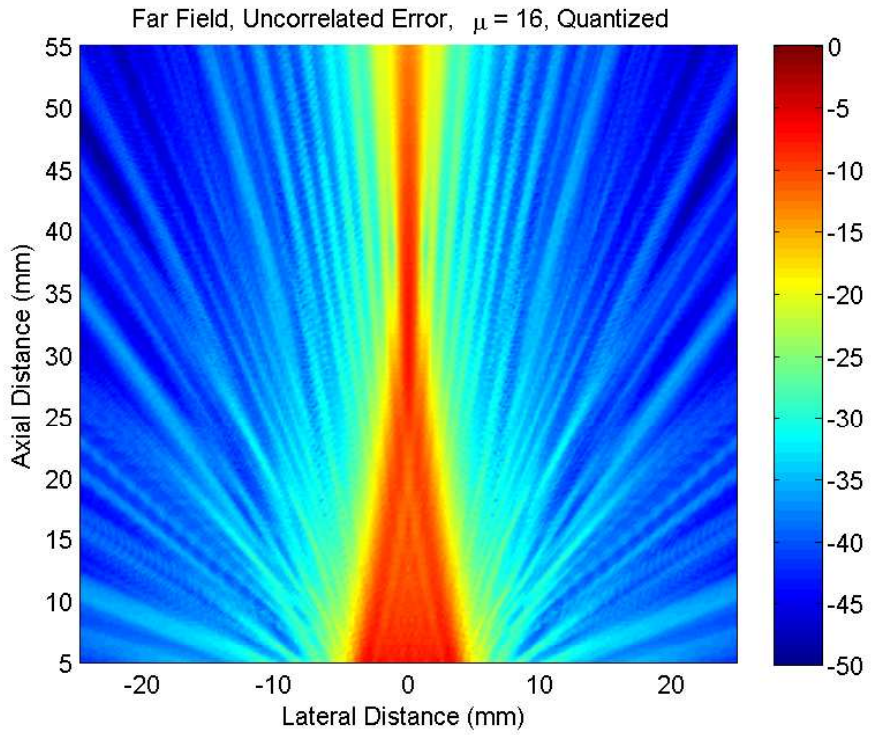

Figure 4.35: Simulated beam profile, 64 element $\lambda/2$ array, focused to 38.4 mm ($z_{\mathrm{TR}}/2$), with delays quantized to $\mu = 16$ (narrowband simulation)

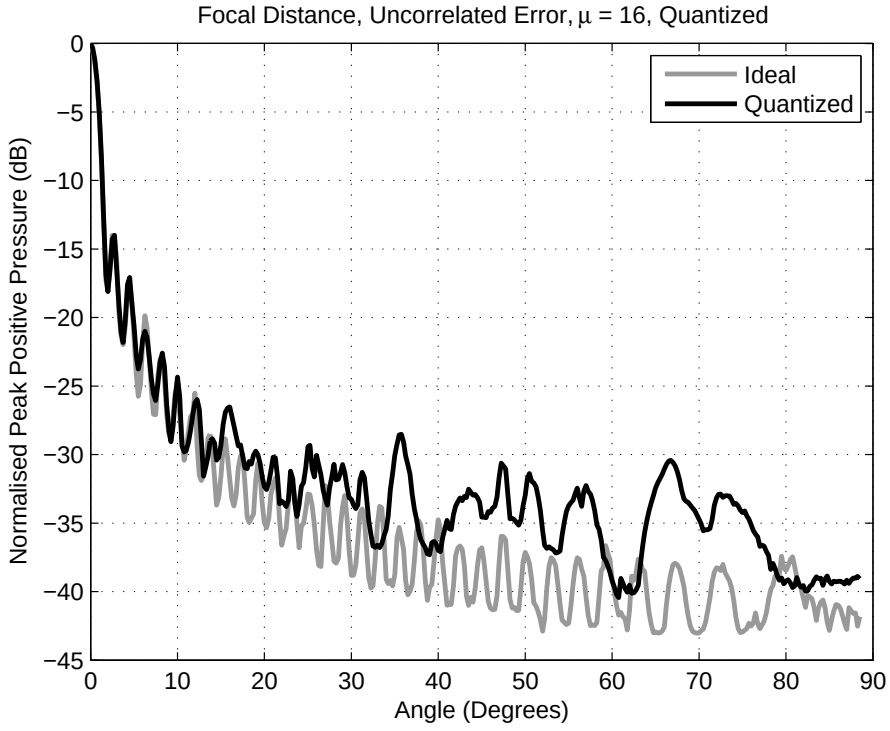

Figure 4.36: Simulated radial field profile, 64 element $\lambda/2$ array, focused to 38.4 mm ($z_{\mathrm{TR}}/2$), with delays quantized to $\mu = 16$ (narrowband simulation)

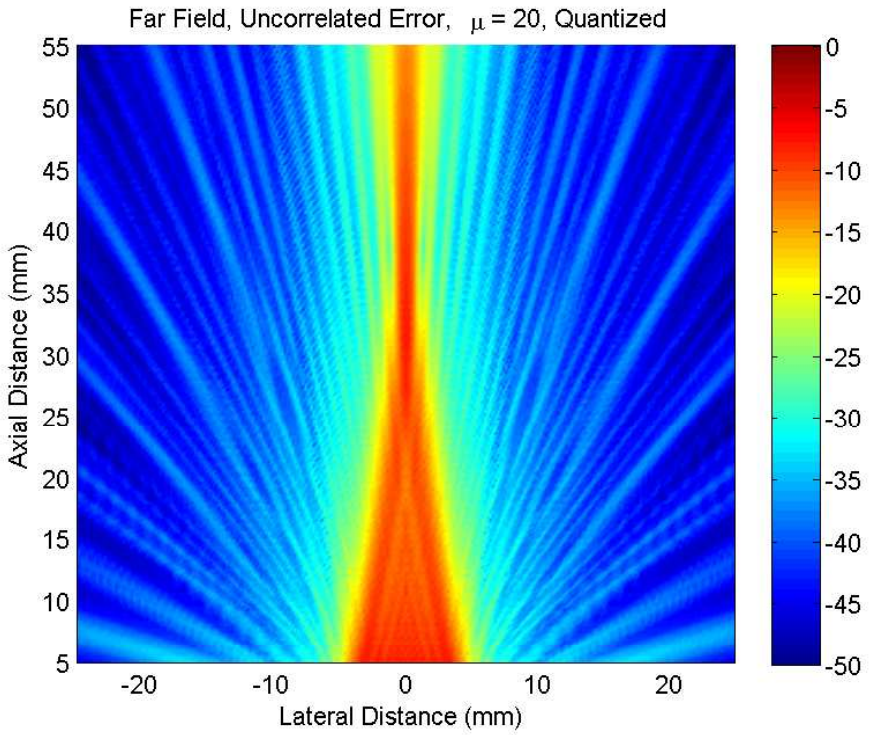

Figure 4.37: Simulated beam profile, 64 element $\lambda/2$ array, focused to 38.4 mm ($z_{\mathrm{TR}}/2$), with delays quantized to $\mu = 20$ (narrowband simulation)

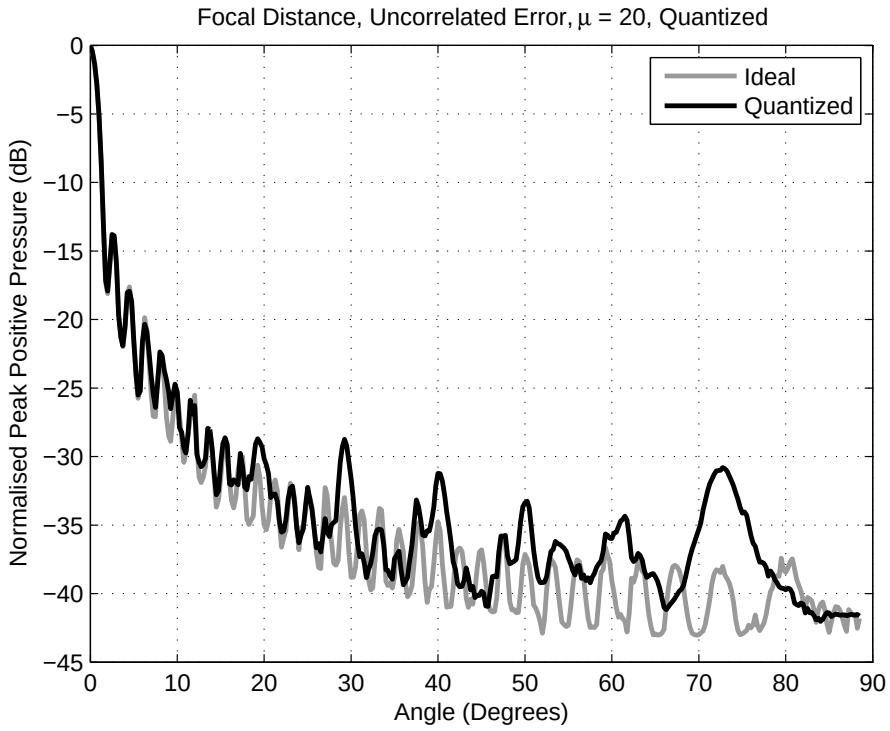

Figure 4.38: Simulated radial field profile, 64 element $\lambda/2$ array, focused to 38.4 mm ($z_{\mathrm{TR}}/2$), with delays quantized to $\mu = 20$ (narrowband simulation)

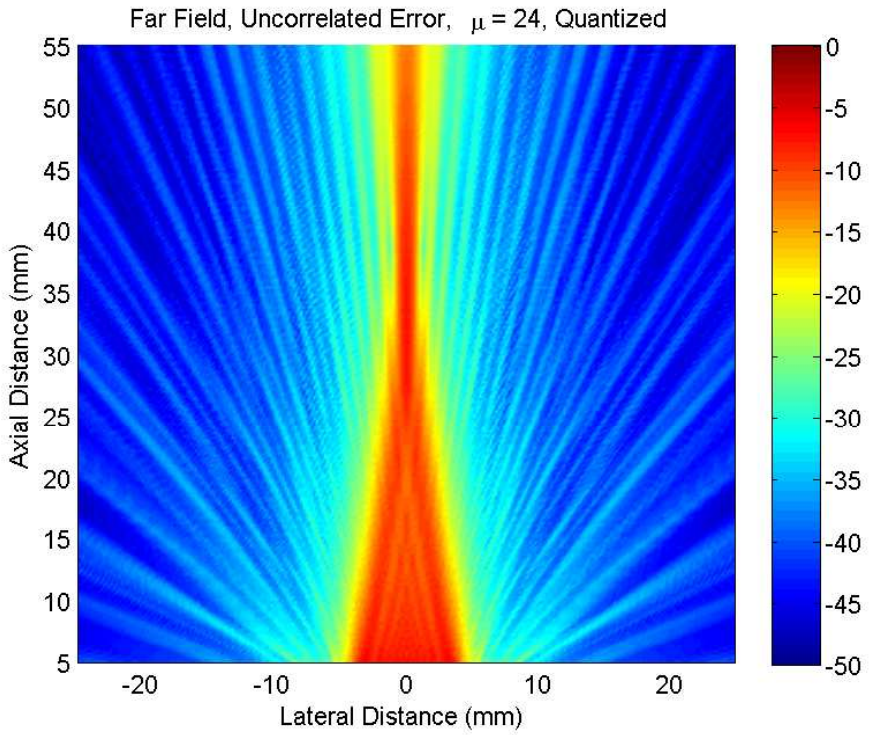

Figure 4.39: Simulated beam profile, 64 element $\lambda/2$ array, focused to 38.4 mm ($z_{TR}/2$), with delays quantized to $\mu = 24$ (narrowband simulation)

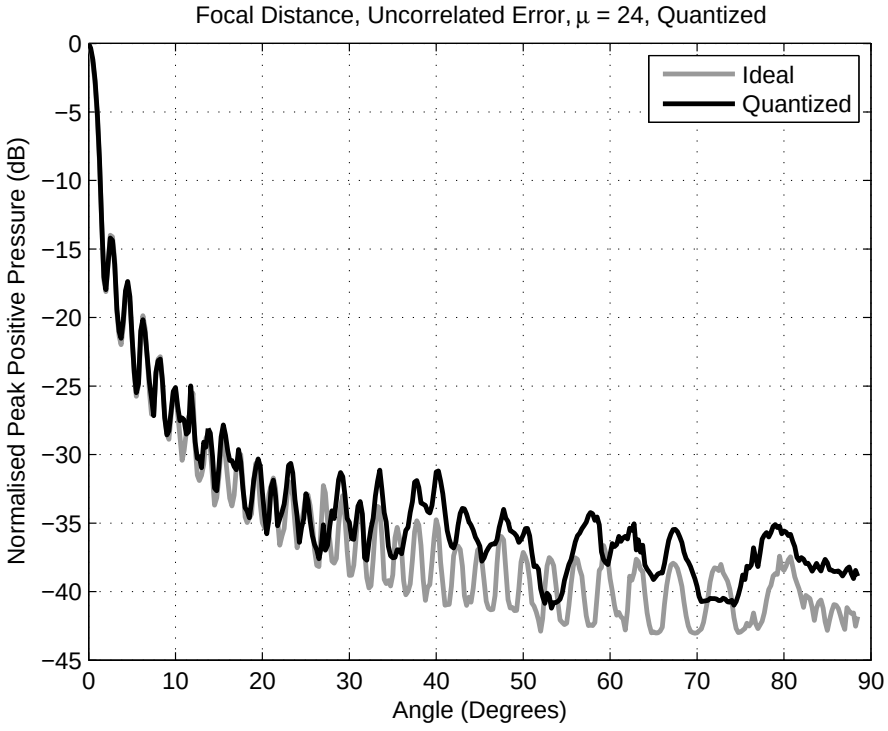

Figure 4.40: Simulated radial field profile, 64 element $\lambda/2$ array, focused to 38.4 mm ($z_{TR}/2$), with delays quantized to $\mu = 24$ (narrowband simulation)

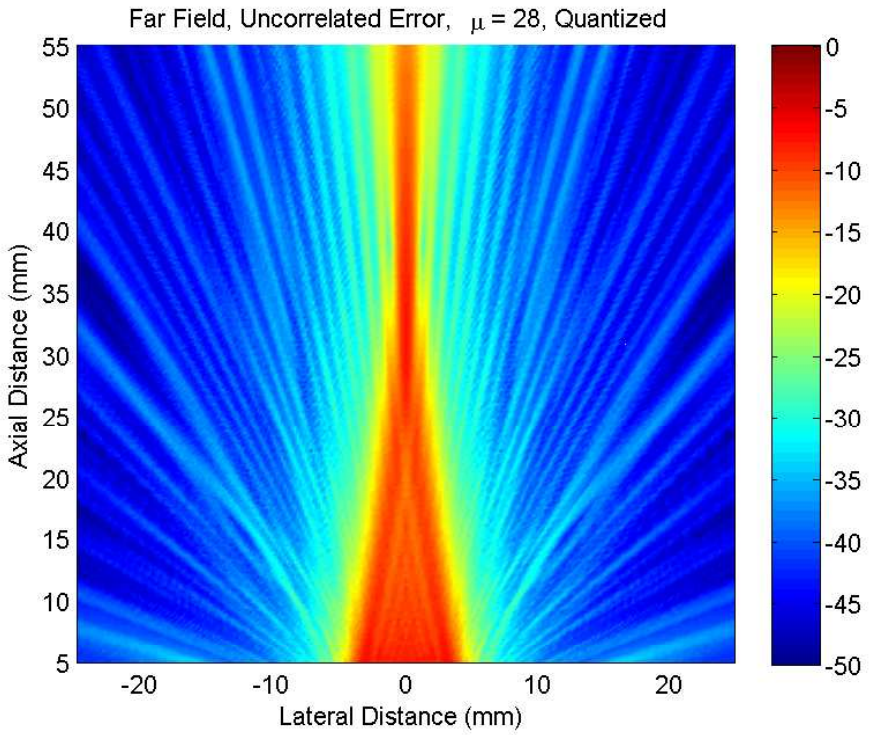

Figure 4.41: Simulated beam profile, 64 element $\lambda/2$ array, focused to 38.4 mm ($z_{\mathrm{TR}}/2$), with delays quantized to $\mu = 28$ (narrowband simulation)

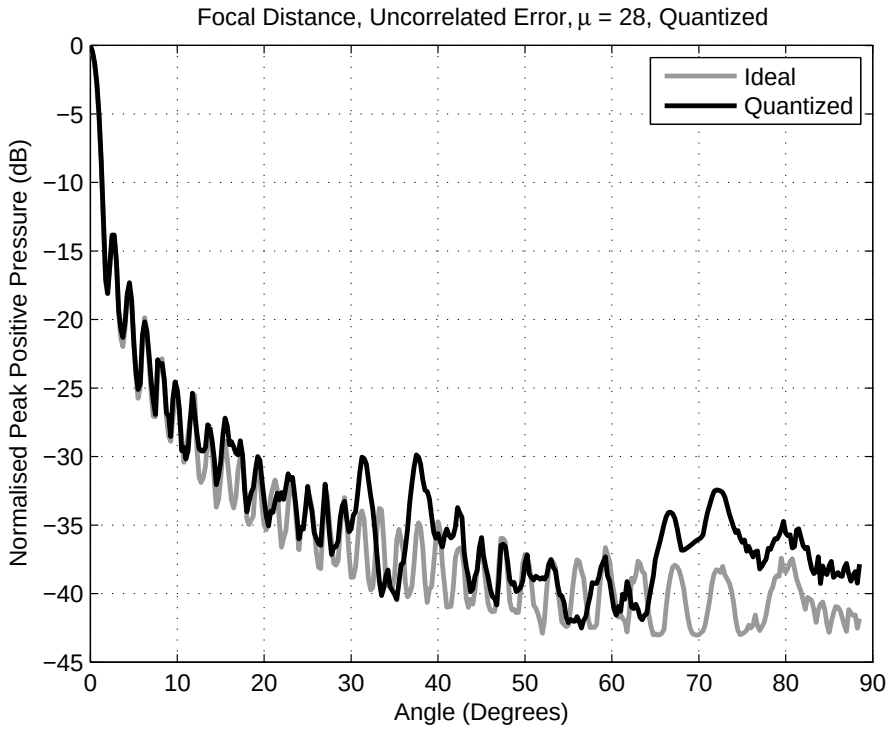

Figure 4.42: Simulated radial field profile, 64 element $\lambda/2$ array, focused to 38.4 mm ($z_{\mathrm{TR}}/2$), with delays quantized to $\mu = 28$ (narrowband simulation)

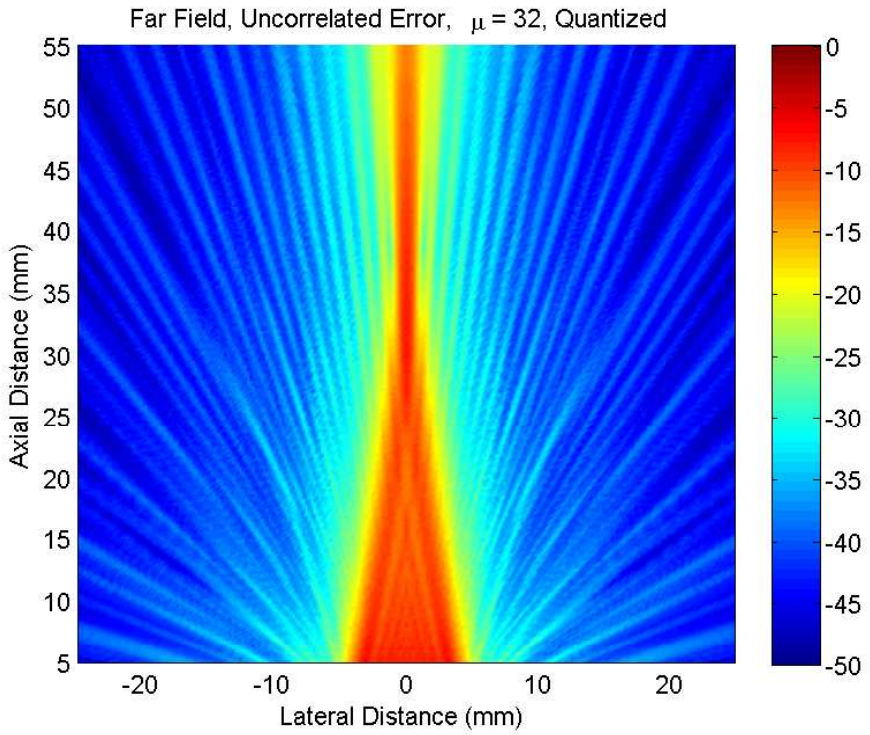

Figure 4.43: Simulated beam profile, 64 element $\lambda/2$ array, focused to 38.4 mm ($z_{\mathrm{TR}}/2$), with delays quantized to $\mu = 32$ (narrowband simulation)

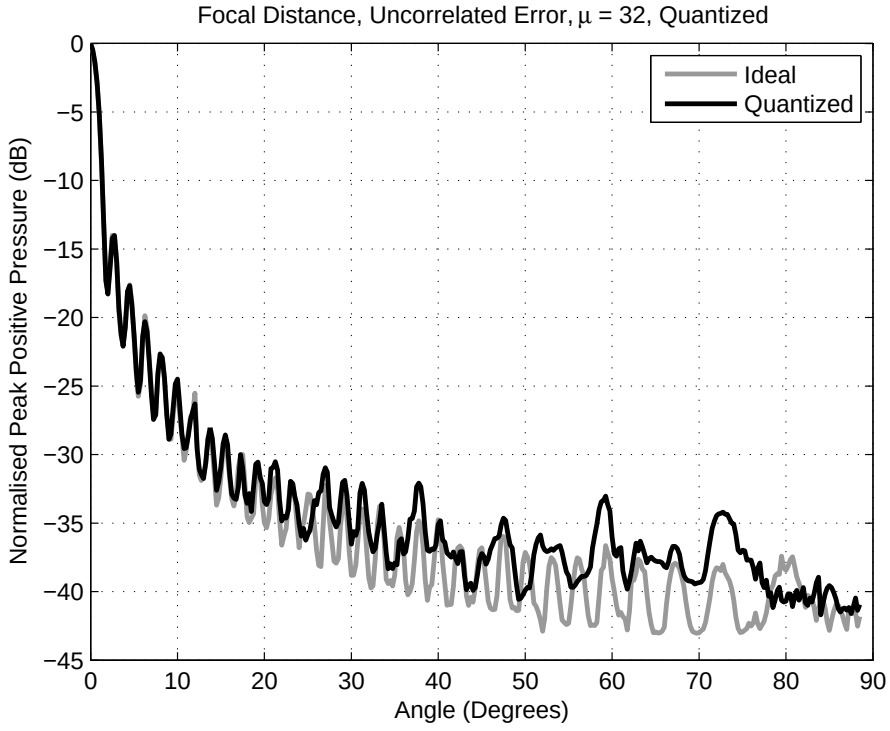

Figure 4.44: Simulated radial field profile, 64 element $\lambda/2$ array, focused to 38.4 mm ($z_{\mathrm{TR}}/2$), with delays quantized to $\mu = 32$ (narrowband simulation)

The continuous wave (narrowband) case shows distinct lobes in the field profile. However, field disturbance is still evident in the pulsed wave (broadband) case. Figures 4.45 to 4.60 show the same array, focused to the same point, but with a three cycle pulse used instead of the continuous wave approximation. It can be seen from the Figures that lobe energy in the far field is reduced when compared with the continuous wave case. However, in the near field, energy surrounding the beam is still prevalent. In both cases, the pressure around the main beam is dependent on the combination of the desired focal profile, and minimum time increment. For example, in Figure 4.54 (radial plot at $\mu = 20$), there appears to be a closer approximation to the 'ideal' case, than when compared with finer quantization as shown in Figure 4.56 (radial plot at $\mu = 24$). The uncorrelated nature of the distribution therefore causes difficulty in determining the level of quantization value necessary to cover all cases.

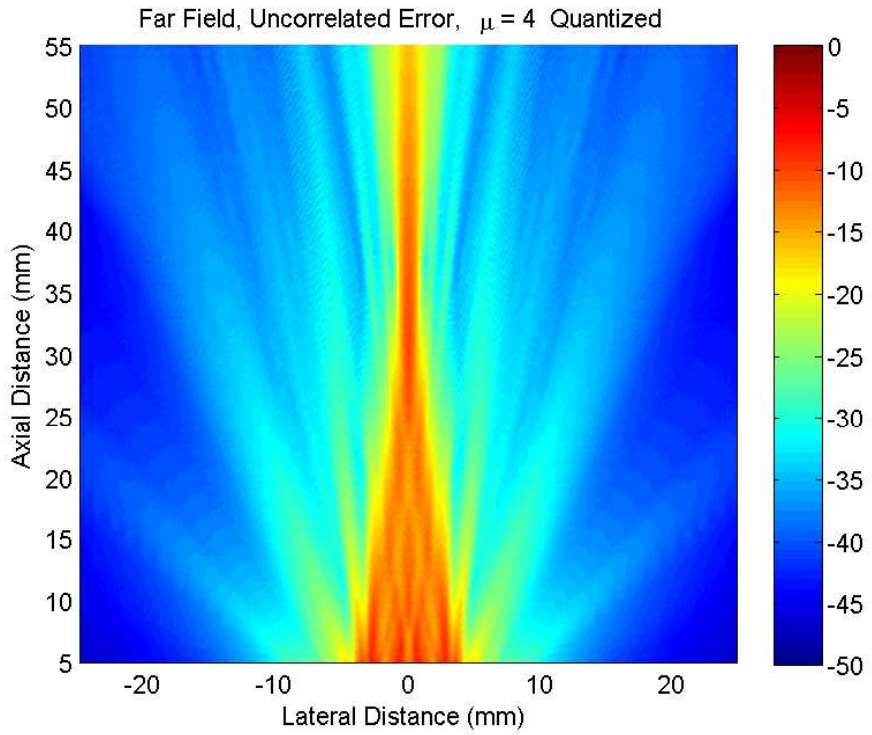

Figure 4.45: Simulated beam profile, 64 element $\lambda/2$ array, focused to 38.4 mm ($z_{TR}/2$), with delays quantized to $\mu = 4$ (broadband simulation)

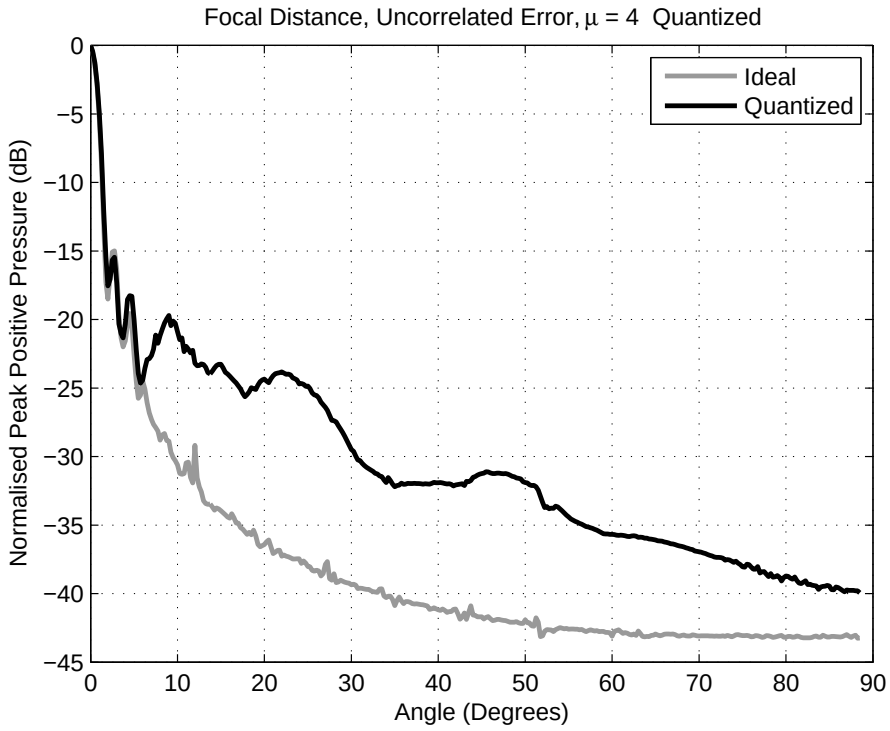

Figure 4.46: Simulated radial field profile, 64 element $\lambda/2$ array, focused to 38.4 mm ($z_{TR}/2$), with delays quantized to $\mu = 4$ (broadband simulation)

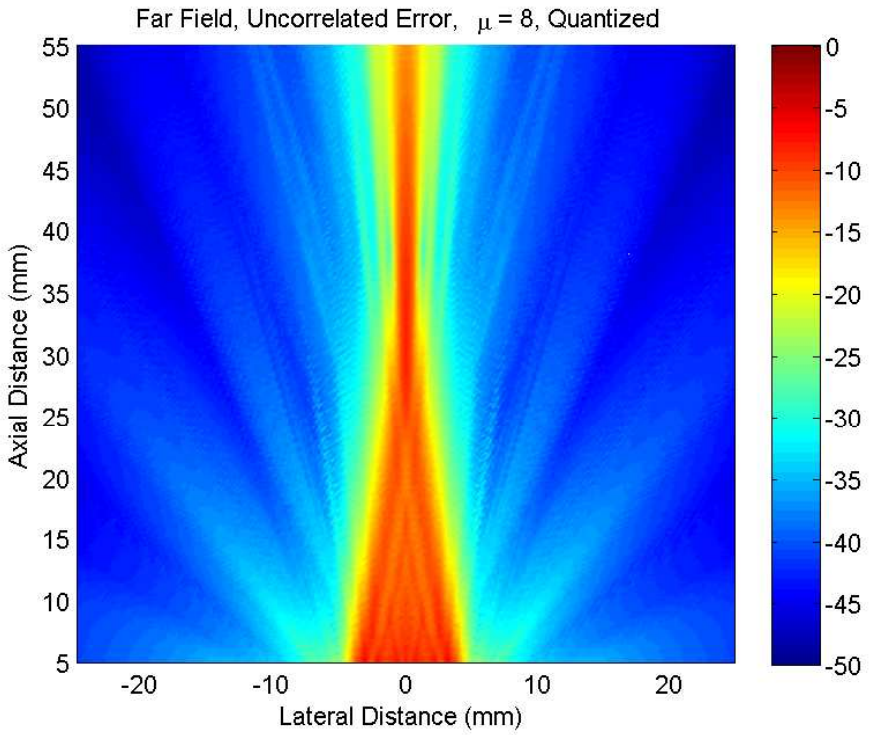

Figure 4.47: Simulated beam profile, 64 element $\lambda/2$ array, focused to 38.4 mm ($z_{\mathrm{TR}}/2$), with delays quantized to $\mu = 8$ (broadband simulation)

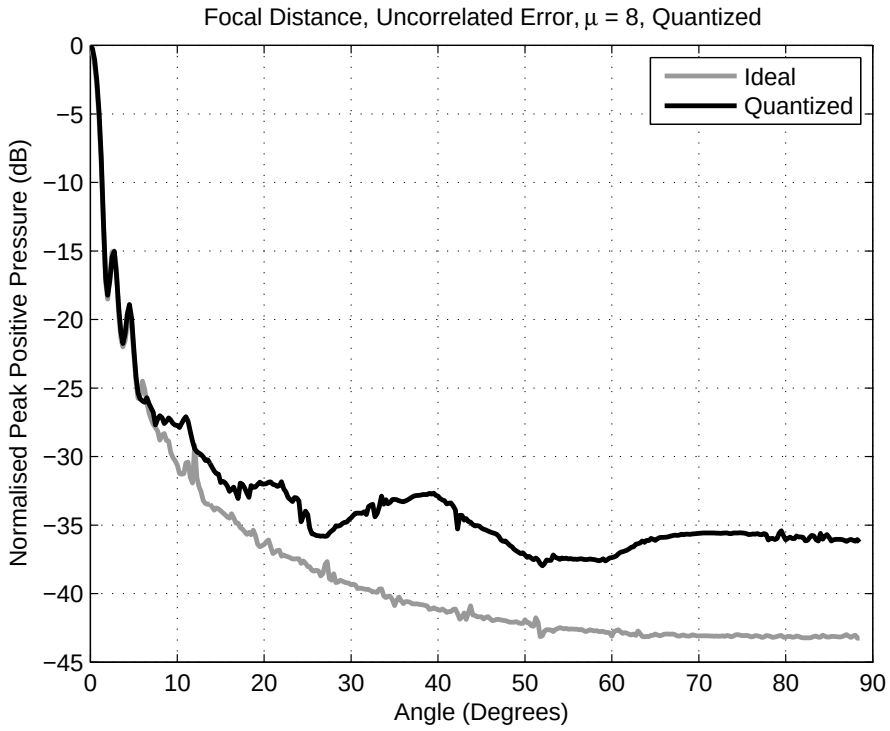

Figure 4.48: Simulated radial field profile, 64 element $\lambda/2$ array, focused to 38.4 mm ($z_{\mathrm{TR}}/2$), with delays quantized to $\mu = 8$ (broadband simulation)

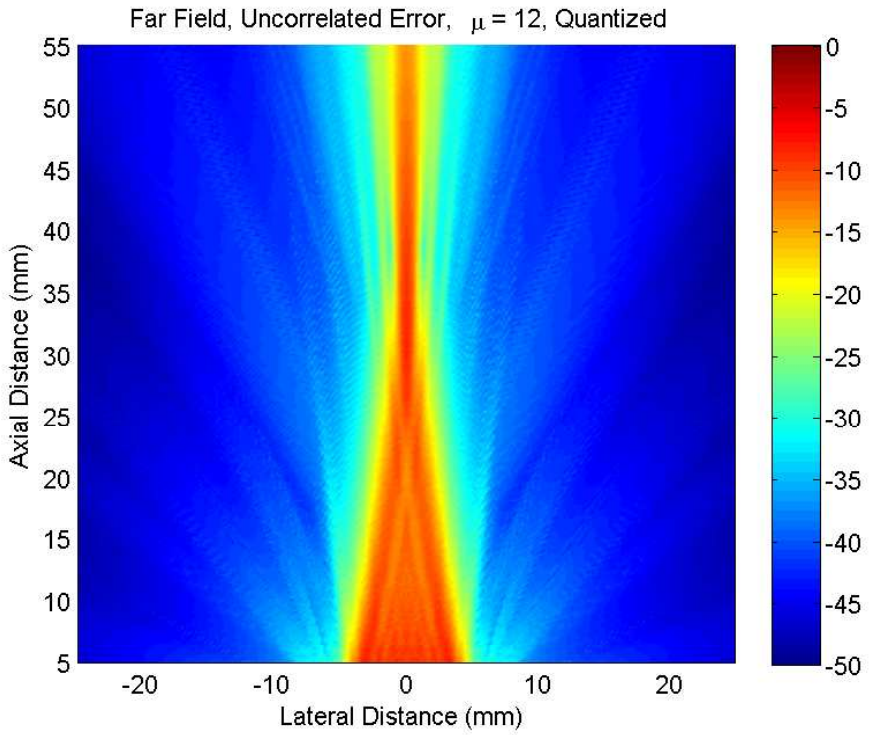

Figure 4.49: Simulated beam profile, 64 element $\lambda/2$ array, focused to 38.4 mm ($z_{\mathrm{TR}}/2$), with delays quantized to $\mu = 12$ (broadband simulation)

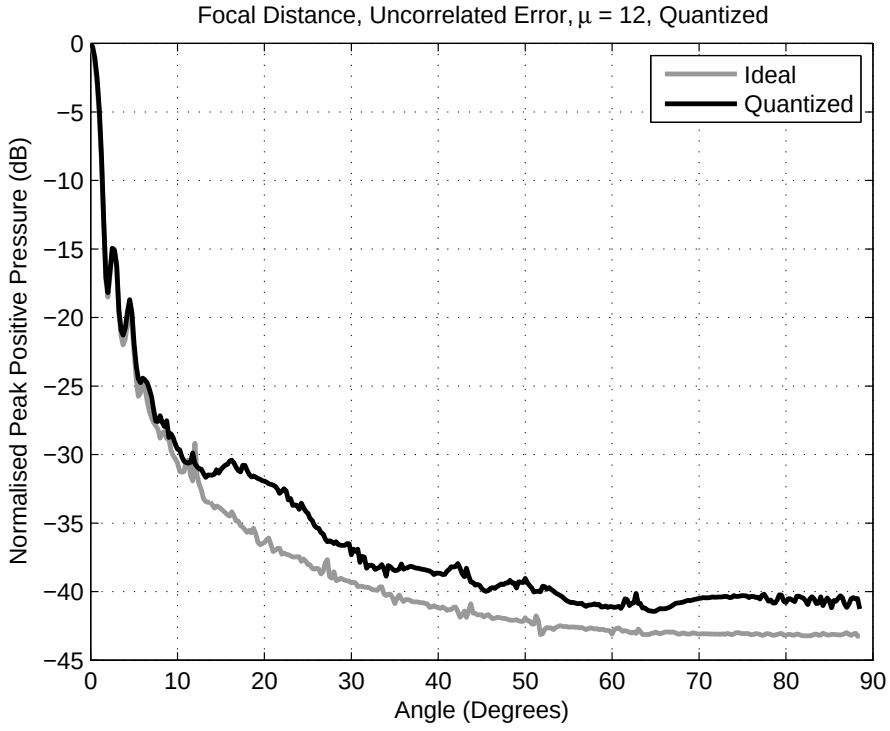

Figure 4.50: Simulated radial field profile, 64 element $\lambda/2$ array, focused to 38.4 mm ($z_{\mathrm{TR}}/2$), with delays quantized to $\mu = 12$ (broadband simulation)

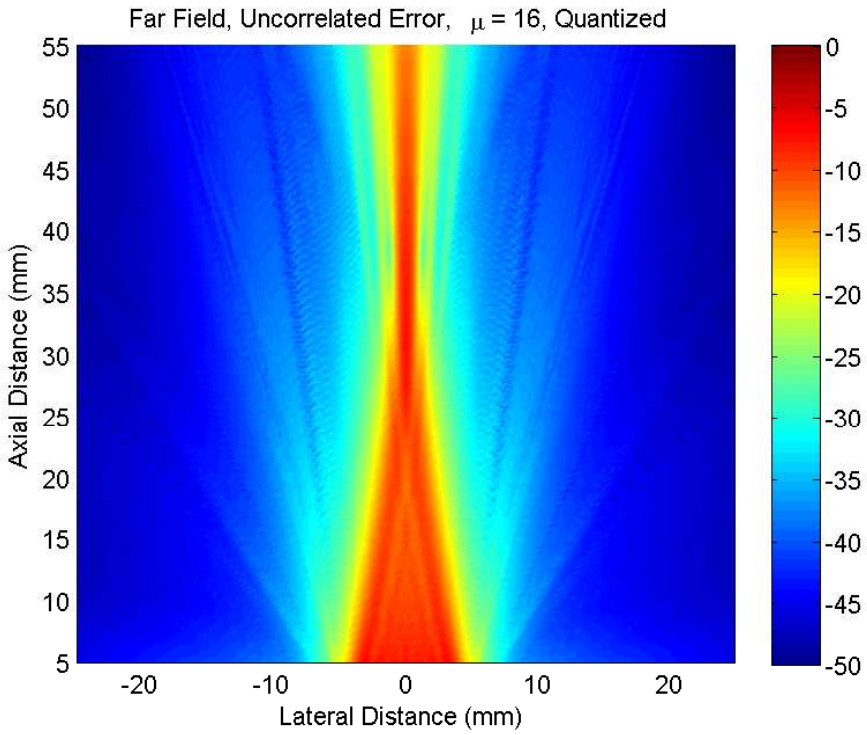

Figure 4.51: Simulated beam profile, 64 element $\lambda/2$ array, focused to 38.4 mm ($z_{\mathrm{TR}}/2$), with delays quantized to $\mu = 16$ (broadband simulation)

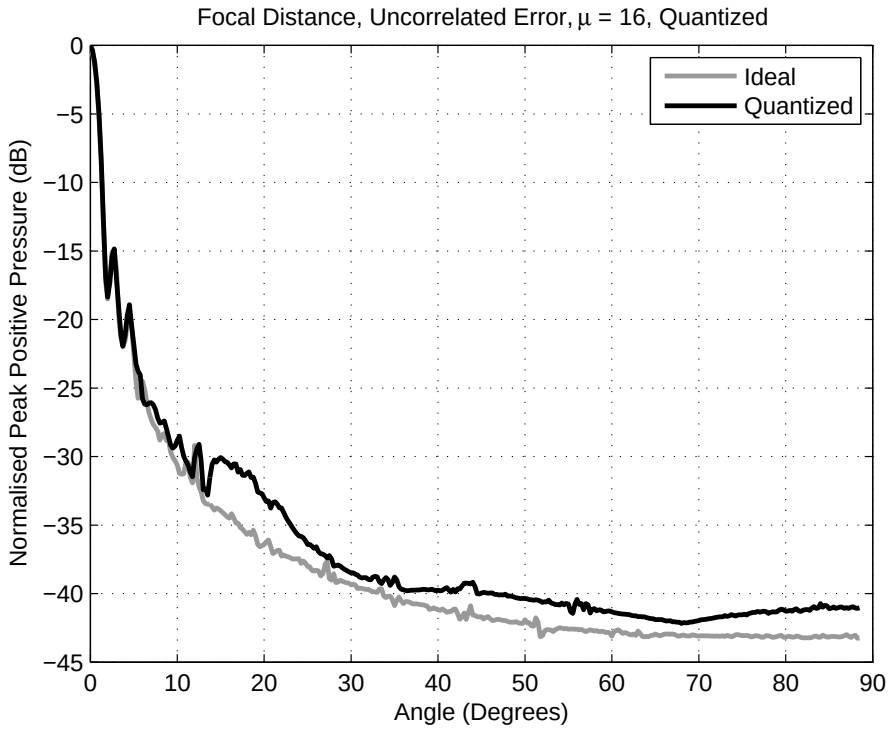

Figure 4.52: Simulated radial field profile, 64 element $\lambda/2$ array, focused to 38.4 mm ($z_{\mathrm{TR}}/2$), with delays quantized to $\mu = 16$ (broadband simulation)

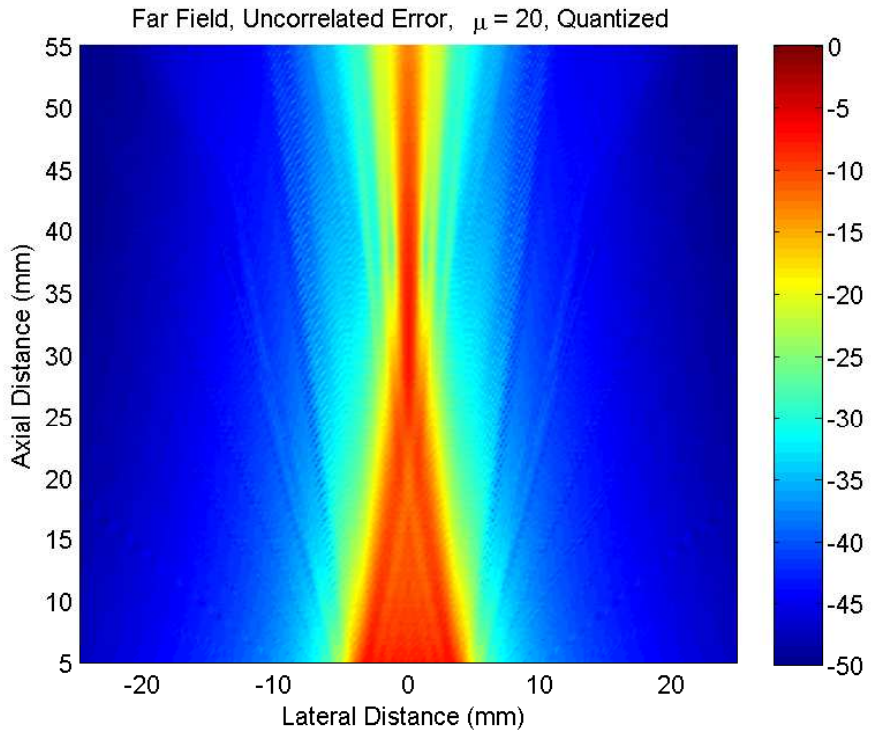

Figure 4.53: Simulated beam profile, 64 element $\lambda/2$ array, focused to 38.4 mm ($z_{\mathrm{TR}}/2$), with delays quantized to $\mu = 20$ (broadband simulation)

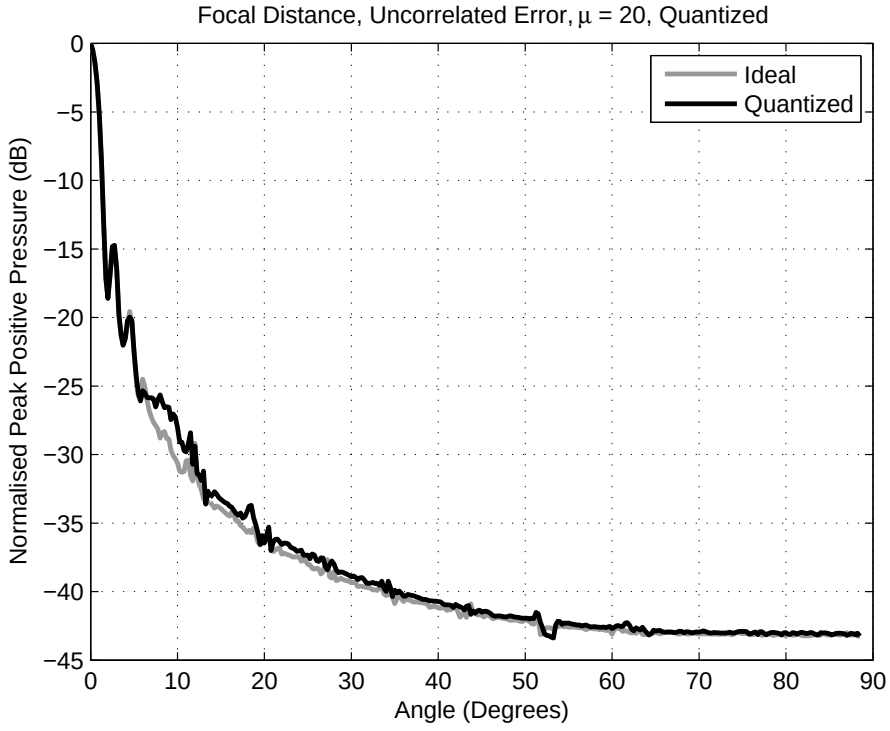

Figure 4.54: Simulated radial field profile, 64 element $\lambda/2$ array, focused to 38.4 mm ($z_{\mathrm{TR}}/2$), with delays quantized to $\mu = 20$ (broadband simulation)

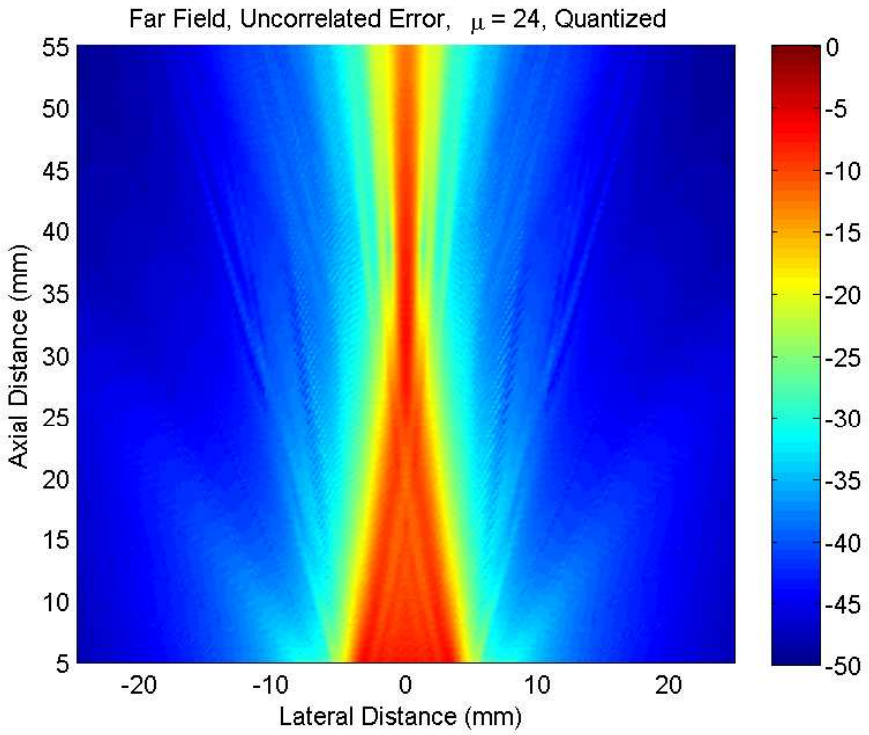

Figure 4.55: Simulated beam profile, 64 element $\lambda/2$ array, focused to 38.4 mm ($z_{\mathrm{TR}}/2$), with delays quantized to $\mu = 24$ (broadband simulation)

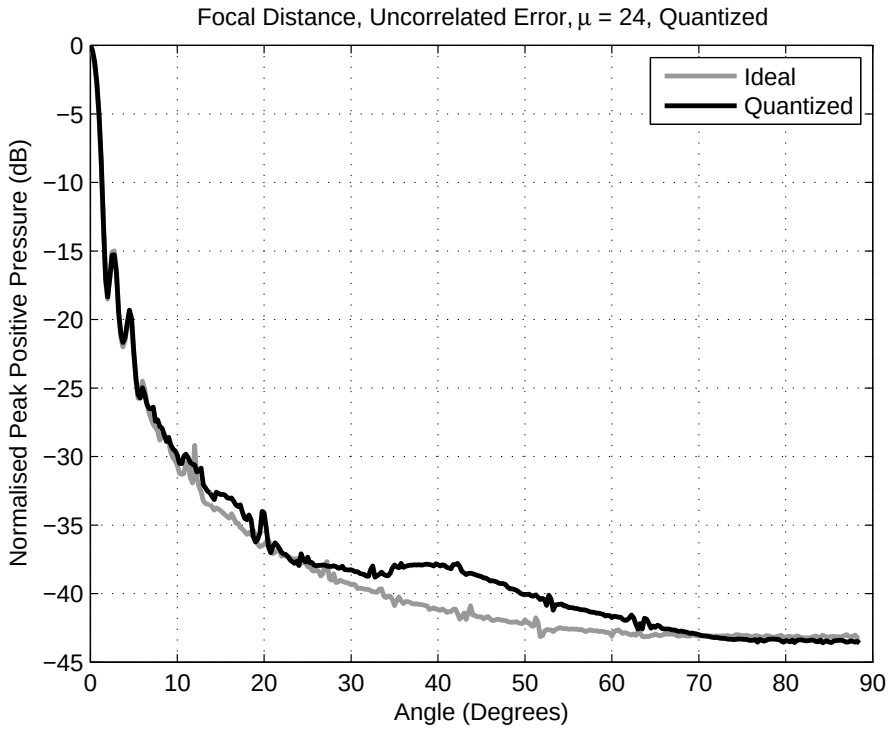

Figure 4.56: Simulated radial field profile, 64 element $\lambda/2$ array, focused to 38.4 mm ($z_{\mathrm{TR}}/2$), with delays quantized to $\mu = 24$ (broadband simulation)

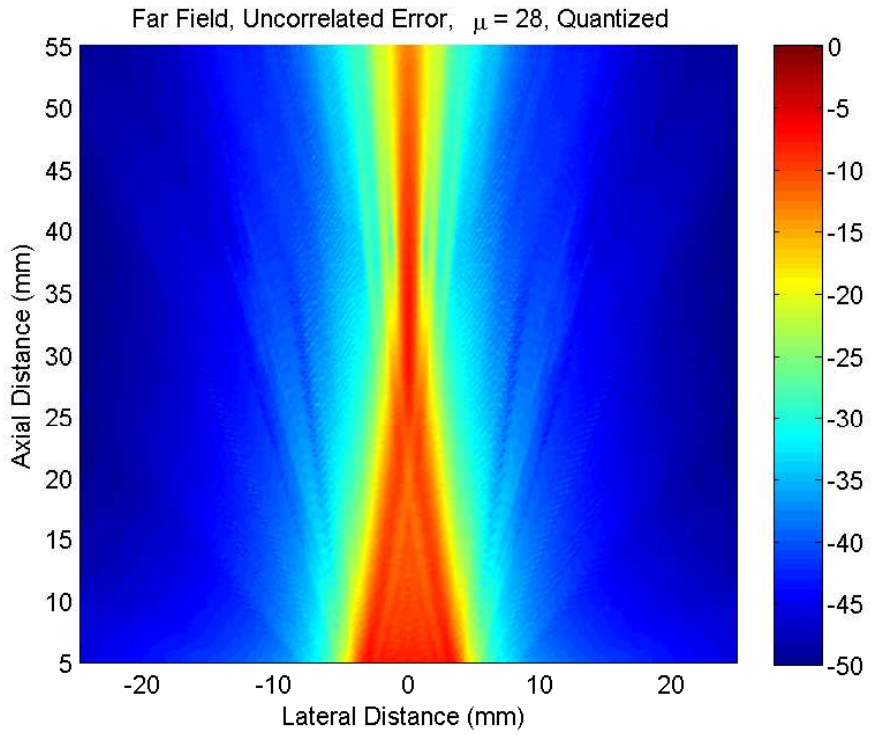

Figure 4.57: Simulated beam profile, 64 element $\lambda/2$ array, focused to 38.4 mm ($z_{\mathrm{TR}}/2$), with delays quantized to $\mu = 28$ (broadband simulation)

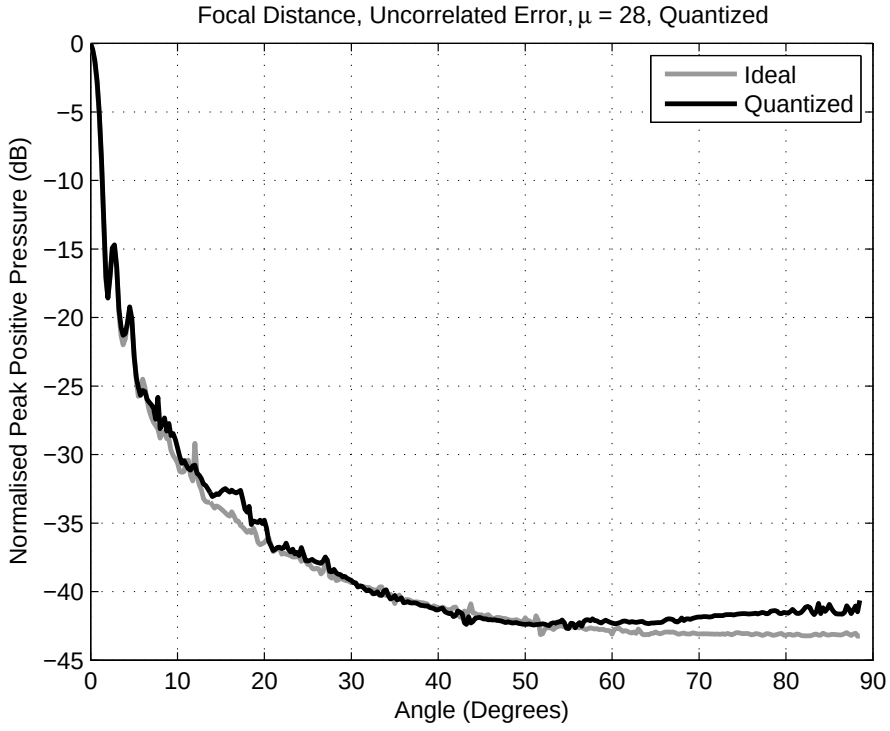

Figure 4.58: Simulated radial field profile, 64 element $\lambda/2$ array, focused to 38.4 mm ($z_{\mathrm{TR}}/2$), with delays quantized to $\mu = 28$ (broadband simulation)

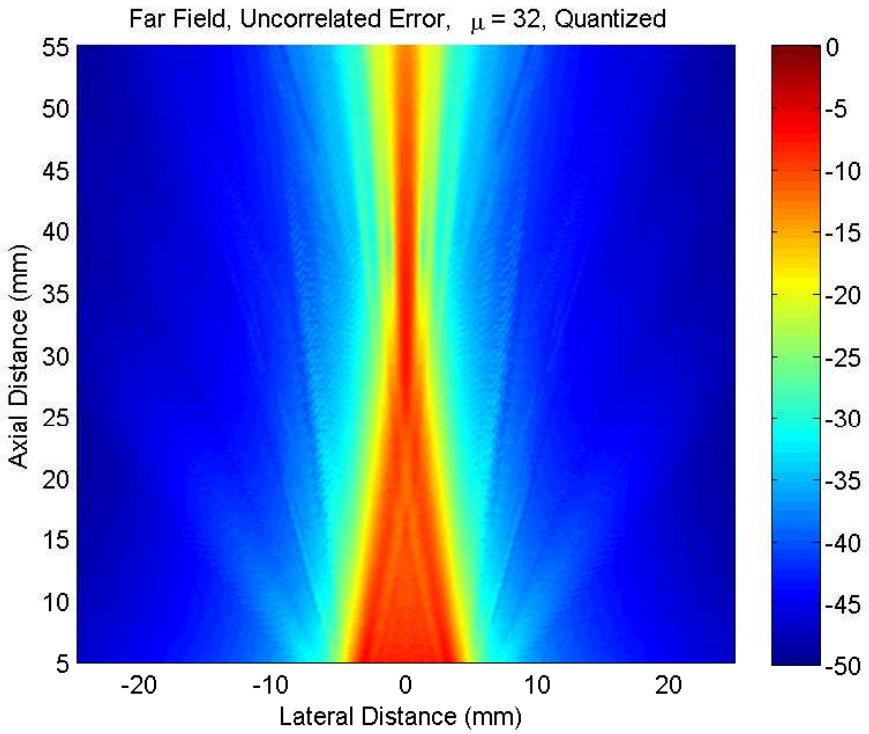

Figure 4.59: Simulated beam profile, 64 element $\lambda/2$ array, focused to 38.4 mm ($z_{\mathrm{TR}}/2$), with delays quantized to $\mu = 32$ (broadband simulation)

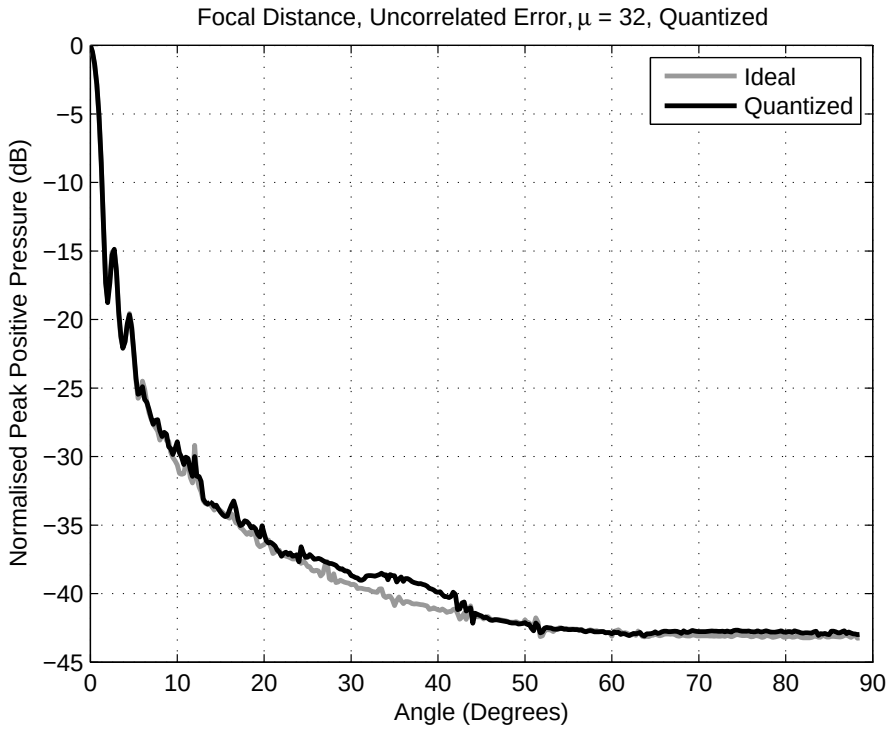

Figure 4.60: Radial field profile, 64 element $\lambda/2$ array, focused to 38.4 mm ($z_{\mathrm{TR}}/2$), with delays quantized to $\mu = 32$ (broadband simulation)

4.7 Other Forms of Random Error

Phase quantization causes degradation of an ideal beam profile, due to energy being directed away an intended position. This can also occur due to other system inaccuracies. For example, focusing profiles are calculated using a single value for speed of sound as shown in (4.3), (4.5) and (4.6). This assumption of constant speed of sound applies only if the medium is homogeneous, or the material has a uniform velocity of sound [108]. In practical cases, e.g. when imaging tissue, or composite materials, the speed of sound may vary considerably at different places, due to different material densitites. For layers such as fat or bone this causes refraction errors that can degrade image resolution and cause overall image distortion [104]. To correct for this, new calculations for delay profiles must be made [108] with perhaps only minor adjustment of focusing delays required. Such a technique can only be made however, with prior knowledge or assumption of the target being imaged, and would be used in an iterative process of adjusting phases and analysing gains in image quality.

Another example of error can be introduced at the transducer, either by differences in element response, or complete failure of elements. These effects have previously been discussed by several authors. A thorough, recent explanation of random errors concerning transducer array performance has been provided by Duxbury *et al.* [106]. In [106] the effects of various cases of element inhomogeneity were demonstrated, including element sensitivity, and dead (extremely low sensitivity) elements, as well as errors in firing delay as discussed previously in the chapter. Duxbury concluded using an acceptance criteria approach that random variations were tolerable for cases that resulted in sidelobe amplitudes less than 8 dB below the mainlobe. These 'acceptable' scenarios included a limit of $\pm 50\%$ of the mean element sensitivity, and up to 9% of elements to be dead. A main conclusion was that random system inaccuracies could cause similar effects to the uncorrelated error cases studied within this Chapter. In a similar paper, Zhang *et al.* [107] discussed random error that distorted post-processing algorithms such as synthetic aperture focusing, and the total focusing method that require capture of all combinations of elements.

When considering all sources of error due to poor phase quantization, or due to other system inaccuracies, the ability to compensate in transmit for random inaccuracies and provide accurate representation of delay profiles has potential in improving quality of acquisition. When considering a transmit beamformer design, this leads us to a set of desired criteria:

- It is desirable to design a transmit beamformer that has high timing resolution so as to reduce the effects of phase quantization across a range of frequencies.
- It is desirable to design a transmit beamformer that can suppress uncorrelated quantization lobe effects which mostly dominate the beam profile, and can not necessarily be predicted when compared with the correlated case.
- It is desirable to design a transmit beamformer that can adapt to other random error scenarios, such as non-ideal or unexpected operation of transducer elements and perturbation or aberration in the field.

4.8 UARP Transmitter Architecture

The UARP system was briefly introduced in Chapter 2, with the transmitter hardware shown in Chapter 3. The motivation of this work was to develop a flexible research platform capable of versatile performance. This section describes the transmit beamforming architecture sub-component that aims to address the criteria discussed in the previous section by achieving accurate and flexible inter-element timing and reduced beam error. The influence of phase quantization error on the transmitted beam profile is governed by the minimum time increment possible between adjacent transmit channels. The influence of random error on the transmitted beam profile is also governed by how adjacent channel delays can be varied. As a consequence, adverse quantization, or error defects are dependent on transmitter implementation and design.

A number of transmit beamformer architectures have been presented in previous literature. Contrasting methods include tapped analogue delay lines, to variable methods such

as storage of signals and offsetting in memory [46]. Other variable delay methods include the use of dedicated integrated delay circuits and micro-controllers as discussed in [120], and the use of external Phase-Locked Loop (PLL) components within front-end designs [121].

The use of PLL-type components has proved popular for phased array applications. Examples in literature have included a method of introducing transmitter phase delays using Voltage Controlled Oscillators (VCOs) with counters for use in ultrasound scanners as described by [97]. Lovejoy *et al.* [121] designed a programmable phased array controller for use as an ultrasound hyperthermia applicator using discrete components such as Logic Gates and RC delay lines to alter signal phases. Whilst this design appears to work well at the intended frequency range (0.3 to 1 MHz), at higher frequencies the chip gate delays within each delay circuit become more critical and become a potentially limiting factor.

An example of an integrated solution using phase shifted clocks was demonstrated by Hatfield [122]. This work focused on an Application Specific Integrated Circuit (ASIC) design intended to be incorporated within the transducer itself. A reported benefit of the design included reducing the unwieldy bundle of cables that accompany a transducer, which increases with the use of more larger transducer devices. A concern with this design however is the lack of transmit excitation flexibility, which may be necessary as ultrasound techniques evolve.

The following section introduces a method using PLLs embedded within current FPGA technology to alter phases of internal clocks with close accuracy in order to improve the inter channel resolution in transmit beam forming.

4.8.1 Phase Locked Loops

Phase locked loops are components used throughout electronic systems to generate and distribute a.c. signals such as clocks. Their main function is to measure phase but adjust frequency [95]. As the name implies, PLLs produce an output signal that is locked to the phase of an input signal. Locking of phase is achieved using a negative feedback loop in conjunction with a phase detector. A phase detector [95] compares two signals, (in this

case the input signal and the current output signal) and generates an output proportional to the difference in phase between the two [95]. Example phase detection circuits can be XOR gates with RC low-pass filters (type I), or edge-sensitive lag and lead phase detectors (type II) [95]. The phase detector converts input phase difference to voltage, with an output signal generated using a VCO, a component that converts voltage to frequency. PLLs are primarily used in digital systems to redistribute clock signals that may be weak or noisy. They can also be used to generate clocks of different frequencies that have a defined phase relationship with the input clock. This is achieved in digital systems using counter stages that can adjust parameters to alter the response of the VCO. A diagram of a PLL including VCO, loop filter, phase detector, pre-scale counter post-scale counter and a feedback counter as described in [123] is shown in Figure 4.61. The counters (P, M

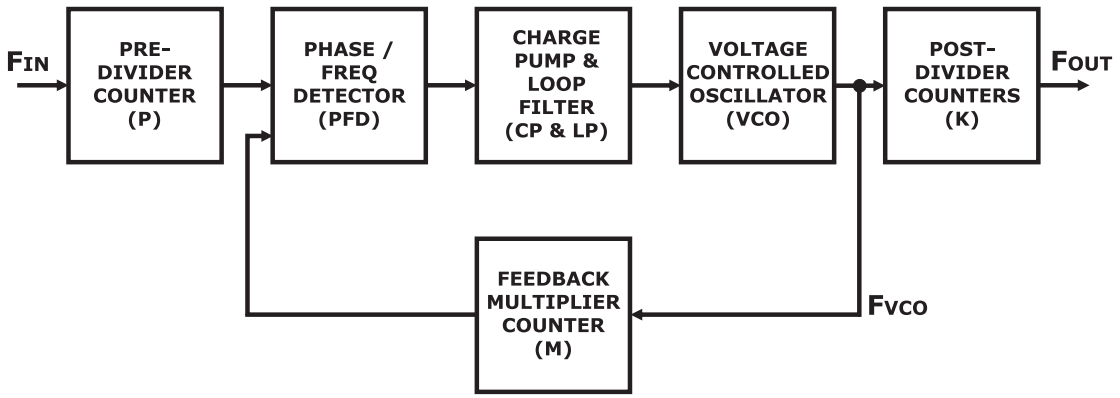

Figure 4.61: Typical PLL architecture

and K in Figure 4.61) can be used to multiply or divide the frequency of the output clocks accordingly using [123]

$$F_{\mathrm{OUT}} = \frac{M \times F_{\mathrm{IN}}}{P \times K} \tag{4.21}$$

where F_{IN} is the input frequency, M is the feedback counter, P is the pre-scale counter and K is the post-scale counter. Higher frequencies can be generated by using the feedback counter M to adjust F_{VCO} by M times [123]. Phase differences between the input and output frequency can be achieved by adjusting the reference phase in the phase detector.

4.8.2 Field Programmable Gate Arrays

Field Programmable Gate Arrays are commonly used as key system components within ultrasound systems; often to control excitation sequences, process data and interface to external devices [30], [46]. Several of the research platforms discussed in Chapter 2 rely heavily on FPGA technology. FPGAs are advantageous when compared with other hardware solutions such as ASICs due to their flexible programmable nature, large amount of input/output, embedded memory and on-chip resources and are available at moderate to low cost. Most FPGAs include dedicated cores which are targeted to perform specific functions. Examples include on-chip processors, digital signal processing blocks and high speed transceiver buffers. As FPGA technology has developed, the IP cores within the devices have become particularly feature rich. The drivers for development of FPGA devices are the increasing requirement for high integration and scalability, reduced system complexity and component count, and the emergence of high speed interfaces.

Another example of dedicated on-chip components are digital PLL cores. PLLs are fundamental within FPGAs as they generate and distribute clock signals necessary to control synchronous logic within the device. These cores operate with the same principle as the generic PLL architecture shown in Figure 4.61, however have other features such as re-programmable flexibility during run-time as demonstrated by both Altera and Xilinx [124], [125].

Programmable phase shift within embedded PLLs is an example of both embedded core development and re-programmable flexibility. This feature permits an individual output clock's phase to be adjusted in fine steps and in real time without interruption to PLL operation or lock [124] [123]. Phase is adjusted using a serial interface to control a multiplexer that selects between several phase-separated clocks according to a minimum step (defined by the PLL resolution) as shown in Figure 4.62 [124].

4.8.3 Switched-Mode Transmit Beamformer with Embedded PLLs

Chapter 3 introduced the UARP's front end design, and the use of switched-mode circuits within packaged MOSFET devices to drive elements of an array transducer. MOSFET

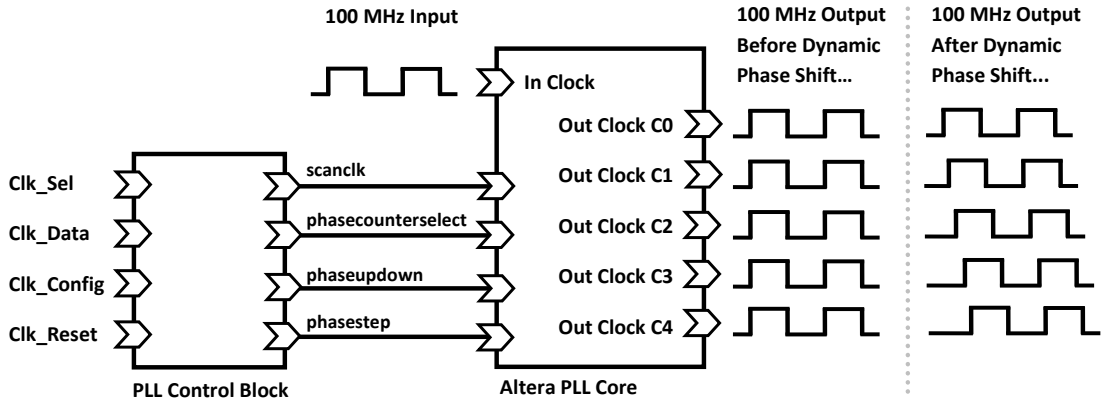

Figure 4.62: Example of embedded PLL phase shift control

switching signals are generated within FPGAs, with time or phase delays applied by sequencing of each channel's switching relative to each other. MOSFET control signals are either generated using a digital Numerically Controlled Oscillator (NCO) which is quantized in amplitude or by upload to a specific AWG logic block.

Each arbitrary waveform generator is clocked with a single global clock (100 MHz frequency in this case) and responds to a global pulse signal. Coarse phase delays of integer multiples of the global clock period (10 ns) can be implemented between channels using values stored in preloaded counters. The MOSFET control signals from each arbitrary waveform generator are fed into a dual flip-flop (dual FF) stage. These flip flops are driven by an individual phase shifted clock per channel generated by an on-chip or embedded PLL as described in Section 4.8.1. Fine phase delays or 'fractional delays' (fractions of the 100 MHz system clock) are implemented using the programmable phase shift function as shown in Figure 4.62. This introduces a phase difference between the global 100 MHz clock which generates the excitation signal and the 100 MHz channel clock used to drive the dual flip-flop output stage. This phase difference is sub-clock period, therefore less than 10 ns. The flip-flop stage is necessary in order to bridge the clock domain between the global 100 MHz clock and the phase shifted 100 MHz clock. It is a combination of coarse delays (system clock periods) and fine delays (phase separated clocks) applied to each channel that realises a particular delay profile across an array. The MOSFET control signals from the dual flip-flop section are then fed off-chip directly into a high voltage pulser device per channel. Both the PLL control blocks and the arbi-

trary waveform generator blocks are controlled using a Nios II soft-core processor. The architecture described is shown in Figure 4.63.

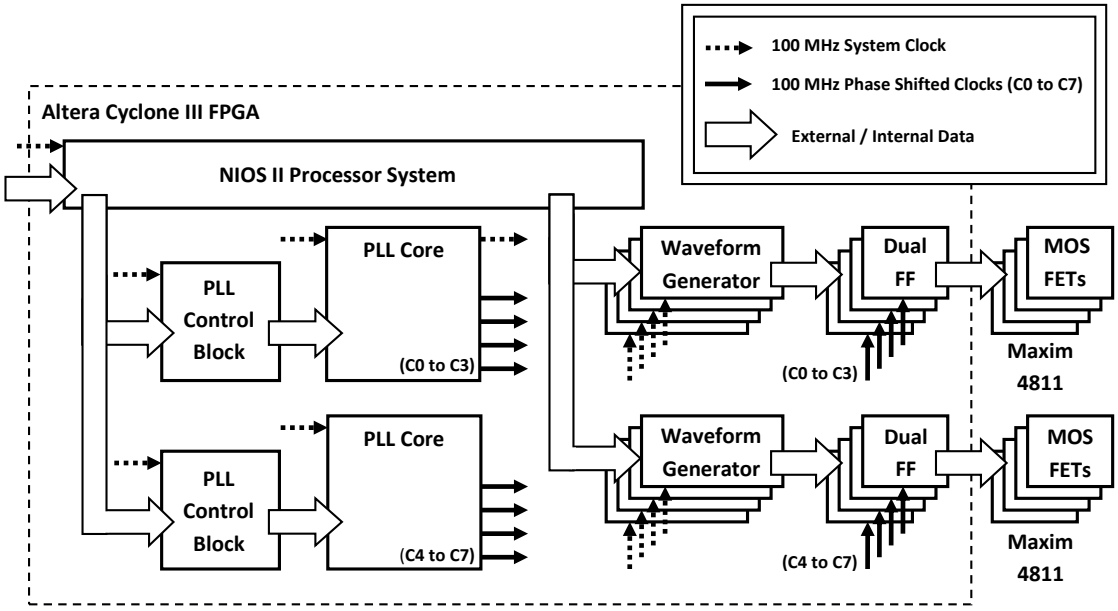

Figure 4.63: System diagram of the UARP eight-channel phased array transmitter architecture using Altera embedded PLLs and implemented within a commercial FPGA (Altera Cyclone III EP3C40Q240C8)

The transmit section of the UARP consists of 12 PCBs, housing eight transmitter channels as shown previously (Figure 3.7). Each eight channels are controlled by a Cyclone III FPGA (Altera EP3C40Q240C8N, Altera Corporation, San Jose, CA), equalling 12 FPGAs, controlled by a master FPGA (Altera Stratix III, EP3SL340H1152C3N, Altera Corporation, San Jose, CA). A diagram of a single transmitter board was shown previously in Chapter 3. A single Cyclone III contains four embedded PLLs, capable of distributing five output clocks throughout the device. Each output clock can be shifted either up or down with a minimum time increment of 96 ps with an accuracy of $\pm$50 ps. PLL output clock jitter is specified at a maximum of 300 ps for frequencies greater than or equal to 100 MHz, however it must be noted that jitter is also dependent on the quality of the input clock. The input clock is generated by the master FPGA, and distributed to each transmitter over a high speed backplane board with matched Low Voltage Differential Signalling (LVDS) traces [54].

4.9 Evaluation of Transmit Beamformer Performance

This section evaluates the performance of the embedded-PLL transmit beamformer method when implementing fine and variable delay methods. Figures 4.64 and 4.65 display screenshots acquired using a digital oscillscope (LeCroy Waverunner 44xi, LeCroy Corporation, Chestnut Ridge, NY, USA) using the infinite persistence setting. 1000 acquisitions of two phase separated channels are plotted. Phase separation of 5 ns is achieved using the embedded-PLL method, and shifting an appropriate number of steps. It can be seen from Figure 4.65 that there is a slight deviation of 440 ps on both of the channels, however as both channels experience this it can be assumed that both signals are aligned. True jitter between each channel would show a greater spread in the persistence plot from the non-triggered channel. Inspection of the sampling parameters (shown in the bottom right of each Figure) show a sampling frequency of 5 GS/s, giving a sampling period of 200 ps, which is comparable to the level of phase accuracy. A variation in triggering of approximately 440 ps can therefore be seen as lower than a deviation of $\pm$ 1 sample.

Figures 4.66 and 4.67 show overlaid plots of averaged measurements (100 acquisitions at each phase separation) showing phase separation in 1 ns steps from 0 ns to 9 ns across the 10 ns period defined by the system clock (100 MHz). Figures 4.68 and 4.68 show similar overlaid plots of averaged measurements (100 acquisitions at each phase separation) with finer phase-steps showing phase separation in the minimum time increment, 208 ps steps.

Table 4.3 shows the difference between the signals shown in the positive edge case (Figure 4.66) for 1 ns separation. The values shown are acquired using scope averaging, and the automated 'horizontal' measurement function Δtime@, which measures the separation between signals. Table 4.3 shows the target separation, the measured separation, and the error.

Table 4.4 shows similar data for the positive edge of the 208 ps case as shown in Figure 4.68.

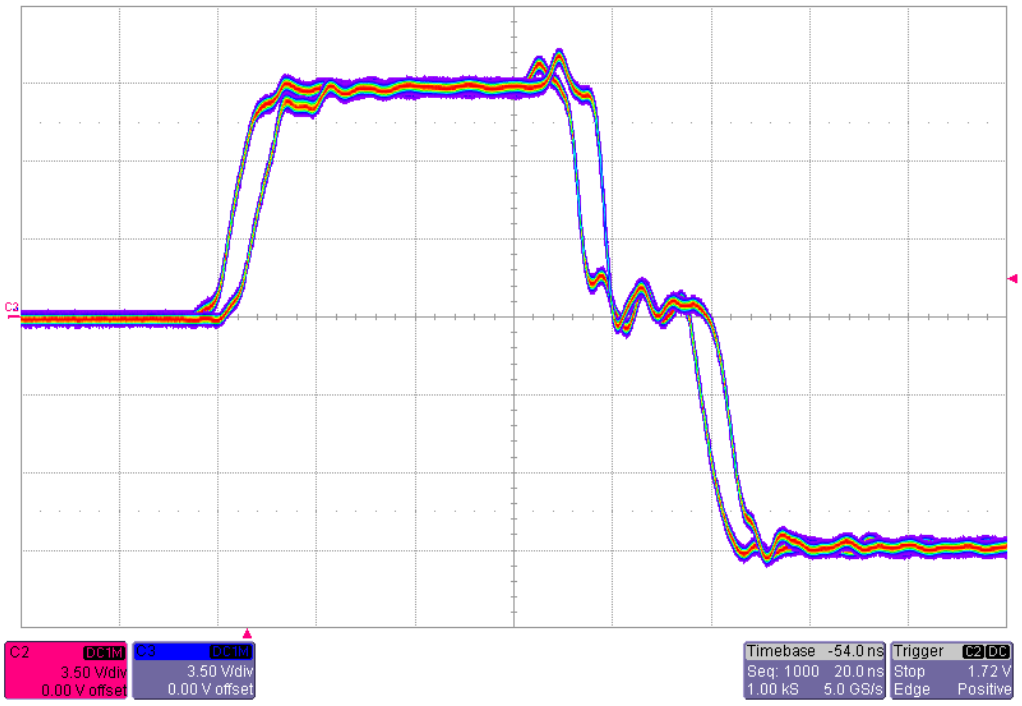

Figure 4.64: Infinite persistence acquisition from LeCroy Waverunner digital oscilloscope of two switched-mode signals from two UARP channels separated by 5 ns (1000 acquisitions)

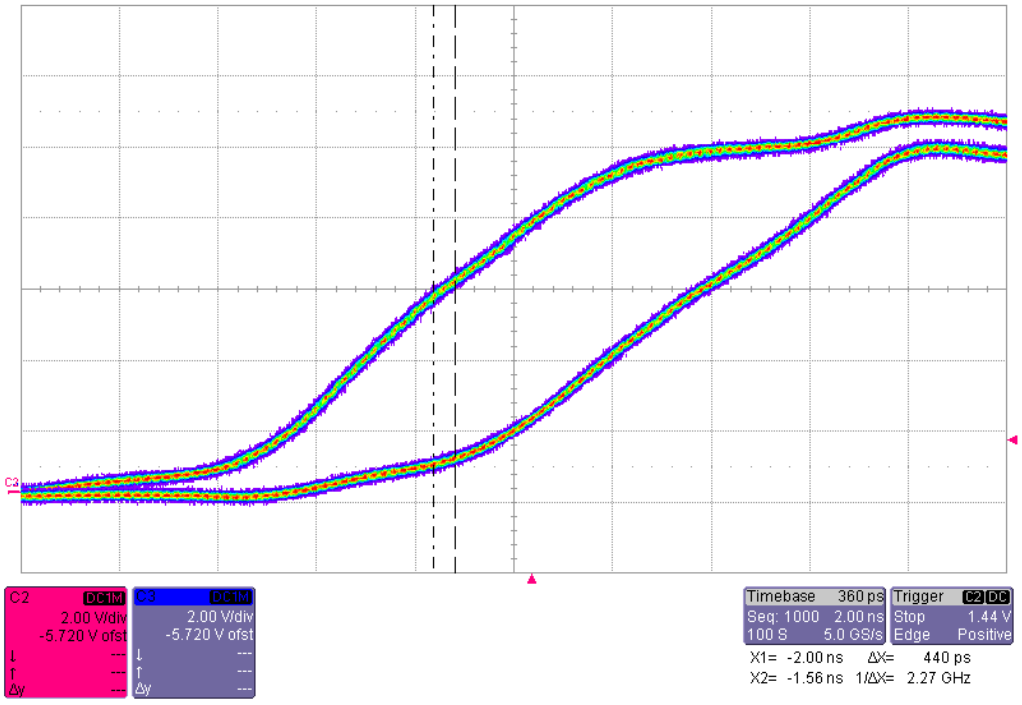

Figure 4.65: Zoom of infinite persistence acquisition from LeCroy Waverunner digital oscilloscope of two switched-mode signals from two UARP channels separated by 5 ns (1000 acquisitions) showing maximum jitter variation

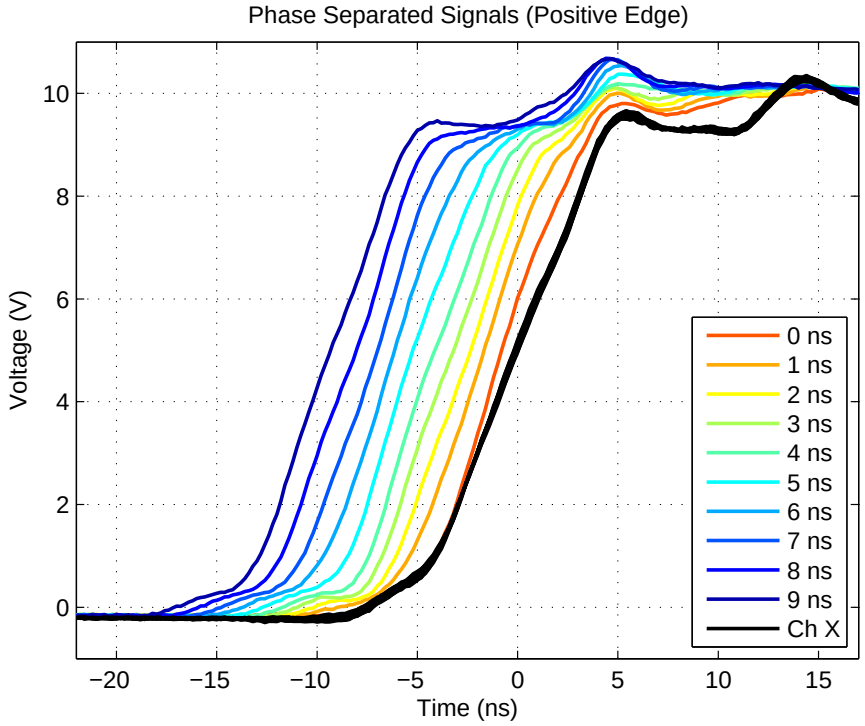

Figure 4.66: Acquired switched-mode signals from two UARP channels (positive edge) overlaid to demonstrate fine delay. Separation from 0 to 9 ns in 1 ns steps (100 signals averaged per waveform)

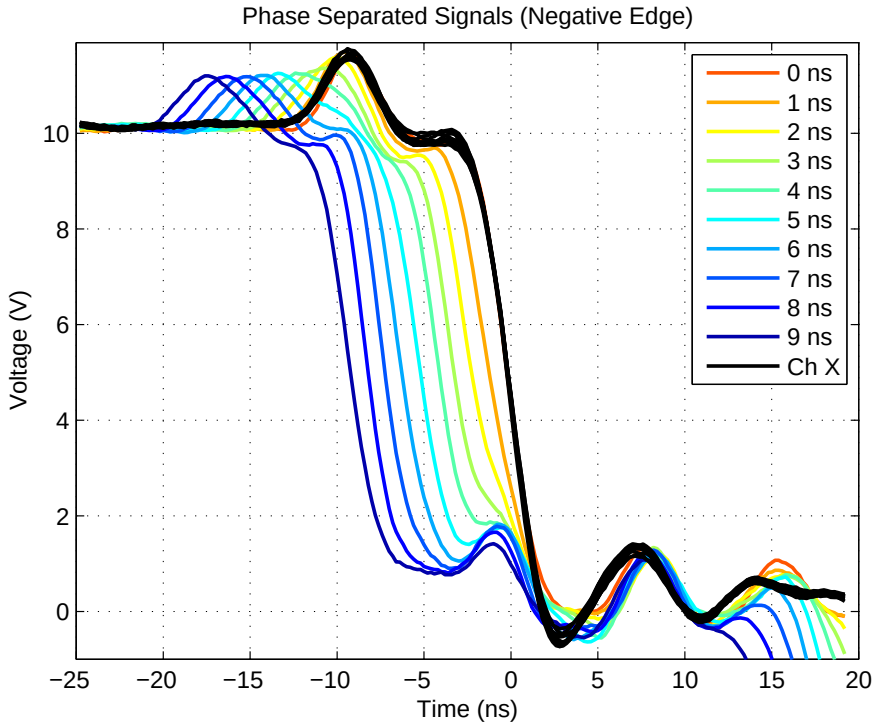

Figure 4.67: Acquired switched-mode signals from two UARP channels (negative edge) overlaid to demonstrate fine delay. Separation from 0 to 9 ns in 1 ns steps (100 signals averaged per waveform)

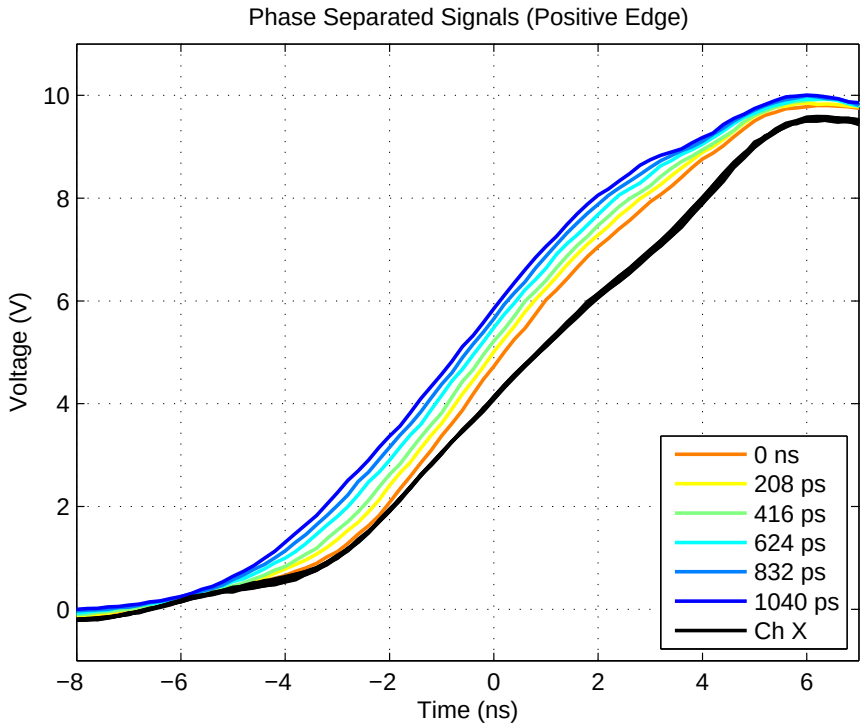

Figure 4.68: Acquired switched-mode signals from two UARP channels (positive edge) overlaid to demonstrate minimum delay resolution. Separation from 0 to 1 ns in 208 ps steps (100 signals averaged per waveform)

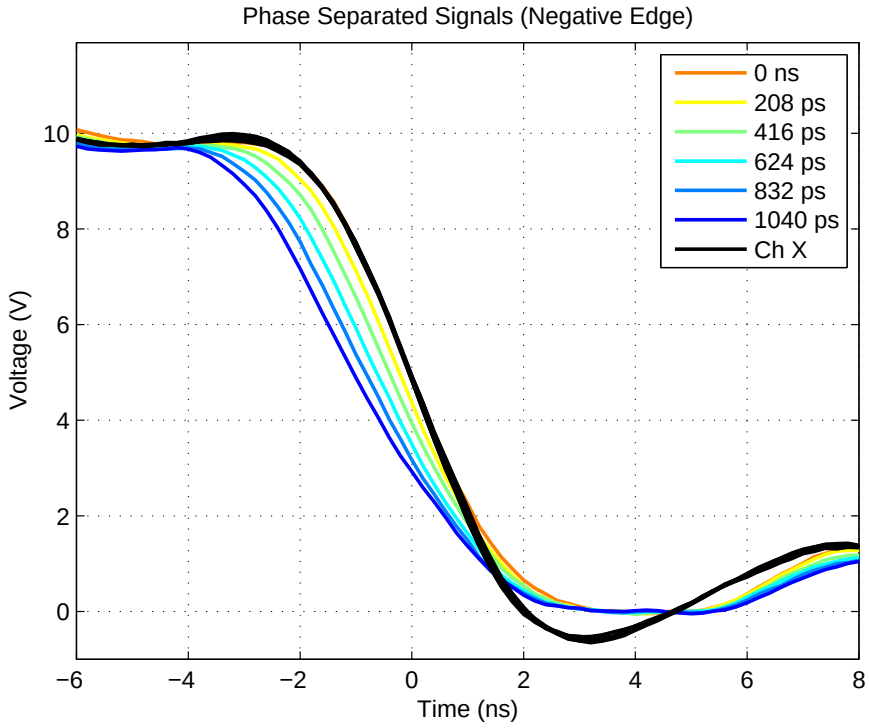

Figure 4.69: Acquired switched-mode signals from two UARP channels (negative edge) overlaid to demonstrate minimum delay resolution. Separation from 0 to 1 ns in 208 ps steps (100 signals averaged per waveform)

Target (ns)	Measured (ns)	Error (ns)
0.000	-0.015	0.015
1.000	1.028	0.028
2.000	2.078	0.078
3.000	3.091	0.091
4.000	3.952	0.048
5.000	5.018	0.018
6.000	6.076	0.076
7.000	7.081	0.081
8.000	8.049	0.049
9.000	9.058	0.058

Table 4.3: Target, measured and error of fine inter-channel phase delay (0 to 9 ns in 1 ns steps)

Target (ns)	Measured (ns)	Error (ns)
0.000	-0.015	0.015
0.208	0.173	0.035
0.416	0.375	0.041
0.624	0.577	0.047
0.832	0.793	0.039
1.040	1.028	0.012

Table 4.4: Target, measured and error of fine inter-channel phase delay (0 to 1 ns in 208 ps steps)

4.9.1 Evaluation Across Frequency

The embedded PLL phase shift method presented in this work has a minimum time increment ($\Delta\tau$) equal to 208 ps. This minimum increment value is defined by PLL settings (4.21) of F_{VCO} = 600 MHz, M = 12, P = 1 and K = 6, and surpasses the required $\mu = 32$ threshold for excitation frequencies up to 50 MHz (requiring $\Delta\tau$ = 625 ps). This section uses the UARP system to demonstrate how fixed minimum time increments (such as those generated by a 100 MHz clock) have an impact on TDR as frequency increases and how the embedded PLL method can be used to improve delay resolution without increasing system clock frequency.

To demonstrate the improvement across excitation frequency without the need to obtain several array transducers, a single array transducer of fixed frequency is used and the $\Delta\tau$ is adjusted in accordance with (4.13), (4.14) and (4.15). The relationship between excitation frequency, f, and oversampling factor, μ, is maintained whilst $\Delta\tau$ is altered to reflect the increase in excitation frequency. Example transformations of $\Delta\tau$ are shown in Table 4.5.

Excitation Frequency (f)	Value of μ at $\Delta\tau$ = 10.0 ns	Equivalent $\Delta\tau$ value for 5 MHz
5 MHz	$\mu = 20$	$\Delta\tau$ = 10.0 ns
10 MHz	$\mu = 10$	$\Delta\tau$ = 20.0 ns
20 MHz	$\mu = 5$	$\Delta\tau$ = 40.0 ns

Table 4.5: Example conversions of the minimum time increment $\Delta\tau$ to simulate higher frequencies using a 5 MHz array.

4.9.2 Beam Profiling

In order to demonstrate an increase in TDR as a result of improved phase delay resolution, the radiated pressure field from a commercial diagnostic 1-D linear array transducer was simulated using Field II and also measured experimentally. The selected transducer, a 128 element L3-8/40EP array transducer (Prosonic Co Ltd., GyongBuk, Korea) was used in simulation and experiments, however only the central 96 elements were excited due to the number of channels in the UARP system. More detailed properties of the transducer are shown in Table 4.6. The excitation used for evaluation was a five cycle, 5 MHz, rectangularly windowed, switched-mode pseudo-tone burst, as described in [52].

Figures 4.70 and 4.71 show simulated beam plots, and radial beam profiles of the 5 MHz array focused to 40 mm, with 5 cycle, rectangularly windowed excitation and with quantization using $\Delta\tau$ = 10 ns. Note that the grey line is the case for phase quantization of 208 ps (the minimum time resolution from the UARP). It can be seen that there is minor deviation between the simulated and expected cases, except at between 30°and 35°where there is the emergence of a quantization lobe 3 dB higher than the noise floor, giving

Transducer Property	Value	Unit
Model	L3-8/40EP	-
Sensitivity (average)	-56.492	dB
Sensitivity (variation)	1.811	dB
Centre Frequency (-6dB, average)	4.79	MHz
Fractional Bandwidth (-6dB, average)	57.261	%
Element Pitch	0.3048 $\pm$0.001	mm
Number of Elements	128	-

Table 4.6: L3-8/40EP array transducer (Prosonic Co Ltd., GyongBuk, Korea)

a TDR value of 31 dB at approximately 7°. Figures 4.72 and 4.73 show the simulated beam profile for the 10 MHz case ($\Delta\tau$ = 20 ns) case compared with the approximately 'ideal' 208 ps case. When compared with the 10 ns case in Figure 4.71, the emergence of spurious lobes can be seen closer to the main lobe, giving a TDR of 29 dB at 5°.

Figures 4.74 and 4.75 show a more extreme case of quantization with $\Delta\tau = 40$ ns. This case replicates using a 20 MHz array with quantization of 10 ns. Figure 4.75 shows a difference of between 5 dB and 12 dB in the angular plot, when compared with the 208 ps case, giving a TDR value of approximately 20 or 25 dB from lobes at 3°or 10°.

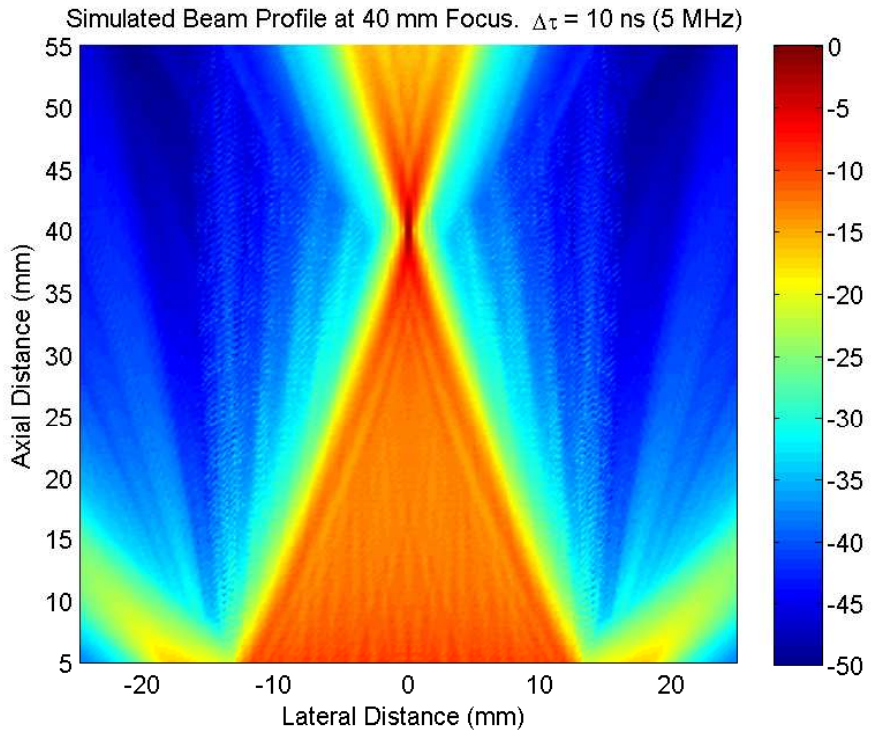

Figure 4.70: Simulated radial beam profile of a 96-element, λ-spaced array, focused to 40 mm, $f = 5$ MHz, $n = 5$, $\Delta\tau = 10$ ns

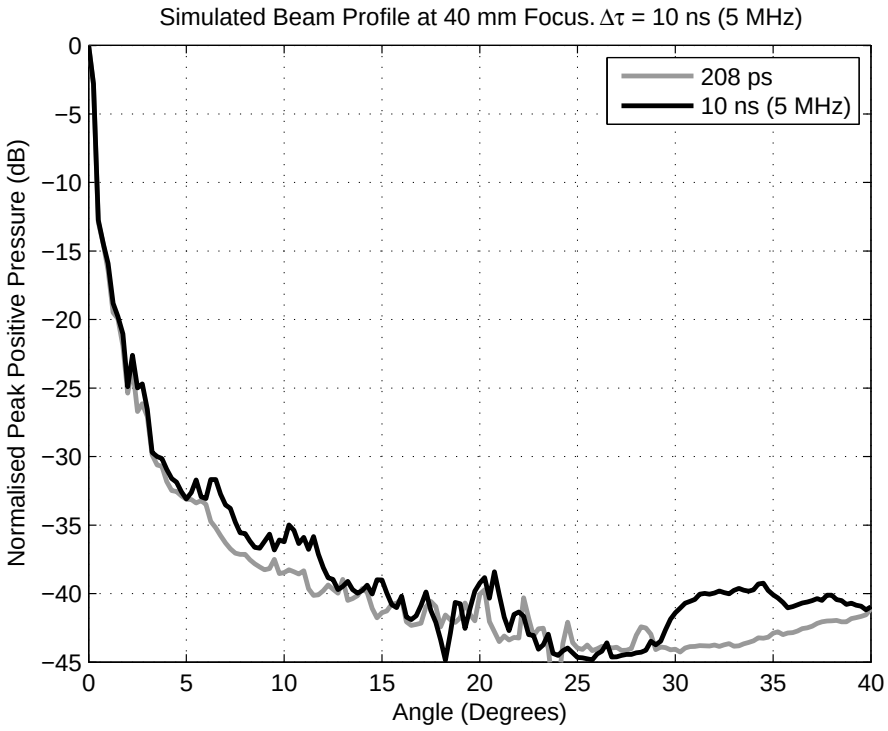

Figure 4.71: Simulated radial beam profile of a 96-element, λ-spaced array, focused to 40 mm, $f = 5$ MHz, $n = 5$, $\Delta\tau = 10$ ns (black line) vs. ideal delays (grey line)

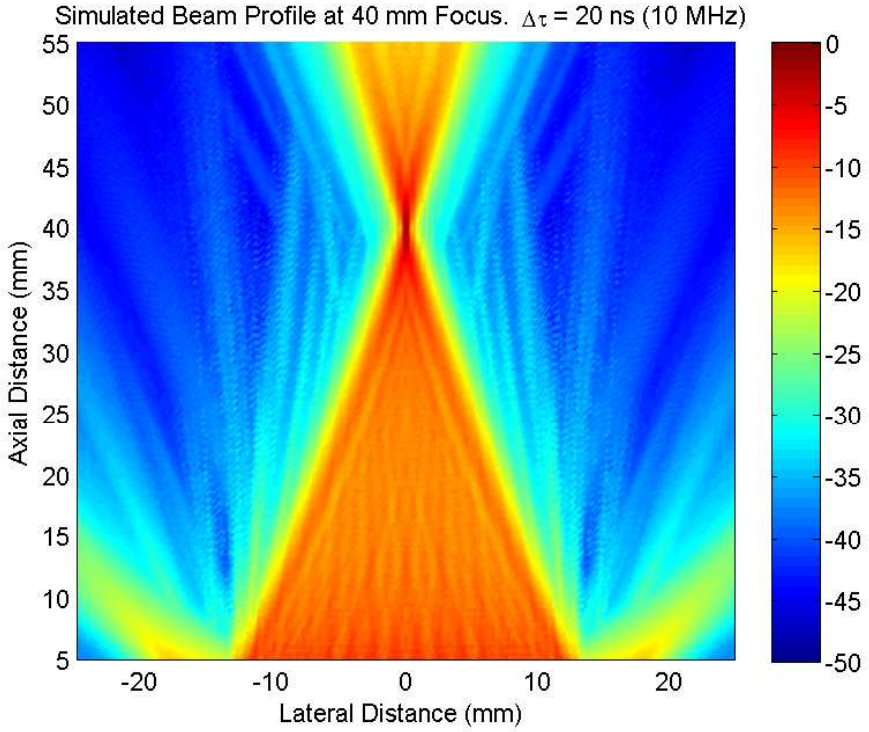

Figure 4.72: Simulated beam profile of a 96-element, λ-spaced array, focused to 40 mm, $f = 5$ MHz, $n = 5$, $\Delta\tau = 20$ ns

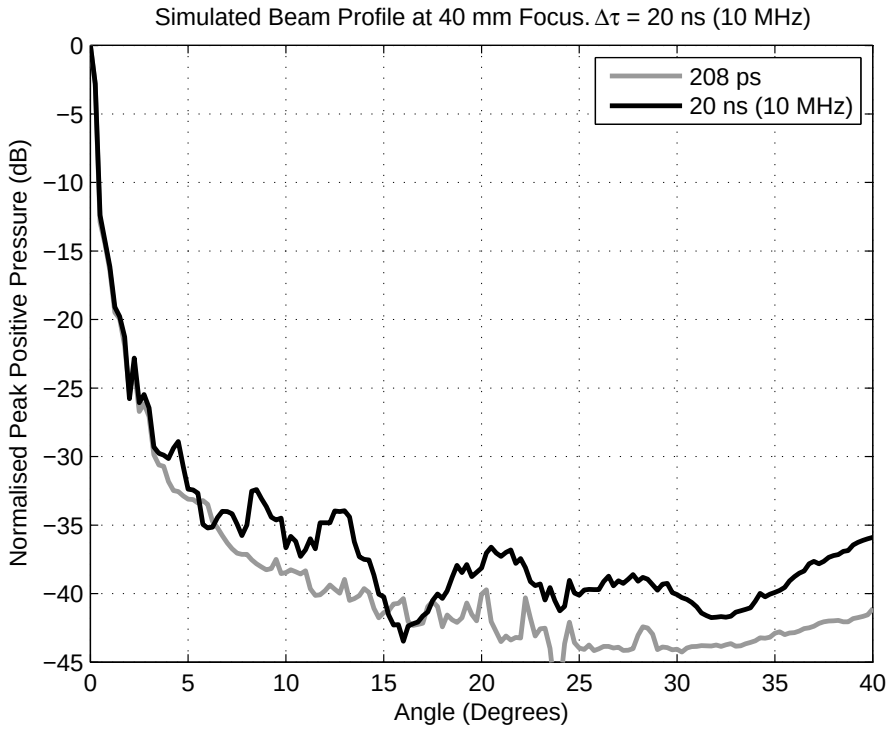

Figure 4.73: Simulated radial beam profile of a 96-element, λ-spaced array, focused to 40 mm, $f = 5$ MHz, $n = 5$, $\Delta\tau = 20$ ns (black line) vs. ideal delays (grey line)

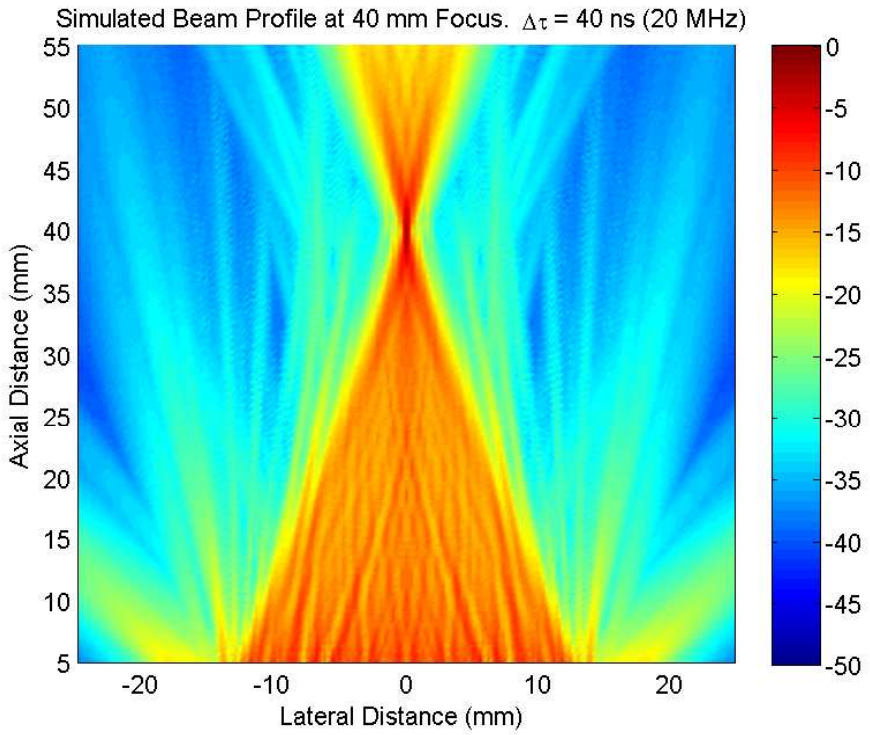

Figure 4.74: Simulated beam profile of a 96-element, λ-spaced array, focused to 40 mm, $f = 5$ MHz, $n = 5$, $\Delta\tau = 40$ ns

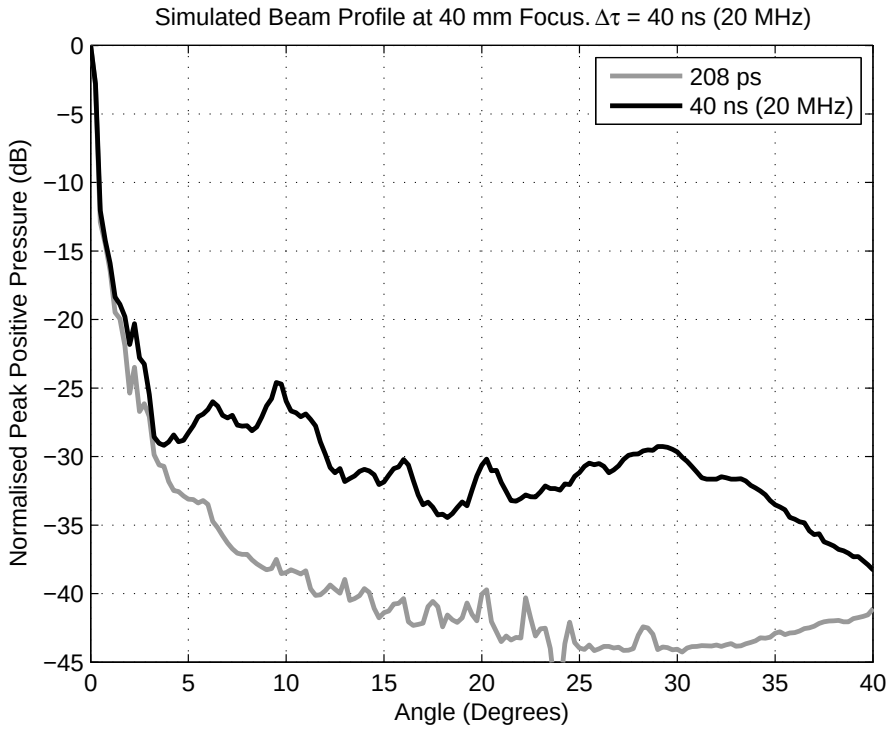

Figure 4.75: Simulated radial beam profile of a 96-element, λ-spaced array, focused to 40 mm, $f = 5$ MHz, $n = 5$, $\Delta\tau = 40$ ns (black line) vs. ideal delays (grey line)

For experimental measurement, the transducer (shown in Figure 4.76 and described in Table 4.6) was placed within an acoustically transparent ultrasound probe cover (CIV-FLEX 610-004, Civco Medical Solutions, Kalona, IA) and submerged within a large tank of filtered, deionized and degassed water at a temperature of 20°C $\pm$ 1°C. A 0.2 mm PVDF (Polyvinylidene Fluoride) Needle Hydrophone (calibrated between 1 MHz to 20 MHz with an acoustic pressure range of 50 kPa to >20 MPa RMS signal-to-noise ratio), shown in Figure 4.77 (Precision Acoustics, Dorchester, Dorset, UK), was mounted on a 3-D computer controlled translation system able to perform lateral and radial scans of the transmitted field. Radial beam plots were obtained at z_F = 40 mm from 0° to 40° in steps of 0.25°. The signal from the hydrophone pre-amplifier at each radial position was digitized using an 8 bit (48 dB dynamic range) digital oscilloscope and then processed in MATLAB. Measurements were taken five times at each point in order to produce averaged beam profiles to increase SNR.

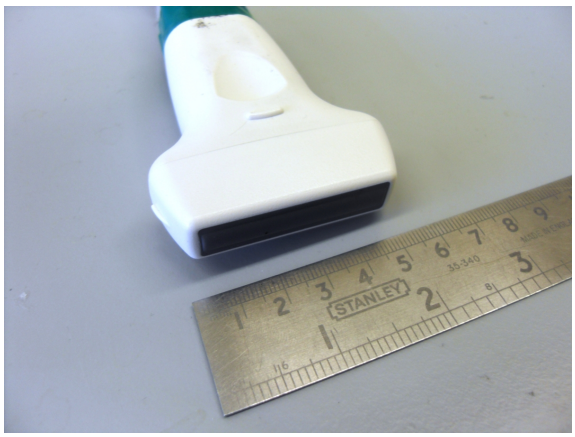

Figure 4.76: Photograph of the L3-8/40EP array transducer (Prosonic Co Ltd., Gyong-Buk, Korea), 128 elements, λ pitch, 4.8 MHz average centre frequency, 57% fractional bandwidth.

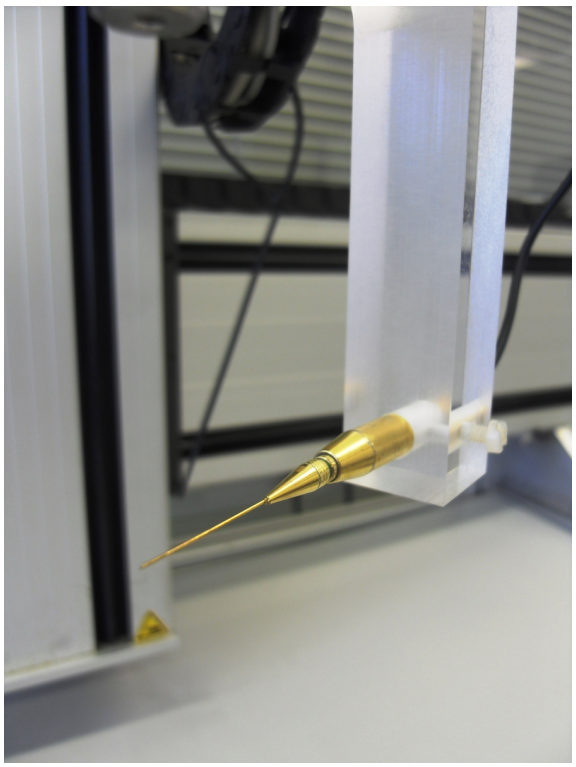

Figure 4.77: Photograph of the 0.2 mm needle hydrophone (Precision Acoustics, Dorchester, UK)

Figure 4.78 presents the experimentally measured transmitted beam profile of the 5 MHz array using, a 5 cycle, 5 MHz, rectangularly windowed excitation, and a delay profile quantized to $\Delta\tau$ = 10 ns (coarse delay resolution) and $\Delta\tau$ = 208 ps (fine delay resolution using the embedded PLL method). At 5 MHz, $\Delta\tau$ = 208 ps is equivalent to $\mu = 961$ and therefore can be classed as ideal, as the timing resolution is much greater than μ = 32, which at this frequency would equal 6.25 ns. The experimental value of TDR for the embedded PLL method is approximately 32 dB governed by a lobe at 3.75°. It can be seen that the first significant lobe in the $\Delta\tau$ = 10 ns result appears at 5° giving a TDR value in this case of 31 dB.

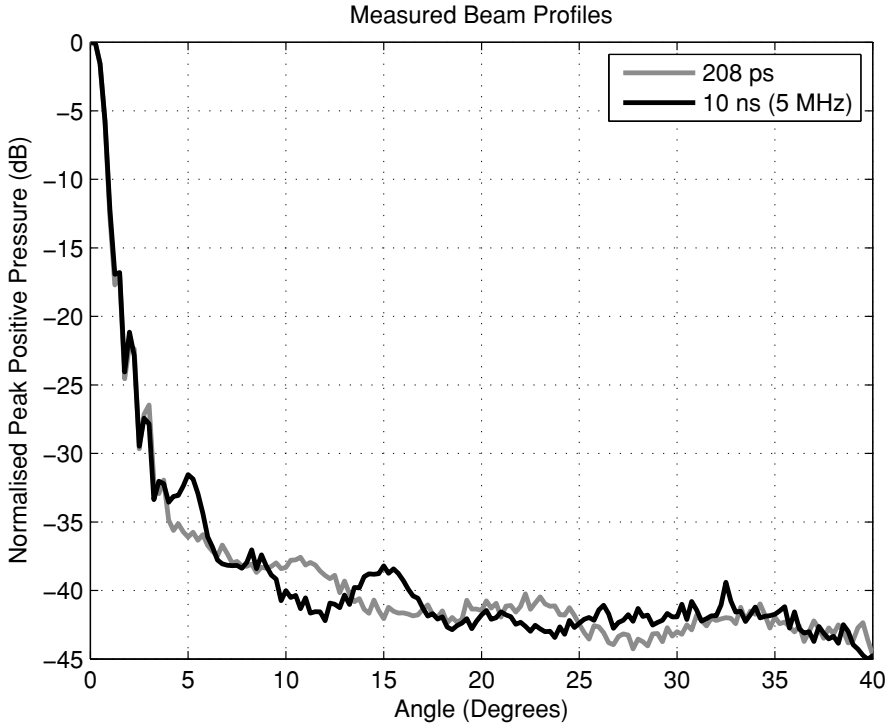

Figure 4.78: Experimentally obtained radial beam profile comparing $\Delta\tau = 10$ ns (black line) vs. $\Delta\tau = 208$ ps (grey line)

Figure 4.79 presents data measured using the same 5 MHz array, however in this case the $\Delta\tau$ value has been adjusted to predict results when the same system is used to drive a higher frequency array. In this case the coarse delay profile is quantized to $\Delta\tau$ = 20 ns (coarse delay resolution). At 10 MHz, $\Delta\tau$ = 208 ps is equivalent to a $\mu = 481$, and as in the previous case, the waveform can be classed as ideal as it surpasses the μ = 32 threshold

which would equal 3.125 ns. In this measurement the value of TDR at an equivalent f of 10 MHz is 27 dB governed by a lobe at 5.5°

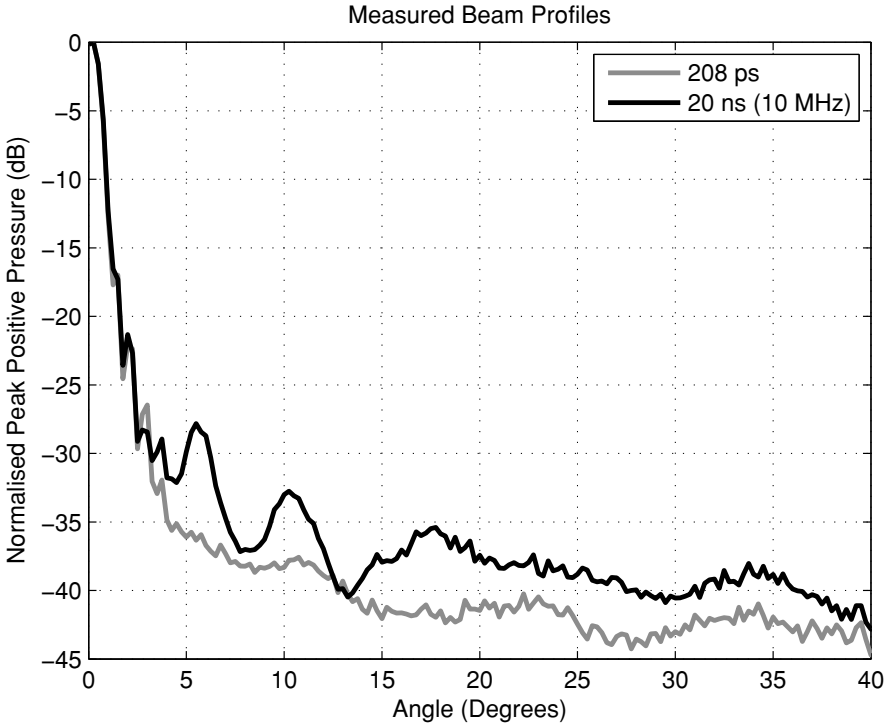

Figure 4.79: Experimentally obtained radial beam profile comparing $\Delta\tau = 20$ ns (black line) vs. $\Delta\tau = 208$ ps (grey line)

Figure 4.80 shows data acquired using the same 5 MHz array, however the $\Delta\tau$ value has again been adjusted to predict results when the UARP system is used with a 20 MHz array, with the coarse delay profile is quantized to $\Delta\tau$ = 40 ns. At 20 MHz, $\Delta\tau$ = 208 ps is equivalent to a $\mu = 240$, and as per the previous cases, the waveform can be classed as ideal as it still surpasses μ = 32 which would equal 1.5625 ns for this frequency. In this case the value of TDR at an equivalent frequency of 20 MHz is 22 dB governed by a lobe at 4°

When comparing the experimental coarse quantized results to the ideal case obtained using the fine embedded PLL method it can be seen that at 5 MHz the gain in TDR is slight (1 dB improvement) however, as frequency increases the gain in TDR becomes significant. At higher frequencies the embedded PLL method provides an extra 5 dB gain in TDR at 10 MHz (when compared with using coarse delays at the same system

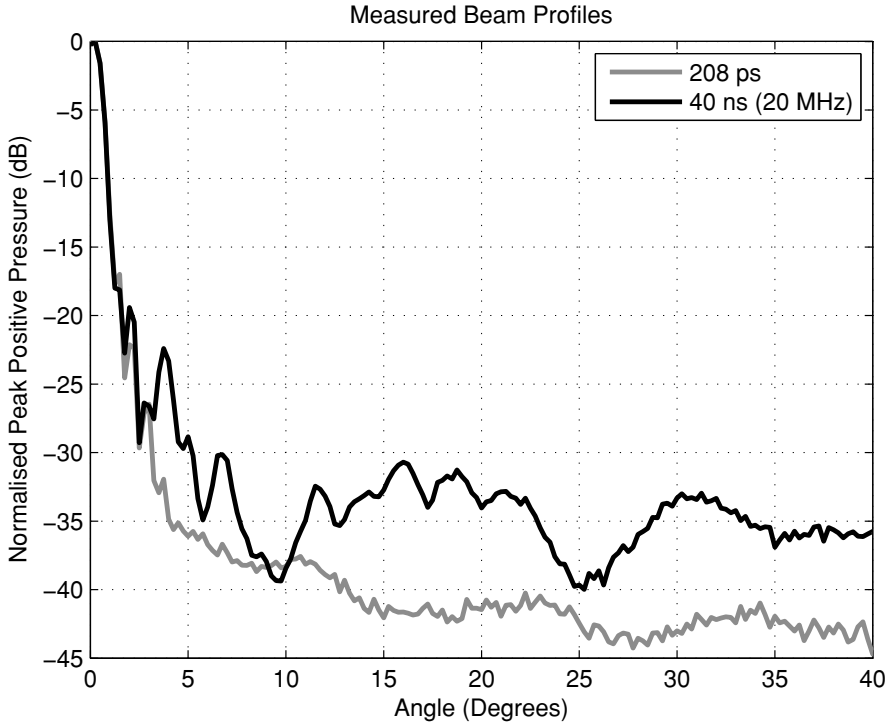

Figure 4.80: Experimentally obtained radial beam profile comparing $\Delta\tau = 40$ ns (black line) vs. $\Delta\tau = 208$ ps (grey line)

frequency) and an extra 10 dB gain when using a 20 MHz array. This data is summarised in Table 4.7.

Excitation Frequency (f)	TDR (dB) $\Delta\tau$ = 10 ns	TDR (dB) $\Delta\tau$ = 208 ps	TDR Gain (dB)
5 MHz	31 dB	32 dB	1 dB
10 MHz	27 dB	32 dB	5 dB
20 MHz	22 dB	32 dB	10 dB

Table 4.7: Experimental TDR Gain: Coarse Delay $\Delta\tau$ = 10 ns vs Fine Delay $\Delta\tau$ = 208 ps

The results also show an increase in the overall sidelobe level as frequency increases and the $\mu = 32$ criteria, as derived by Kino and (4.16), is not met.

4.10 Discussion

The impact of phase quantization when minimum time increments are fixed is dependent on excitation frequency. The embedded PLL method presented and implemented in the

UARP system shows greater improvement when used with higher frequency arrays such as those discussed in this work. Both simulations and experiments conducted show that achieving the $\lambda/32$ criterion as described by previous authors reduces sidelobe levels in the transmitted beam profile to a level which mirrors the ideal case. Whilst some minor differences may exist between simulated data and experimental results (such as those described by Aitkenhead *et al.* [126]), simulated results shows a comparable trend in TDR with the experimental data. Note however that direct comparison between experimental measurement and the Field II simulations may not be appropriate. Field II calculates pressure without considering non-linear propagation or shock-wave formation. During non-linear propagation at high pressures, such as in the focal point, the peak positive pressure is greater than the peak negative pressure. In Field II simulation, at the focal point, peak positive and negative pressures are equal, therefore estimations of absolute sidelobes may not correlate. Also, some inaccuracies may be introduced in the modelling of the transducer that change the directivity of elements, when considering element widths and heights, and speed of sound [98]. These subtle changes can alter the field position of certain lobes, including grating lobes. What can be seen however, is the overall reduction of sidelobe levels when using the 208 ps quantization, for all cases.

As ultrasound systems seek to operate over broader bandwidth, achieving the correct quantization threshold across a large number of independent channels is particularly challenging. Whilst FPGAs are capable of generating excitation pulses at high frequencies, quantization error effects are likely be present in the transmitted beam profile if $\Delta\tau$ is not sufficiently small. At 20 MHz for example the $\lambda/32$ threshold corresponds to a $\Delta\tau$ value of 1.56 ns, whilst at 40 MHz the $\lambda/32$ value corresponds to a $\Delta\tau$ value of 781 ps. Solving this problem using external discrete circuits increases system design and complexity, particularly as channel count increases. The implementation shown in this work can achieve the $\lambda/32$ threshold for these high frequency cases and does so by merely taking advantage of resources (perhaps not intended for such an application) but readily available within FPGAs.

For optimal implementation, the embedded PLL method does require additional software to convert and track phase shifts of each channel. Such data can easily be stored in dedicated registers within the FPGA software.

As an aside, the embedded PLL method presented could also be used to correct or compensate for array defects and inconsistencies in array manufacture, particularly with respect to timing variability as discussed by Zhang *et al.* [107]. Other areas with which the embedded PLL method is applicable could include compensating for subtle changes in focal delays due to temperature, boundaries between materials, or to compensate for focal errors caused by non-ideal propagation in a medium. Using the embedded PLL method described, it would be possible to incorporate additional time offsets as part of a calibration routine or to fine-tune delay parameters in order to optimise the radiation pattern.

4.11 Conclusions

Phase quantization effects such as increased sidelobe levels and phase quantization lobes can be reduced by close approximation to the ideal delay profile for a focused and/or steered beam in a phased array system. Most ultrasound phased array imaging suffers only from errors associated with focusing delay profiles (uncorrelated error) as opposed to periodic error caused by steering delay profiles (correlated error). Imaging may also suffer as a result of other uncorrelated error introduced by the transducer or in the medium during propagation.

Previous literature have evaluated the effect of phase quantization particularly with respect to receive beamforming. Suggested values of maximum tolerable phase error have been proposed such as $\lambda/8$ value by Von Ramm *et al.* and then $\lambda/32$ [114],[69],[115],[116]. These thresholds however are dependent on excitation frequency which can vary with application, imaging modality or transducer. In most cases the hardware system used is a common platform which must be able to meet the demands that these various applications and techniques impose. This work describes the implementation of a transmit beamforming method able to surpass these suggested maximum tolerable phase error values across

a range of frequencies in order to increase transmit dynamic range, and when combined with receiver beamforming strategies increase total image dynamic range.

Programmable and flexible embedded PLL components are now common in commercial FPGAs. These embedded PLLs are highly functional and allow for real time phase shifting of clocks by simple serial interface. Presented in this work is a method to take advantage of these embedded PLLs to create a phased array transmitter design which can provide inter-element resolution of 208 ps using multiple phase shifted 100 MHz clocks. This phase delay solution is coupled with previous work into generation of coded excitation waveforms using MOSFET devices [52] and replicated to form part of the University of Leeds UARP.

Experimental evaluation with the UARP system demonstrates that the proposed embedded PLL architecture can achieve and surpass the $\lambda/32$ criterion across a range of frequencies. Results obtained with a 5 MHz array transducer have been used to evaluate potential reductions in sidelobe levels when used at higher frequencies such as 10 MHz and 20 MHz. Results show up to 12 dB improvement at 20 MHz in peak sidelobe level, or transmit dynamic range.

This chapter described and demonstrated a transmit beamformer architecture for sequencing of switched-mode signals with fine delay and variable control. Demonstration of the transmit beamformer architecture has shown ability to vary fine delays that are sub-clock period (in this case 10 ns). With this fine delay control and variable nature, the transmitted field can be further enhanced by compensating for other forms of random error such as transducer defects or inaccuracies using the embedded PLL transmit architecture described. The next chapter discusses another method of improving the pressure wave from the UARP's switched-mode transmitter, considering the best method for pulse-width encoding to generate arbitrary waveform sequences.

Chapter 5

Switched-Mode PWM Method for Ultrasound Power Control

5.1 Introduction

Chapter 3 introduced the use of switched-mode circuits as an alternative over linear power amplifiers. Chapter 4 described how contributions from multiple array elements, excited by switched-mode signals, can be combined to generate focused beam patterns. It also discussed how these field patterns can be optimised by accurate excitation sequencing. Chapters 5, 6 and 7 investigate how to utilise switched-mode circuits for optimised pressure output.

Advances in areas of ultrasound such as high frequency imaging [39] and portable, low-cost system development [11], [12], place a burden on the complexity and requirements of an ultrasound transmitter, particularly when the design is required to be scaled over many channels. Complexity may also increase as future trends seek to integrate excitation electronics into the transducer probe head which has a number of benefits, including improved impedance matching and reducing the unwieldy cable bundle between system and probe [127].

High frequency linear power amplifiers are well-suited to the electrical requirements of ultrasound transmitters, however are often large, bulky and expensive components as

described in Chapter 3. An alternative transmitter solution to analogue power amplifiers is the use of MOSFET semi-conductor pulser devices operated in a switched-mode as discussed in previous chapters. These components use switched excitation to select between several positive and negative voltage levels. Switching between discrete levels results in square-wave or staircase (stepped) pulses which approximate sinusoidal signals as described in [39], [11], [12], [85], [127], [86], [89], [13], [90], [92], [14]. MOSFETs are advantageous particularly over linear power amplifiers as they are capable of delivering high currents to piezo-electric loads [88], in small scale, low-cost, integrated packages and are more suited for use with arrays of channels. High currents are required due to the capacitive nature of a piezo-electric element and the large inrush current drawn when excited by an excitation signal, especially when a square wave excitation is used, as previously discussed in Chapter 3 and (3.4). The nature of MOSFET switched excitation often results in pulses with uniform fixed amplitude. Whilst it is possible to adjust switching levels between firings, it is often desirable to control pulse amplitude throughout the duration of the excitation for several applications within therapeutic and diagnostic ultrasound.

Pulse width modulation (PWM) is an established technique used throughout engineering to control switched mode output. This form of output stage was briefly discussed in the review of amplifier technology in Chapter 3. In its simplest form, the duty cycle or on/off ratio of a square wave is adjusted in proportion to a desired, time-averaged output i.e. the pulse-width is modulated according to desired output level.

Pulse widths can be determined using one of a number of methods. Examples include integration based methods, carrier based methods or direct modulation methods. Carrier based methods are often used due to their simplicity and performance in both analogue and digital representations. Carrier based methods compare a generated reference carrier to the desired or modulating waveform, for implementation this can be solved either with a comparator circuit, or using *if... else...* statements in software. Pulse widths are derived based upon the relative position of the carrier to the modulating waveform. The form of the carrier is of particular importance. Carrier form not only dictates pulse width, but also pulse position and pulse abundance (number of pulses per time period). Pulse abundance

is characterised by the relationship between the carrier frequency, and the modulating frequency. As an example, a carrier with a frequency ten times greater than the modulating wave will produce ten PWM pulses per cycle. Pulse position can be controlled by using symmetrical or asymmetrical modulation. Symmetrical modulation uses a carrier such as a triangular carrier, which is symmetrical in the carrier period. In symmetrical carrier based modulation, both edges of the square wave pulses are modulated with the centre of the pulse located at the centre of the carrier wave period. In asymmetric modulation one edge is fixed, and either the leading or trailing edge is modulated. In this case the carrier is not symmetrical, such as when the carrier is a sawtooth wave. Pulse width in carrier based schemes is determined by using the intersection of the carrier with the modulating wave. If the modulating wave is a function such as a triangular or sawtooth wave then the pulse width is linearly scaled, because the carrier function is linear. As an example, if the modulating wave intersects the carrier at 25% of its amplitude, then the pulse will be on for 25% of the carrier period and off for the remaining 75%.

PWM has a wide range of applications due to its relatively low cost, ease of implementation and high efficiency. For many applications the ratio between the carrier frequency (f_c) and the modulating frequency (f_m) is often large (e.g. $f_c \geq 10 f_m$). In digital implementations, the carrier is a discrete version of a continuous waveform, and is therefore sampled itself by a clock of higher frequency (f_s). The relationship between f_s and f_c determines the number of available PWM states. In addition to this, sampling frequency may dictate the specification of the modulator circuit, as the frequency f_s defines the minimum pulse width or time to switch on and off. As an example, if a sampling frequency or system clock of 100 MHz is used, then the minimum pulse and pulse increment would equal 10 ns. Ultrasound frequencies are often defined in the kHz to tens of MHz range. To implement PWM with a modulating wave at these frequencies places a burden on the hardware required. It is therefore advantageous to design the carrier with appropriate frequency as to generate either one or two PWM pulses per half cycle. This reduces the sampling frequency f_s and also the bandwidth requirement of the modulating output

circuit. Additional advantages also exist in terms of power requirements and switching losses.

Previous literature within ultrasound has described adjusting switching thresholds (and hence pulse widths) of square wave pulses to eliminate harmonics in the transmitted output [13]. The objective of [13] was not to control pulse shape or amplitude however, but to reduce harmonic content. A recent paper [14] discussed the advantages of MOSFET bipolar pulsers, particularly with respect to the large amplitude outputs available, but dismissed the use of MOSFETs for generating arbitrary excitation, stating a lack of control over pulse characteristics. In contrast, authors such as Persson have previously described varying the width and shape of very short square-wave pulses to effect the transmitted pressure output [82] which showed potential for amplitude control. It is the motivation of this work to propose a PWM strategy for Ultrasound applications, capable of providing control of pulse characteristics using switched mode sequences.

There are many forms and implementations of PWM, particularly in power converters where a wealth of literature is available as summarised in [128]. For ultrasound applications, a number of aspects differ from conventional implementations. Traditional PWM strategies use a multitude of pulses to describe the modulating waveform. This requires rapid switching of the transmitter circuit at a rate much greater than the output frequency and is often used in combination with an output filter [129]. This form of rapid switching and reconstruction is similar to a sigma-delta modulation strategy as proposed by Huang and Li [130]. A sigma-delta implementation generates multiple switching events in response to an integration stage operating on a sample by sample basis. The train of pulses are time-averaged over the duration of the half cycle, with the density of the pulses defining the resultant output amplitude. Consequently, for low- or mid-amplitude signals, multiple sparsely distributed pulses are generated with pulse-widths that are very small. The technique proposed in this Chapter differs, as it seeks to minimize the number of switching events to one pulse per half cycle as in a pseudo-chirp representation, but modulate the width of each of the pulses in the sequence at the fundamental frequency. Widths are modulated by using the characteristics of the transducer as a bandpass filter

as described in Chapter 3 and considering the transducer's response to a square-wave input. The method provides a solution to addresses the reported inflexibility of high voltage bipolar pulser devices for generation of windowed or arbitrary waveforms, as described in recent literature such as [92] and [14].

5.2 PWM and Multi-Level PWM

5.2.1 Overview of Carrier-Based PWM

Conventional carrier-based PWM compares a carrier of known form to a desired output level or modulating wave thus generating pulses of varying widths [131]. Figure 5.1 shows three examples of modulation with an often-used triangular carrier generating three symmetrically modulated pulses after comparison with desired d.c voltage levels [128].

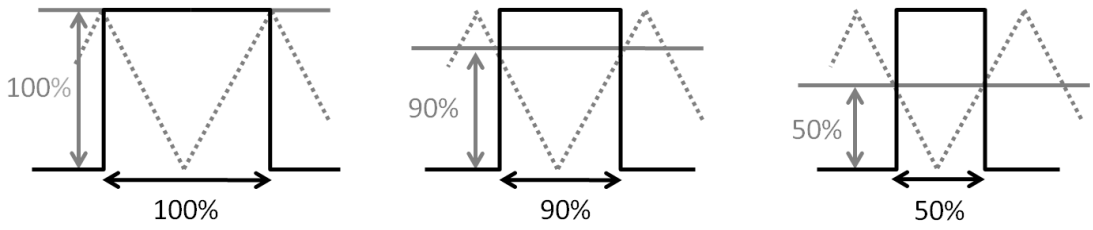

Figure 5.1: Example of triangular symmetrical, carrier-comparison, pulse-width modulation

Figure 5.1 shows a carrier (dotted line), and a desired output level (grey solid line). A comparison algorithm using the carrier and a desired level, generates a width modulated pulse (black solid line). The triangular form of the carrier generates symmetrically modulated PWM with both the leading-edge, and trailing-edge of the square-wave modulated. Other modulation types exist that use an asymmetric carrier that modulates the leading or trailing edge only. The conventional triangular carrier assigns a pulse width from a desired output level in a linear fashion. The width of the pulse is therefore directly proportional to the desired d.c. level. A linear triangular carrier may be defined as:

$$c(t) = A \cdot \left| (2/\pi) \left(\sin^{-1} (\sin (\omega t + \phi)) \right) \right| + L \tag{5.1}$$

where A is a scaling factor, t is time, ϕ is phase, L is an arbitrary d.c. offset and $\omega = 2\pi f$. The triangular carrier described by (5.1) can be used to modulate the widths of successive pulses by comparing said carrier to a modulating wave $m(t)$. With this method, the square wave is 'high' or 'on' whilst $c(t) < m(t)$. In most applications, $m(t)$ is of much lower frequency than the carrier, resulting in multiple pulses of varying widths, with the ratio of carrier frequency to modulating frequency determining the number of pulses per cycle, as demonstrated in Figure 5.2. In this context, 'carrier' refers to the wave used to encode PWM sequences, and not necessarily the fundamental frequency of an amplitude modulated pulse. In digital implementations of PWM, both the carrier and modulating

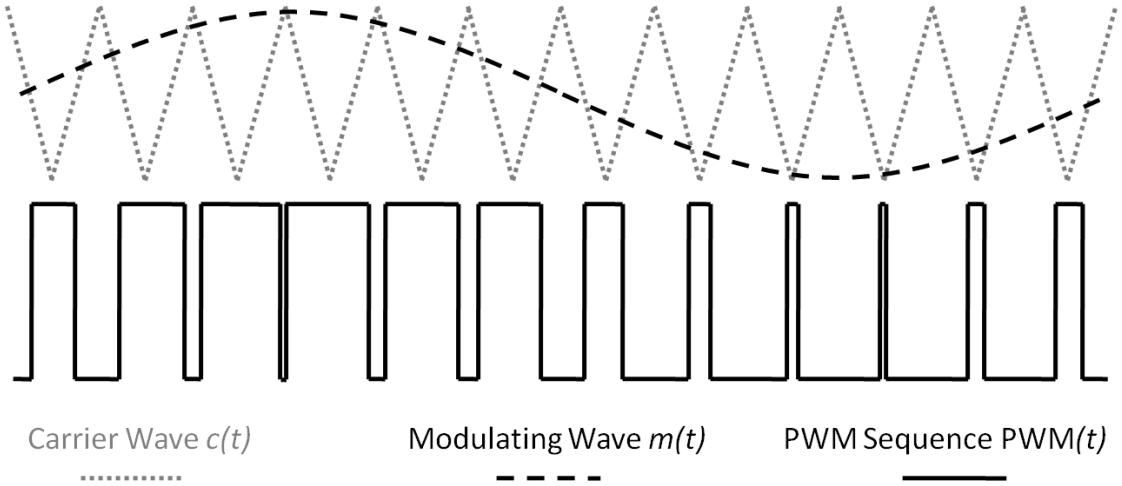

Figure 5.2: Diagram of conventional carrier-based PWM featuring the carrier $c(t)$ and modulating wave $m(t)$.

wave are discrete representations of a continuous signal. Comparison occurs by using logic components as opposed to comparator amplifiers in analogue representations. A second relationship then exists between $c(t)$, $m(t)$ and the overall sampling frequency f_s. The high fundamental frequency of ultrasound places great burden on carrier sampling, switching frequency and pulse abundance. As a consequence, due to the high frequency of the excitation signal to be described, a single pulse per half cycle relationship was chosen, resulting in two width-modulated (one positive and one negative) pulses for a single cycle. This reduces switching losses, lowers the required sampling frequency and relaxes the specification of the transmit output circuitry. That is to say that high power

MOSFET devices typically switch hundreds of volts in the tens of ns range, and therefore very rapid switching is limited by this factor.

5.2.2 Fundamental Frequency Output Relationship

For ultrasound applications, and for a single half cycle square-wave pulse, it can be shown that the output pressure is not directly proportional to the width of the pulse. In other words, the output pressure does not follow a linear relationship with a linear increase in pulse width, and therefore a triangular or sawtooth carrier as defined in (5.1) and shown in Figure 5.1 and Figure 5.2 is not appropriate.

The relationship between harmonic content and switching angle for square wave signals can be calculated using Fourier series analysis [129] [53].

Figure 5.3 shows a bipolar square wave, $f(x)$, with variable angle δ and Fourier series

$$f(x) = \frac{a_0}{2} + \sum_{n=1}^{\infty} (a_n \cos(nx) + b_n \sin(nx)) \tag{5.2}$$

where

$$a_0 = \frac{1}{\pi} \int_{-\pi}^{\pi} f(x) dx \tag{5.3}$$

$$a_n = \frac{1}{\pi} \int_{-\pi}^{\pi} f(x) \cos(nx) dx \tag{5.4}$$

$$b_n = \frac{1}{\pi} \int_{-\pi}^{\pi} f(x) \sin(nx) dx \tag{5.5}$$

$$f(x) = \begin{cases} -V, & \text{if } -\pi + \delta < x < -\delta \\ V, & \text{if } \delta < x < \pi - \delta \\ 0, & \text{otherwise} \end{cases} \tag{5.6}$$

$f(x)$ is anti-symmetric about the vertical axis, and is therefore classed as an odd signal with

$$a_n = 0, \tag{5.7}$$

as $f(x)$ has no overall d.c. offset, the a_0 coefficient is also equal to zero

$$a_0 = 0, \tag{5.8}$$

This leaves the b_n coefficient in (5.2) to be calculated using (5.5).

$$b_n = \frac{1}{\pi}\left[-V\int_{-\pi+\delta}^{-\delta}\sin(nx)\,dx + V\int_{\delta}^{\pi-\delta}\sin(nx)\,dx\right] \tag{5.9}$$

$$b_n = \frac{V}{\pi}\left[-\int_{-\pi+\delta}^{-\delta}\sin(nx)\,dx + \int_{\delta}^{\pi-\delta}\sin(nx)\,dx\right] \tag{5.10}$$

$$b_n = \frac{V}{\pi}\left[\frac{\cos(nx)}{n}\Big|_{-\pi+\delta}^{-\delta} - \frac{\cos(nx)}{n}\Big|_{\delta}^{\pi-\delta}\right] \tag{5.11}$$

$$b_n = \frac{V}{n\pi}\left[\cos(nx)\Big|_{-\pi+\delta}^{-\delta} - \cos(nx)\Big|_{\delta}^{\pi-\delta}\right] \tag{5.12}$$

$$b_n = \frac{V}{n\pi}\left[\left(\cos(n(-\delta)) - \cos(n(-\pi+\delta))\right) - \left(\cos(n(\pi-\delta)) + \cos(n(\delta))\right)\right] \tag{5.13}$$

using the relationship

$$\cos(\alpha) = \cos(-\alpha) \tag{5.14}$$

$$b_n = \frac{2V}{n\pi}\left[\cos(n\delta) - \cos(n(\pi-\delta))\right] \tag{5.15}$$

which can be expanded to

$$b_n = \frac{2V}{n\pi}\left[\cos\left(n\delta\right) - \cos\left(n\pi - n\delta\right)\right] \tag{5.16}$$

and can be simplified using the relationships

$$\cos\left(\alpha - \beta\right) = \cos\left(\alpha\right)\cos\left(\beta\right) - \sin\left(\alpha\right)\sin\left(\beta\right) \tag{5.17}$$

and

$$\sin\left(n\pi\right) = 0 \tag{5.18}$$

$$\cos\left(n\pi\right) = \left(-1\right)^n. \tag{5.19}$$

Therefore, b_n can simplify to

$$b_n = \frac{2V}{n\pi}\left[\cos\left(n\delta\right)\left(1 - \left(-1\right)^n\right)\right] \tag{5.20}$$

giving

$$f\left(x\right) = \sum_{n=1}^{\infty}\left(\frac{2V}{n\pi}\left[\cos\left(n\delta\right)\left(1 - \left(-1\right)^n\right)\right]\sin\left(nx\right)\right). \tag{5.21}$$

If δ is varied linearly between 0 and $\pi/2$, then the magnitude of the b_n coefficient in (5.20) decreases as shown in Figure 5.4 and described previously for power converters by Bedford and Hoft [129]. It can be seen from Figure 5.4 that the relationship between a linearly increasing switching threshold or square wave pulse width, and the magnitude of the harmonic component, that the relationship between the pulse width and fundamental output is indeed not linear, but trigonometric [129]. This non-linear relationship between pulse width and peak pressure can also be demonstrated with Field II simulation [118][119]. Figure 5.5 shows an exemplar set of 4-cycle switched-mode tone-burst signals. Each of the signals has positive and negative cycles of differing widths corresponding to a percentage of half cycle duration moving from 10% to 90%, where 100% would mean maximum half cycle pulse width. The minimum pulse-width resolution is

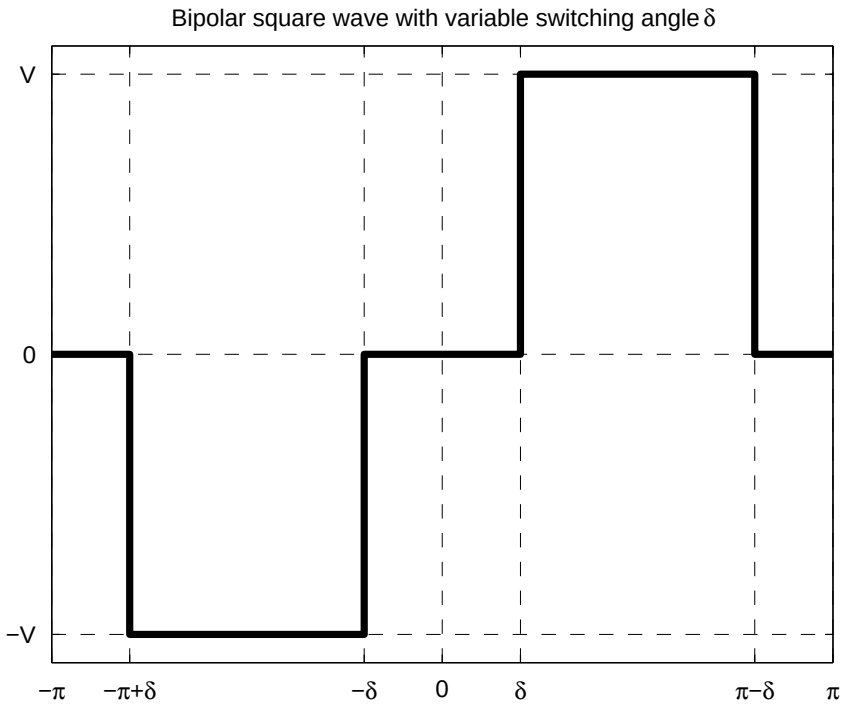

Figure 5.3: Bipolar square wave with variation of switching angle δ

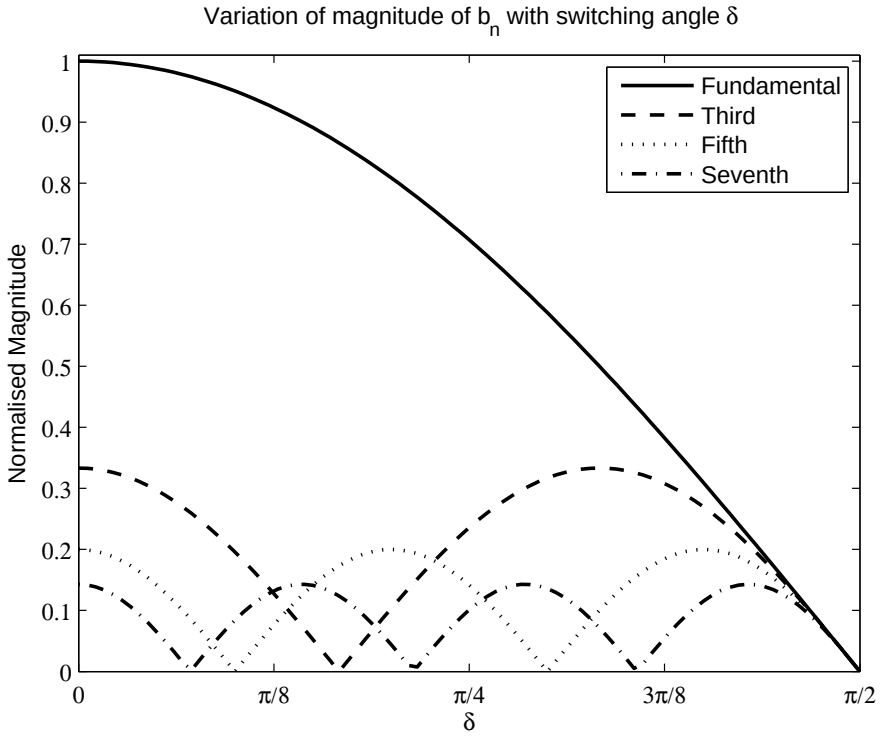

Figure 5.4: Harmonic energy within a PWM square wave of increasing width with switching angle. Absolute values are normalised to the fundamental

10%, and odd numbers are used to ensure that the middle of the pulse is located at the same point for each case. When passed through a suitable transducer the pressure output shows variation in amplitude (Figure 5.6). Figure 5.7 shows an FFT of each signal, demonstrating comparable frequency characteristics. Inspection of Figures 5.6 and 5.7 shows that there is a non-linear increase in peak pulse amplitude. This peak amplitude can be plotted against percentage width as shown in Figure 5.8, and shows a non-linearity that is similar to Figure 5.4.

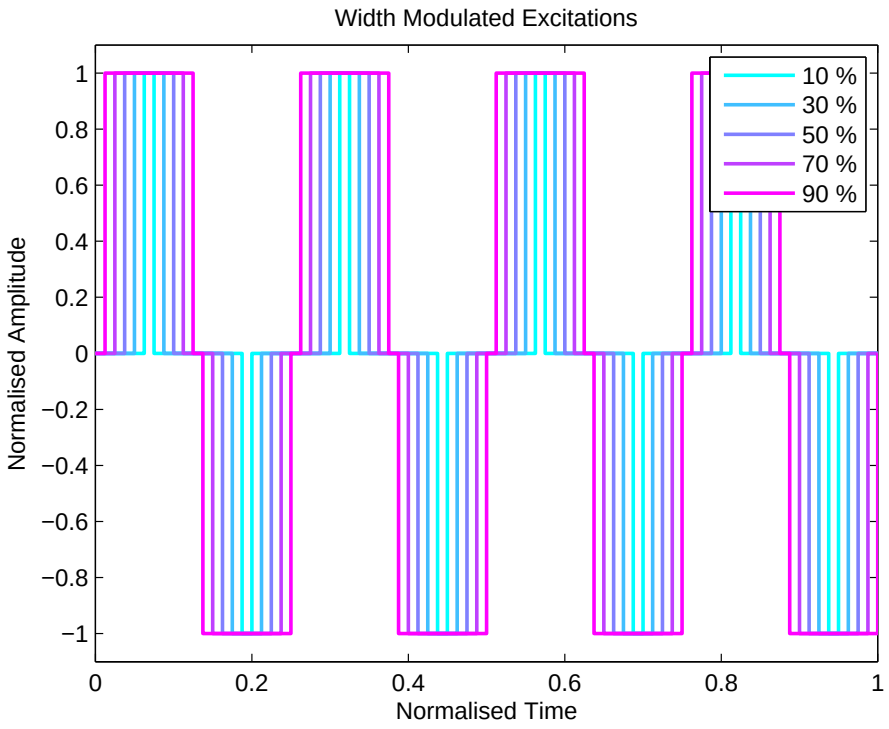

Figure 5.5: Variation in pulse width of a switched-mode signal

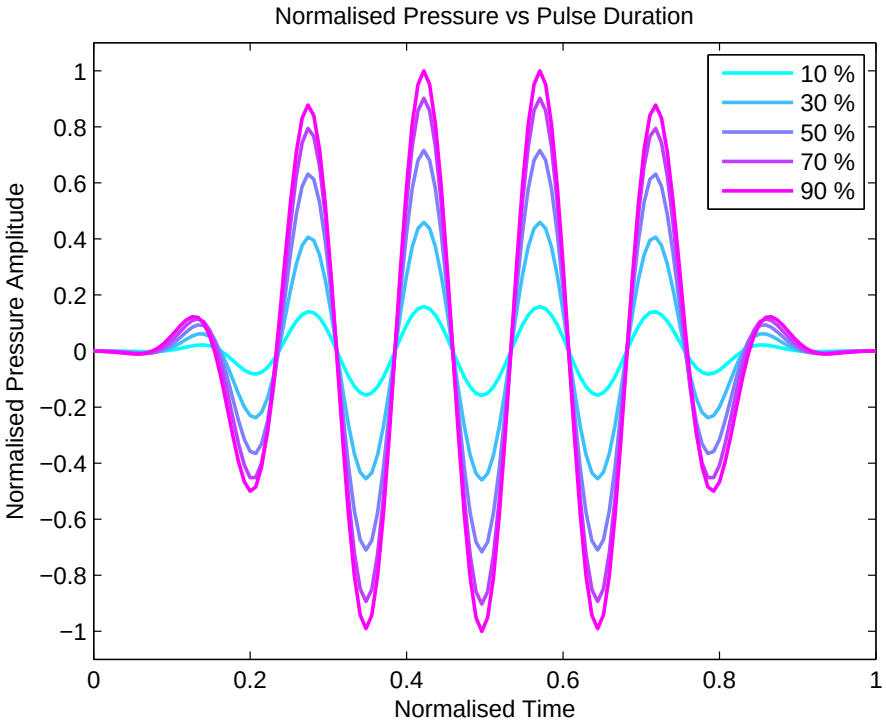

Figure 5.6: Pressure from pulse-width modulated signals

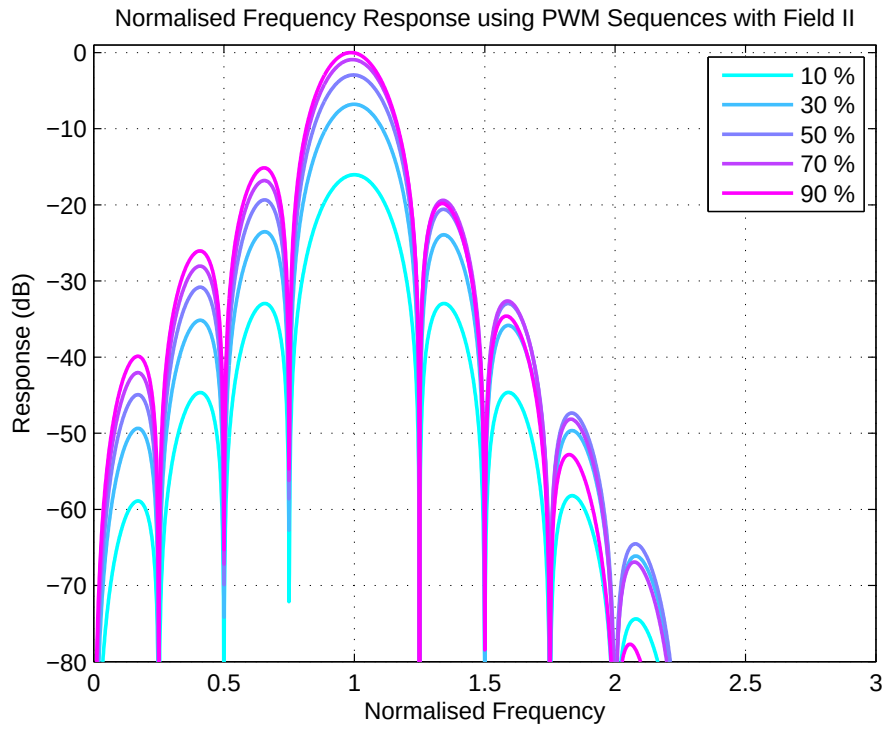

Figure 5.7: FFT of pulse-width modulated pressure signals

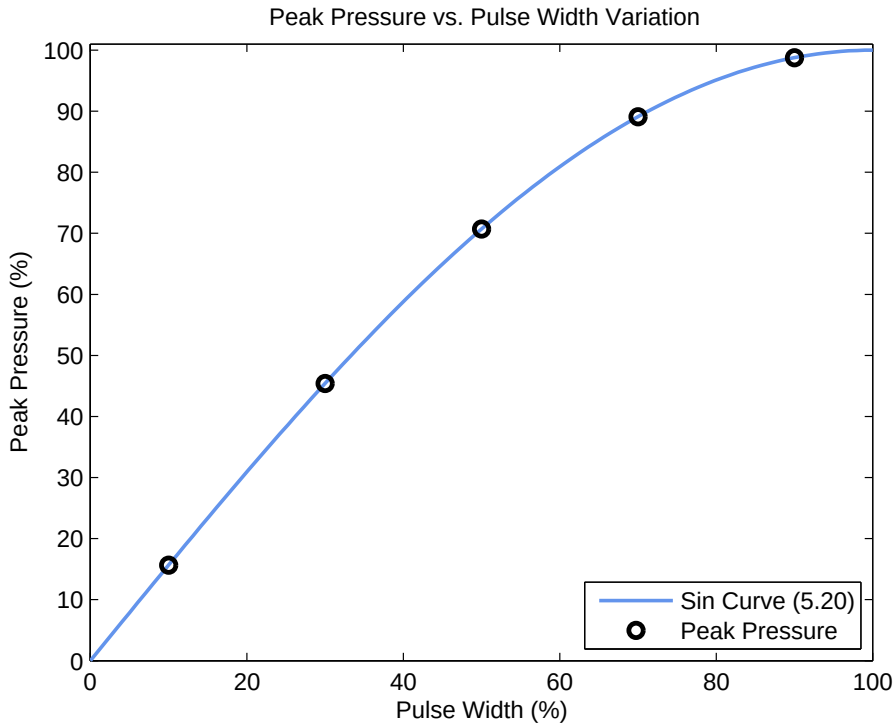

Figure 5.8: Variation in peak pressure according to pulse width. Pressure varies according to a trigonometric relationship as described by (5.20)

If the magnitude of the fundamental is considered of most importance due to the influence of the transducer, then pulse widths must be assigned according to this relationship.

A patent by Haider [132] has also discussed this relationship. In [132], a thresholding method to to encode a desired pulse width for a desired output amplitude was discussed. To convert between the two, an inverse trigonometric function ($\cos^{-1}$) was used. A thresholding method such as [132] derives a single pulse width for a fixed desired amplitude. A carrier comparison based method however can encode successive widths of a train of pulses according to a fluctuation in desired amplitude, and can also encode the position of pulses within a sequence. It is therefore the aim of this work to utilise the simplicity of a carrier comparison method, but adjust it to reflect the trigonometric variation in amplitude. For carrier comparison PWM a change in carrier form is required.

5.2.3 Optimization: Trigonometric Carrier Definition

Optimization of the carrier to provide a non-linear increase in pulse width for a linearly increasing desired output can be defined like so:

$$c(t) = A \cdot |\ \cos(\omega t + \phi)\ | + L \tag{5.22}$$

When the carrier defined by (5.22) is used in a carrier-comparison PWM method, symmetrically modulated PWM sequences are generated, with both the leading and trailing edges modulated simultaneously [131]. Figure 5.9 demonstrates the difference between a traditional triangular carrier and the proposed trigonometric carrier, with both carriers scaled within the range $0 \leq c(t) \leq 1$.

5.2.4 Extension to Multi-Level PWM

Typically, several d.c. voltage levels are used to describe the desired excitation. Indeed, the use of multiple level MOSFET switching circuits is commonplace for switching inverters [133] but also applies to ultrasound as shown in literature such as [52, 92] and patents [61] [60]. The use of multiple levels is advantageous for PWM as it doubles the

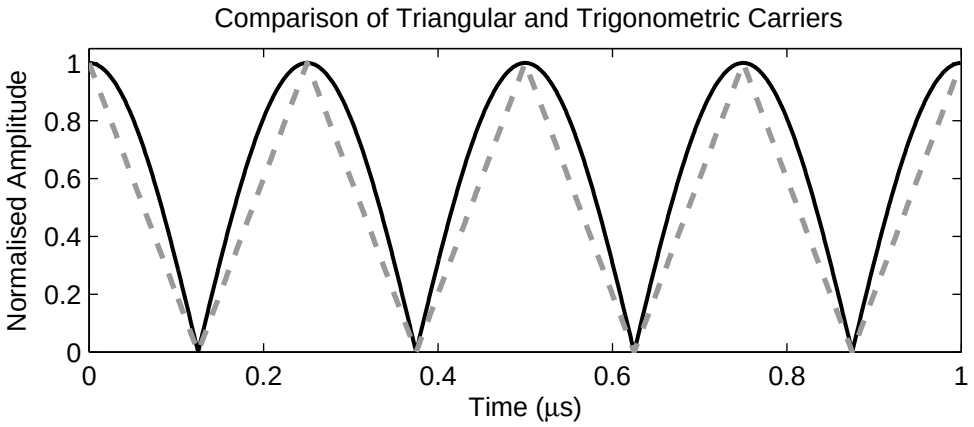

Figure 5.9: Comparison of a triangular (grey dashed) vs a trigonometric (black solid) carrier.

number of available states with which to describe the desired amplitude, at a slight cost of increased hardware. Figure 5.10 shows a multi-level waveform, $f(x)$. $f(x)$ can be

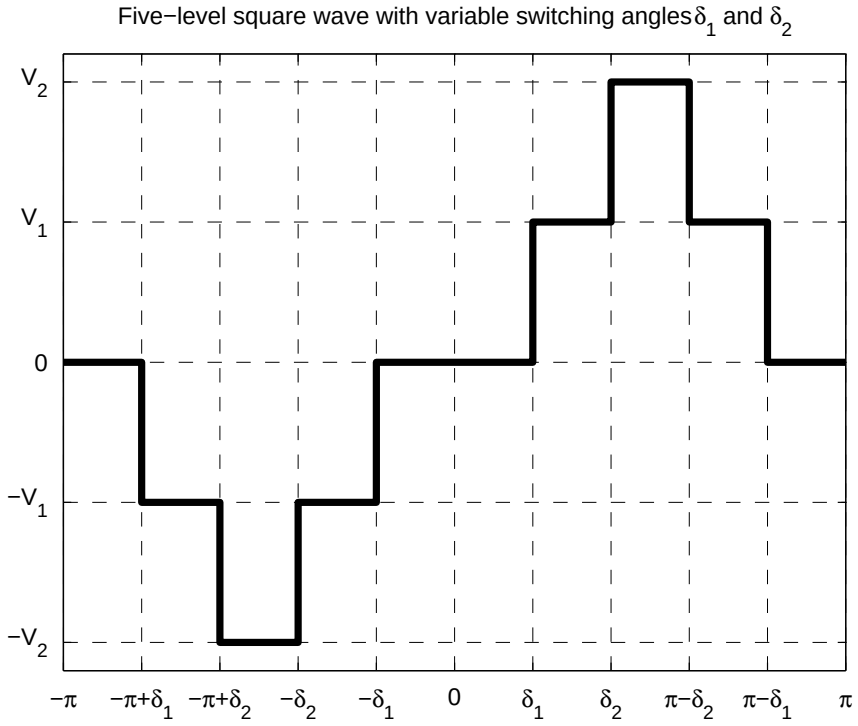

Figure 5.10: Five-level bipolar square wave with variation of switching angle δ_1 and δ_2

represented by the piecewise function

$$f(x) = \begin{cases} -V_1, & \text{if } -\pi+\delta_1 < x < -\pi+\delta_2 \\ -V_2, & \text{if } -\pi+\delta_2 < x < -\delta_2 \\ -V_1, & \text{if } -\delta_2 < x < -\delta_1 \\ V_1, & \text{if } \delta_1 < x < \delta_2 \\ V_2, & \text{if } \delta_2 < x < \pi-\delta_2 \\ V_1, & \text{if } \pi-\delta_2 < x < \pi-\delta_1 \\ 0, & \text{otherwise} \end{cases} \tag{5.23}$$

with $\delta_1 < \delta_2 < \pi$. As in the previous case, the signal is odd, with no DC offset, therefore the a_n and a_0 coefficients are as previously in (5.8) and (5.8), and the b_n coefficient should be calculated using (5.5).

$$b_n = \frac{1}{\pi}\left[-V_1\int_{-\pi+\delta_1}^{-\pi+\delta_2}\sin(nx)\,dx - V_2\int_{-\pi+\delta_2}^{-\delta_2}\sin(nx)\,dx - V_1\int_{-\delta_2}^{-\delta_1}\sin(nx)\,dx \right. \\ \left. + V_1\int_{\delta_1}^{\delta_2}\sin(nx)\,dx + V_2\int_{\delta_2}^{\pi-\delta_2}\sin(nx)\,dx + V_1\int_{\pi-\delta_2}^{\pi-\delta_1}\sin(nx)\,dx\right] \tag{5.24}$$

performing integration gives

$$b_n = \frac{1}{\pi}\left[V_1\frac{\cos(nx)}{n}\Big|_{-\pi+\delta_1}^{-\pi+\delta_2} + V_2\frac{\cos(nx)}{n}\Big|_{-\pi+\delta_2}^{-\delta_2} + V_1\frac{\cos(nx)}{n}\Big|_{-\delta_2}^{-\delta_1} \right. \\ \left. - V_1\frac{\cos(nx)}{n}\Big|_{\delta_1}^{\delta_2} - V_2\frac{\cos(nx)}{n}\Big|_{\delta_2}^{\pi-\delta_2} - V_1\frac{\cos(nx)}{n}\Big|_{\pi-\delta_2}^{\pi-\delta_1}\right] \tag{5.25}$$

using (5.14)

$$b_n = \frac{V_1}{n\pi}\left[\cos(nx)\Big|_{-\pi+\delta_1}^{-\pi+\delta_2} + \cos(nx)\Big|_{-\delta_2}^{-\delta_1} - \cos(nx)\Big|_{\delta_2}^{\delta_1} \right. \\ \left. - \cos(nx)\Big|_{\pi-\delta_2}^{\pi-\delta_1}\right] + \frac{V_2}{n\pi}\left[\cos(nx)\Big|_{-\pi+\delta_2}^{-\delta_2} - \cos(nx)\Big|_{\delta_2}^{\pi-\delta_2}\right] \tag{5.26}$$

$$b_n = \frac{V_1}{n\pi}\left[\cos\left(n\left(-\pi+\delta_2\right)\right) - \cos\left(n\left(-\pi+\delta_1\right)\right) + \cos\left(n\left(-\delta_1\right)\right) - \cos\left(n\left(-\delta_2\right)\right)\right.$$
$$\left. - \cos\left(n\left(\delta_2\right)\right) + \cos\left(n\left(\delta_1\right)\right) - \cos\left(n\left(\pi-\delta_1\right)\right) + \cos\left(n\left(\pi-\delta_2\right)\right)\right]$$
$$+ \frac{V_2}{n\pi}\left[\cos\left(n\left(-\delta_2\right)\right) - \cos\left(n\left(-\pi+\delta_2\right)\right) - \cos\left(n\left(\pi-\delta_2\right)\right) - \cos\left(n\left(\delta_2\right)\right)\right] \quad (5.27)$$

collecting terms gives

$$b_n = \frac{V_1}{n\pi}\left[2\cos\left(n\left(\pi-\delta_2\right)\right) - 2\cos\left(n\left(\pi-\delta_1\right)\right) + 2\cos\left(n\delta_1\right) - 2\cos\left(n\delta_2\right)\right] \quad (5.28)$$

therefore

$$b_n = \frac{2V_1}{n\pi}\left[\cos\left(n\delta_1\right) - \cos\left(n\delta_2\right) - \cos\left(n\left(\pi-\delta_1\right)\right) + \cos\left(n\left(\pi-\delta_2\right)\right)\right]$$
$$+ \frac{2V_2}{n\pi}\left[\cos\left(n\delta_2\right) - \cos\left(n\left(\pi-\delta_2\right)\right)\right]. \quad (5.29)$$

This can be further expanded to

$$b_n = \frac{2V_1}{n\pi}\left[\cos\left(n\delta_1\right) - \cos\left(n\delta_2\right) - \cos\left(n\pi-n\delta_1\right) + \cos\left(n\pi-n\delta_2\right)\right]$$
$$+ \frac{2V_2}{n\pi}\left[\cos\left(n\delta_2\right) - \cos\left(n\pi-n\delta_2\right)\right]. \quad (5.30)$$

Then using (5.17), (5.18) and (5.19) b_n simplifies to

$$b_n = \frac{2V_1}{n\pi}\left[\cos\left(n\delta_1\right)\left(1-(-1)^n\right) - \cos\left(n\delta_2\right)\left(1-(-1)^n\right)\right]$$
$$+ \frac{2V_2}{n\pi}\left[\cos\left(n\delta_2\right)\left(1-(-1)^n\right)\right], \quad (5.31)$$

giving

$$f(x) = \sum_{n=1}^{\infty}\left\{\left(\frac{2V_1}{n\pi}\left[\cos\left(n\delta_1\right)\left(1-(-1)^n\right) - \cos\left(n\delta_2\right)\left(1-(-1)^n\right)\right]\right.\right.$$
$$\left.\left. + \frac{2V_2}{n\pi}\left[\cos\left(n\delta_2\right)\left(1-(-1)^n\right)\right]\right)\sin\left(nx\right)\right\} \quad (5.32)$$

For multi-level carrier comparison PWM, strategies exist in power converter theory which are applicable to ultrasound. In the case of level-shifted carrier comparison PWM, each switching leg or MOSFET is assigned a carrier, with the carriers scaled to cover the defined region of switching, contiguous in amplitude, but with a d.c. offset [131] as described in (5.22). Examples of three-level and five-level carrier definitions using level-shifted carriers are shown in Figure 5.11.

5.2.5 Generation of PWM Sequences

The carrier comparison method as shown in Figure 5.2 generates PWM sequences using an algorithmic approach. It is therefore appropriate to first explain conventional algorithms as discussed in common literature before explaining the proposed algorithmic change. Therefore, bipolar (three-level) PWM sequences can be generated with two, level-shifted carriers and an algorithm as shown in (5.33).

$$\mathrm{PWM}(t) = \begin{cases} 1, & m(t) \geq c_{\mathrm{POS}}(t) \\ -1, & m(t) \leq c_{\mathrm{NEG}}(t) \\ 0, & \text{otherwise} \end{cases} \tag{5.33}$$

where $m(t)$ is the modulating signal and $c_{\mathrm{POS}}(t)$ and $c_{\mathrm{NEG}}(t)$ are carriers which span the positive and negative regions respectively. This algorithm can then be extended for multiple levels by introducing additional carriers and levels as described by (5.34).

$$\mathrm{PWM}(t) = \begin{cases} 1, & m(t) \geq c_{\mathrm{POS2}}(t) \\ 0.5, & m(t) \geq c_{\mathrm{POS1}}(t) \\ -1, & m(t) \leq c_{\mathrm{NEG2}}(t) \\ -0.5, & m(t) \leq c_{\mathrm{NEG1}}(t) \\ 0, & \text{otherwise} \end{cases} \tag{5.34}$$

where $c_{\mathrm{POS1}}(t)$ and $c_{\mathrm{POS2}}(t)$ are carriers that span the positive ranges between 0 to 0.5 and 0.5 to 1 respectively and $c_{\mathrm{NEG1}}(t)$ and $c_{\mathrm{NEG2}}(t)$ span the ranges between 0 to -0.5 and 0.5

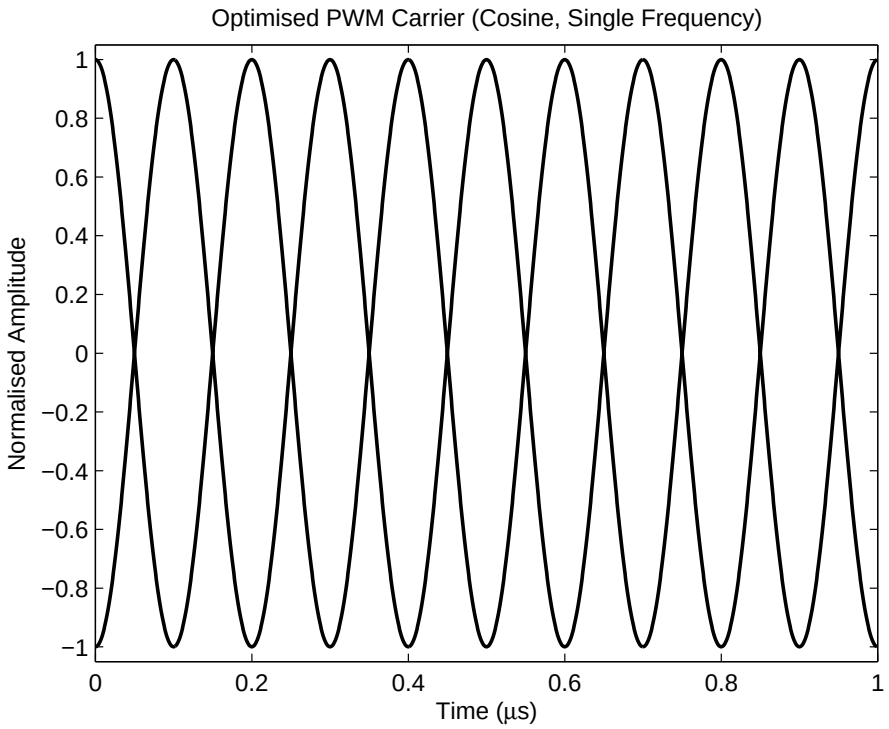

(a) Three-Level Single Frequency Optimised Carrier

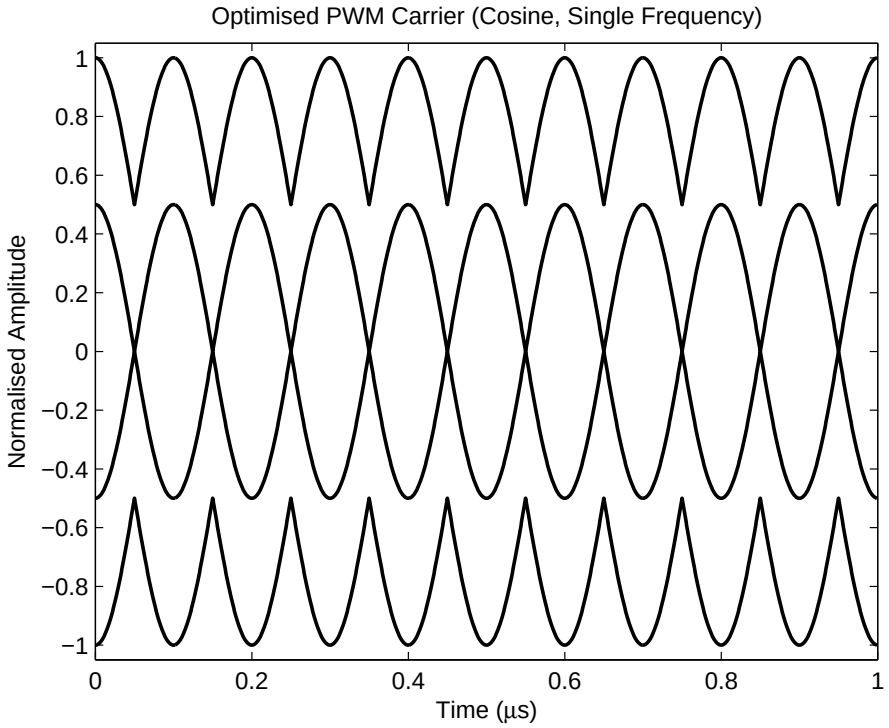

(b) Five-Level Single Frequency Rectified Cosine Carrier

Figure 5.11: Carrier scaling for multi-level PWM generation using the proposed trigonometric carrier. The carrier is replicated a number of times, scaled and then level-shifted in order to span the range of the modulating signal $m(t)$

to -1 respectively. The algorithms described in (5.33) and (5.34) take a conventional low frequency signal and generate multiple pulses per cycle. For ultrasound, due to the high frequency output signal, the proposed method modifies traditional algorithms to generate a single, width-modulated pulse per half cycle at the desired frequency. The proposed algorithm compares two signals: a sinusoidal signal and a desired amplitude function with the carrier setup. Two versions of the desired amplitude function are created, the original which spans from 0 to 1, and the inverse from -1 to 0. The full algorithm is shown in (5.35):

$$\mathrm{PWM}(t) = \begin{cases} \text{if} \quad s(t) \geq 0 & \\ \quad 1, & m_{\mathrm{POS}}(t) \geq c_{\mathrm{POS2}}(t) \\ \quad 0.5, & m_{\mathrm{POS}}(t) \geq c_{\mathrm{POS1}}(t) \\ \quad 0, & \text{otherwise} \\ \text{else} & \\ \quad -1, & m_{\mathrm{NEG}}(t) \leq c_{\mathrm{NEG2}}(t) \\ \quad -0.5, & m_{\mathrm{NEG}}(t) \leq c_{\mathrm{NEG1}}(t) \\ \quad 0, & \text{otherwise} \end{cases} \tag{5.35}$$

where $s(t) = A \cdot \sin(\omega t + \phi)$ and is scaled from -1 to 1, and where $m_{\mathrm{POS}}(t)$ and $m_{\mathrm{NEG}}(t)$ are positive and negative (or inverse) versions of the desired window function respectively. For clarity an example is shown in Figure 5.12. Using the proposed encoding scheme frequency information is stored within the carrier, and amplitude information is stored within the modulating function.

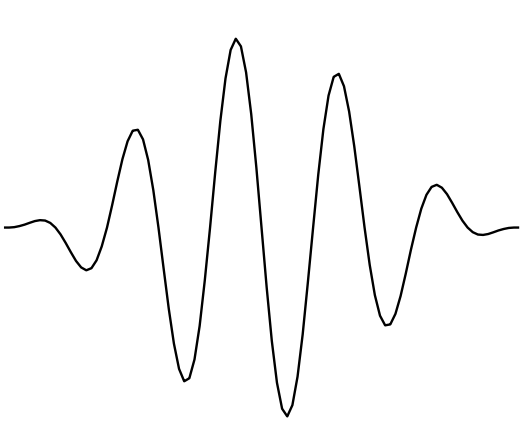

(a) Desired Signal

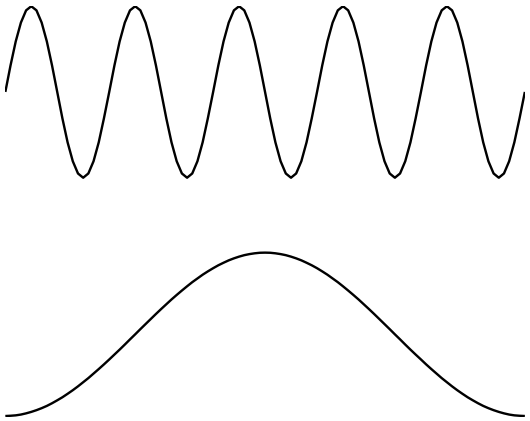

(b) $s(t)$ (top) and $m(t)$ (bottom)

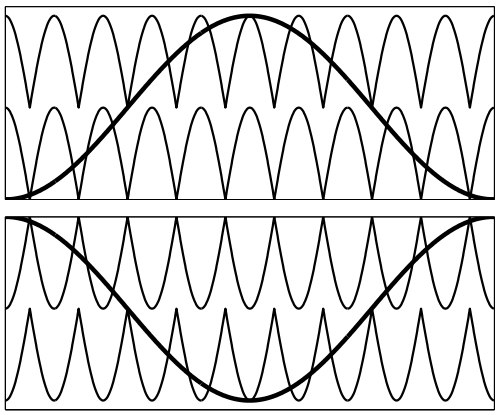

(c) $m_{\mathrm{POS}}(t)$ and $m_{\mathrm{NEG}}(t)$ with multi-level trigonometric carriers

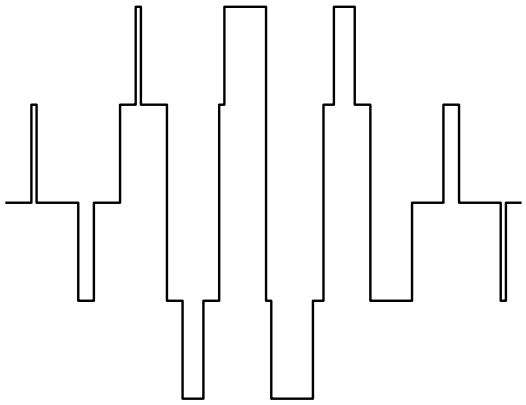

(d) PWM(t) sequence

Figure 5.12: Construction of PWM encoded signals. The desired waveform 5.12(a) is a tone burst with an applied window function, and can be split into its constituent parts $s(t)$ and $m(t)$ 5.12(b). The desired amplitude function is duplicated to form positive and negative window functions 5.12(c). Using the sign of $s(t)$ comparison between either positive or negative comparisons are performed to generate the resultant PWM sequence as shown in 5.12(d).

5.3 Demonstration of Pressure Control

Using the algorithm defined in (5.35), multi-level arbitrary waveform sequences can be designed which give the desired output signal once filtered by the transducer. It is possible to simulate the filtering effect of the transducer by measuring its impulse response, and convolving this with the PWM signal [134]

$$y(t) = s(t) * h(t) \tag{5.36}$$

where $s(t)$ is the excitation signal and $h(t)$ is the impulse response of the transducer and $y(t)$ is the simulated pressure output through the transducer. Note that $s(t)$ can be substituted for the PWM signal $\mathrm{PWM}(t)$ to give the response to PWM encoded signals.

$$y(t) = \mathrm{PWM}(t) * h(t) \tag{5.37}$$

The simulated pressure output can then be compared with the measured output.

To show that conversion from a triangular to trigonometric carrier is necessary, simulation and experiments were conducted with arbitrary waveform sequences using three and five level circuits within the UARP. Figure 5.14 shows a simulated example of a linearly increasing amplitude function applied to a 10 µs 4.8 MHz tone-burst sampled at 100 MHz. The PWM sequence has been convolved with the impulse response of the array transducer used in Chapter 4 (see Table 4.6). It can be seen in Figure 5.14(a) that encoding with the linear carrier does not give the desired output. Instead, a curved amplitude function is prevalent. When compared with the trigonometric case in Figure 5.14(b) it can be seen that there is a better approximation to the desired case, but with a degree of ripple. This ripple is due to a low resolution of PWM states, and can be improved either by increasing sampling frequency or by increasing the number of levels to select from. Increasing sampling frequency requires sourcing faster switching MOSFETs (of which there is limited choice). Moving to multiple levels however requires replication of the circuit as shown in Figure 3.6 and is a more simplistic choice, especially as multi-level components are on the market.

Figure 5.15 shows the impact of increasing the number of levels to five, and consequently the number of available states on the waveform. Firstly, with respect to the simulated triangular carrier, it can be seen that the the use of an additional level set has produced a ‘double-hump’ in the transition between high and low levels as shown in Figure 5.15(a). Figure 5.15(b) shows the the result of convolution using the trigonometric encoded PWM. This approximates the desired linearly increasing pulse with much greater accuracy than both the triangular case, and the three level trigonometric case.

Figures 5.16 and 5.17 show comparable data, but measured experimentally using a 1 mm Hydrophone shown in Figure 5.13 (Precision Acoustics, Dorchester, UK).

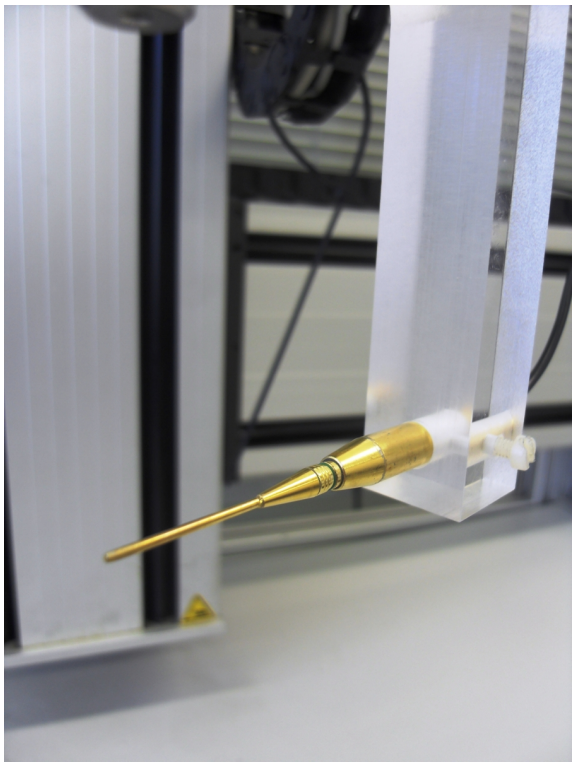

Figure 5.13: Photograph of the 1 mm needle hydrophone (Precision Acoustics, Dorchester, UK)

The hydrophone was aligned to the transducer and separated by a distance of 20 mm. Low amplitude was used to reduce non-linear effects for better comparison with the simulated cases. Each measurement was acquired using a digital oscilloscope and processed using MATLAB. The frequency response of the hydrophone was corrected using an inverse filter. It can be seen that the triangular and trigonometric cases are matched to their simulated equivalents, with the triangular carrier encoded signals giving a curved waveform. For the trigonometric cases in Figure 5.16(b) and 5.17(b), as with the simulated case, the desired amplitude function is generated as in the five-level case. Notice however a slight difference between the five-level simulated (Figure 5.15(b)) and the experimental case (Figure 5.17(b)) at the mid-level point, or crossover between the low switch switching, and the high switch switching. This appears as a dip in amplitude, and is caused by the effect of MOSFET rise and fall time. At this stage a minimum pulse width (10 ns due to 100 MHz) is required by the high level switch, however due to the rise time of

the MOSFET full amplitude is not reached before falling again. This generates a smaller pulse height than predicted with simulation.

A second set of arbitrary waveform examples can be seen in Figures 5.18 and 5.19 (simulation) and Figures 5.20 and 5.21 (measured). In this second case, a triangular function is applied to the 10 µs, 4.8 MHz tone-burst. This example function further accentuates the inaccuracy of the triangular carrier for both the three and five-level cases. As can be seen in Figures 5.18(a) and 5.20(a) the three level triangular case gives a curved output, resembling a cosine window as opposed to the desired triangular window. The three-level trigonometric case in Figures 5.18(b) and 5.20(b) approximate the desired with greater accuracy, however exhibit a slight ripple as a consequence of a low number of available states. Moving to five-levels shows a noticeable 'double-hump' in the simulated triangular modulated case (Figure 5.19(a)). This is also seen in the experimentally measured case Figure 5.21(a). For the five-level trigonometric encoded sequences (simulation Figure 5.19(b) and experimental Figure 5.21(b)) it can be seen that the desired amplitude function is shown, albeit with a small amount of crossover distortion between the low switch and high switch.

A last example is provided of a Hann windowed sequence. The three-level (Figures 5.22 and 5.24) and five-level (Figures 5.23 and 5.25) cases are shown here. The triangular encoded cases show a large difference in desired output. For the trigonometric encoded cases much more accurate representation of the desired function is provided, although with slight ripple in the three-level case as discussed in the previous cases, and minor crossover distortion in the five-level case. These slight variations however should not detract away from the performance of the trigonometric encoding scheme over the triangular encoding scheme, and merely demonstrate the practical implementation issues surrounding the method.

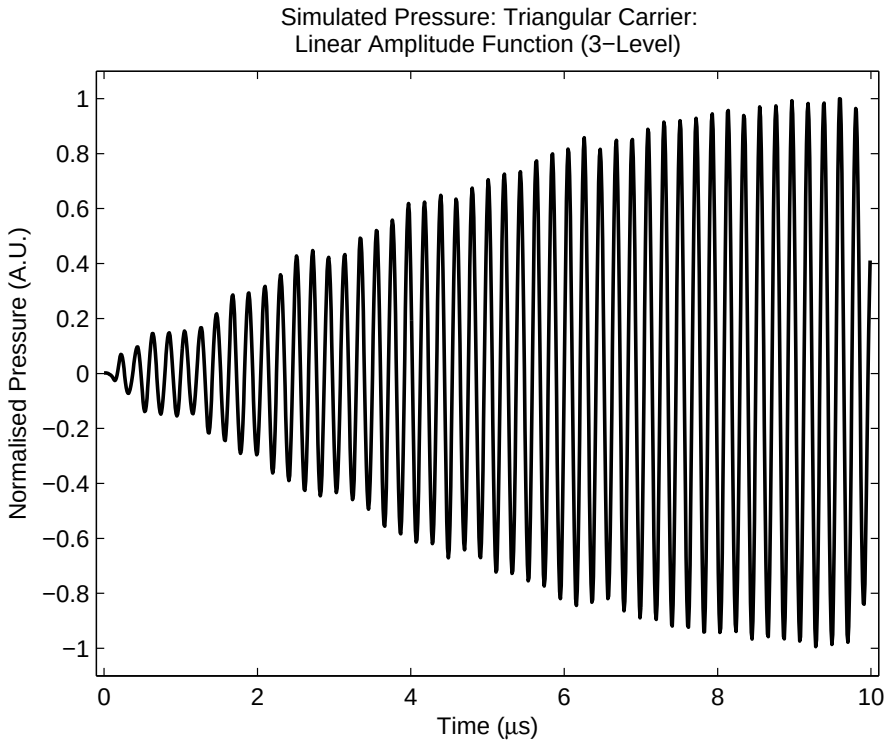

(a) Triangular Carrier

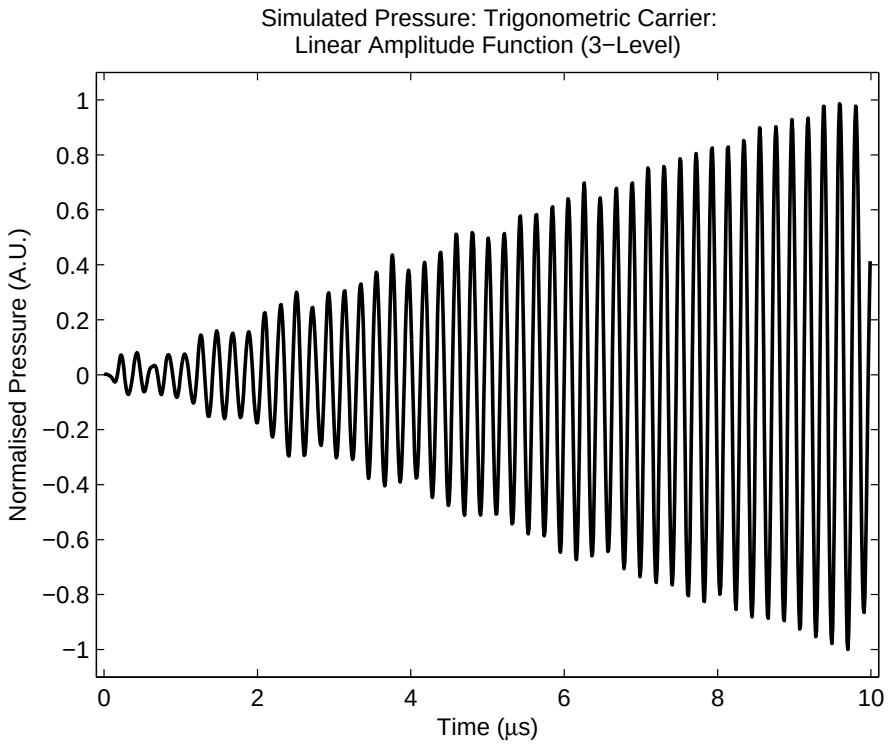

(b) Trigonometric Carrier

Figure 5.14: Comparison between simulations of three-level triangular based comparisons vs. trigonometric based comparisons. Linearly increasing ramp window function applied

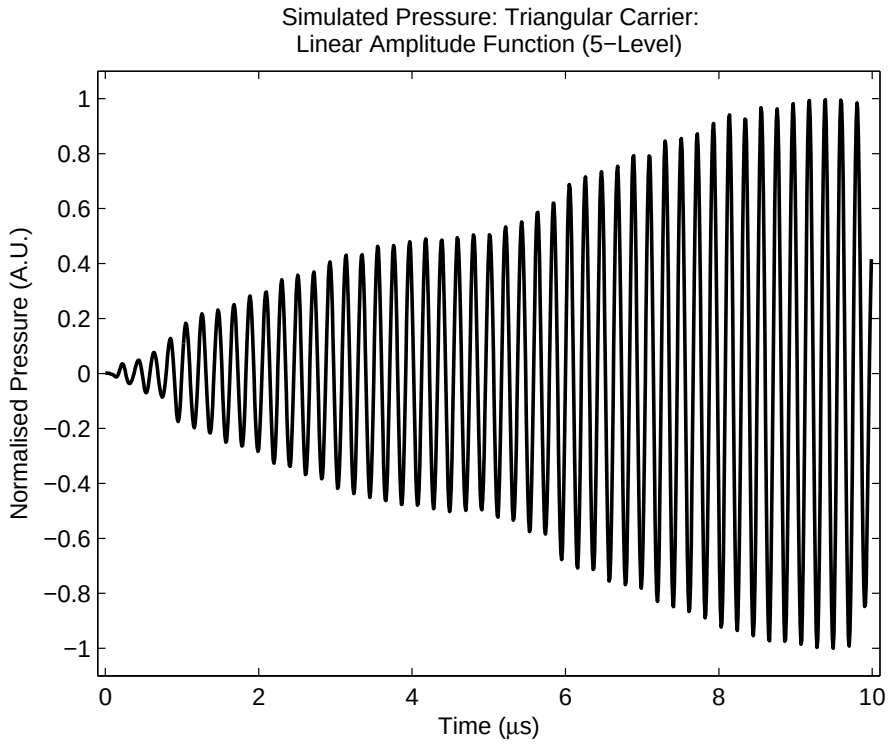

(a) Triangular Carrier

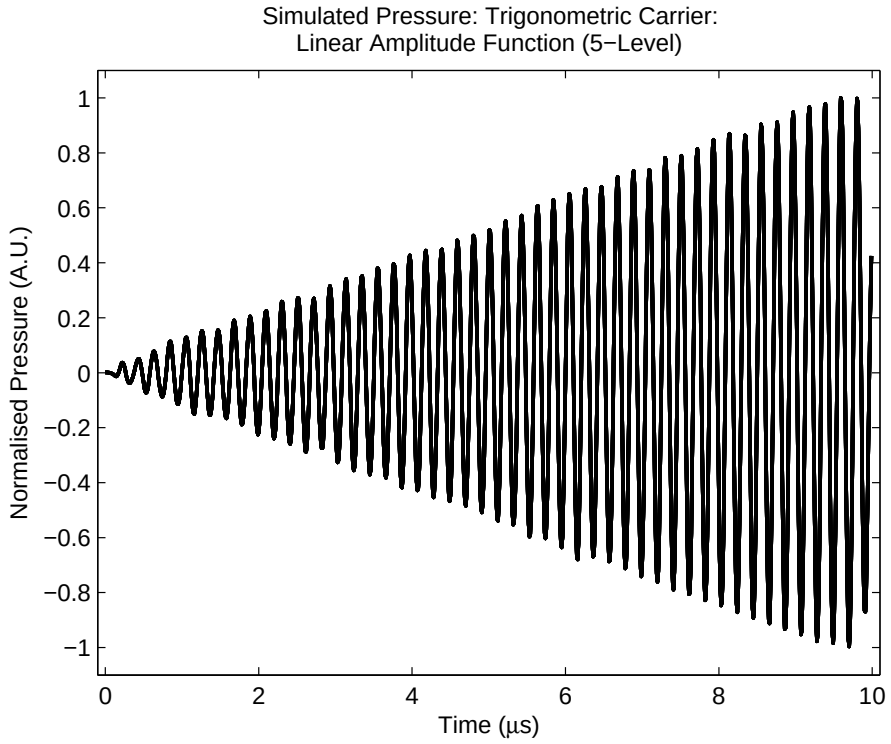

(b) Trigonometric Carrier

Figure 5.15: Comparison between simulations of five-level triangular based comparisons vs. trigonometric based comparisons. Linearly increasing ramp window function applied

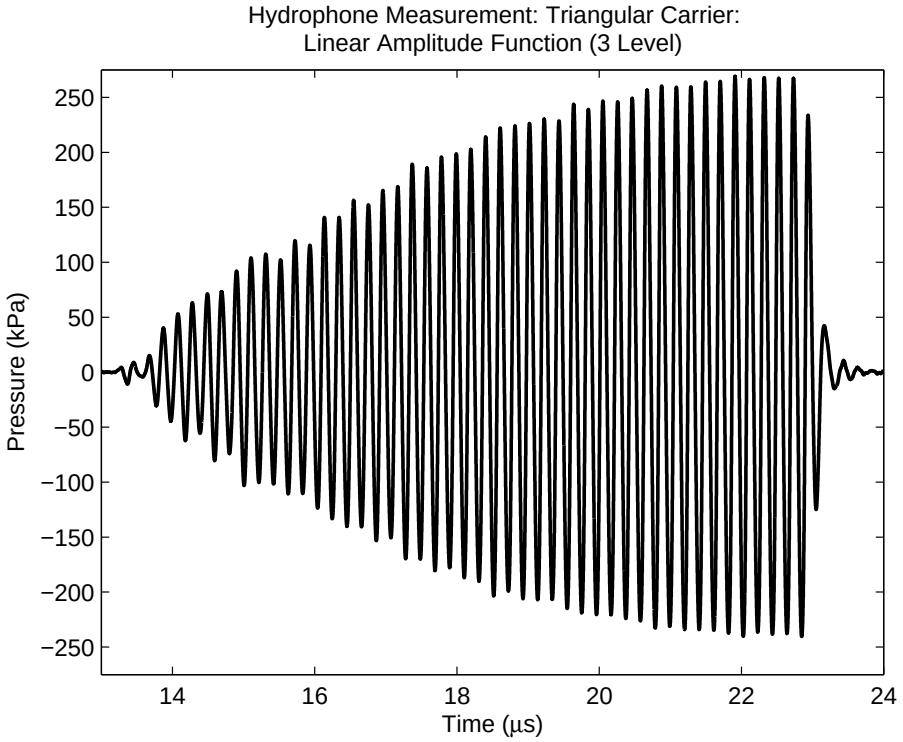

(a) Triangular Carrier 3-level

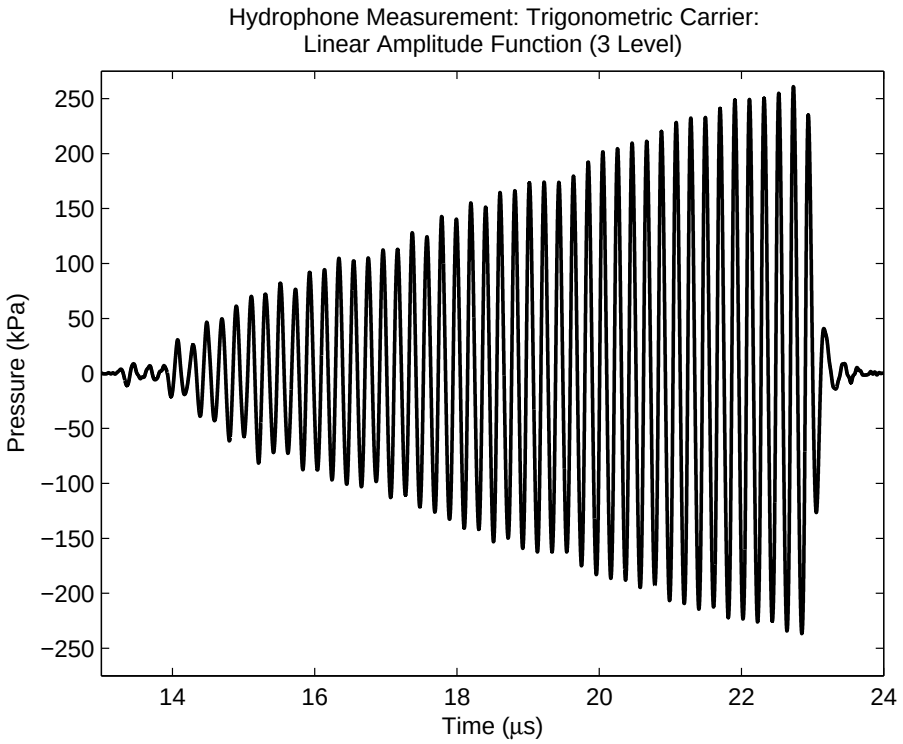

(b) Trigonometric Carrier 3-level

Figure 5.16: Comparison between experimentally obtained three-level triangular based comparisons vs. trigonometric carrier. Linearly increasing ramp function applied (single acquisition)

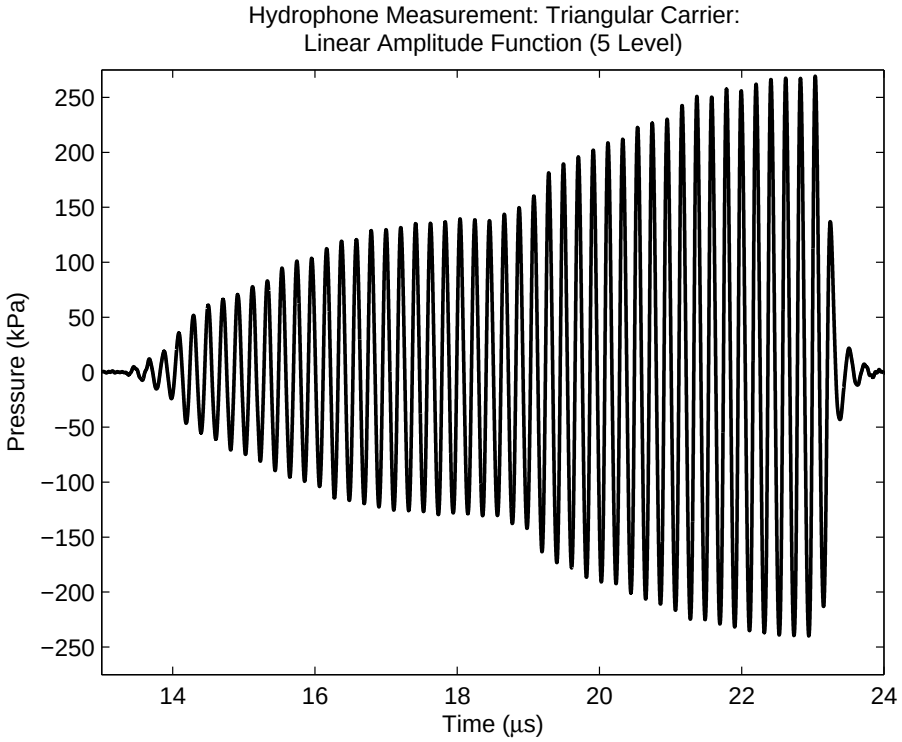

(a) Triangular Carrier 5-level

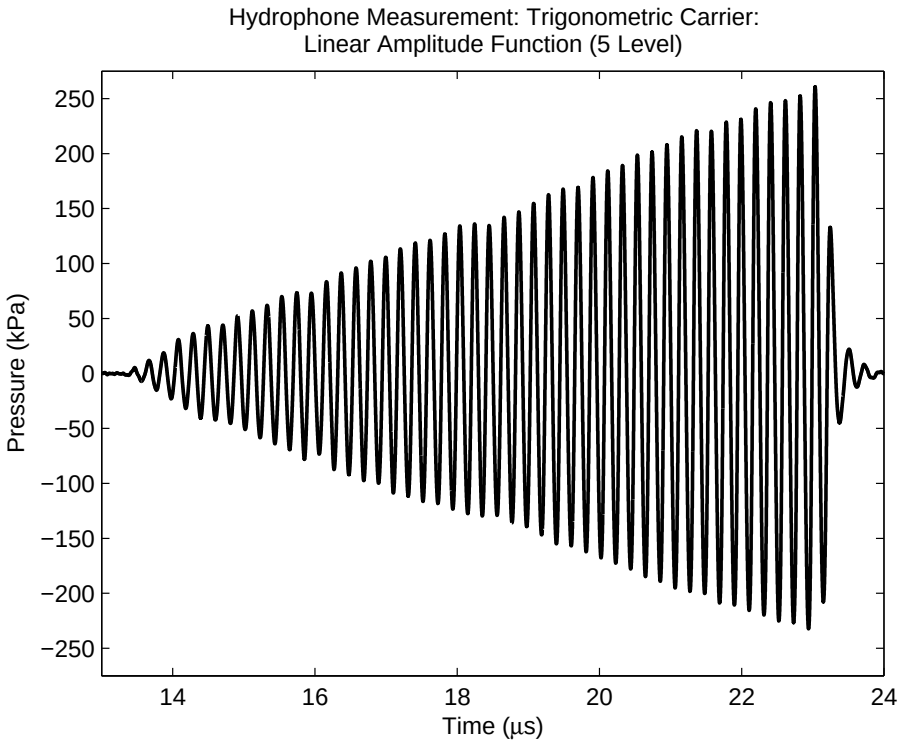

(b) Trigonometric Carrier 5-level

Figure 5.17: Comparison between experimentally obtained five-level triangular based comparisons vs. trigonometric carrier. Linearly increasing ramp function applied (single acquisition)

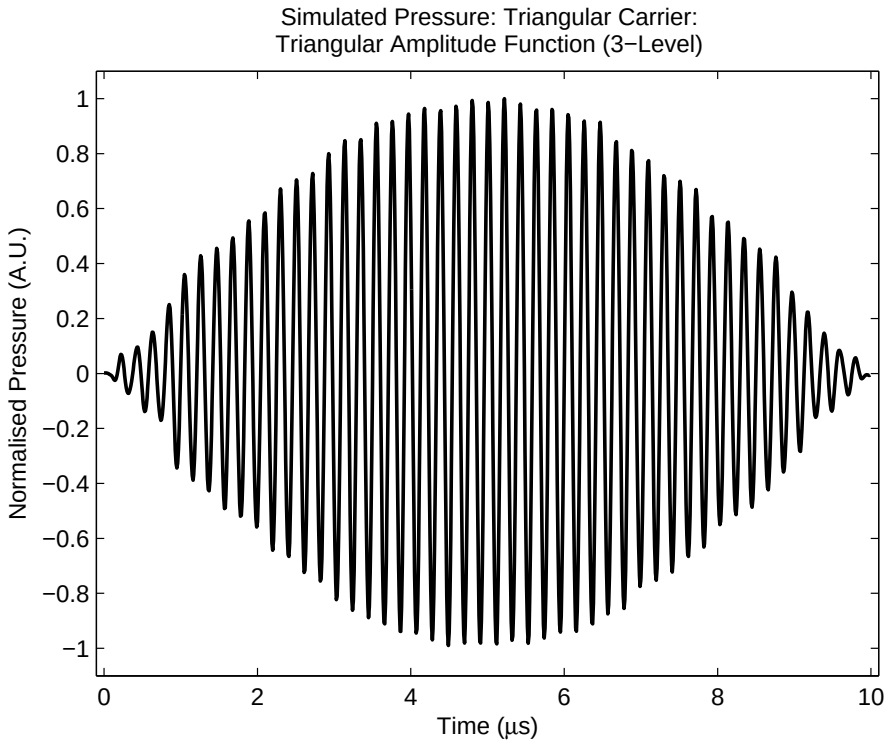

(a) Triangular Carrier

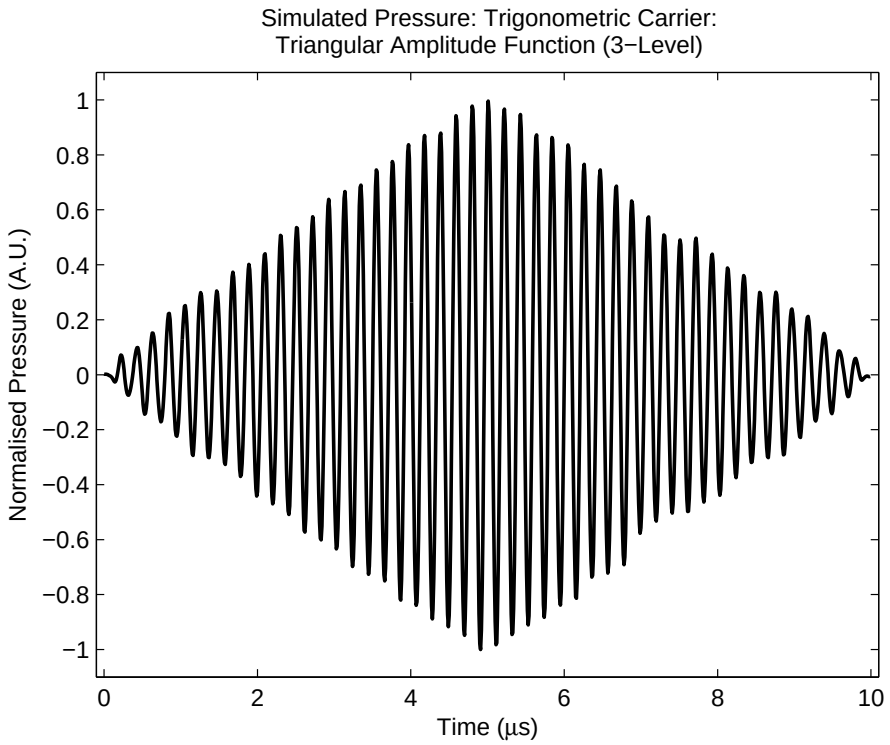

(b) Trigonometric Carrier

Figure 5.18: Comparison between simulations of three-level triangular based comparisons vs. trigonometric based comparisons. Triangular window function applied

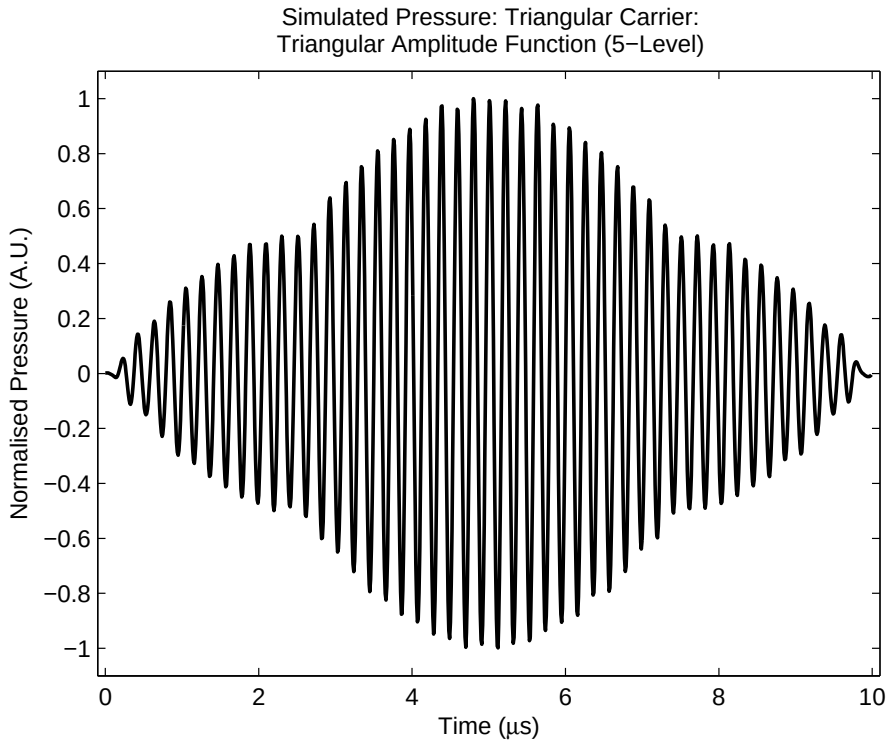

(a) Triangular Carrier

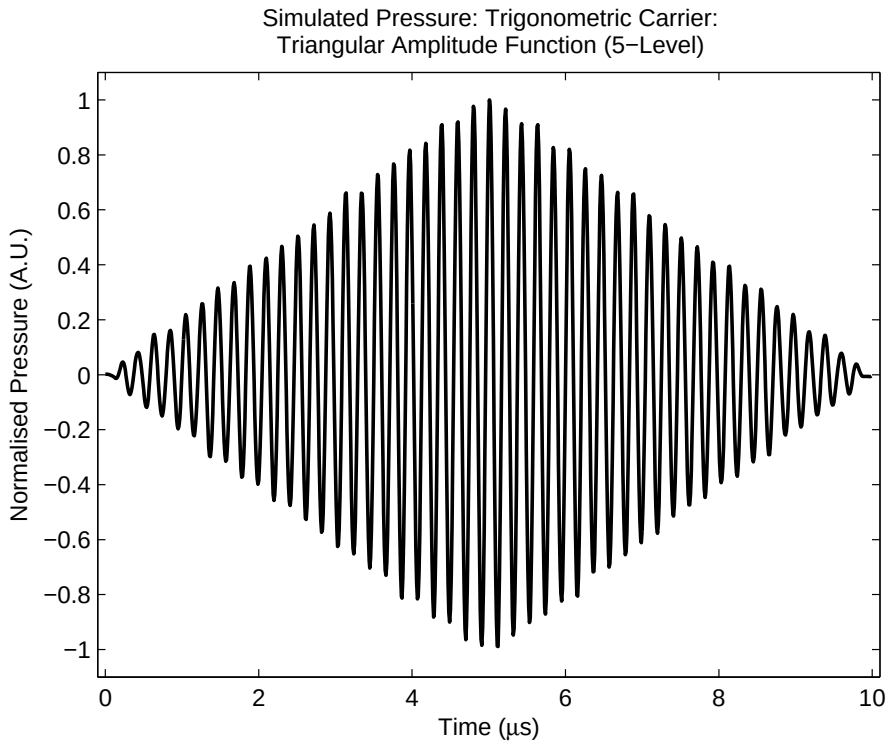

(b) Trigonometric Carrier

Figure 5.19: Comparison between simulations of five-level triangular based comparisons vs. trigonometric based comparisons. Triangular window function applied

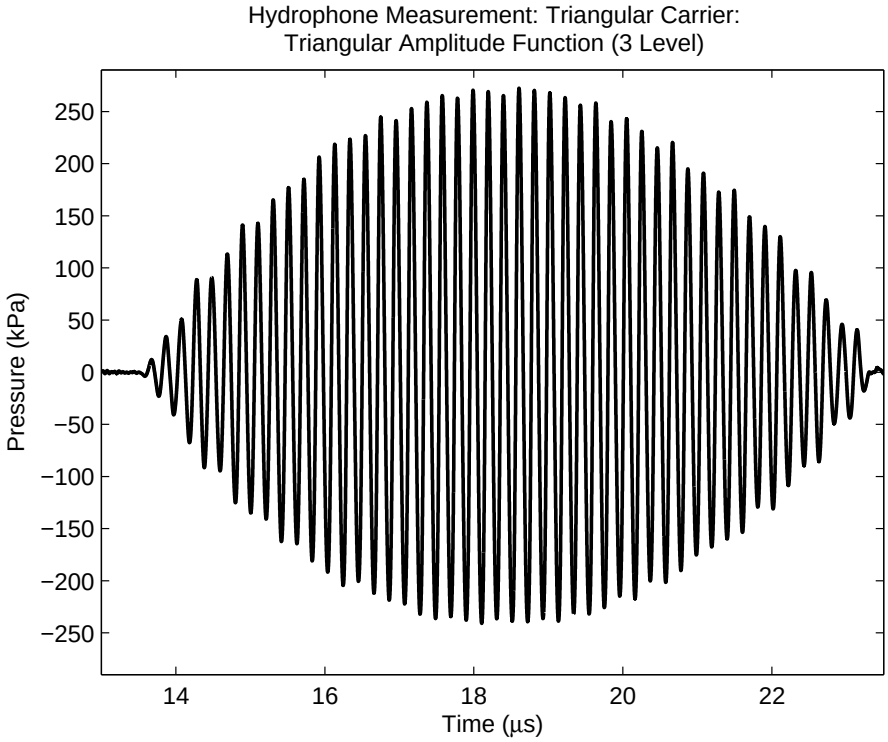

(a) Triangular Carrier 3-level

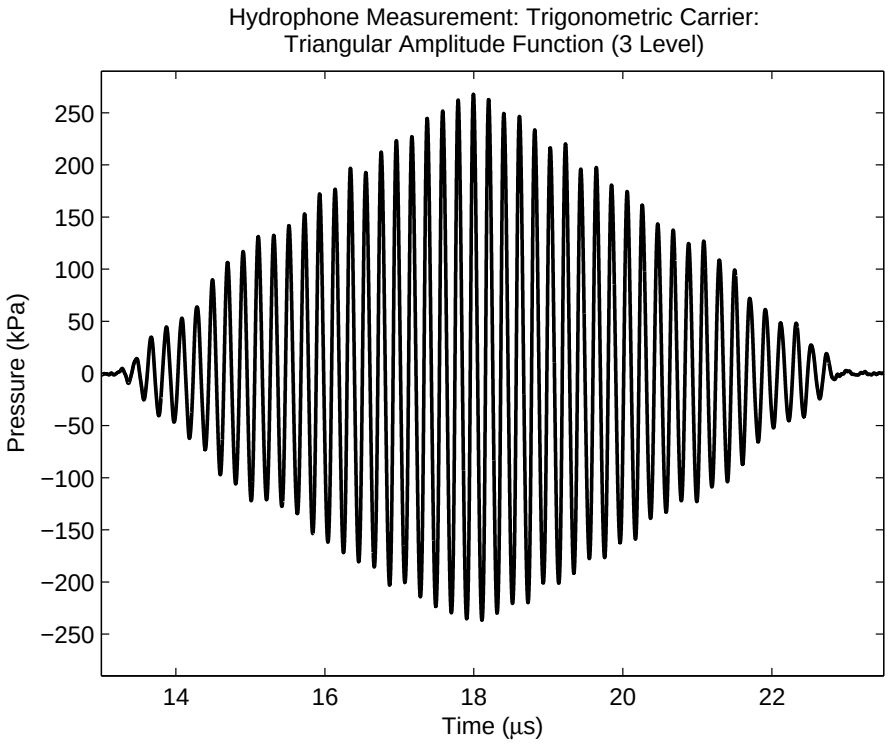

(b) Trigonometric Carrier 3-level

Figure 5.20: Comparison between experimentally obtained three-level triangular based comparisons vs. trigonometric carrier. Triangular window function applied (single acquisition)

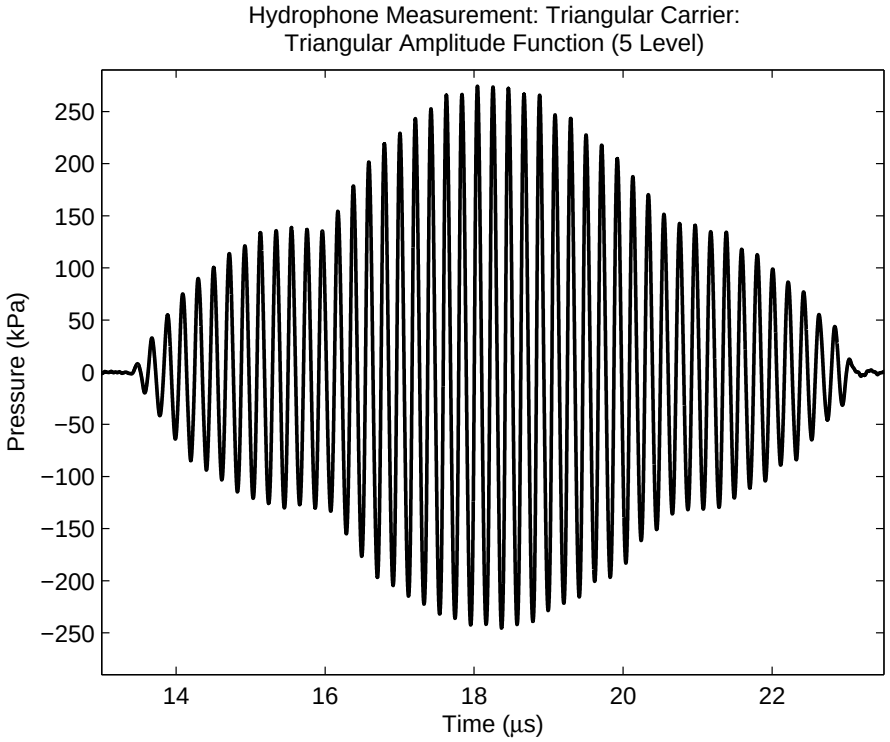

(a) Triangular Carrier 5-level

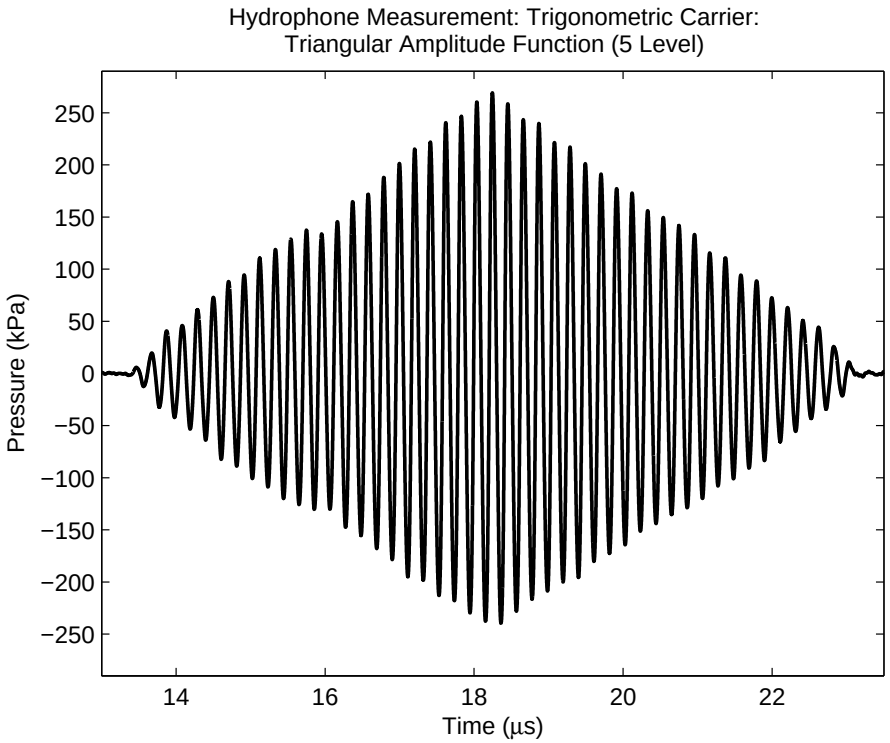

(b) Trigonometric Carrier 5-level

Figure 5.21: Comparison between experimentally obtained five-level triangular based comparisons vs. trigonometric carrier. Triangular window function applied (single acquisition)

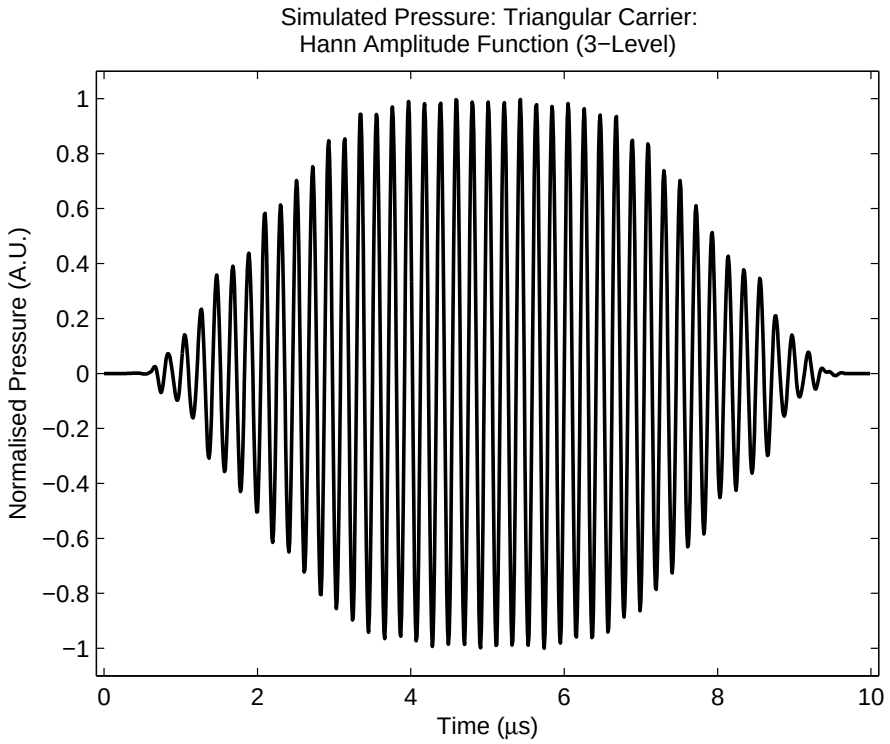

(a) Triangular Carrier

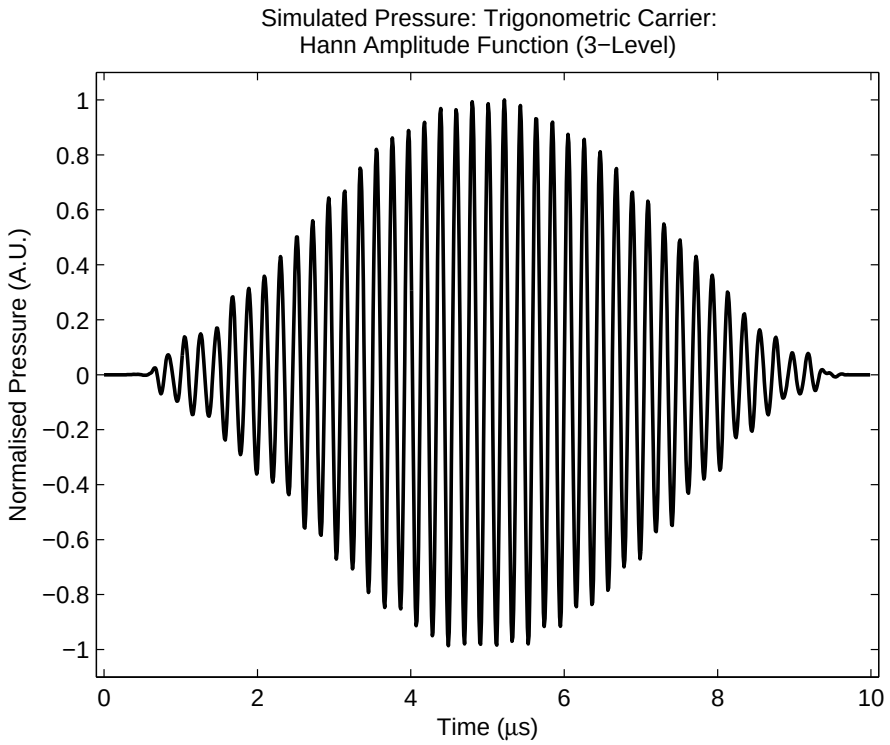

(b) Trigonometric Carrier

Figure 5.22: Comparison between simulations of three-level triangular based comparisons vs. trigonometric carrier. Hann window function applied

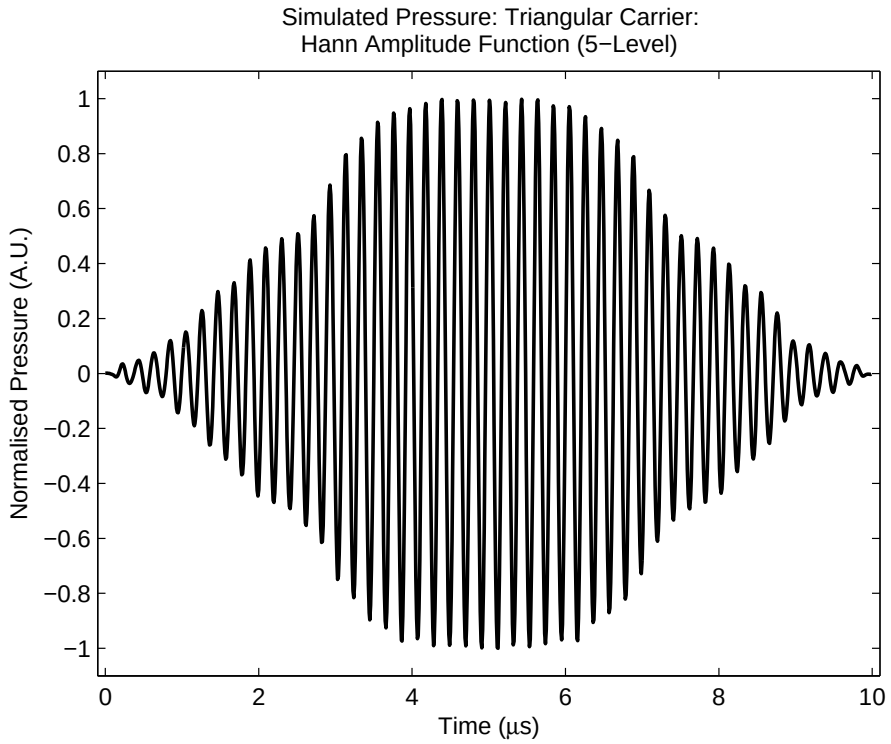

(a) Triangular Carrier

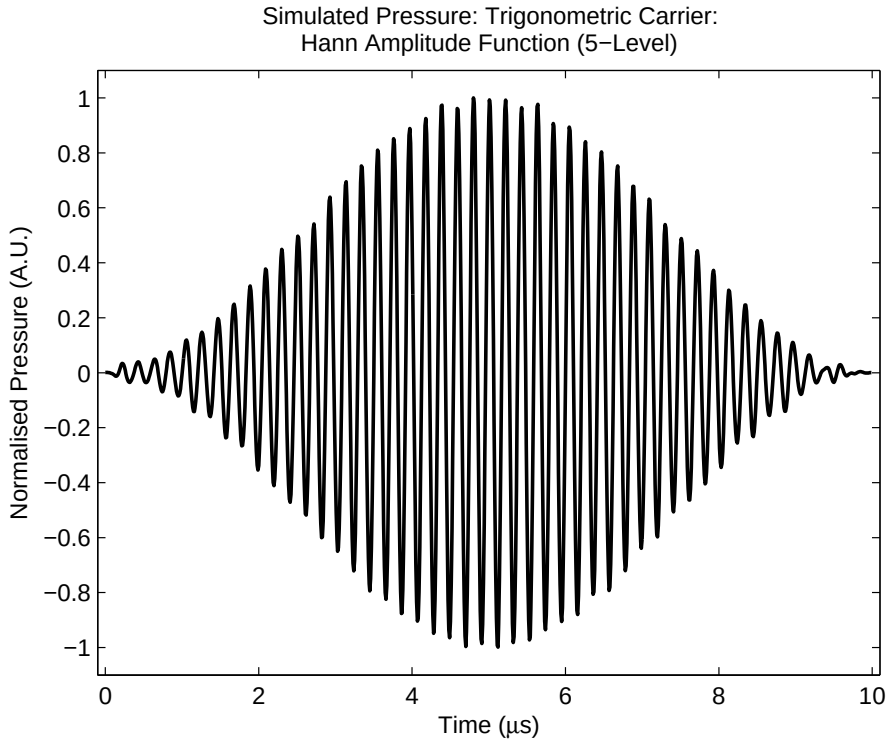

(b) Trigonometric Carrier

Figure 5.23: Comparison between simulations of five-level triangular based comparisons vs. trigonometric carrier. Hann window function applied

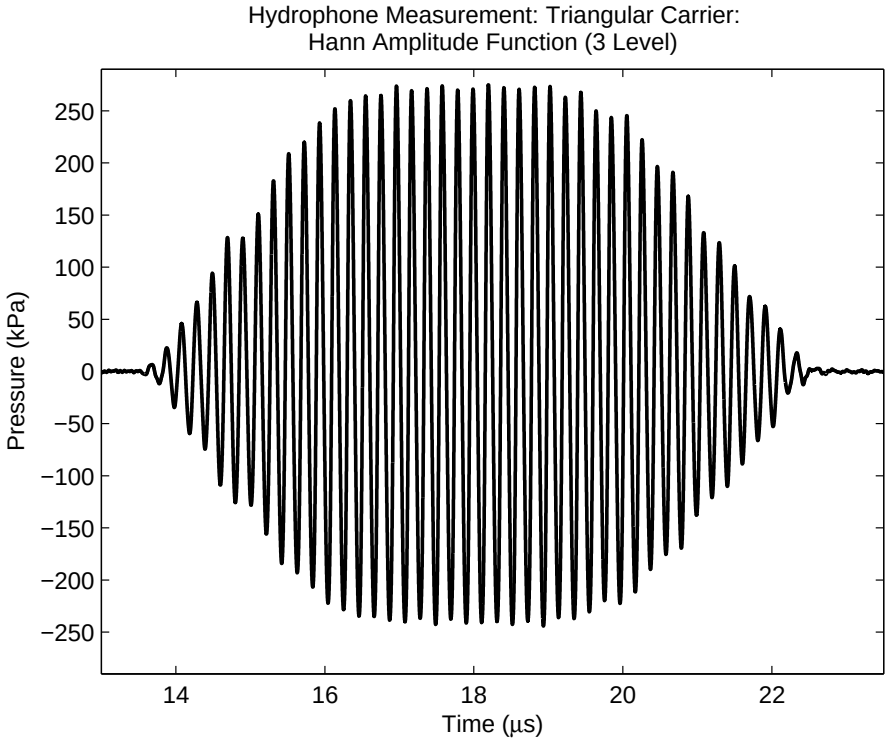

(a) Triangular Carrier 3-level

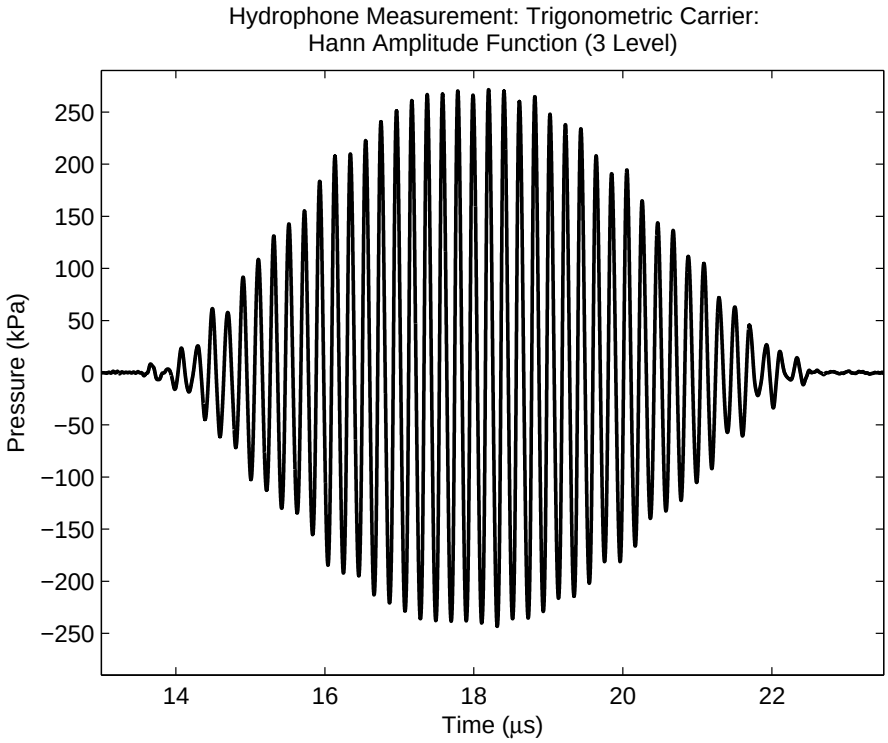

(b) Trigonometric Carrier 3-level

Figure 5.24: Comparison between experimentally obtained three-level triangular based comparisons vs. trigonometric carrier. Hann window function applied (single acquisition)

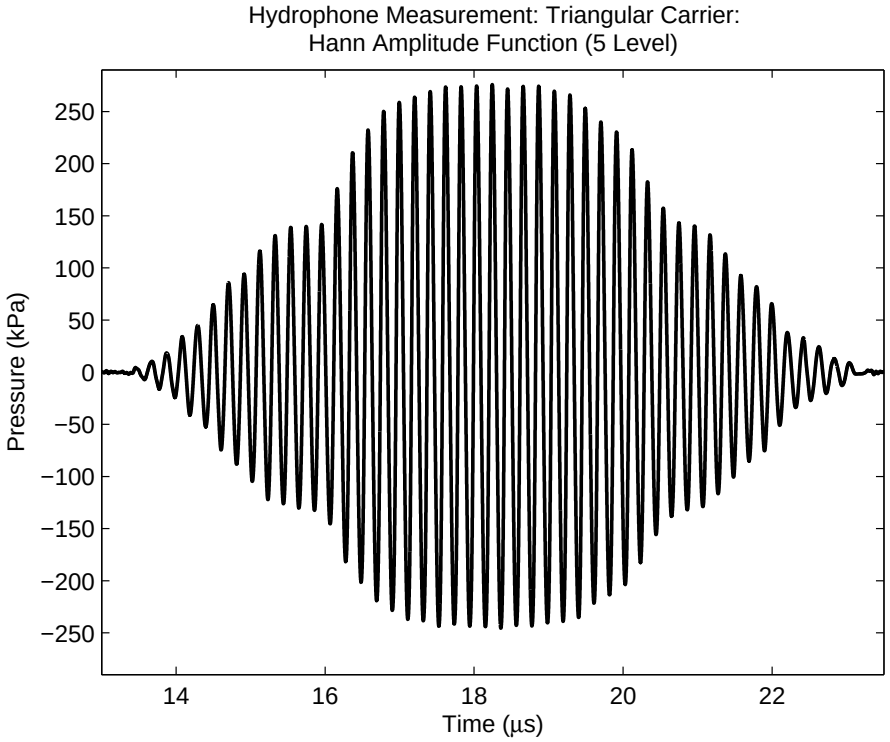

(a) Triangular Carrier 5-level

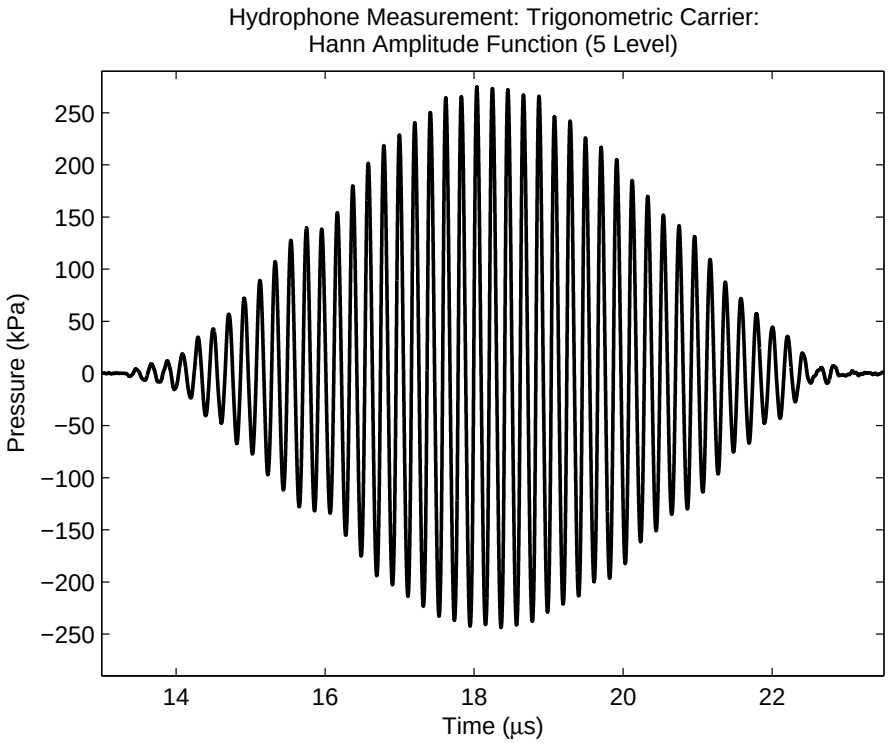

(b) Trigonometric Carrier 5-level

Figure 5.25: Comparison between experimentally obtained five-level triangular based comparisons vs. trigonometric carrier. Hann window function applied (single acquisition)

In order to provide quantitative measurements to accompany qualitative observations, each of the simulated cases were compared using the normalised root mean square deviation between an ideal 'analogue' case, and each of the PWM cases using triangular (conventional) or trigonometric (proposed) carriers. The normalised root mean square deviation or error provides a percentage mean deviation between the two pressure signals on a sample by sample basis, and is defined by equations (5.38) and (5.39).

$$RMSD = \sqrt{\frac{\sum_{i=1}^{k} \left(x_1[i] - x_2[i]\right)^2}{k}} \tag{5.38}$$

$$NRMSD = \frac{RMSD}{x_{\text{Max}} - x_{\text{Min}}}\% \tag{5.39}$$

Results of the comparison are shown in Table 5.1. Particularly of note is that the trigonometric error cases are never above 2% root mean square error, whilst every triangular carrier case is above 2% root mean square error. Indeed it can be seen that when comparing the use of the three-level trigonometric encoding case and the five-level triangular case, the five-level trigonometric case achieves closer approximation to the ideal. What is also noticeable is that the five-level trigonometric case has less than 1% normalised root mean square error for each of the amplitude functions tested.

Note that quantitative comparison between simulated and experimentally measured waveforms is more difficult to obtain due to differences in phase and sampling. The normalised root mean square metric used on the simulated cases operates on a sample by sample basis, and therefore is not a time invariant process. It is evident from the Figures shown previously that the experimental cases match closely with the simulated cases.

	Normalised Root Mean Square Deviation (%)		
Amplitude Function	Linear	Triangular	Hann
Triangular Carrier 3-Level	4.708	5.029	4.365
Trigonometric Carrier 3-Level	1.057	1.165	0.815
Triangular Carrier 5-Level	2.376	2.497	2.376
Trigonometric Carrier 5-Level	0.771	0.717	0.662

Table 5.1: Quantitative measurements of pressure simulations using triangular (conventional) and trigonometric (proposed) PWM carriers using normalised root mean square deviation (NRMS)

5.4 Array Apodization with Pulse Shaping

Figures 5.14 to 5.25 have provided examples of successful arbitrary waveform generation using the proposed PWM carrier-comparison method with a trigonometric carrier. This method can also be used for power control from an element, as well as pulse shaping. Another example technique is known as apodization. Apodization increases the sensitivity of the main beam emitted from an aperture, by suppressing energy at the sidelobe. High sidelobe energy is present when the emitting aperture has unity amplitude across all elements (described as a rectangular aperture). Decreasing the amplitude of pulses at the extremities of the aperture reduces sidelobe interference at the cost of mainlobe widening, which can be tolerated.

Hoen [135] and Cincotti [136] described a method of switched-mode array apodization by control of single cycle pulse widths, mapped according to the area within the square wave pulse. A patent by Haider [132] described a thresholding method specifically for generating pulse sequences for apodization. The method described by Haider [132] however did not demonstrate pulse shaping (amplitude modulation throughout the duration of the pulse), and apodization across the array. Figure 5.26 shows a plot demonstrating such a case, with PWM excitation sequences created for apodization of an array transducer and also shaping of the transmitted pulse. In this example a 5-cycle, 5-MHz Gaussian windowed pulse has been designed with Gaussian apodization across an aperture of 48 elements Figure 5.26(a). Experimental data obtained using the UARP system and a 0.2 mm hydrophone (Precision Acoustics, Dorset, UK) shows the applicability of

PWM for array apodisation when compared with a rectangular aperture (no array apodization) in Figure 5.26(b). Interpretation of the Figure shows decreased pressure sidelobe, and increased mainlobe width as a result of applied array apodization. Note that with reference to Chapter 4 the same level of phase quantization has been used.

The proposed PWM method enables shaping of pulses and output amplitude control using switched excitation as demonstrated in Figures 5.17 and 5.26. The PWM method described can be used to modulate arbitrary pulse sequences by altering the designed amplitude function in accordance with the desired pulse shape. Pulse shaping is particularly important in coded imaging where it is advantageous to taper the pulse to suppress sidelobe.

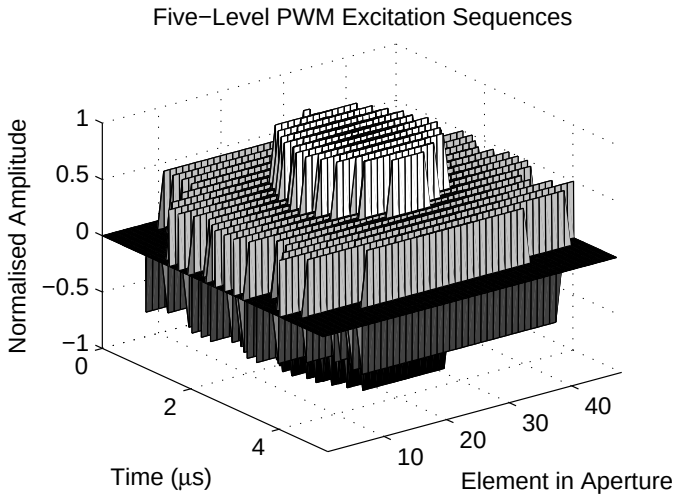

(a)

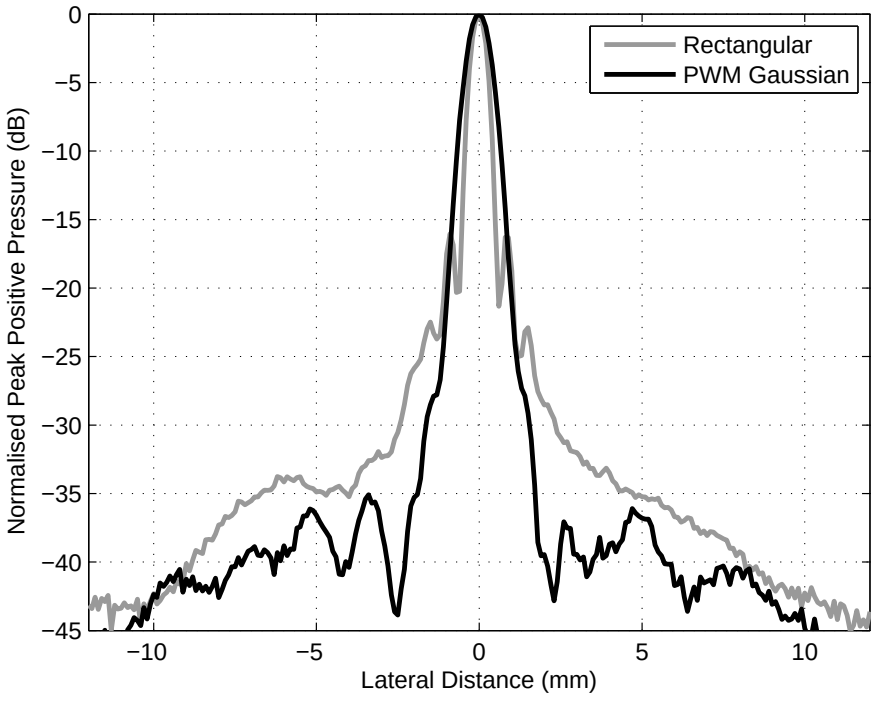

(b)

Figure 5.26: Example of PWM encoded sequences showing tapering in time and apodization across the array. MOSFET drive sequences are encoded for 5 MHz, 5 cycle Gaussian windowed excitations, with Gaussian array apodization over an aperture of 48 elements, Figure 5.26(a). Experimental measurements (50 averages) show decreased sidelobe levels in the lateral beam plot at 30 mm focus when compared with a rectangular aperture with applied time tapering using the PWM strategy, Figure 5.26(b).

5.5 Effect of Sampling Frequency

The proposed PWM method uses digitally generated carriers and amplitude functions to modulate pulse-widths. As a consequence it is appropriate to discuss the effect of the sampling frequency on the transmitted pressure, and pass comment on some interesting observations. Firstly, it can be seen that although the carrier comparison scheme can provide excellent accuracy when compared with an analogue waveform (see Table 5.1), such accuracy may not be present for all cases. Figure 5.27 shows such a case, a 5 MHz 20 μs tone-burst sampled at 100 MHz, with the linearly increasing amplitude function applied. Notice that instead of the expected smooth linearly increasing amplitude function seen in previous cases (at 4.8 MHz) there is in fact a discrete number of steps.

If the sampling frequency is reduced to 97 MHz (the nearest lowest prime number) then the desired amplitude function can be seen as shown in Figure 5.28. This unsatisfactory effect shown in Figure 5.27 occurs when the ratio between sampling frequency and fundamental frequency is equal to any even order integer. This ratio is the same as μ previously used in (4.14) when discussing phase quantization in Chapter 4.

$$\mu = \frac{fs}{f} \qquad \mu \in \mathbb{N} : \mu/2 \in \mathbb{N} \tag{5.40}$$

This behaviour is mostly observed for long sequences, where the number of cycles exceeds the number of PWM states, and the value of μ is as defined by (5.40).

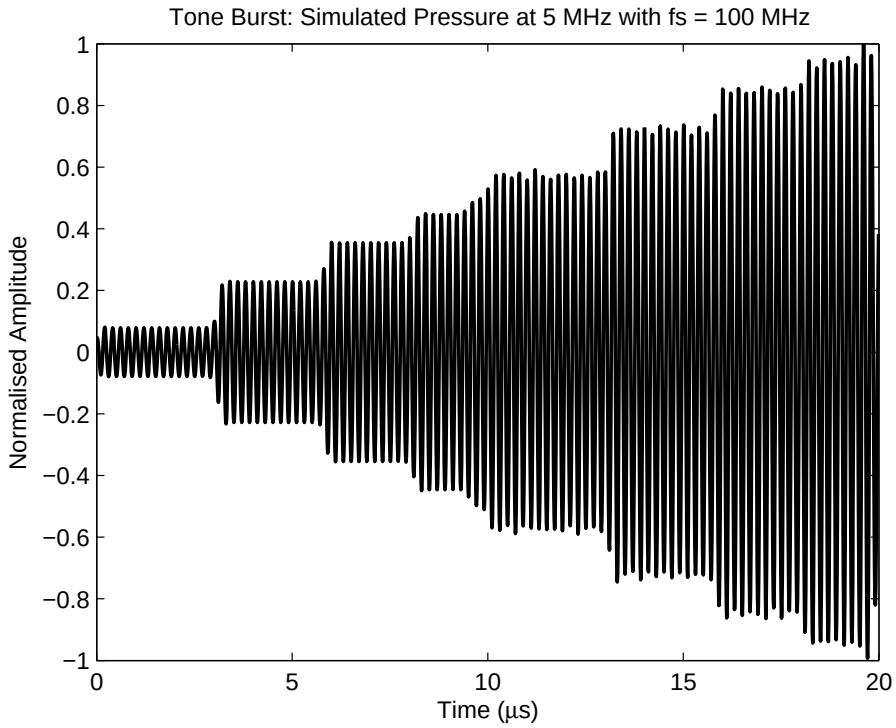

Figure 5.27: Shaped tone burst signal showing even integer relationship between fs and f

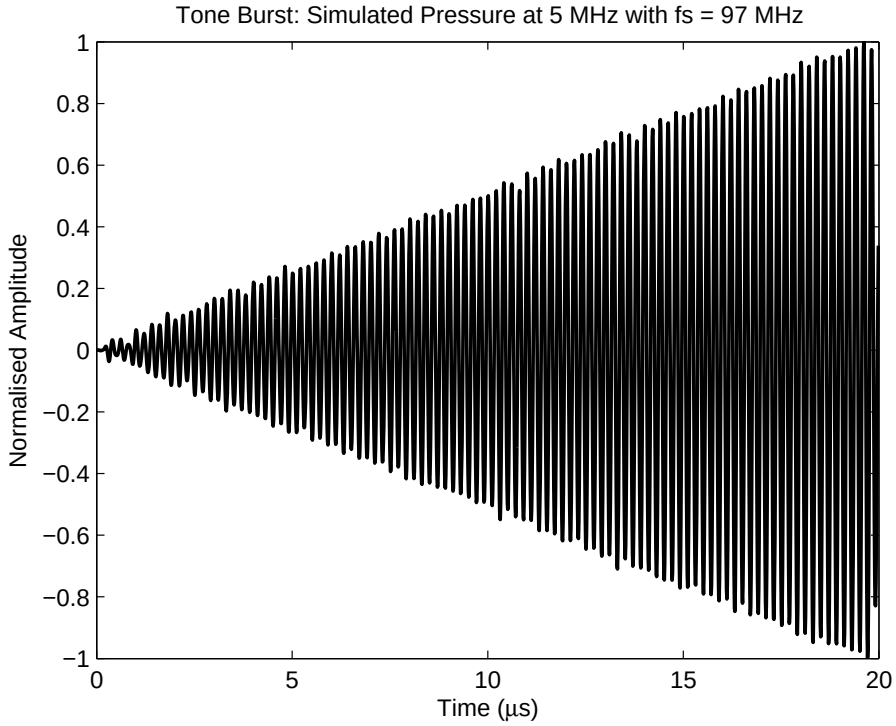

Figure 5.28: Shaped tone burst signal showing non-integer relationship between fs and f

5.6 Comparison with Sigma Delta Modulation

The introduction to this Chapter briefly mentioned a sigma-delta modulation method of switched mode operation. Such a method was also discussed in the review of amplifier classes in Chapter 3. Huang and Li [130] proposed the use of a sigma-delta algorithm for LFM chirp coded sequences, which require arbitrary waveform capability, and also frequency modulation. Sigma-Delta relies on rapid switching between two states and is similar to PWM however is classed as pulse-density modulation. A sigma-delta stage consists of an integrator, and a quantizer [130]. Switching rapidly increases noise, requires fast-acting MOSFETs and also increases power consumption. A comparison between a first-order sigma-delta for Ultrasound as reported by [130] and the proposed fundamental trigonometric carrier comparison method (described in this Chapter) is shown in Figures 5.29 to 5.31. Note that in both cases, waveforms have been sampled at 100 MHz as described in the proposed method. In each figure the desired pressure output is the dashed line, whilst the switching signal is the solid line. It can be seen that for the proposed PWM method, a single positive and negative switch per half cycle is required for a single switching event. In comparison with the sigma-delta method, multiple commutations are seen.

Following the sigma-delta modulation in [130] was a 'code-tuning' stage which was an iterative algorithm, using the impulse response of the transducer to tune for best performance. The advantages of the carrier-comparison method presented here is that it does not require a tuning stage, as the effect of the transducer has already been considered in the encoding stage. Also, the number of commutations can be reduced so that switching is at the fundamental rate.

The authors stated that the proposed sigma-delta method is advantageous as it utilises the benefits bipolar square-wave pulse circuits to generate arbitrary waveforms. Chapter 6 seeks to extend the PWM method for arbitrary waveform generation in chirp LFM coded imaging.

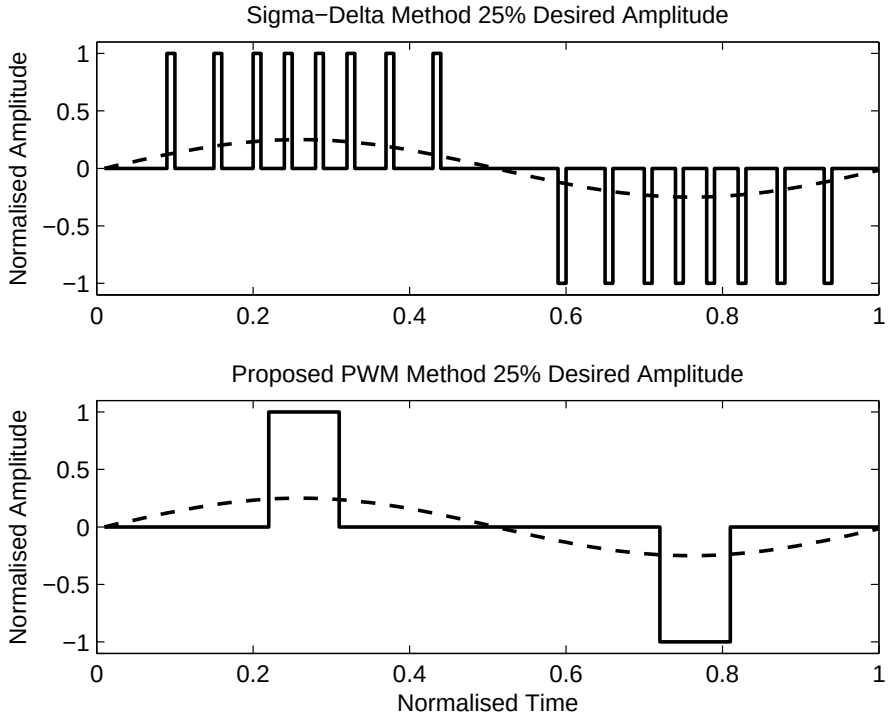

Figure 5.29: Comparison with Sigma-Delta modulation 25% amplitude

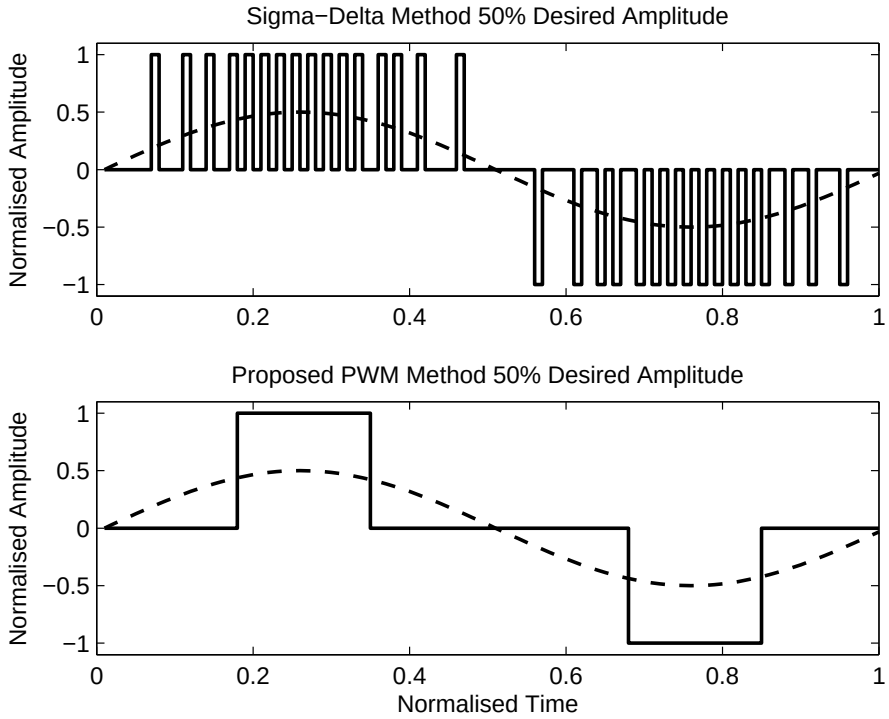

Figure 5.30: Comparison with Sigma-Delta modulation 50% amplitude

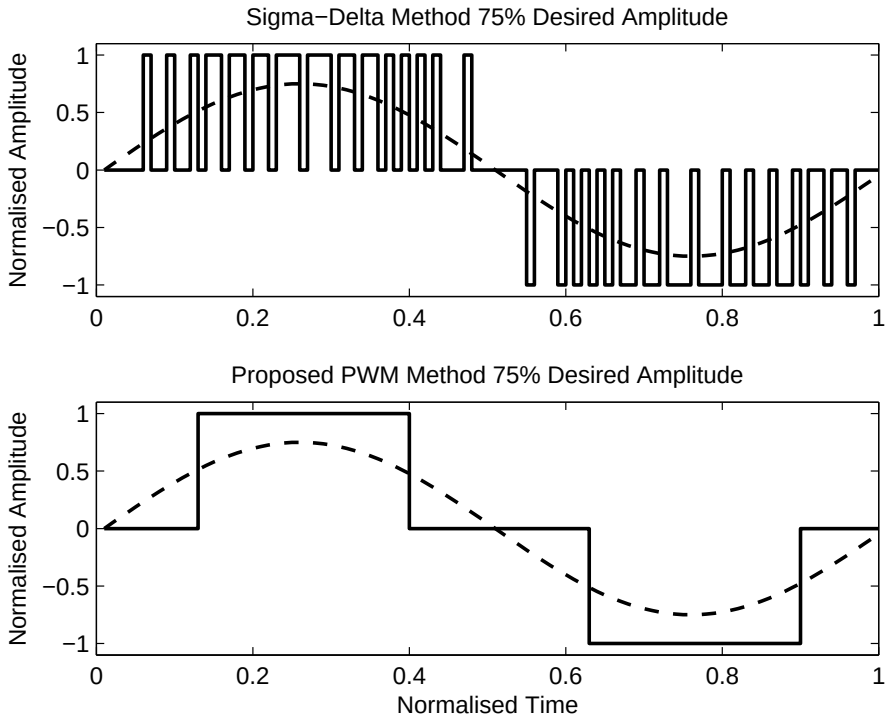

Figure 5.31: Comparison with Sigma-Delta modulation 75% amplitude

5.7 Conclusions

This chapter has demonstrated a trigonometric carrier-comparison, pulse-width modulation method for encoding multi-level switched-mode trigger signals. These signals control a switched-mode, class-D type, output stage as discussed in Chapter 3. Conventional carriers such as triangular or sawtooth rely on rapid switching, often at 10 or 20 times greater than the fundamental frequency. For digital PWM implementations this places a burden on sampling frequency, especially at ultrasound frequencies in the MHz range. Increasing the frequency of operation of switched-mode devices also increases switching losses. Switching at approximately fundamental frequency ensures a reduction in switching losses and sampling frequency, however conventional triangular carriers do not encode pulse widths optimally. This chapter has shown through Fourier analysis and simulated and experimental comparison that the carrier requires a different form, in fact a rectified trigonometric carrier. This carrier modification has been shown to successfully encode square wave signals that provide the expected pressure waveform once filtered by the transducer.

Chapter 6

Switched-Mode PWM Method for Ultrasound Coded Imaging

6.1 Introduction

Coded imaging is an established technique of increasing SNR in ultrasound systems and has been well discussed in previous literature such as [137], [138], [52] and set of papers [139], [140], [141]. In general, the technique relies on the correlation between the transmitted pulse and received signal to distinguish between low intensity echoes generated by weak scatterers and the ambient noise floor. Most often, linear frequency modulated (LFM) signals are chosen over phase modulated signals as they do not require multiple transmissions and do not contain abrupt changes in phase [140]. In the case of frequency modulated signals, the embedded 'code' is the rate of the increase (or decrease) from a start frequency to the stop frequency, over time. At the receiver, a 'pulse compression' filter is necessary to detect the coded signal and indicate correlation or a matched response. The pulse compression filter is also known as a matched filter. One optimal design for the matched filter is to use the inverse (or time-reversed, complex-conjugate) of the transmitted sequence [139], [140]. Tapering of the excitation pulse and applying a window to the filter can also provide additional benefits, as the nature of the taper or window function can offer gains in SNR at a cost of decreased axial resolution. This chapter aims

to extend the trigonometric PWM carrier comparison method for LFM chirp coded ultrasound imaging, and demonstrate the efficacy of the multi-level PWM discussed in the previous Chapter to accurately describe a number of tapering functions, and advantage over conventional pseudo-chirps [86].

6.2 LFM Chirp Coding

6.2.1 Linear Frequency Modulated Chirp Design

Digitally generated LFM signals as described by Misaridis and Jensen in [140] (equation (3)) are defined as

$$s(t) = a(t) \cdot \exp\left\{ j2\pi \left[\left(f - \frac{B}{2} \right) t + \frac{B}{2T} t^2 \right] \right\} \quad \text{with } 0 \leq t \leq T \tag{6.1}$$

where B is the signal bandwidth, $a(t)$ is an applied window function or taper and the LFM signal sweeps from $f_{\text{START}} = f - B/2$ to $f_{\text{STOP}} = f + B/2$ in time T, at rate $R = B/T$ [140]. This equation is a more convenient expression, as it defines an LFM signal without the use of negative time. For signal detection, an appropriate pulse compression or matched filter is designed. A conventional matched filter is the complex conjugate of the signal $s(t)$, $s^*(t)$. Thus the pulse-compressed output is the auto-correlation of the signal, in the ideal case, which can be expressed as described by [140]

$$R_{ss}(\tau) = \int_{-\infty}^{\infty} s(t)\, s^*(t+\tau)\, dt \tag{6.2}$$

Note that in the practical case the output will be a cross-correlation between the matched filter and the received signal after propagation. The pulse compression filter demodulates the signal, with the output approximating a sinc function [140]. If no additional tapering or weighting is applied then the signal is said to have a rectangular window function. Rectangular window functions cause sidelobes at approximately -13.2 dB below the peak

in the correlation output response as discussed by numerous authors, most prominently [142]. Applying a window function to the match filter design, by altering $a(t)$ successfully reduces near sidelobe at a cost of widening the mainlobe. If a rectangular windowed signal is transmitted, and a window function applied to the match filter (now called a 'mis-matched filter') near sidelobe levels can be estimated as reported in [142], [143], [144].

The performance of the pulse compression system is also defined by the time-bandwidth product TB. For large TB values (i.e. exceeding 100) the performance of the system is similar to that discussed in coded radar literature [145]. In ultrasound however, the TB product is limited by the transducer's bandwidth, and the signal duration. It is therefore unusual to have very high TB products when imaging closely spaced targets, as their matched filter responses will overlap in time and frequency as discussed in [146]. Also, long duration sequences restrict imaging of targets very close to the transducer. For LFM signals with low TB products and rectangular window functions, their amplitude spectrum contains significant Fresnel ripples. These ripples cause distortion in the pulse compressed output referred to as far sidelobes that are not removed by the windowed matched filter. Indeed as reported by Misaridis "Amplitude tapering is the most efficient way to reduce the Fresnel ripples of the spectrum, if the power amplifier allows control of the transmitted pulse rise time" [140], and as reported by Behar *et al.* "the effectiveness of an excitation/compression scheme depends on the combination of the amplitude taper and the filter weighting" [134].

In this work, tapering of a frequency modulated excitation can be achieved by using the PWM strategy previously discussed, but with extension for use with LFM signals.

6.2.2 Windowing and Tapering Functions

The optimum for pulse compression is to taper the excitation signal to reduce Fresnel ripples and far sidelobes, and design a weighted matched (mis-matched) filter to reduce near sidelobes. When this is the case, the expected sidelobe level (ignoring the effect of the transducer) can be estimated by considering the frequency response of the product of

the two time domain windowing functions. This differs from expected values reported in [142], [143], [144] and can also be affected by the TB product.

6.2.3 Swept-Frequency Level-Shifted Carrier-Comparison Method

The previous sections discussed generation of PWM sequences for amplitude control of single frequency tone-burst signals with a carrier-comparison method. The carrier comparison method requires a rectified, scaled and phase-shifted copy of the desired signal to be used as a carrier. Therefore to generate PWM sequences of LFM signals with defined bandwidth it is necessary to apply the same frequency modulation to the carrier signal. This ensures that a single, multi-level pulse per half cycle is generated at the correct position, is symmetrically modulated, and maintains frequency information. The frequency modulated carrier can therefore be seen as an extension of (5.22) and is defined as

$$c(t) = A \cdot |\ \cos(\omega\prime t + \phi)\ | + L \tag{6.3}$$

where $\omega\prime = 2\pi((f - \frac{B}{2}) + \frac{B}{2T})$, with B the bandwidth of the signal. Figure 6.1 shows examples of the frequency modulated carrier arranged for generation of multi-level PWM sequences which can be used with (5.35) according to the following process:

- Generate a frequency modulated signal $s(t)$ of desired duration, centre frequency and bandwidth.
- Define the carrier of same duration, centre frequency, and bandwidth, but with a $\pi/2$ phase shift.
- Scale and level shift the carriers so they are contiguous and describe the range -1 to 1.
- Generate an appropriate excitation tapering function or time window, e.g. Hann, Hamming or Raised Cosine window as described in [142]:
- Create positive and negative versions of the window function.

- Use the sign of $s(t)$ to switch alternately between comparisons of the positive window function to the positive carriers (when $s(t)$ is positive), to comparisons of the negative window function to the negative carriers (when $s(t)$ is negative).

Note that this process is the same process used to generate signals described in Chapter 5.

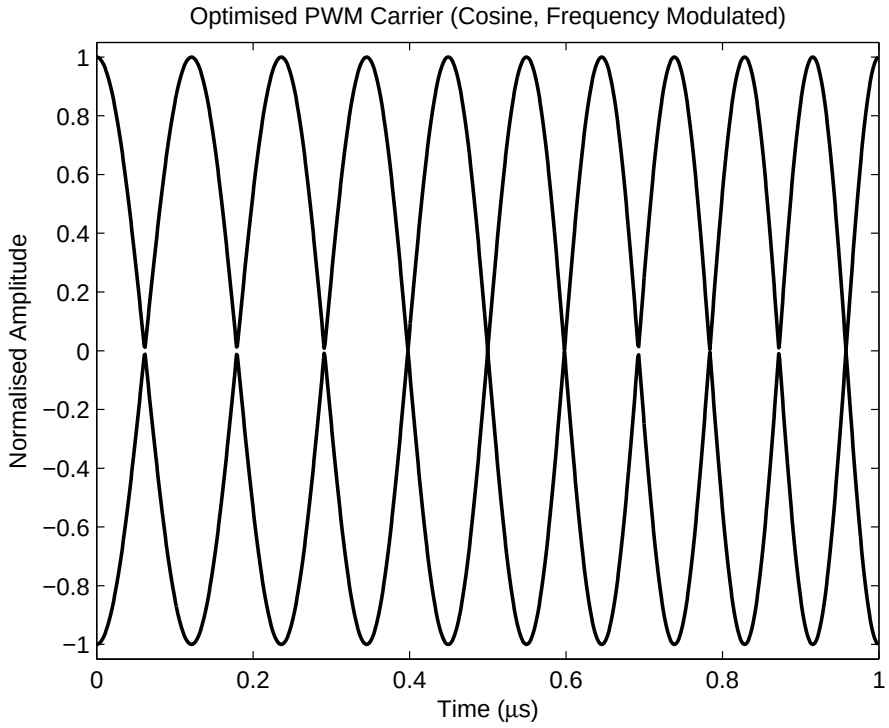

(a) Three-Level Swept Frequency Optimised Carrier

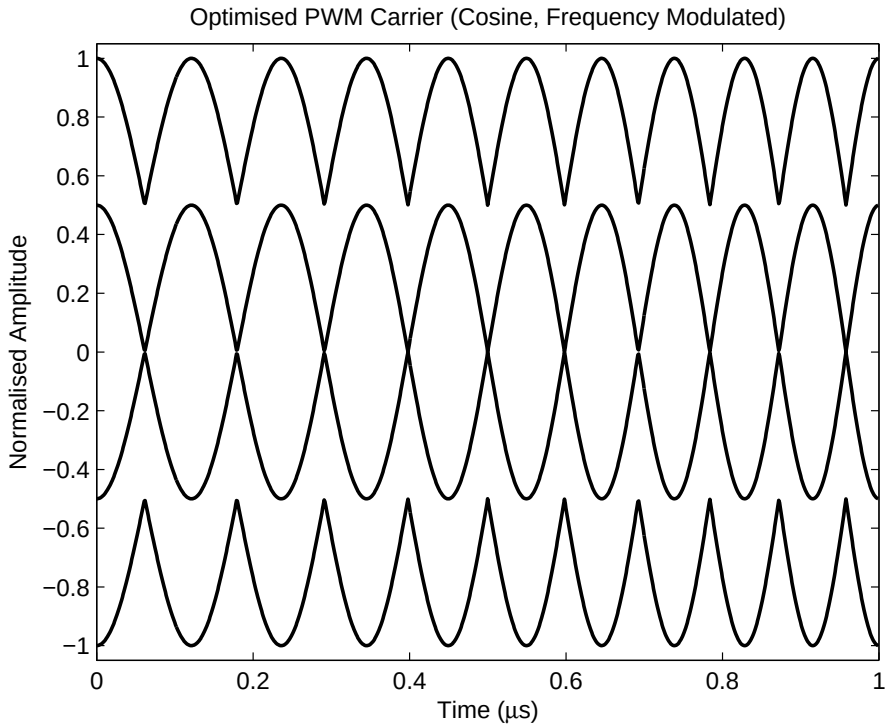

(b) Multi-Level Swept Frequency Rectified Cosine Carrier

Figure 6.1: Linear frequency modulation of the trigonometric carrier

6.3 LFM Chirp Coded Imaging

Examples of coded images using multi-level chirp coded PWM sequences are described in this section. The PWM sequences are encoded with the optimised, frequency-modulated, rectified cosine carrier method described in Section 6.2.3. A wire phantom consisting of five wires separated by 1.27 mm is constructed and submerged in deionized degassed water, and imaged with a medical array transducer as shown in Figure 4.76, and described in Table 4.6 (128 Elements, L3-8, Prosonic, Korea), and the UARP system. Coded PWM signals with applied tapering functions have been designed and used to excite 96 elements of the linear imaging transducer following a standard linear imaging principle as shown in Figure 4.2. An aperture of 48 elements is sequentially moved across the 96 elements, with a focused beam (focal point 60 mm) transmitted toward the wire phantom. The same 48 elements of the aperture are used to receive echoes sampled at 50 MHz. The raw radio frequency data is then interpolated, apodised and beamformed according to standard delay and sum principles to form a single line, focused at 60 mm. A weighted pulse compression filter as described previously is then used for mismatched filtering. Two signals have been used in each case, firstly a fixed-width, square wave pseudo-chirp [85] [86] fluctuating between two levels (referred to as 'Bipolar (Fixed Width)') and secondly a PWM chirp sequence encoded using five levels, with a carrier setup as shown in Figure 6.1(b). Both signals are switched-mode square wave excitations which are subject to the bandpass characteristics of the transducer and have the same weighted mismatched filter applied. Any difference between sidelobe level or mainlobe width between the two signals is therefore as a result of excitation tapering.

Figure 6.3 shows experimentally obtained images of the wire phantom plotted with a 45 dB dynamic range. Each of the five wires appear as bright spots. Only one of the wires appears at the focal point. Other wires that are not in focus appear blurred or spread laterally. The excitation signal used in this case is a Hamming windowed chirp of 5 MHz centre frequency, 2 MHz bandwidth, and 10 μs duration. Both switched excitation sequences (fixed width and width modulated) have been generated with a 100 MHz sampling frequency. The corresponding bipolar and PWM encoded MOSFET gate drive-

signals are shown in Figure 6.2. For the fixed width pulse case shown in Figure 6.3(a),

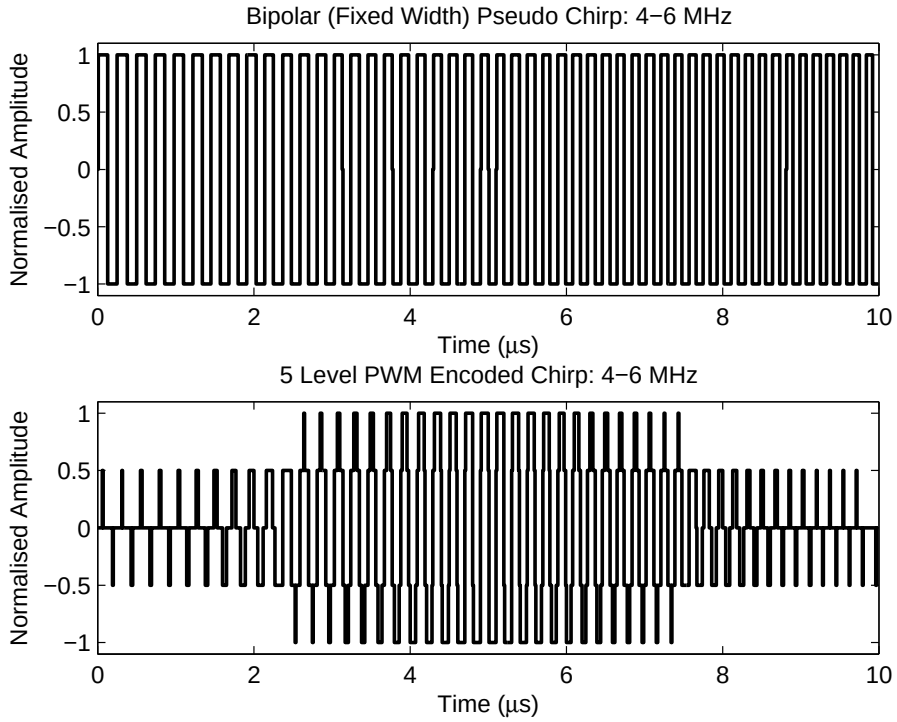

Figure 6.2: MOSFET gate drive signals of the bipolar (fixed width) chirp signal (top) and the 5-level PWM-encoded chirp signal (bottom) 10 µs, Hamming windowed, 4-6 MHz.

high sidelobes are apparent in areas between wires. These appear as a lighter grey regions indicating sidelobes at -30 dB. When compared with the five-level PWM case in Figure 6.3(b), the sidelobes have been reduced, however the wire at the focal point (seen at approximately 65 mm in the reconstructed image) has been lengthened slightly. This is as a consequence of both the excitation taper and the filter windowing function as described in [140].

Sidelobe levels can be more accurately compared by plotting the central line of the image which intersects the five wires. As these images are produced using a single focus, it is appropriate to compare the single wire in the focal region. Figure 6.4 shows simulated and experimental results of the image centre line, showing the wire at the focal point. Simulations are performed in MATLAB using the ultrasound simulation toolbox, Field II [119], [147] as used in previous chapters. Care has been taken to ensure that the simulation environment is as close to the experimental environment as possible, with the measured transducer impulse response used in simulation. Analysis of Figure 6.4 shows

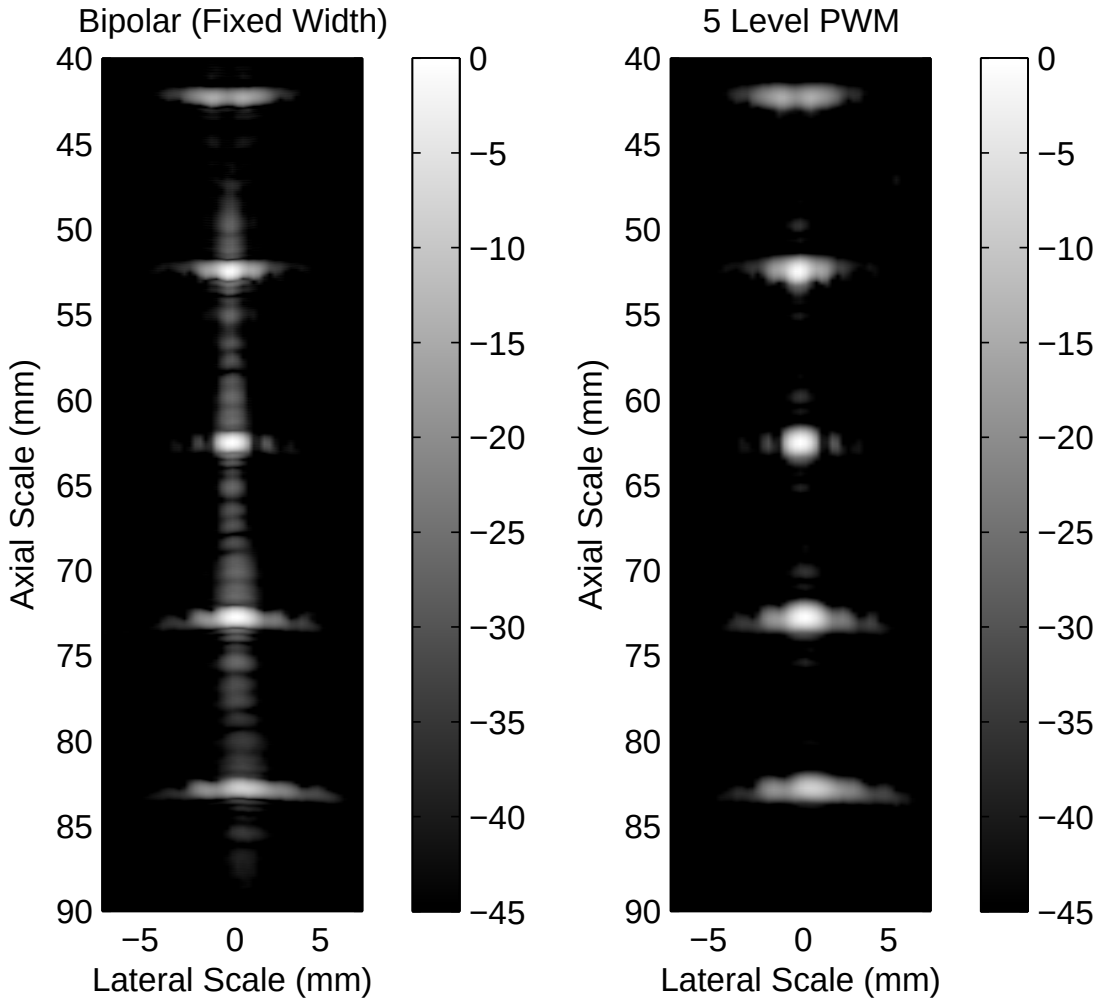

(a) (b)

Figure 6.3: Experimental wire phantom images using a 10 μs Hamming 4-6 MHz signal.

an expected improvement of 11 dB in peak sidelobe level when using the PWM signals according to simulation (-26 dB to -37 dB), with an experimentally observed improvement of 10 dB (-26 dB to -36 dB) in peak sidelobe level. Also noticeable is an increase in mainlobe width for the PWM case as a consequence of the applied tapering function.

For comparison, a convolution of the ideal signals and matched filter has been performed in MATLAB simulation using (6.2). In this case two signals, one with a rectangular taper and a signal with a Hamming taper have been convolved with a Hamming-weighted matched filter. All other signal parameters correspond to the simulated and experimental cases shown in Figure 6.4. In order to ease direct comparison with the experimental cases, Figure 6.5 shows the distance axis instead of time, and with a 50 dB dy-

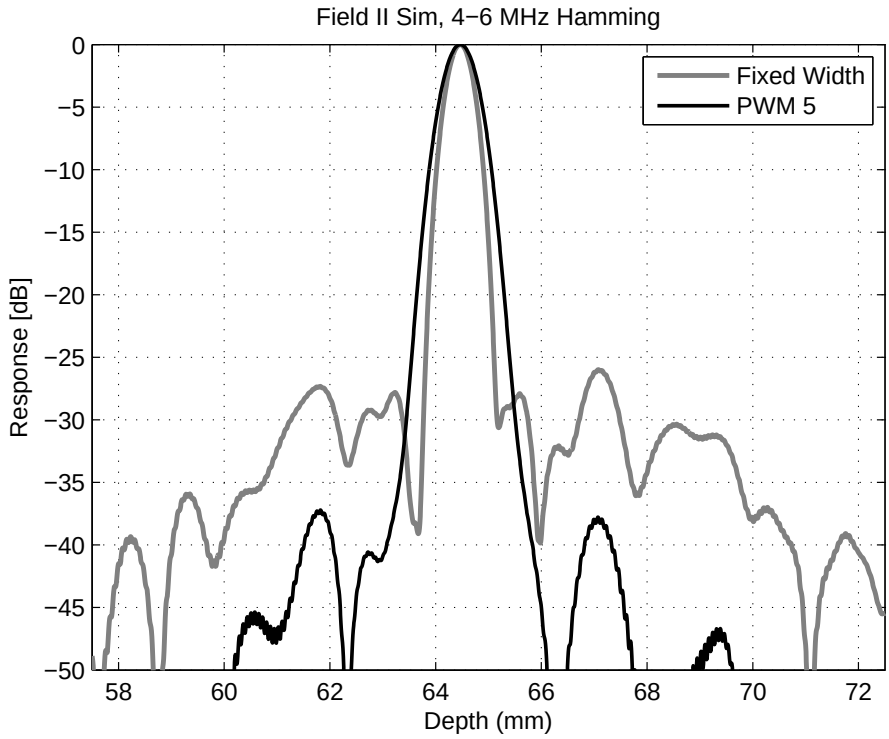

(a) Simulation

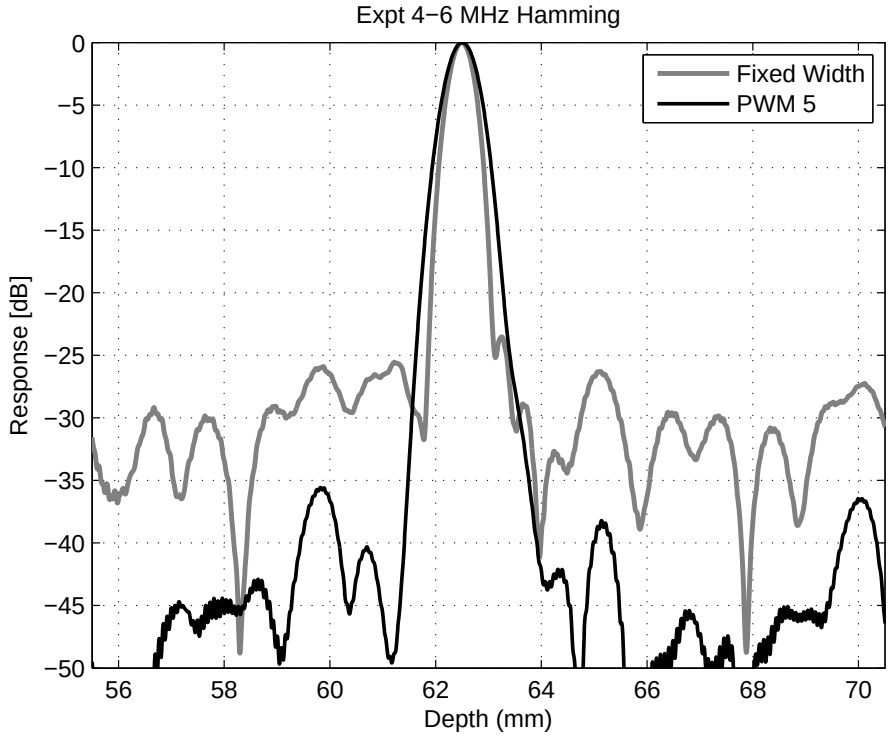

(b) Experimental

Figure 6.4: centre line plotted limited to view a single wire at the focal point. Simulated data in the Figure 6.4(a). Experimentally obtained in Figure 6.4(b).

namic range. Conversion of time to distance was performed with a speed of sound equal to 1482 m/s. It can be seen that for the ideal case using 'analogue' signals the sidelobe levels

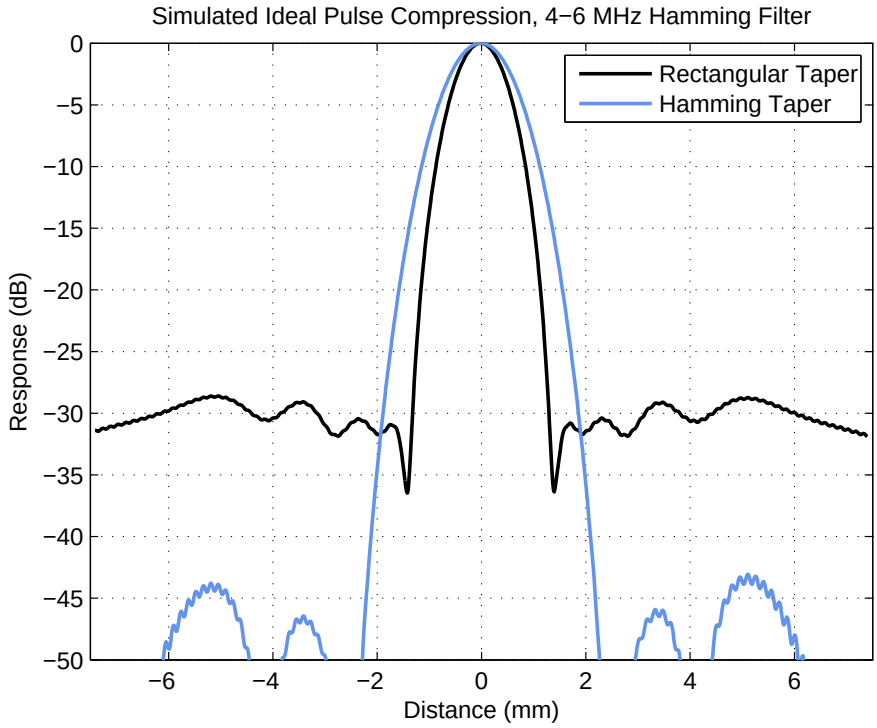

Figure 6.5: Ideal convolution of 4-6 MHz, 10 µs signals with Hamming weighted matched filter. 50 dB dynamic range, distance axis

of the rectangular chirp are centred at approximately -30 dB with the maximum sidelobe value of -28.6 dB. When compared with the ideal Hamming tapered signal through the same Hamming-weighted filter a -15 dB decrease in sidelobe level can be seen, with the peak sidelobe level at -43.8 dB with most sidelobe levels centreed between -46 to -50 dB. Also apparent is the widening of the mainlobe due to amplitude tapering. Comparing Figure 6.5 with Figure 6.4 it can be seen that the rectangular tapered signal is closely matched in terms of expected sidelobe level, and also mainlobe width. However compared with the ideal Hamming tapered case, it can be seen that the mainlobe is wider, and also the sidelobes are further reduced, indicating improved compression. This is reflected in the increase in dynamic range when using the ideal signals (15 dB) than when using the PWM signals (10 to 11 dB) showing a 4 dB difference in sidelobe level. This can be expected however due to the time quantization associated with the sampling frequency of the PWM process, when compared with an approximately analogue solution.

Figure 6.7 shows a second example of experimentally obtained images of the wire phantom. The excitation signal used in this case is a Hamming windowed chirp of 4.8 MHz centre frequency, 2.88 MHz bandwidth, and 10 µs duration. Corresponding MOSFET drive signals are shown in Figure 6.6. This bandwidth was chosen to match the reported bandwidth of the transducer. It can again be seen that the sidelobes in the region between targets are reduced when comparing the fixed width sequence to the PWM sequences.

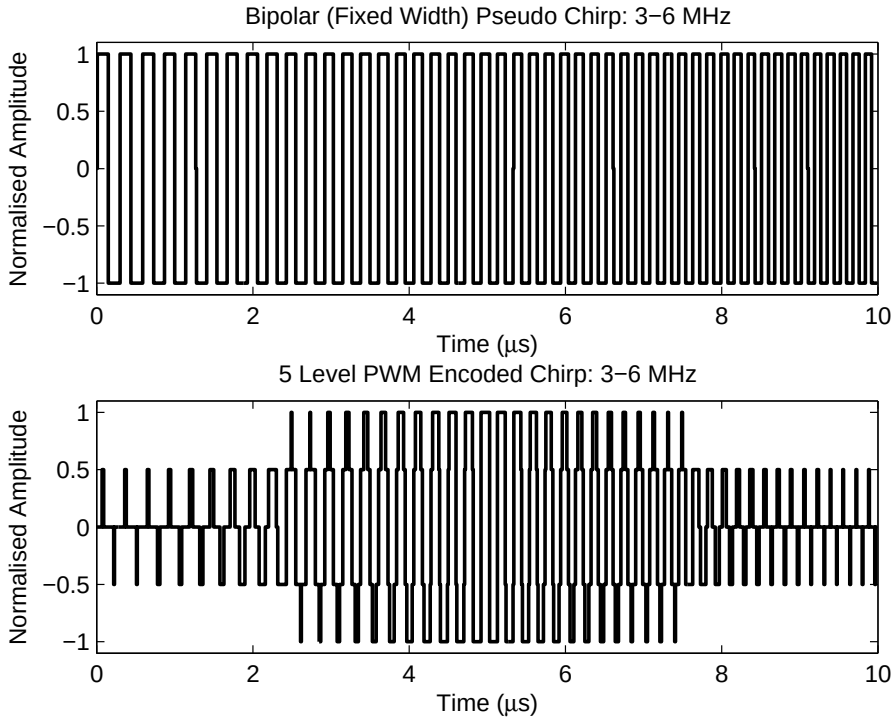

Figure 6.6: MOSFET gate drive signals of the bipolar (fixed width) chirp signal (top) and the 5-level PWM-encoded chirp signal (bottom) 10 µs, Hamming windowed, 3-6 MHz.

Figure 6.8 shows simulated and experimental results of the image centre line, showing the wire at the focal point. In this case simulation predicts an improvement in peak sidelobe level when using PWM sequences of approximately 7 dB (-30 dB to -37 dB), with experimental measurement showing an improvement in 8 dB (-30 dB to -38 dB). Also noticeable, when compared with the previous case in Figure 6.4 is a slight increase in axial resolution as a result of increased bandwidth. In the case of the PWM results, the mainlobe width is increased slightly due to amplitude tapering. Once again this can be compared with convolutions of ideal signals sampled at 100 MHz. Figure 6.9 shows the

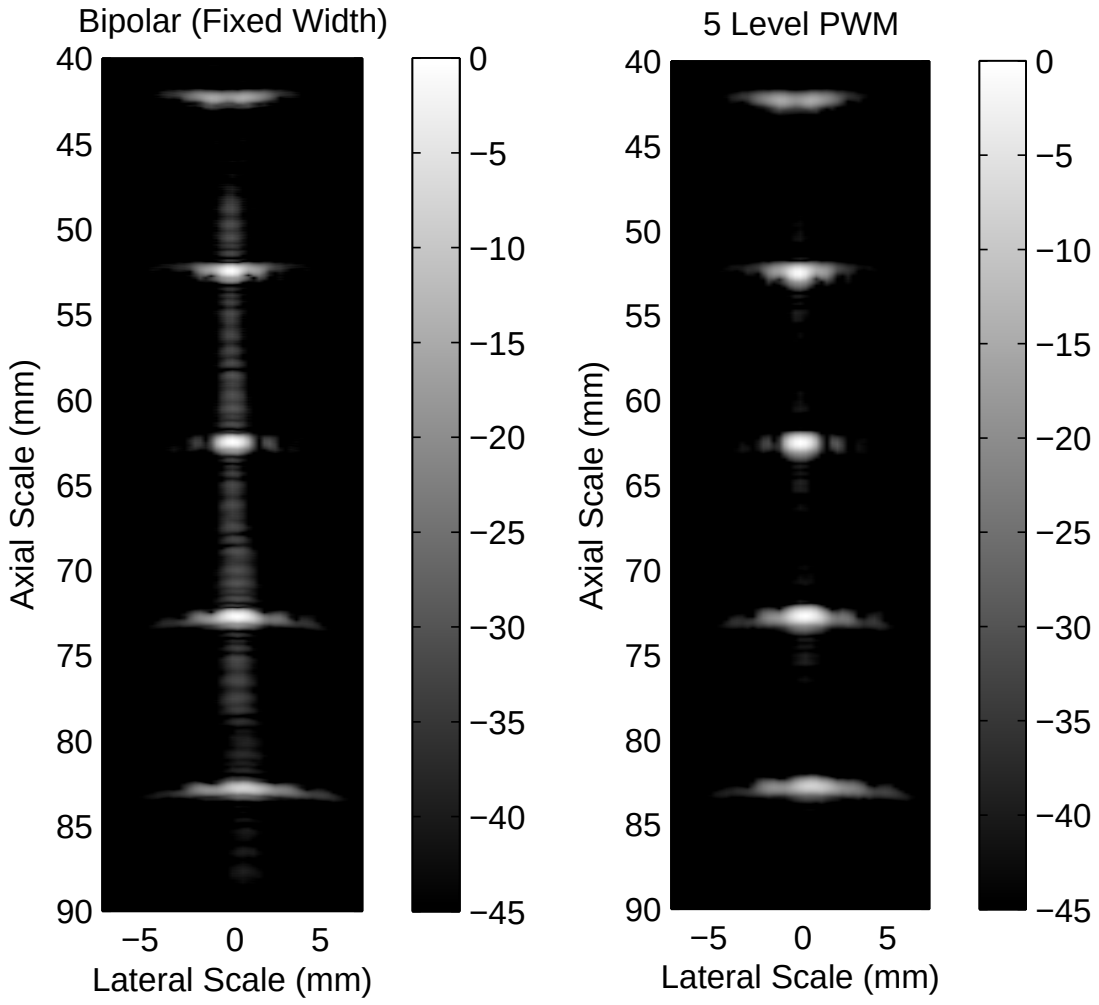

(a) (b)

Figure 6.7: Experimental wire phantom images using a 10 μs Hamming 3-6 MHz signal.

result of convolutions using non-switched-mode signals with rectangular and Hamming tapering functions through a Hamming-weighted matched filter. It can be seen that there is a difference in peak sidelobe level of 13 dB, with peak sidelobe levels of the rectangular and Hamming tapered signals at -32 dB and -45 dB respectively. When compared with the PWM case it can be seen that the ideal signal provides slightly wider mainlobe and lower sidelobe levels due to ideal compression and tapering.

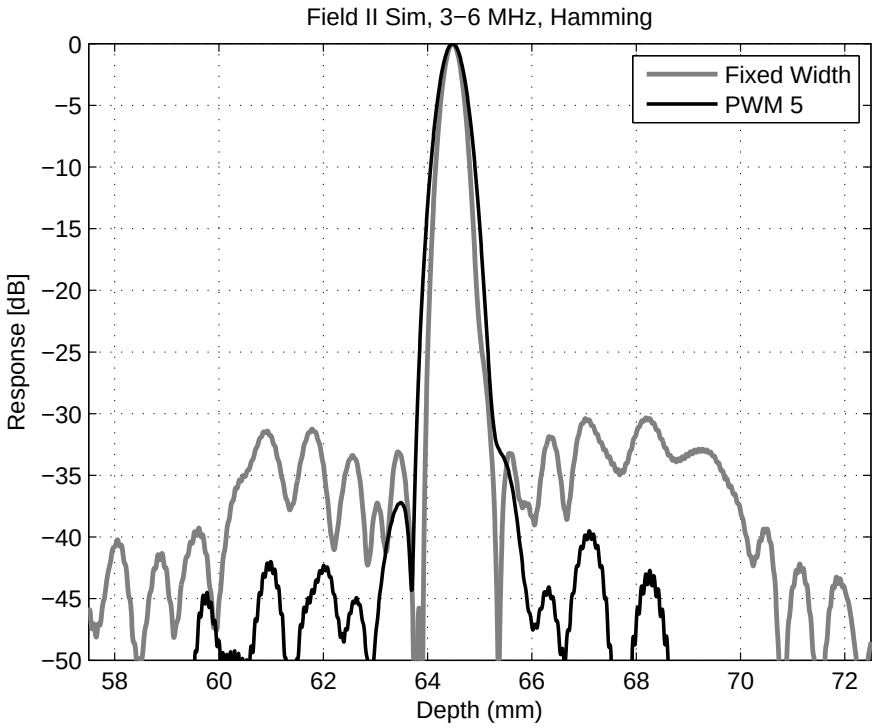

(a) Simulation

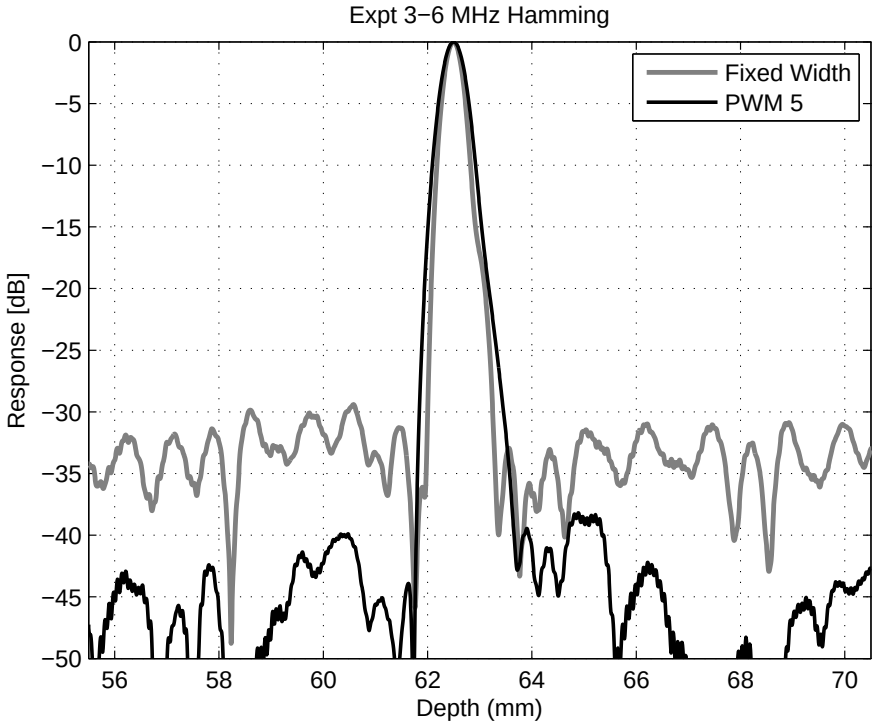

(b) Experimental

Figure 6.8: centre line plotted limited to view a single wire at the focal point. Simulated data in Figure 6.8(a). Experimentally obtained data in Figure 6.8(b).

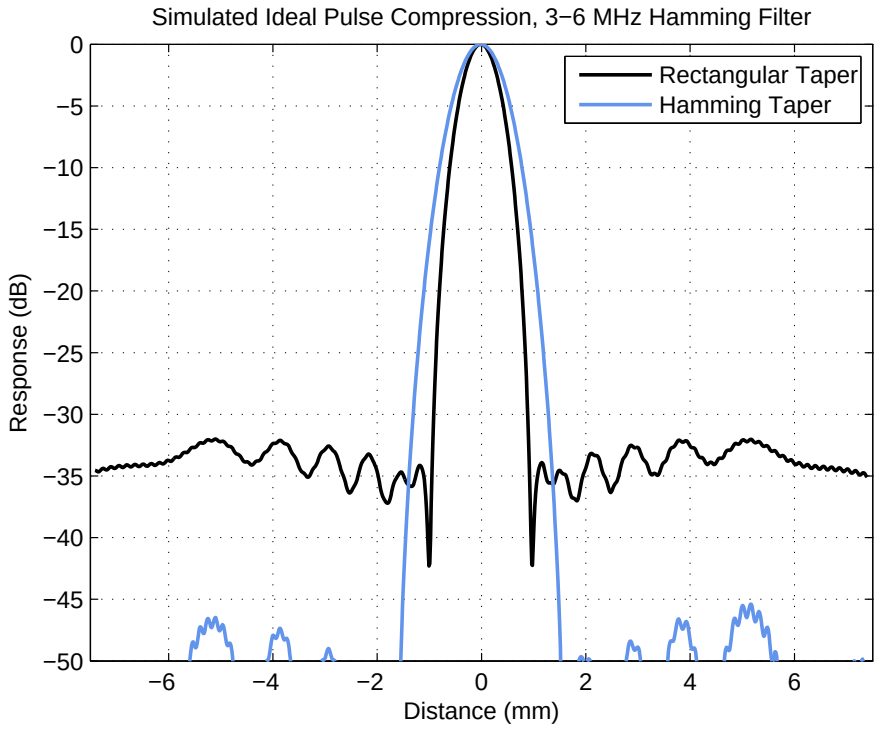

Figure 6.9: Ideal convolution of 3-6 MHz, 10 µs signals with Hamming weighted matched filter. 50 dB dynamic range, distance axis

6.4 Transducer Pre-Distortion

Weighting the pulse-compression filter to generate a mismatch has been shown to reduce sidelobes in the compressed output. however, the transducer, naturally weights both the outgoing, and incoming wide-bandwidth chirp signal with a separate amplitude function derived by its own frequency response. This distorts the envelope of the transmitted waveform as shown in [3].

Furthermore, propagation of the signal in an attenuating medium will cause an apparent frequency shift when received as a function of frequency dependent attenuation. Estimation of the frequency dependent attenuation can be incorporated in the matched filter design, therefore to create a depth-dependent matched filter which matches to an estimated (or measured) new correlation function.

A different proposal is to estimate the effect of either the transducer, or attenuation to pre-distort the transmitted signal by applying a different amplitude function to the chirp signal to compensate. This idea may be particularly relevant to harmonic imaging, where

signals are located at inefficient regions of a transducer, so as to encompass the fundamental and harmonic [3].

References such as [148], [149], [33] have all discussed such an idea, but have used a DAC or AWG with power amplifier as a transmit circuit solution. [3] demonstrated the use of the coded PWM method to apply a compensation weighting for the transducer, to potentially improve harmonic imaging. Figure 6.10 shows a 10 µs, 15% Tukey-windowed, 3-4 MHz chirp signal pre-transducer. Figure 6.11 shows the same signal recorded using a 0.2 mm needle hydrophone (shown in Figure 4.77), showing attenuation at the lower frequency as a consequence of the transducer's bandwidth. The transducer used is shown in Figure 4.76 with details given in Table 4.6. Figure 6.12 shows a pre-distorted chirp signal, with a weighting applied to compensate for the estimated attenuation. This weighting has been calculated using inverse filtering techniques [3]. Figure 6.13 shows the hydrophone measured signal of the pre-distorted chirp. Comparison between Figures 6.11 and 6.13 show that the arbitrary nature of the PWM method can provide solutions in many applications.

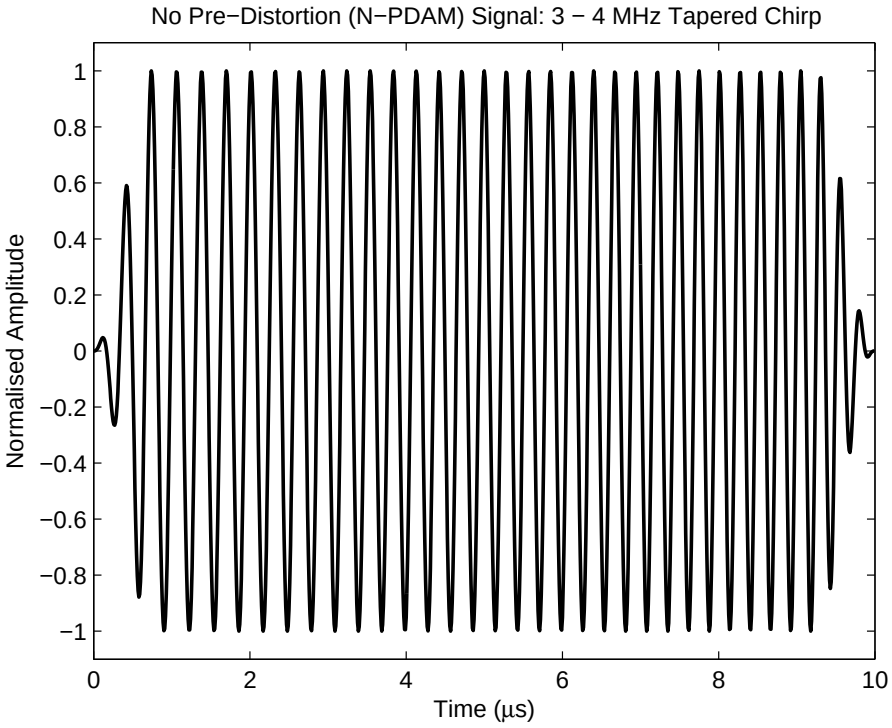

Figure 6.10: Desired 3-4 MHz chirp signal

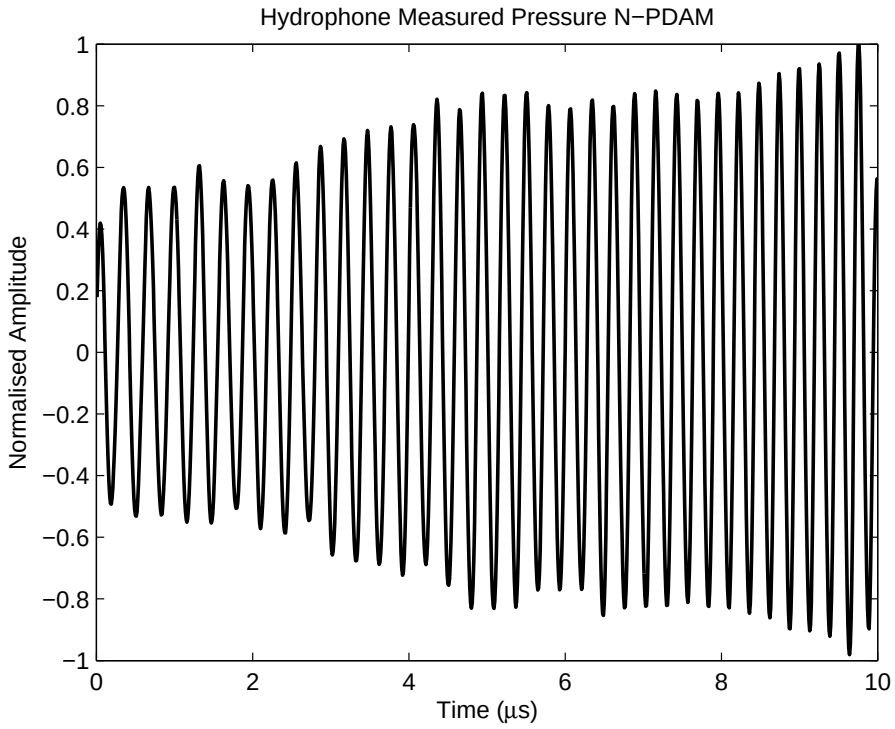

Figure 6.11: Hydrophone measured 3-4 MHz chirp signal through transducer

Compensation for the transducer may also have an effect in therapeutic applications as demonstrated in [150]. For this work the coded PWM method was used to compensate for the impulse response of the transducer, thus delivering approximately constant pressure across frequency. This is advantageous for microbubbles and a technique known as sonoporation, a technique where acoustic signals stimulate microbubbles that vibrate and open non-permanent 'pores' in cell membranes. This technique can be used to increase uptake of therapeutic agents into specific targeted areas using ultrasound. Sonoporation is most effective when largest shear stress is exerted onto the cell membrane. Largest shear stress is generated by a microbubble when it is insonated at it's resonant frequency. A microbubble's resonant frequency varies depending on size. A polydisperse microbubble population will therefore have a range of resonant frequencies. It is therefore advantageous to transmit a signal, such as a LFM chirp, to excite a population of polydisperse microbubbles with a range of resonant frequencies, with a wide-bandwidth signal and at high pressure [150]. Using the PWM method described, equal pressure across frequency can be achieved by using an inverse function of the transducer's impulse response as the desired amplitude function.

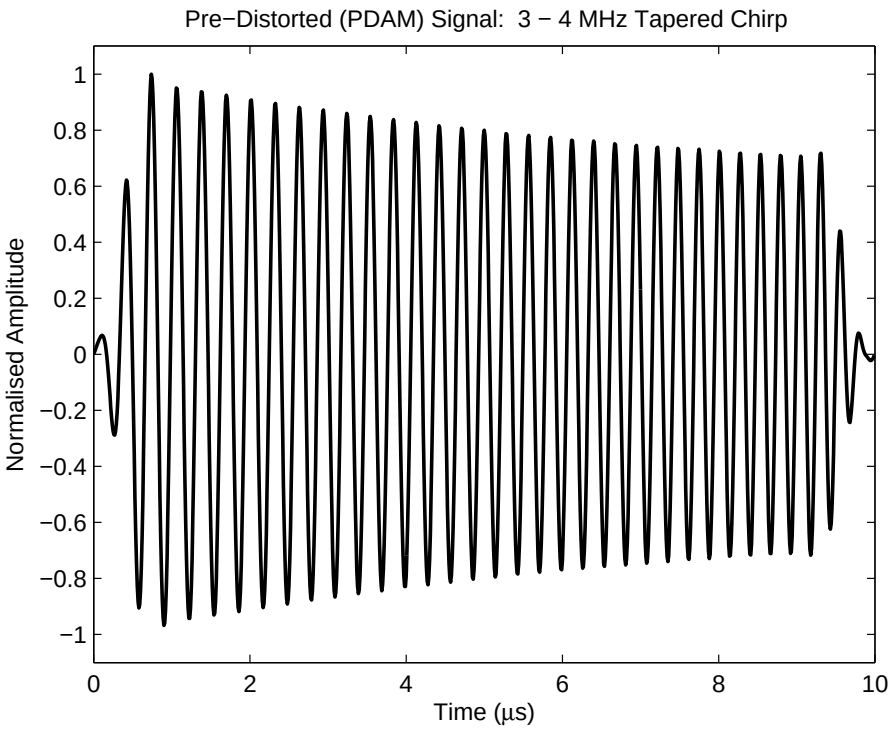

Figure 6.12: Pre-distorted 3-4 MHz chirp signal taking into account transducer response

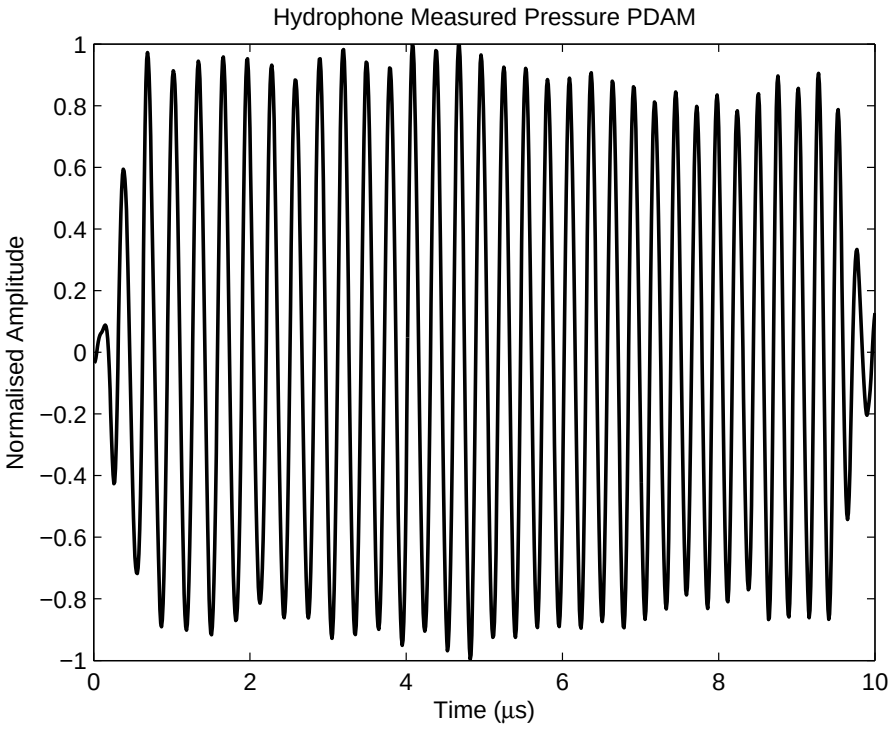

Figure 6.13: Hydrophone measured pre-distorted 3-4 MHz chirp signal through transducer

6.5 Discussion

The PWM method described in Chapter 5 previously demonstrated accurate implementation of tone-burst, windowed signals. With this carrier-comparison method, frequency information was stored within the trigonometric rectified carrier, with amplitude information defined in the modulating wave. The carrier was symmetrically modulated, meaning that the lowest part of the carrier defined the middle of each pulse within the sequence. To generate LFM coded PWM waveforms the carrier must also be frequency modulated at the desired chirp parameters. This ensures that frequency modulation and amplitude coding are encoded. A similar technique was described by Banjanin *et al.* in a patent dated 2006 [151]. However, the carrier comparison method described in this Chapter specifically takes into account the fundamental response of the transducer to modulate widths. Due to the nature of patents the author's method for encoding is not fully disclosed, and merely the form of the waveforms is suggested. The work in this chapter however has derived necessary carrier comparison forms, generate algorithms for encoding and provided experimental comparison between pseudo-chirps and PWM signals using simulation, the UARP system and wire phantom measurements. As a consequence this Chapter provides a much more rigorous explanation of encoding PWM sequences for coded ultrasound imaging.

It is important to know that the carrier itself is digitally sampled. As a consequence, it is a quantized, non-ideal version of an analogue waveform. Note that due to frequency modulation, the effects of even integer sampling as discussed in the previous chapter do not apply, as the value of μ changes over the length of the desired amplitude function. As a consequence this effect can be disregarded in the frequency modulated cases. At low modulation values however, some slight anomalies can be seen at the start and end of pulse sequences. For example, in Figure 6.2. There is a 'missing' positive pulse due to the sampled carrier not intersecting the desired signal. To ensure best performance, a high carrier sampling ratio should be used.

6.6 Conclusions

Frequency modulation and coded ultrasound is a useful technique of improving the SNR of weak signals. For best results however, the technique requires an arbitrary waveform generator that can provide both frequency modulation and amplitude control to taper the pulse. This Chapter has demonstrated a switched-mode method for use with coded imaging. The effectiveness of the switched-mode PWM method has been shown for decreasing 'self-noise' in wire-phantom coded imaging. Also demonstrated is the ability to pre-compensate for amplitude distortion as a result of transmission of a wide-bandwidth signal through a transducer.

A concern of the use of switched-mode circuits however is it spectral content. This is particularly limiting for harmonic imaging, where signal coding is used to improve the SNR of received harmonics. The next chapter aims to address this concern.

Chapter 7

Switched-Mode PWM Method for Ultrasound Harmonic Imaging

7.1 Introduction

Switched-mode signals have high harmonic content [13] [92] [152]. This is due to sharp transients within the square-wave signals generated by switching between two (or more) discrete levels. Harmonic content is a concern, as it introduces harmonic distortion, causes energy to be taken away from the fundamental frequency, and can disturb techniques such as harmonic imaging, a method that relies on excitation spectral integrity. This chapter discusses the impact of undesired harmonic content for ultrasound applications and aims to combine the multi-level switched-mode PWM strategy shown in Chapters 5 and 6 with Selective Harmonic Elimination (SHE) strategies. Evaluation of the main source of undesired harmonic content, the third harmonic, is discussed with a strategy to reduce this harmonic whilst still preserving amplitude control.

7.2 Harmonic Imaging and Harmonic Leakage

Harmonic imaging is an established technique in diagnostic ultrasound and is capable of providing many benefits over conventional fundamental imaging. These benefits include enhanced image resolution (both laterally due to a reduction in beamwidth in the harmonic

beam profile, and axially due to an increased number of waveform cycles, and decrease in waveform duration in the harmonic signal [153]), reduced sensitivity to off-axis scatterers, and improvement in image quality for patients that are described as 'technically difficult' when imaged conventionally [154], [155], [156], as the harmonic increases through propagation, and therefore objects nearer to the transducer are lower in sensitivity. A harmonic signal is defined as a signal that occurs at a multiple of the fundamental [155]. Harmonic signals may be generated in two ways: either by re-radiation from material (e.g. Ultrasound Contrast Agent); or perhaps most commonly, through non-linear propagation in a medium such as water or tissue [155]. Harmonics are generated during propagation as the compression phase causes a change in medium density, due to the medium of propagation not being completely incompressible [155]. As a consequence, the longitudinal velocity changes and the acoustic wave travels slightly faster when the medium has higher density, thus changing the shape of the pressure wave. This effect accumulates over distance, and leads to harmonic generation. As harmonics are generated by the medium under test, they can provide additional information beyond the scope of fundamental signals. For example, as described in a paper by Harput *et al.* [22], signal processing techniques were applied to harmonic signals from tissue and ultrasound microbubble contrast agent in order to differentiate between the two mediums. In this analysis, Harput *et al.* proved that second harmonic signals provided more information about the medium than with fundamental signals, as regions of tissue and contrast agent could be distinguished separately, even though both types of non-linear scatterer provided second harmonic.

A much reported issue in harmonic imaging is the difference in energy between the fundamental and harmonic signals. Furthermore, weak fundamental scatterers generate almost no harmonic signal [155] and require high sensitivity from the imaging system [154]. Other harmonic based methods shown to boost SNR include coded harmonic imaging (as discussed in Chapter 6) and combination of multiple higher order harmonics (termed 'superharmonic' imaging) [154]. Issues surrounding harmonic and superharmonic techniques include insufficient transducer bandwidth and low SNR of the received harmonics [157]. The low SNR of harmonic signals may also be compounded by

harmonic leakage effects or transmission of harmonics from the excitation signal [157]. Harmonic leakage describes conditions where undesired spectral content is present in (or leaks into) the frequency band of interest, as discussed in a comprehensive review by Shen and Li [152]. For example, harmonic signals may already be present in the ultrasound system, as opposed to being generated via propagation. In this case, the harmonic signal will contain two components, the desired harmonic signal e.g. from tissue or contrast agent, and harmonic leakage from the imaging or ultrasound system [152]. In [152] various sources of harmonic leakage including the nature of the transmit waveform, signal bandwidth, signal duration, and system non-linearity e.g. in the receive path on the processed harmonic signal for tissue harmonic imaging. Shen and Li concluded that harmonic imaging performance is optimised by accurate control of the frequency content of the waveform before propagation [152]. When coupled with coded techniques that are shown to increase SNR, but require a flexible arbitrary waveform transmitter, there exists a requirement for both harmonic and amplitude control from a switched-mode excitation waveform.

7.3 Wide Bandwidth Transducer Types

Before analysing the harmonic content of switched-mode excitation signals in greater detail, it is appropriate to consider another fundamental component for harmonic imaging. Namely the properties of the transducer. Chapter 3 discussed the composition of array transducers from materials such as PZT and PVDF. Harmonic imaging requires a transducer technology that has sufficient bandwidth to contain the fundamental frequency and the desired harmonic. For techniques such as second harmonic imaging, PZT transducers with 60% bandwidth are sufficient, as conventional harmonic imaging transmits at 2/3 and receives at 4/3 of the transducer's centre frequency. For other techniques such as third harmonic imaging [158], superharmonic imaging [154], [159], and coded harmonic imaging [160] wider bandwidth transducer technologies are required. Such technology exists in the form of PVDF, but as discussed in Chapter 3, PVDF has a relatively poor transmission coefficient and is therefore mostly used for signal reception. Authors have

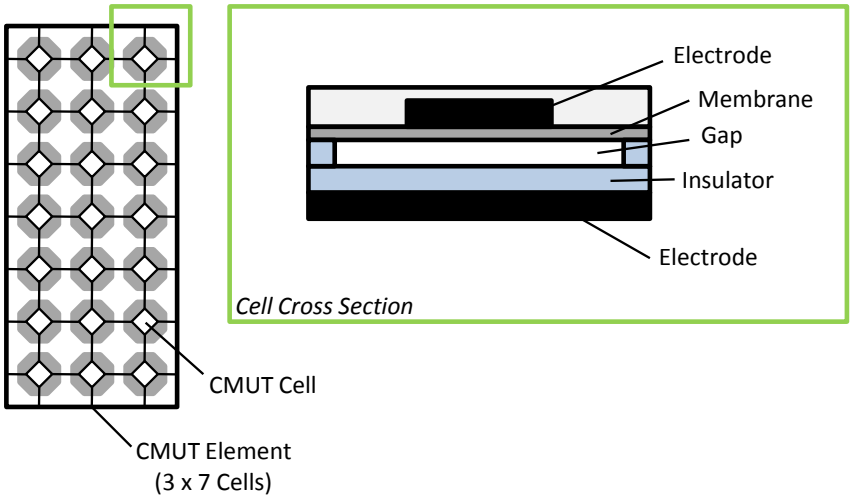

Figure 7.1: A CMUT element composed of many CMUT cells

previously suggested array transducers developed with interleaved high frequency, and low frequency elements [160] or with PZT and PVDF materials for transmit and receive respectively [161]. Therefore using the high bandwidth receive capability of PVDF, in conjunction with the normal transmission properties of PZT. Interleaving elements in this fashion causes complexity of fabrication to increase.

An alternative technology exists in the form of Capacitive Micromachined Ultrasonic Transducers (CMUT). A CMUT cell is composed of a membrane, between two electrodes, suspended over a gap. The membrane is held in tension by a bias voltage. Application of an a.c. signal causes the membrane to vibrate which generates pressure waves. Incoming pressure on the membrane causes the membrane to fluctuate, thus creating a current. This current is converted to a voltage signal by means of a transimpedance amplifier [116]. CMUT cells are small in size, and therefore multiple 'cells' are used to create an element. Each cell is connected together by means of a matrix interconnecting scheme. Figure 7.1 shows the composition of an example CMUT element composed of 21 cells. Note that it is normal that the array contains many more rows and columns of cells than shown in the Figure. A cross section of the cell is also shown in Figure 7.1, with the electrodes, membrane and gap marked for reference.

CMUTs are seen as the next transducer technology, and offer several distinct advantageous over PZT materials. These advantages include ease of fabrication, wide band-

width response, high yield, and potential for integration with other auxiliary electronics [116]. The production method is similar to transistor manufacture, and consequently, many CMUT cells can be fabricated in bulk, with the process lending itself to easier production of 1-D and 2-D arrays. The nature of fabrication of CMUT devices also suits integration with MOSFET or switched-mode circuits for excitation. The use of CMUT technology enables very wide-bandwidth array transducers to be fabricated. Some CMUT arrays have reported to be designed with elements having greater than 100% bandwidths [162], [163], [164], [165], [166] nearly double the 60% normally seen in PZT arrays. As a consequence, techniques such as superharmonic and coded harmonic imaging become more feasible using a single transducer, overcoming the concerns of transducer bandwidth, such as those discussed in [157]. Whilst CMUT devices may solve the bandwidth problem for harmonic imaging, the two other issues of harmonic leakage, and low SNR still exist. As previously mentioned, the latter can be addressed by using coded harmonic imaging as described in [167]. However spectral integrity to remove harmonic leakage becomes more important, especially for switched-mode signals. First however, an introduction to coded harmonic imaging is provided.

7.4 Coded Harmonic Imaging

Chapter 6 introduced coded imaging using the fundamental frequency. Coded imaging improves SNR by transmitting and detecting an embedded code within a long duration signal. This embedded code can be detected in the presence of noise, and the long duration pulse can be compressed to a narrow peak when detected using an appropriate filter. Chapter 6 discussed the use of LFM signals, and demonstrated imaging using pulse compression. LFM signals are also appropriate for harmonic imaging. In fundamental coded imaging, the bandwidth of the chirp typically matches, or is slightly greater than the bandwidth of the transducer. For harmonic coded imaging, the bandwidth of the chirp is limited by encompassing the fundamental bandwidth, and the harmonic bandwidth within the transducer's frequency range, with a 'guard band' to prevent harmonic leakage. This most often results in the fundamental and harmonic LFM signals located

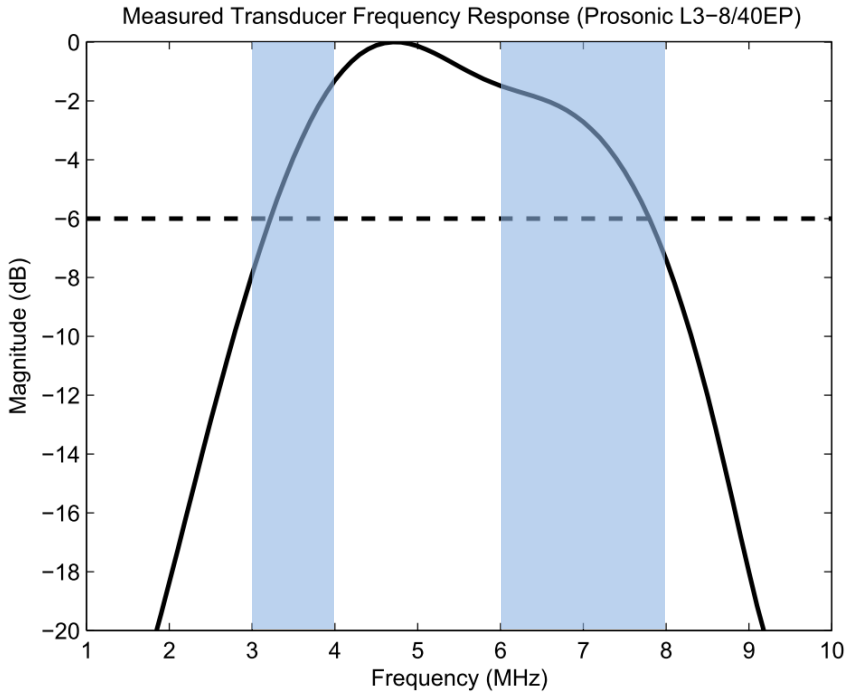

Figure 7.2: Frequency response of PZT medical imaging transducer. Fundamental and harmonic regions are shown in the shaded areas.

at inefficient regions of the transducer's frequency response as shown by the shaded sections in Figure 7.2 [3]. It is advantageous in coded imaging to increase the TB product for maximum compression gain. Also, resolution in a coded imaging system is dependent on the bandwidth of the LFM signal. System efficiency can therefore be maximised by using wider bandwidth devices. Also important, as discussed in Chapter 6 is the requirement to taper the excitation signal. Tapering using switched-mode signals has been demonstrated in Chapters 5 and 6 using a PWM strategy for switched-mode excitation of transducers, with the benefits when compared with 'fixed width' bipolar LFM signals demonstrated. Switched-mode operation is desirable as an alternative to other amplifier methods for replication across multiple channels suitable for driving arrays of elements, as discussed in Chapters 3 and 5. This requirement also exists for harmonic imaging with or without coding techniques. The remaining part of this chapter discusses the harmonic content of switched-mode signals, elimination of harmonics using SHE strategies, and how the PWM strategy previously discussed can be developed to provide arbitrary waveform capability with reduced harmonic content.

7.5 Switched-Mode Selective Harmonic Elimination

SHE is a technique well-reported in power converter theory. Its basis depends on careful choice of appropriate switching angles to move from each of the switched-mode states. By doing this, harmonic components can be reduced using a principle of phase inversion or cancellation. A primary example of this was discussed for ultrasound by Tang and Clement [13]. In [13] a switched-mode power inverter was shown as suitable for driving piezo-electric load, but with reduced third harmonic. To achieve this, the positive and negative legs of switching were phase-separated by $\pi/3$. With reference to Figures 5.3 and 5.4 and Equation (5.20) this equates to a switching angle $\delta = \pi/6$ which, on inspection of Figure 5.4 is located at a point with no third harmonic magnitude. This can be implemented using an amplitude or phase thresholding method, where a sinusoidal signal can be quantized to three levels. An example amplitude thresholding algorithm is shown in (7.1)

$$f(x) = \begin{cases} 1, & \text{if } g(x) > \sin(\delta) \\ -1, & \text{if } g(x) < -\sin(\delta) \\ 0, & \text{otherwise} \end{cases} \tag{7.1}$$

Tang and Clement discussed that removal of the third harmonic also eliminates other $3n$ order harmonics [13]. Work by Cowell [53] [5] [7] showed that this can be extended for multi-level circuits. For example, in [53] and [7] Cowell discussed the relationship between harmonic cancellation and switching angle δ where the angle of separation, θ_δ, is defined by

$$\theta_\delta = \frac{\pi}{h_n}, \tag{7.2}$$

where h_n is the desired harmonic to cancel, and the switching angle is derived using

$$\delta = \frac{\theta_\delta}{2}. \tag{7.3}$$

Equations (7.2) and (7.3) describe the three-level case previously discussed. For multiple level excitation circuits, Cowell also demonstrated calculation of multiple switching

angles [7]. For example, a five-level circuit has two switching angles, δ_1 and δ_2 as shown in Figure 5.10. As there exists an additional switching angle, there is opportunity to cancel an additional harmonic. For example, cancellation of the third and fifth harmonic, h_3 and h_5 respectively. To achieve this, the angle of separation can be calculated using (7.2) for each harmonic, therefore

$$\theta_{\delta 3} = \frac{\pi}{3}, \tag{7.4}$$

$$\theta_{\delta 5} = \frac{\pi}{5}. \tag{7.5}$$

Application of (7.3) for both cases leads to switching angles $\delta_{h3} = \pi/6$ as in the previous example, and $\delta_{h5} = \pi/10$. These angles do not describe angles δ_1 and δ_2 in Figure 5.10, as these are calculated using the following relationship [7]

$$\delta_1 = \delta_{h1} - \delta_{h2}, \tag{7.6}$$

$$\delta_2 = \delta_{h1} + \delta_{h2}. \tag{7.7}$$

Consequently, in this case, final switching angles can be calculated that simultaneously cancel both the third and fifth harmonic, using (7.6) and (7.7) that equate to

$$\delta_1 = \frac{\pi}{15}, \tag{7.8}$$

$$\delta_2 = \frac{4\pi}{15}. \tag{7.9}$$

In the same way, other harmonics in the series will be cancelled, i.e. all $3n$ harmonics $(3, 6, 9...)$, and all $5n$ harmonic $(5, 10, 15...)$. In addition to this, due to the symmetry of the switched waveform, all even harmonics are cancelled as discussed in the Fourier Series analysis in Chapter 5. After cancellation, the next-lowest harmonic will therefore be the 7th, which will have the largest harmonic magnitude over subsequent harmonics.

The relationship between levels required, and odd harmonics cancelled can be expressed by [7]

$$n_L = 1 + 2^h \tag{7.10}$$

where n_L is the number of voltage levels required, and h is the number of odd harmonics to be cancelled. Consequently, to cancel a single harmonic, three levels are required. To simultaneously cancel two harmonics, five levels are required. To cancel three harmonics, nine levels are required as shown in [5].

Parallels can be drawn between the method of generating switched-mode signals with SHE, and the carrier comparison method shown previously. In this case, the 'carrier' or comparison signal is merely a fixed level at thresholds defined by (7.1). Figure 7.3 graphically demonstrates third harmonic cancellation with a bipolar three level signal. The desired 'analogue' signal is shown in the top plot. The particular thresholds for third harmonic elimination are also plotted in light blue. The comparison algorithm generates a switched waveform as shown in the lower plot, with the positive and negative voltages selected when the desired waveform is greater or less than the positive and negative thresholds respectively, and zero otherwise.

Figure 7.4 shows a different case, where the fifth harmonic is cancelled, using a switching angle of $\pi/10$. Again, the thresholds have been plotted against the desired waveform, with the intersection of the threshold and signal causing a switching event.

A third example is shown in Figure 7.5. In this case, the multi-level strategy has been applied, with switching angles calculated as per (7.2), (7.8) and (7.9). It can be seen that there are two sets of positive and negative thresholds, with the blue threshold controlling switching of the lower voltage, and the pink threshold controlling the higher voltage.

Thresholding using a single switching angle, generates switched-mode waveforms composed of pulses with equal and fixed widths, according to the intersection of the desired waveform and the threshold. Chapter 5 discussed the need for amplitude control from a switched-mode transmitter system. Chapter 6 showed the advantages of width-modulation within switched-mode sequences for coded imaging. Varying widths accord-

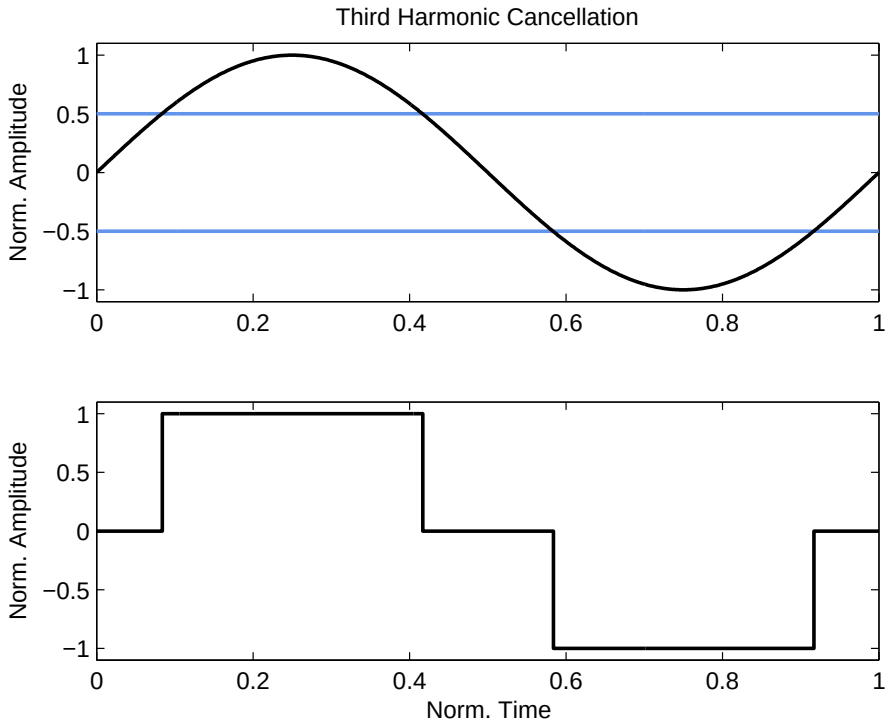

Figure 7.3: Third harmonic cancellation switching using amplitude thresholding at $\sin(\pi/6)$

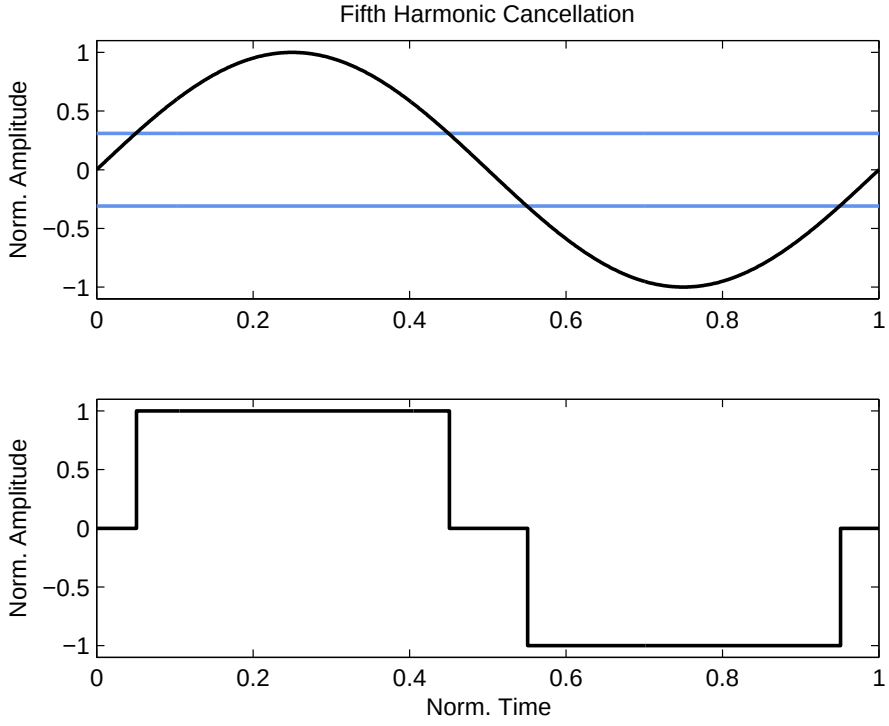

Figure 7.4: Fifth harmonic cancellation switching using amplitude thresholding at $\sin(\pi/10)$

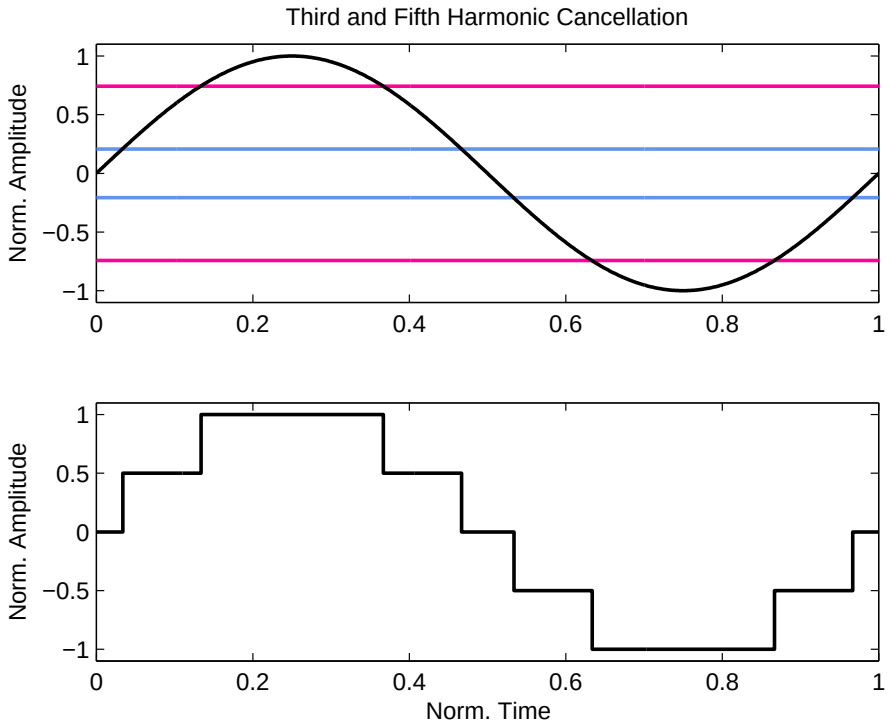

Figure 7.5: Simultaneous third and fifth harmonic cancellation switching using amplitude thresholding at $\sin(\pi/15)$ and $\sin(4\pi/15)$

ing to the carrier derived in (6.3) does not control harmonic content. Controlling harmonic content by means of a single threshold gives undesirable results for tapered or shaped arbitrary sequences. Figure 7.6 demonstrates that the thresholding method does not encode switched-mode sequences for harmonic, and amplitude control. As thresholds are based on the full amplitude of the waveform, the threshold can be scaled according to the amplitude function. This is demonstrated in Figures 7.7, 7.8 and 7.9, however it can be seen that there is still a lack of amplitude control. To provide both, a different approach is required, one which can adjust widths according to both harmonic content, and amplitude. The following section describes such a method using the carrier-comparison procedure as a basis.

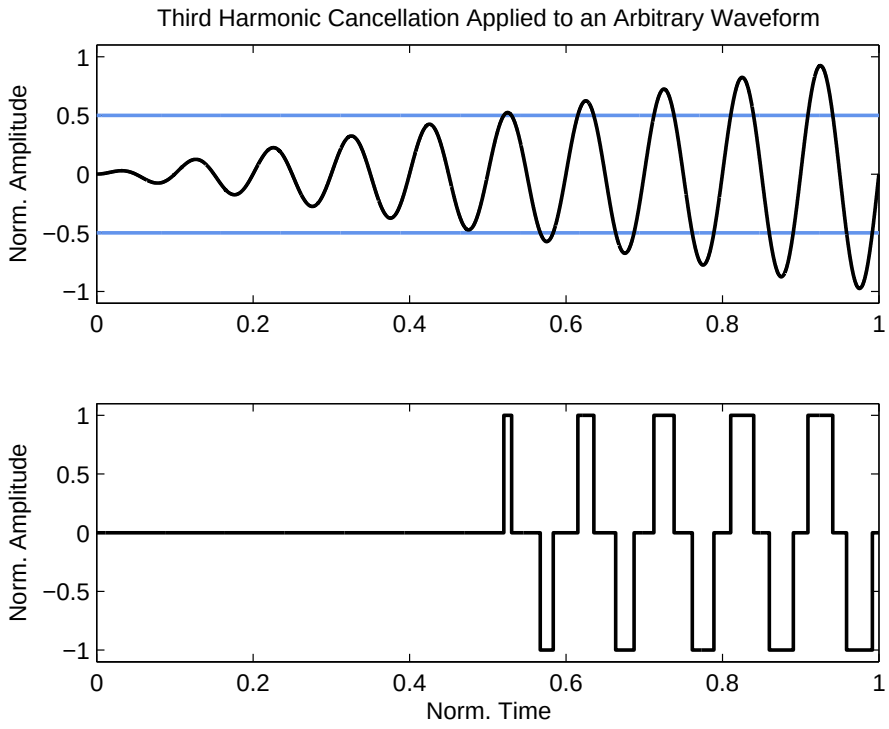

Figure 7.6: Failure of SHE comparison method for harmonic and amplitude control

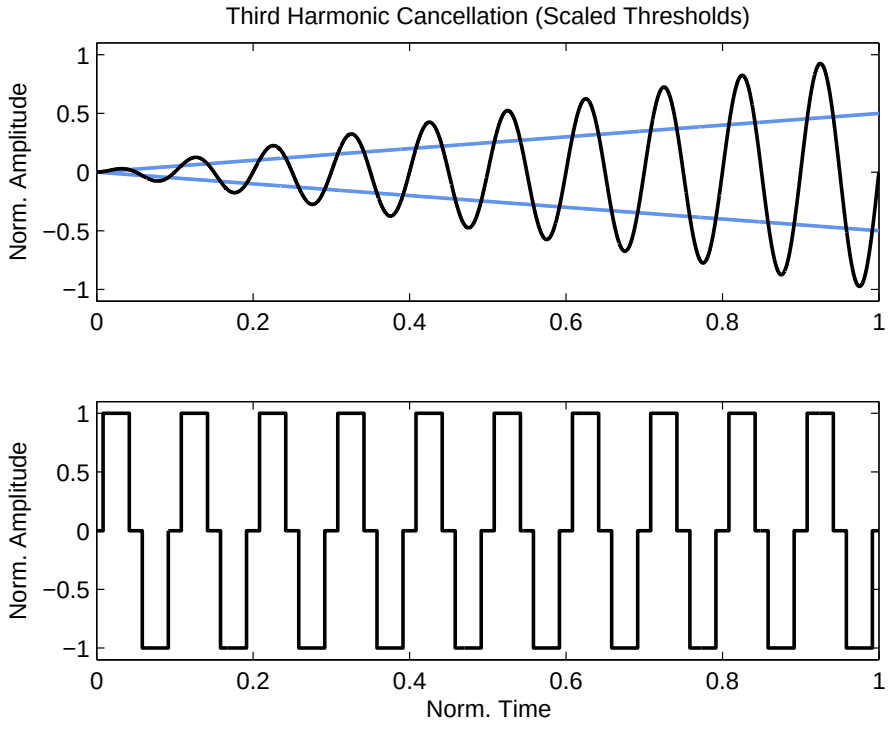

Figure 7.7: Threshold scaling to provide third harmonic control, but loss of amplitude control

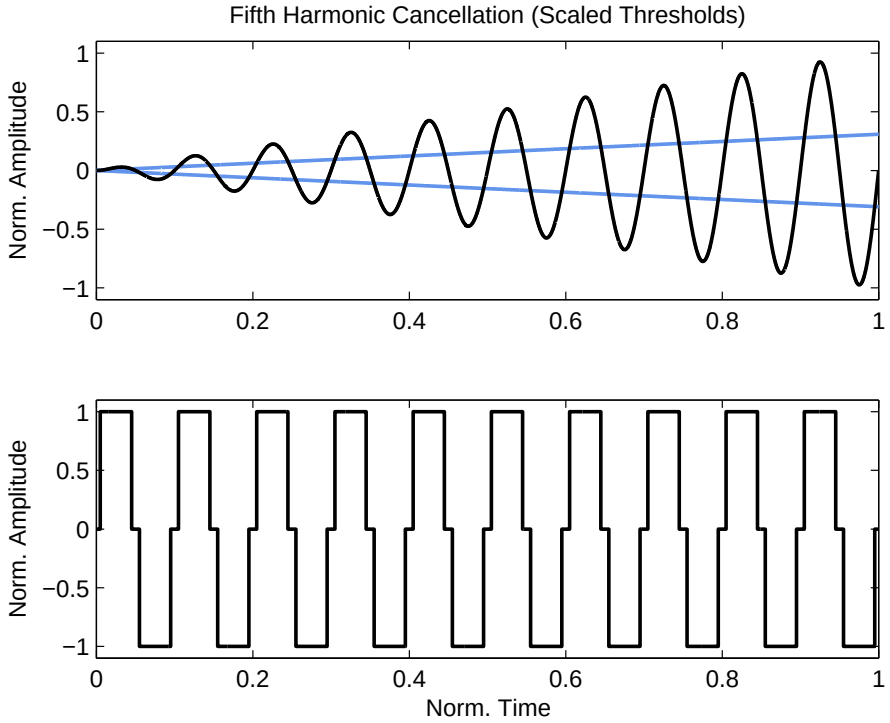

Figure 7.8: Threshold scaling to provide fifth harmonic control, but loss of amplitude control

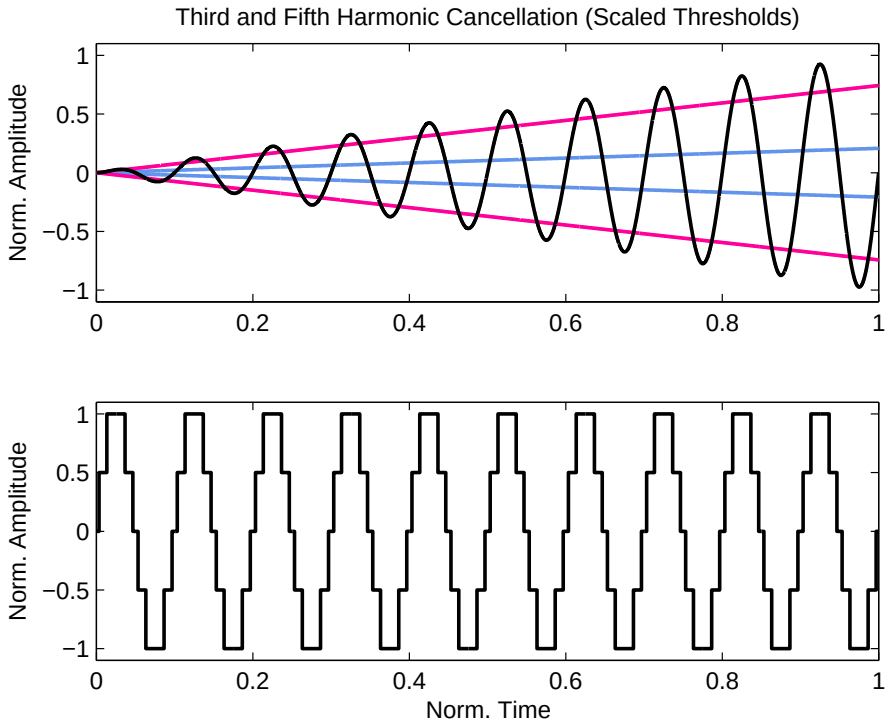

Figure 7.9: Threshold scaling to provide third and fifth harmonic control, but loss of amplitude control

7.6 Harmonic Reduction Pulse Width Modulation

The carrier optimisation discussed in Chapter 5 converted a 'linear' PWM carrier, such as a triangular or sawtooth carrier to a trigonometric carrier. This trigonometric carrier was a sine or cosine function that had been rectified to generate symmetrically modulated pulse-width modulated switched-mode sequences. To encode pulse widths according to the expected output from the transducer, it was necessary to generate a carrier that matched the expected fundamental frequency response from the transducer. This section explores whether switched-mode sequences can be encoded by considering the response of the fundamental frequency, together with a harmonic frequency.

Figure 5.4 showed how the fundamental and third harmonic magnitude deviated according to switching angle for the three-level Fourier series described by (5.21). It can be seen for a single switching angle, there is a single δ that eliminates the third harmonic. Introducing a second level in turn introduces a second switching angle. This switching angle can be used to simultaneously remove two harmonics as shown in Section 7.5, and also provides more states for PWM without increasing sampling frequency. An alternative approach suggested in power inverters is to keep the same number of levels, and introduce a second commutation [129]. This second commutation provides a set of simultaneous equations which can be solved to provide angles of separation.

Considering the multi-level case shown previously in Figure 5.10 we can plot combinations of switching angles δ_1 and δ_2 with respect to the Fourier series coefficient b_n as defined in (5.32). Figure 7.10 shows the magnitude of the fundamental coefficient, b_1 plotted for angles δ_1 and δ_2 [53]. Note that a triangular region is plotted, as δ_2, the higher level switching angle can only be valid when it is less than δ_1. For the PWM case discussed in Chapters 5 and 6, the path from least fundamental amplitude to most fundamental amplitude was described by moving from top to bottom, and right to left along each axis, as shown in Figure 7.11. It can be seen that the lowest fundamental magnitude exists at the top right hand corner ($\delta_1 = \delta_2 = \pi/2$) with largest fundamental magnitude at the bottom left hand corner ($\delta_1 = \delta_2 = 0$). Plotting along this line shows a trigonometric variation in fundamental amplitude as shown in Figure 7.12, and is exactly equivalent to

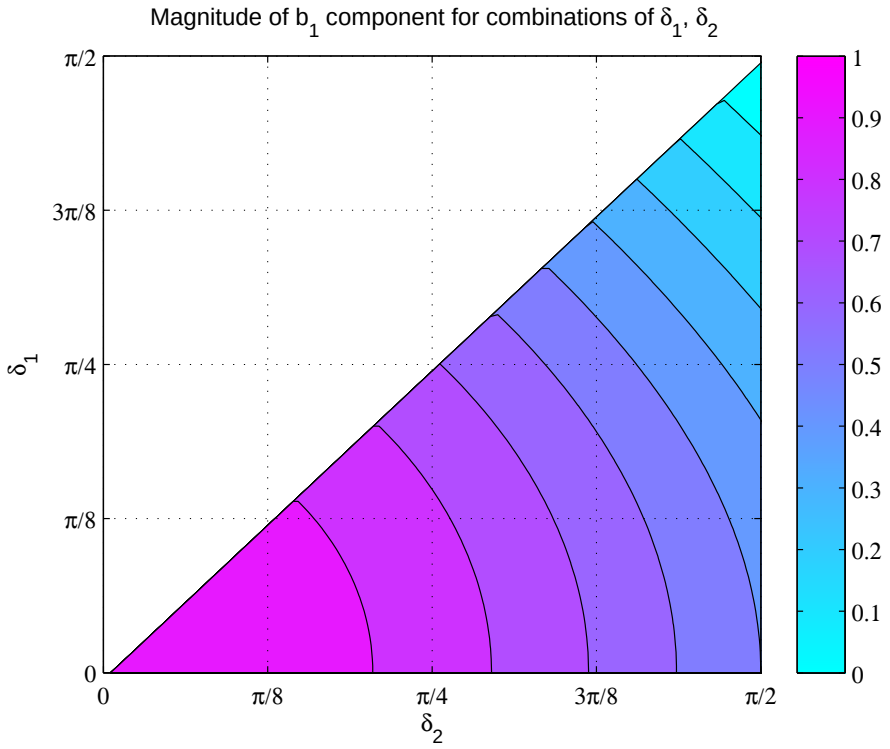

Figure 7.10: Magnitude of fundamental for switching angles δ_1 and δ_2 (normalised) in the range $0 < \delta_1, \delta_2 < \pi/2$

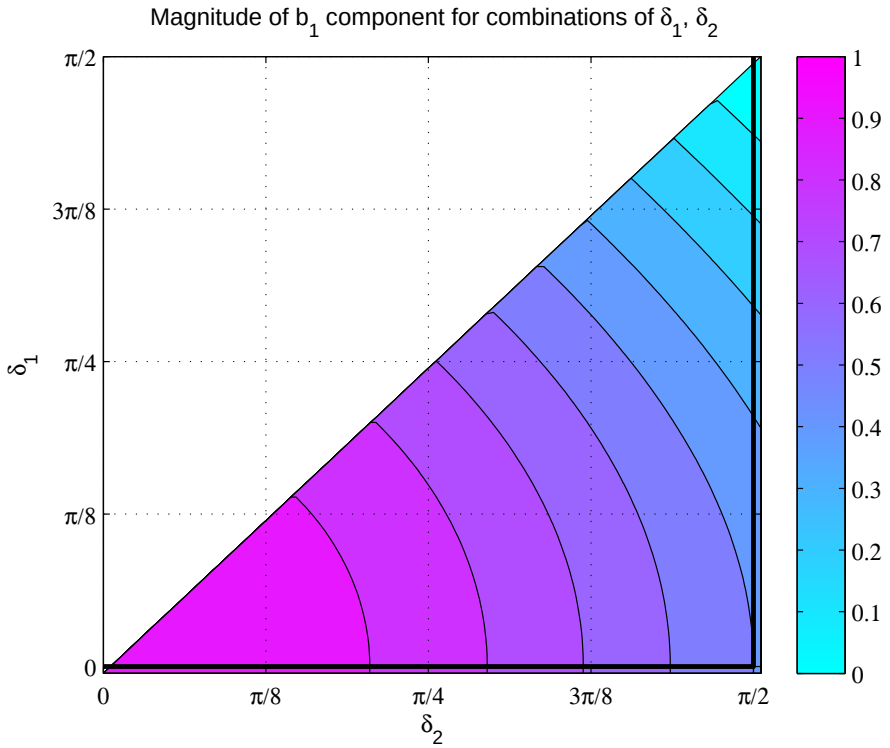

Figure 7.11: Path of multi-level PWM encoding described in Chapter 5

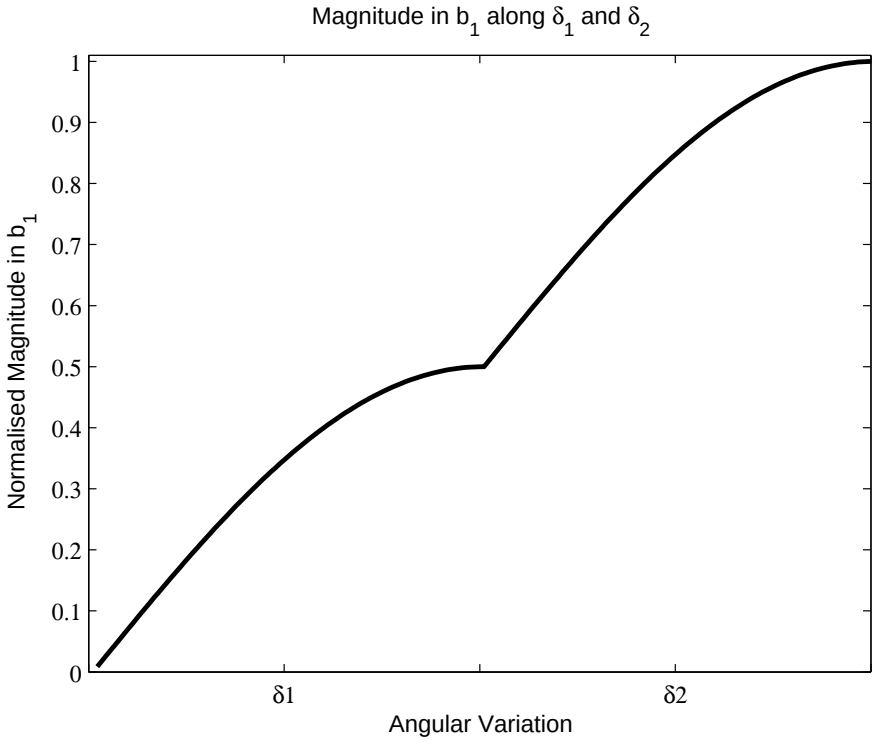

Figure 7.12: Fundamental amplitude variation moving along δ_1 and δ_2. The region marked δ_1 shows deviation of δ_1 when $\delta_2 = \pi/2$ (low level switch switching). The region marked δ_2 shows deviation of δ_2 when $\delta_1 = 0$ (high level switch switching)

the single switching angle case and Figure 5.4, however here two switching angles are defined for multiple levels. Figure 7.13 plots the magnitude of the third harmonic Fourier coefficient b_3. It can be seen that distinct regions of high and low third harmonic exist. To reduce the third harmonic and provide amplitude control, it is possible to traverse through this region, whilst considering the fundamental magnitude. The change in fundamental magnitude can then be used as the basis for a new carrier definition. This carrier would differ from the carrier described in Chapter 5 as the previous carrier can be defined by modulating δ_1 with $\delta_2 = \pi/2$, and then modulating δ_2 with $\delta_1 = 0$.

Figure 7.14 shows a path that starts from zero fundamental amplitude ($\delta_1 = \delta_2 = \pi/2$) and progresses toward higher amplitude. For clarity the Figure has been extended from $\pi/2$ to $2\pi/3$. It can be seen that a 'path of reduced third harmonic' can be drawn (black line) that starts at $\delta_1 = \delta_2 = \pi/2$ before moving into a path of 'zero third harmonic' which moves diagonally up again. Note that moving in a path diagonally across the plot requires simultaneous alteration of switching angles, as opposed to the previous PWM

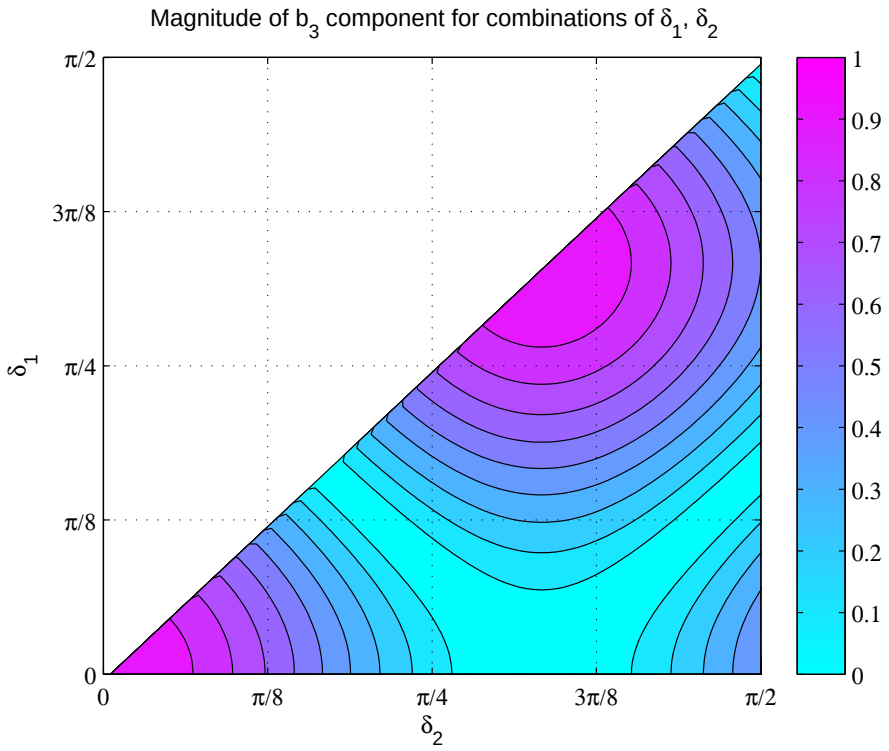

Figure 7.13: Magnitude of third harmonic for switching angles δ_1 and δ_2 (normalised) in the range $0 < \delta_1, \delta_2 < \pi/2$

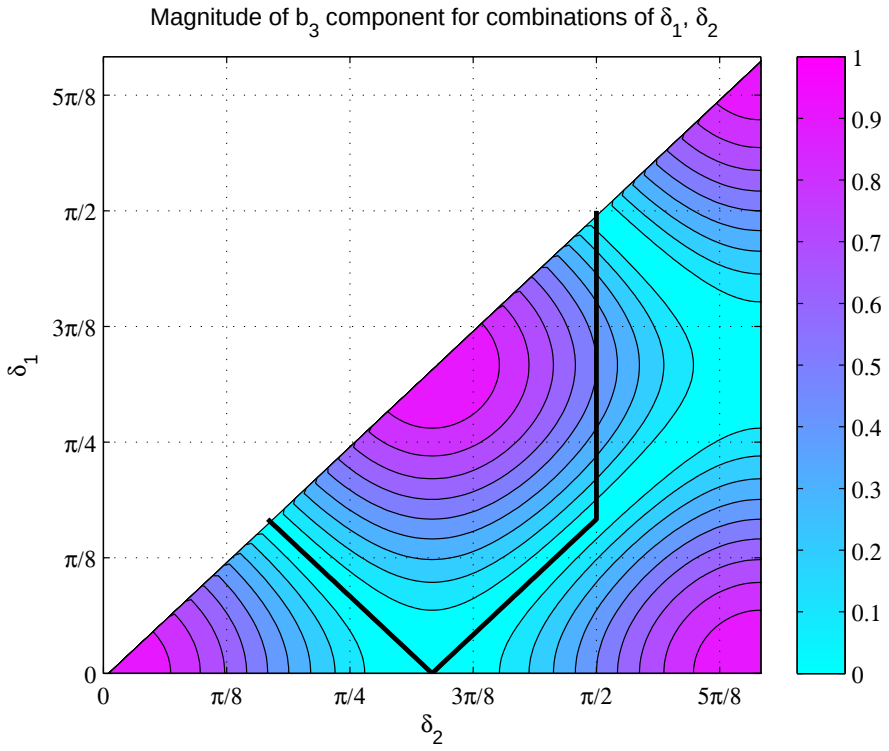

Figure 7.14: Initial path of reduced (but not 'least') third harmonic considering angle range $0 < \delta_1, \delta_2 < 2\pi/3$

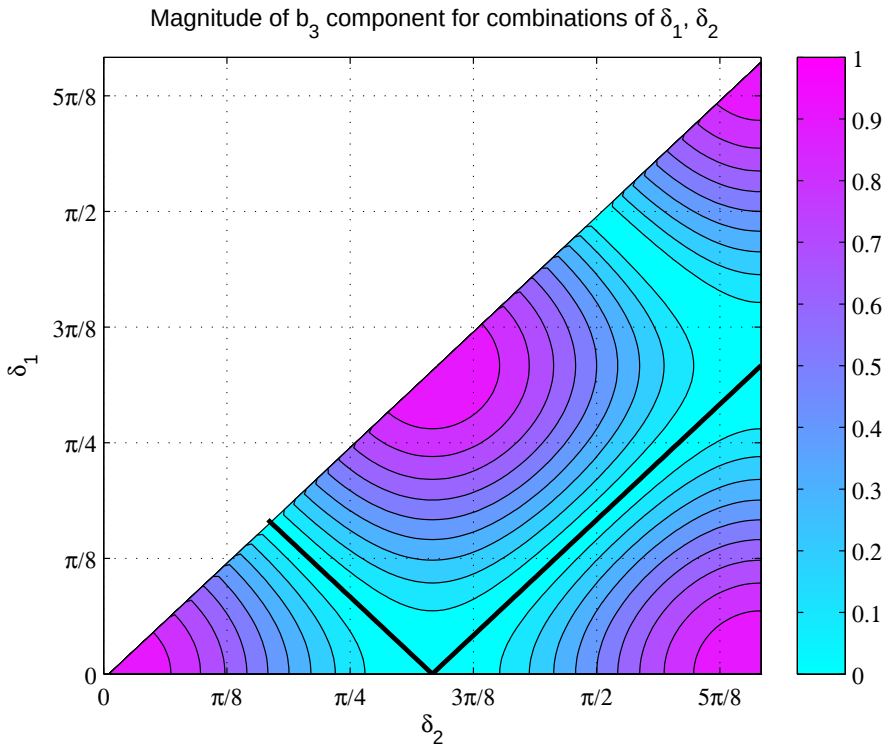

Figure 7.15: Extension of path of least third harmonic to cover range $0 < \delta_1, \delta_2 < 2\pi/3$

case where a single switching angle was changed in isolation. Notice that extension of the graph also shows that at angles $> \pi/2$ the region of least third harmonic magnitude continues. Therefore if the constraint of switching to $\pi/2$ is ignored, then a true path of least third harmonic can be followed. This is shown in Figure 7.15 with the path starting from the right hand side and moving from right to left along the solid black line to describe least fundamental magnitude to highest fundamental magnitude. This variation in fundamental magnitude can be verified by plotting this 'path of least third harmonic' onto the fundamental b_1 plot, as shown in Figure 7.16.

Now that this 'path of least third harmonic' has been defined, it is possible to evaluate the magnitude of the fundamental along this path, and then use that to define an appropriate carrier function. This method is therefore a 2-D extension of the method used in Chapter 5 to define the trigonometric carrier as opposed to the linear carrier. Plotting each angle against the the magnitude of the fundamental along this path of least harmonic gives a plot as shown in Figure 7.17. This shape defines a carrier that when used with a suitable comparison algorithm, can encode switched-mode sequences with amplitude control through consideration of the fundamental response through the transducer, and elimina-

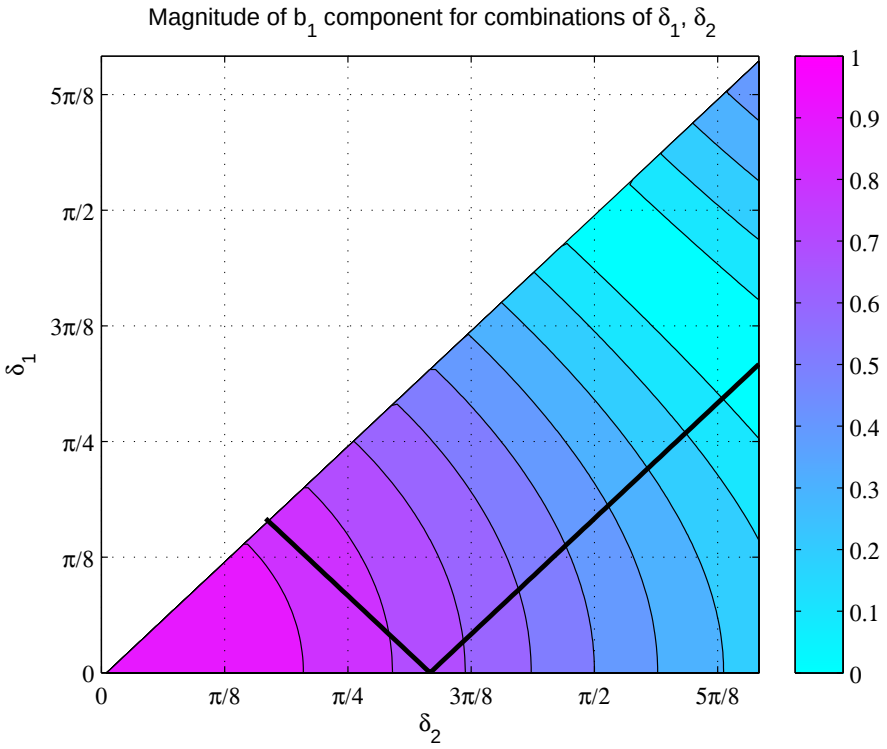

Figure 7.16: Overlay of path of least third harmonic onto magnitude of fundamental for switching angles δ_1 and δ_2 (normalised) in the range $0 < \delta_1, \delta_2 < 2\pi/3$

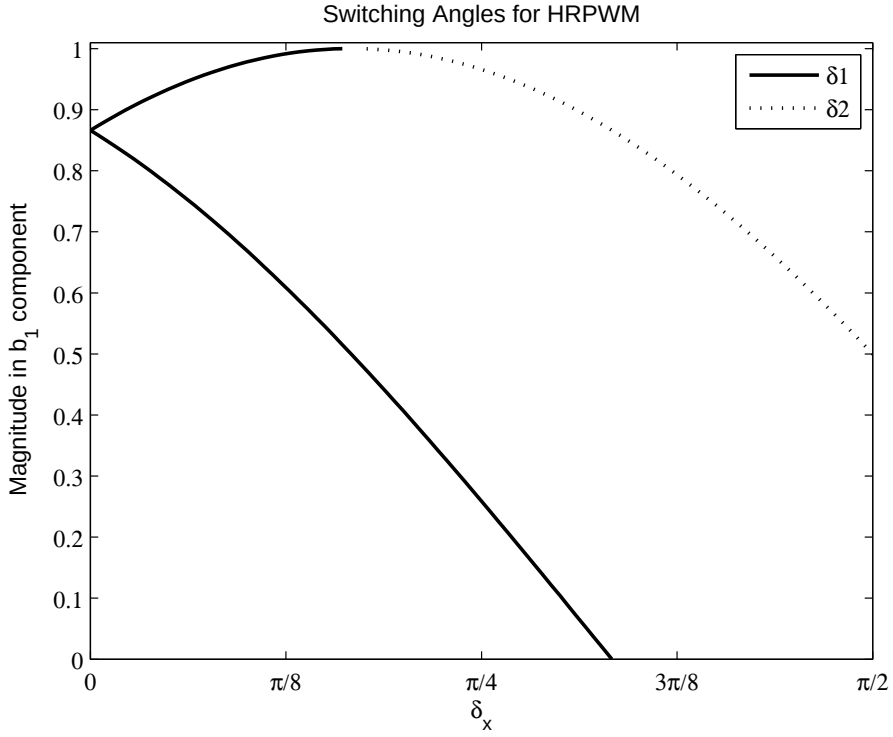

Figure 7.17: HRPWM switching angles vs. fundamental magnitude

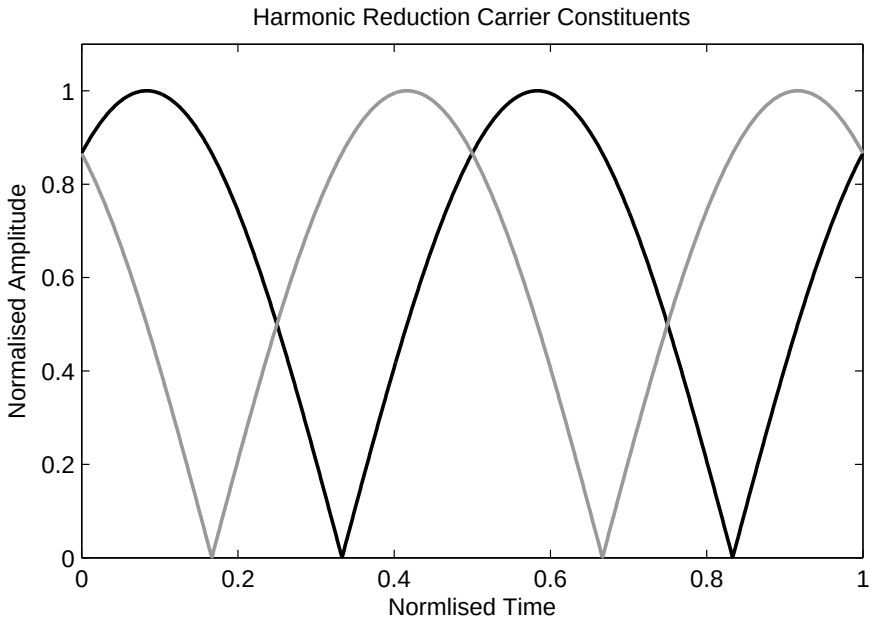

Figure 7.18: Phase-separated, rectified, trigonometric waveforms used for design of HRPWM carrier constituents

tion of the third harmonic by selecting only combinations of switching angles where zero third harmonic exists.

The waveforms shown in Figure 7.17 can be approximated by two phase-separated rectified waveforms as shown in Figure 7.18.

Where each waveform is

$$C_L(t) = |\cos(\omega t - \pi/6)| \tag{7.11}$$

$$C_T(t) = |\cos(\omega t + \pi/6)| \tag{7.12}$$

and both waveforms are separated by $\pi/6$. Waveforms C_L and C_T form the basis for the carrier design and merely describe the combination of switching angles δ_1 and δ_2 for a desired output amplitude. These signals cannot directly be used to modulate harmonic reduction PWM sequences. Instead carriers must be constructed that modulate the pulse widths of each high and low switch. Note that the 'path of least third harmonic' moves diagonally across the plot, indicating that at all times δ_1 and δ_2 change simultaneously. This manifests itself in a carrier comparison method as periods of overlap for each carrier and differs from the multi-level carrier defined in Chapter 5 which were contiguous. Also, the change in direction means that the width of δ_1 reduces at higher fundamental amplitudes. Carriers can be defined for the low level switch (Carrier 1) as follows

$$\text{Carrier 1a}(t) = \begin{cases} C_T(t), & \text{if } C_T(t) \leq C_L(t) \\ C_L(t), & \text{otherwise} \end{cases} \tag{7.13}$$

The low switch carrier, Carrier 1, has two parts (a and b) due to the width increasing and then decreasing. Such behaviour cannot be described by a single function.

$$\text{Carrier 1b}(t) = \begin{cases} \text{if } C_L(t) > \sqrt{3}/2 \\ \qquad 1, \qquad \text{if } C_T(t) < 0.5 \\ \qquad C_L(t), \quad \text{otherwise} \\ \text{else if} \quad C_T(t) > \sqrt{3}/2 \\ \qquad 1, \qquad \text{if } C_L(t) < 0.5 \\ \qquad C_T(t), \quad \text{otherwise} \\ \text{else} \\ \qquad 1, \end{cases} \tag{7.14}$$

The carrier to modulate the high level switch can be defined with

$$\text{Carrier 2}(t) = \begin{cases} \text{if } C_L(t) = C_T(t) \\ \qquad 1, \\ \text{else if } C_L(t) > C_T(t) \\ \qquad C_L(t), \quad \text{if } C_T(t) \leq 0.5 \\ \qquad 1, \qquad \text{if } C_L(t) \geq \sqrt{3}/2 \\ \qquad C_L(t), \quad \text{otherwise} \\ \text{else} \\ \qquad C_T(t), \quad \text{if } C_L(t) \leq 0.5 \\ \qquad 1, \qquad \text{if } C_T(t) \geq \sqrt{3}/2 \\ \qquad C_L(t), \quad \text{otherwise} \end{cases} \tag{7.15}$$

Note that these carriers have been designed to generate symmetrically modulated PWM at the lowest switching frequency or close to the fundamental, in line with the PWM

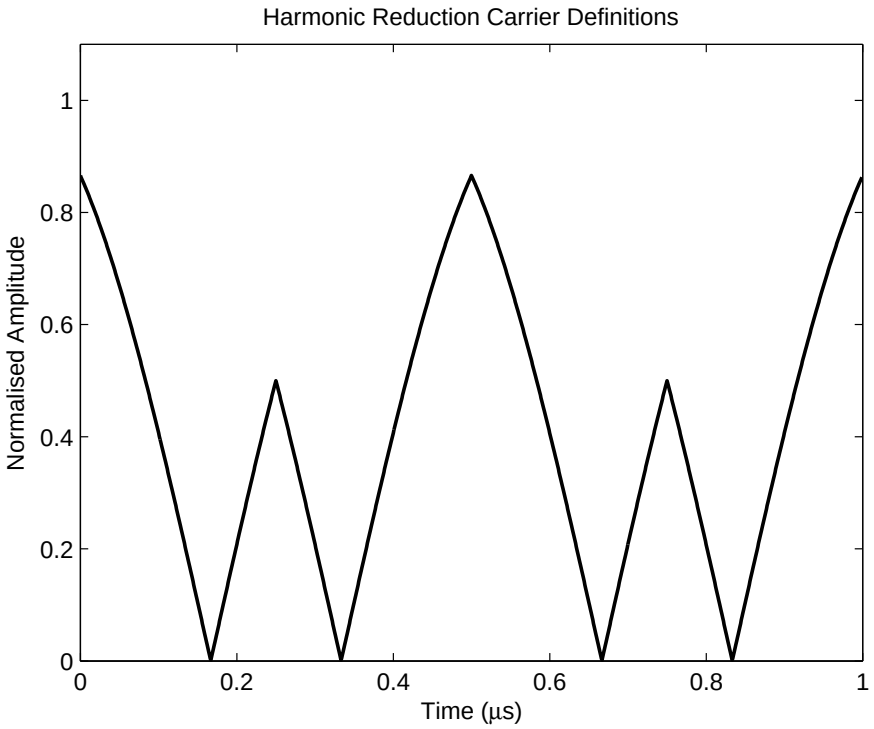

Figure 7.19: HRPWM low-switch modulator Carrier 1a

method described in Chapter 5. Figures 7.19 to 7.21 show each of the carrier parts in a symmetrically modulated mode. Figure 7.22 shows all carrier parts combined to show modulation across the full range of amplitudes (0 to 1).

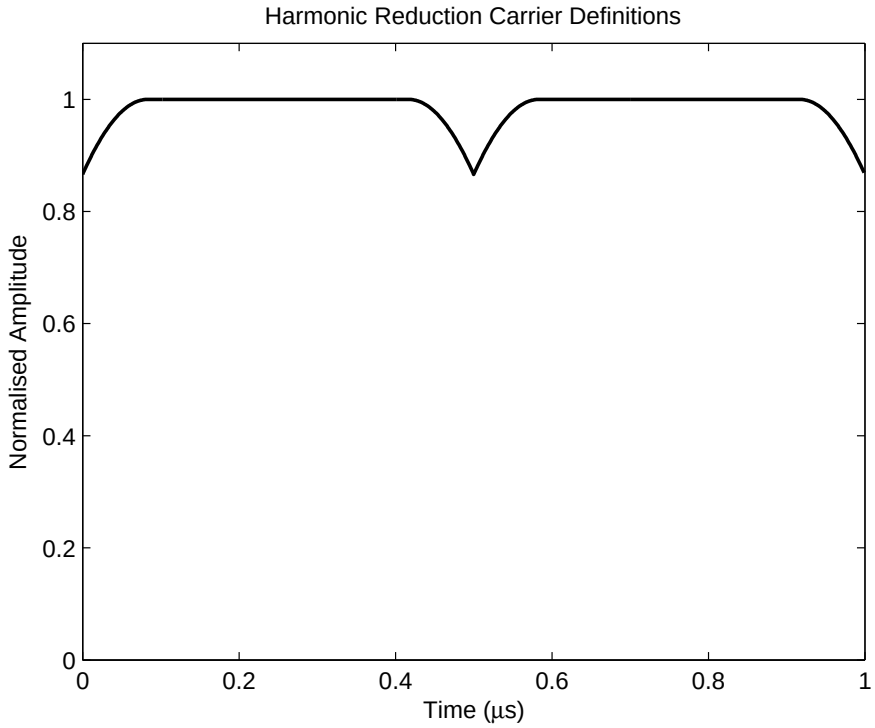

Figure 7.20: HRPWM low-switch modulator Carrier 1b

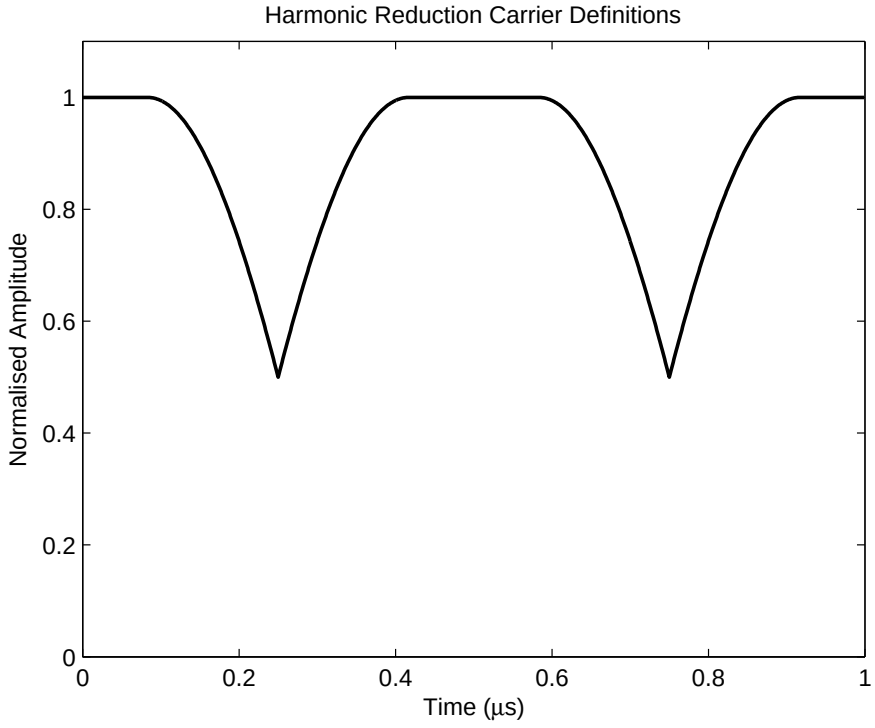

Figure 7.21: HRPWM high-switch modulator Carrier 2

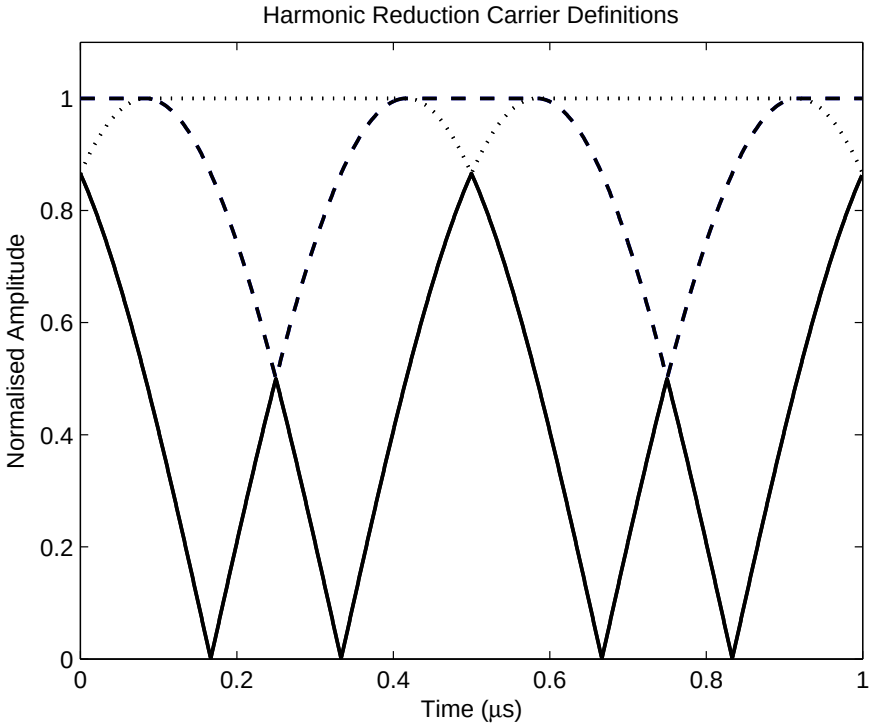

Figure 7.22: Combined Carriers

The carrier arrangement shown in Figure 7.22 can be inverted and used to generate five-level HRPWM sequences for tone burst or LFM excitations as shown in previous chapters. Due to the nature of the carriers, an altered algorithm has been defined in order to truly modulate both switches for harmonic reduction. This algorithm can be described with

$$\mathrm{PWM}_L(t) = \begin{cases} \text{if} \quad s(t) \geq 0 \\ \qquad \text{if} \quad m_{\mathrm{POS}}(t) < \sqrt{3}/2 \\ \qquad\quad 0, \qquad m_{\mathrm{POS}}(t) \leq \text{Carrier 1a}(t) \\ \qquad\quad 0.5, \qquad \text{otherwise} \\ \qquad \text{else} \\ \qquad\quad 0.5, \qquad m_{\mathrm{POS}}(t) \leq \text{Carrier 1b}(t) \\ \qquad\quad 0, \qquad \text{otherwise} \\ \text{else} \\ \qquad \text{if} \quad m_{\mathrm{NEG}}(t) > -\sqrt{3}/2 \\ \qquad\quad 0, \qquad m_{\mathrm{NEG}}(t) \geq -\text{Carrier 1a}(t) \\ \qquad\quad -0.5, \quad \text{otherwise} \\ \qquad \text{else} \\ \qquad\quad -0.5, \quad m_{\mathrm{NEG}}(t) \geq -\text{Carrier 1b}(t) \\ \qquad\quad 0, \qquad \text{otherwise} \end{cases} \tag{7.16}$$

$$\mathrm{PWM}_H(t) = \begin{cases} \text{if} \quad s(t) \geq 0 \\ \qquad 0, \qquad m_{\mathrm{POS}}(t) \leq \text{Carrier 2}(t) \\ \qquad 0.5, \qquad \text{otherwise} \\ \text{else} \\ \qquad 0, \qquad m_{\mathrm{NEG}}(t) \geq -\text{Carrier 2}(t) \\ \qquad -0.5, \quad \text{otherwise} \end{cases} \tag{7.17}$$

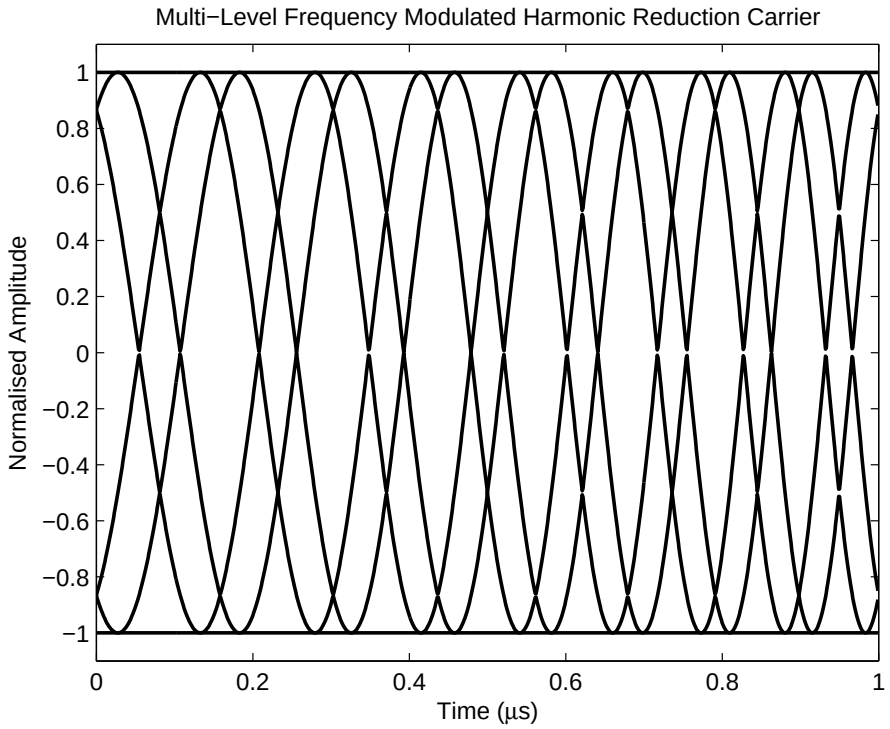

Figure 7.23: Multi-Level Swept Frequency Harmonic Reduction Carrier

$$\mathrm{PWM}(t) = \mathrm{PWM}_L(t) + \mathrm{PWM}_H(t) \tag{7.18}$$

LFM HRPWM excitations can be created similar to the previous PWM case discussed, by merely applying frequency modulation to the base waveforms described in (7.11) and (7.12). An example of multi-level carrier definition with frequency modulation is shown in Figure 7.23.

To elucidate the carrier setup further, it is appropriate to provide some examples of modulation. Figures 7.24 to 7.28 show example modulations for 20%, 40%, 60%, 80% and 100% amplitudes indicated by d.c. levels shown with the solid grey line.

Considering the first case at 20% modulation in Figure 7.24, the carrier comparison method described in (7.16) to (7.18) shows that at 20% desired amplitude only the low switch needs to switch, and is only covered by the range of Carrier 1a. The switch is 'on' when the carrier value is less than the desired amplitude, and 'off' when the carrier is above the desired level as in the previous carrier comparison technique. It can be seen that the carrier actually generates what can be seen as two pulses, which varies slightly from

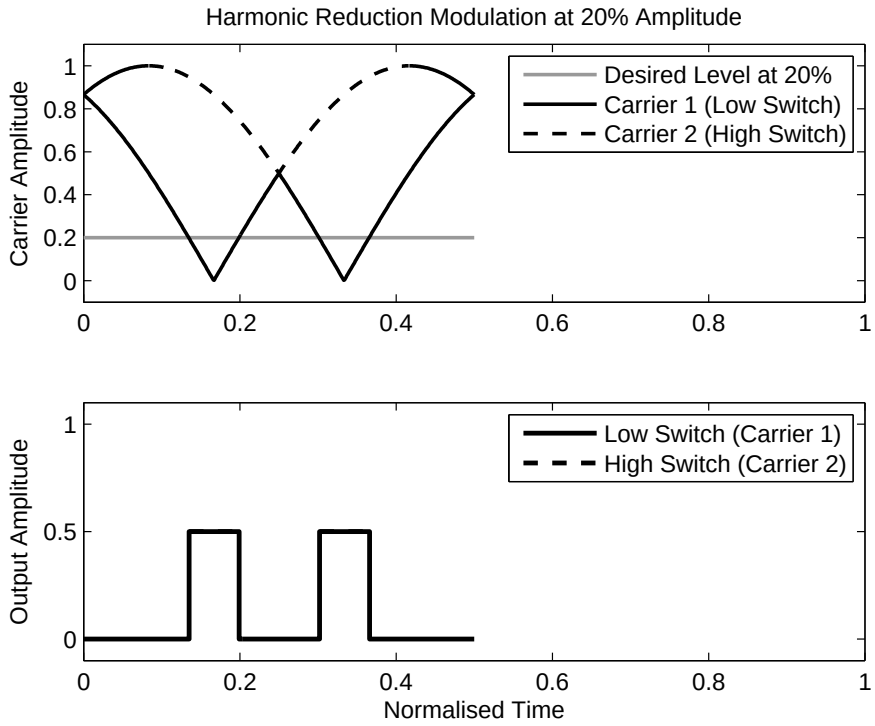

Figure 7.24: Encoding of HRPWM signals at 20% amplitude

the previous 'fundamental' mode of switching. When considering the case at 40% desired amplitude in Figure 7.25, it can be seen that the width of the two pulses has increased, with the gap between the pulses decreasing. At 60% amplitude, shown in Figure 7.26 it can be seen that the desired level now intersects the high level carrier, Carrier 2. As a consequence, both the low level and high level switches are on. Also notice that the low level pulse has now joined into a single pulse. Figure 7.27 shows a higher desired level. Notice that the low level pulse width is very wide, almost at its maximum point. When compared with the 100% case (maximum amplitude) shown in Figure 7.28 it can be seen that the desired level now intersects the second carrier part, Carrier 1b, and thus the 'path of least third harmonic' has now changed direction, with δ_1 now reducing. Analysis of the high switch shows that this pulse width still increases, to finally match the width of the low level pulse. This is a non-intuitive phenomenon, as essentially, the width of the low level switch is decreasing for an increase in desired output level.

Figures 7.29 to 7.32 demonstrate examples of single cycle 1 MHz waveforms of 25%, 50%, 75% and 100% amplitude indictating the desired output signal, and the HRPWM

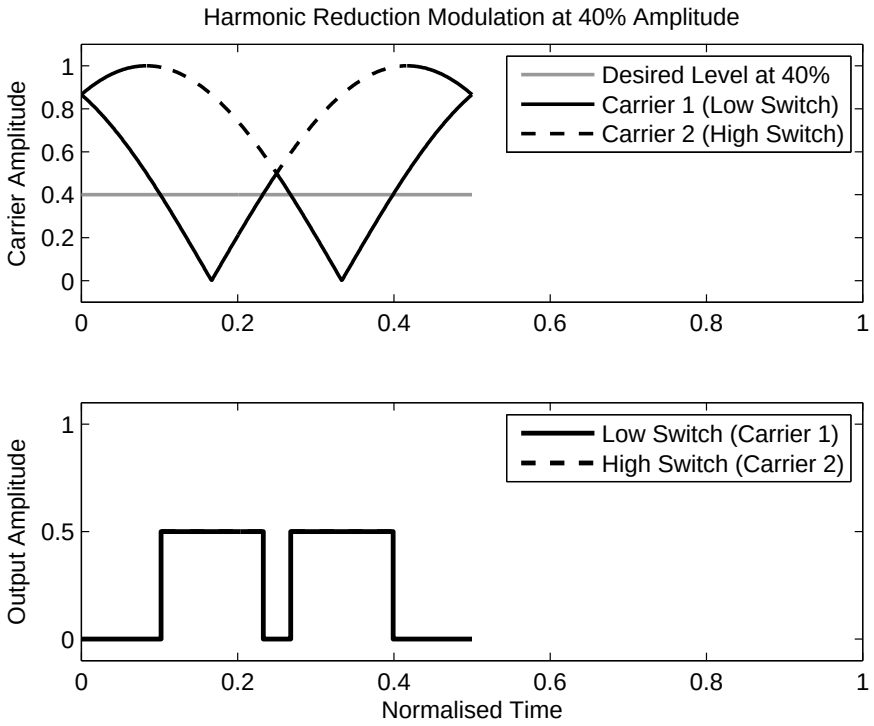

Figure 7.25: Encoding of HRPWM signals at 40% amplitude

encoded switched mode signal. Again it can be seen that the width of the pulse generated by the low switch increases and decreases with increasing desired amplitude.

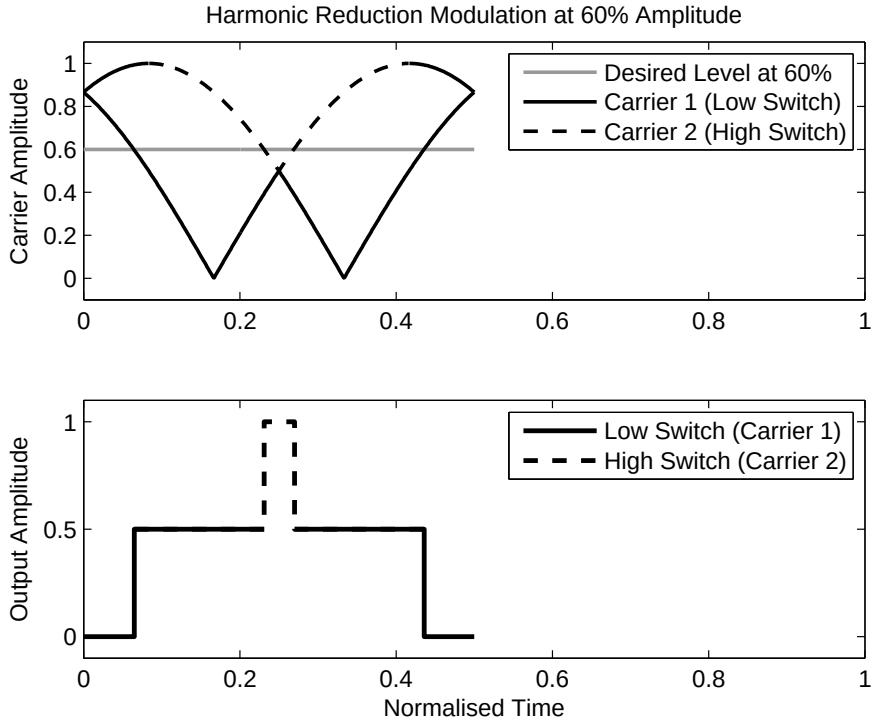

Figure 7.26: Encoding of HRPWM signals at 60% amplitude

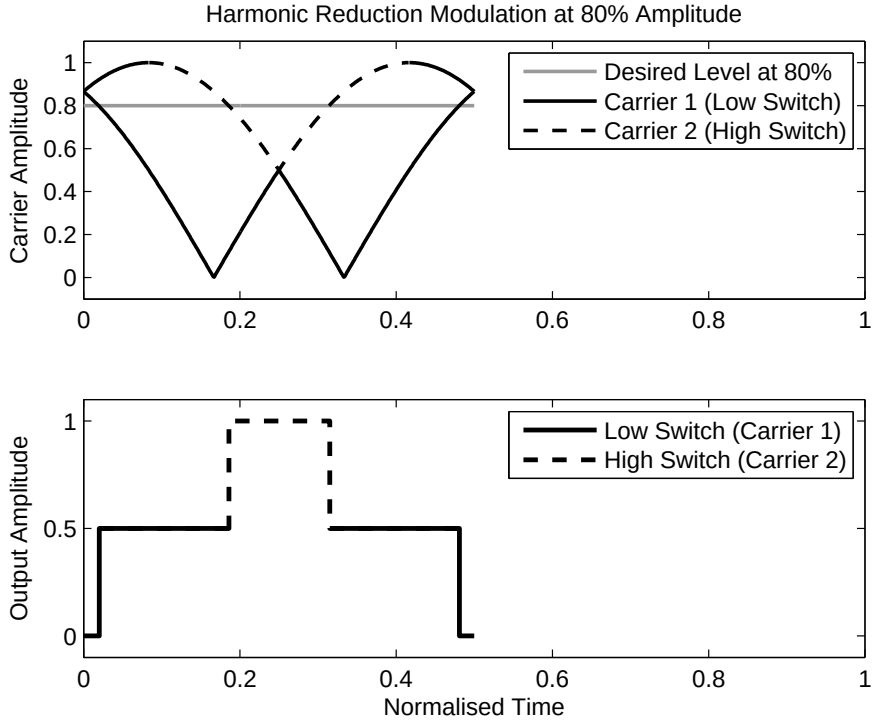

Figure 7.27: Encoding of HRPWM signals at 80% amplitude

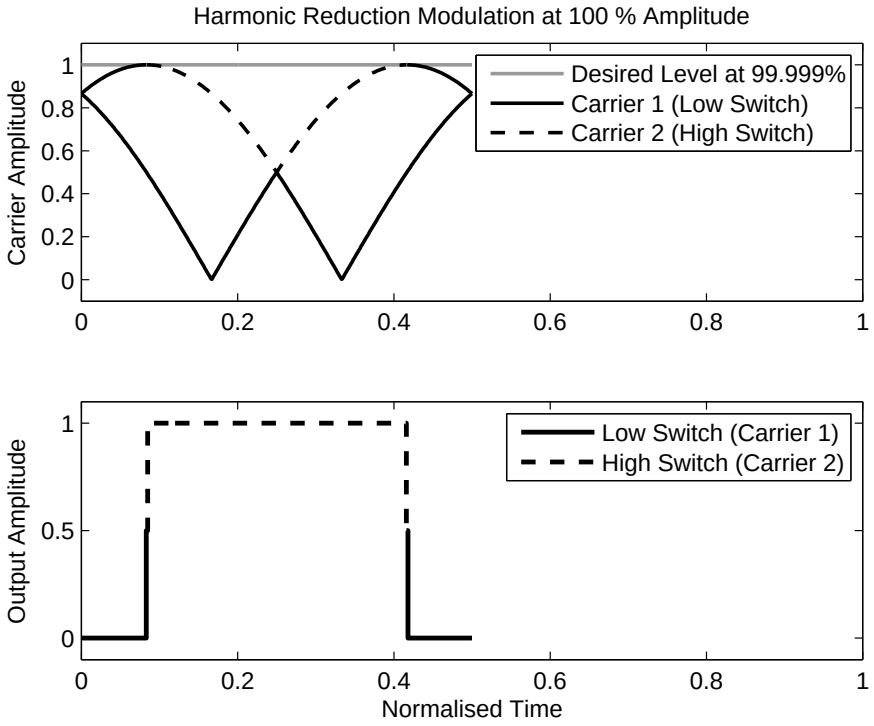

Figure 7.28: Encoding of HRPWM signals at 100% amplitude

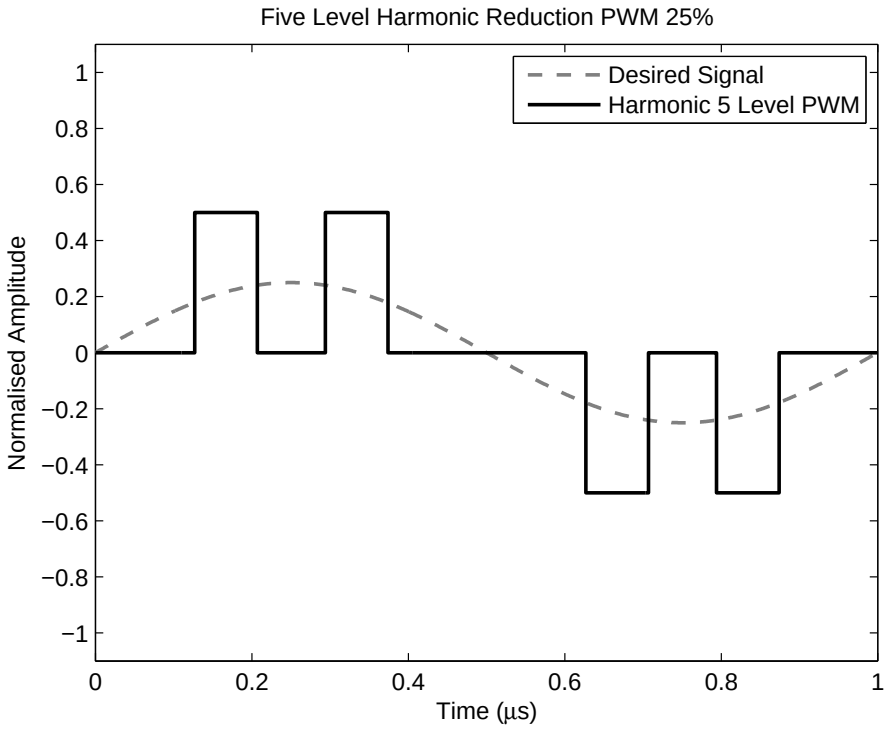

Figure 7.29: HRPWM 25% Amplitude

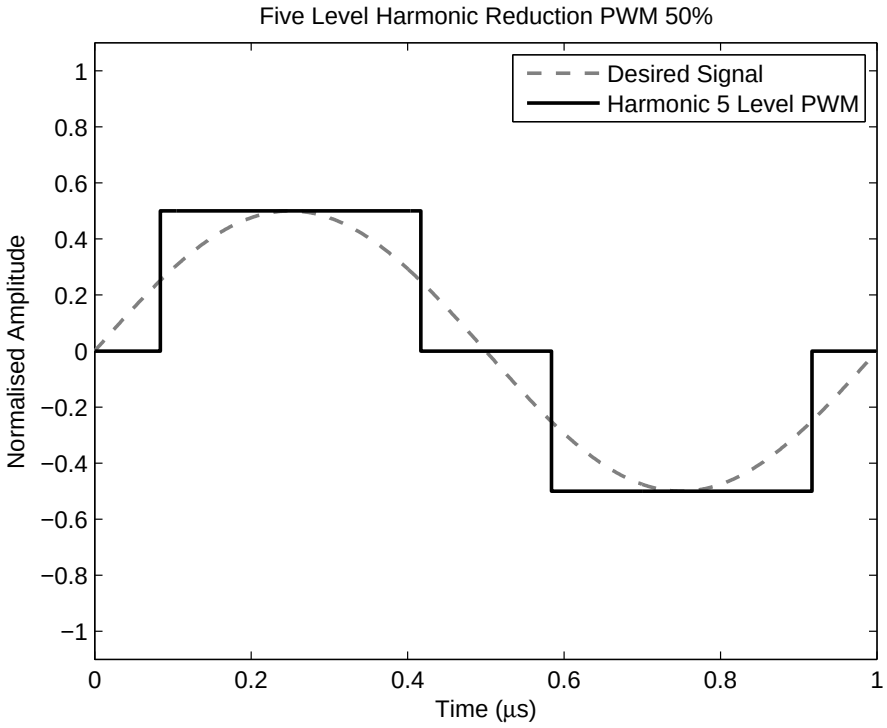

Figure 7.30: HRPWM 50% Amplitude

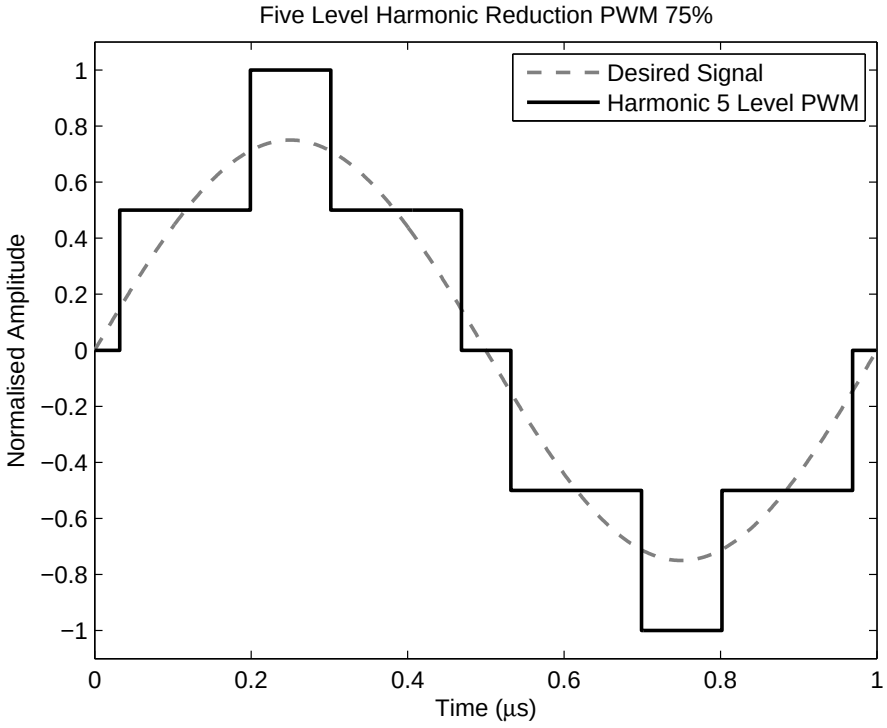

Figure 7.31: HRPWM 75% Amplitude

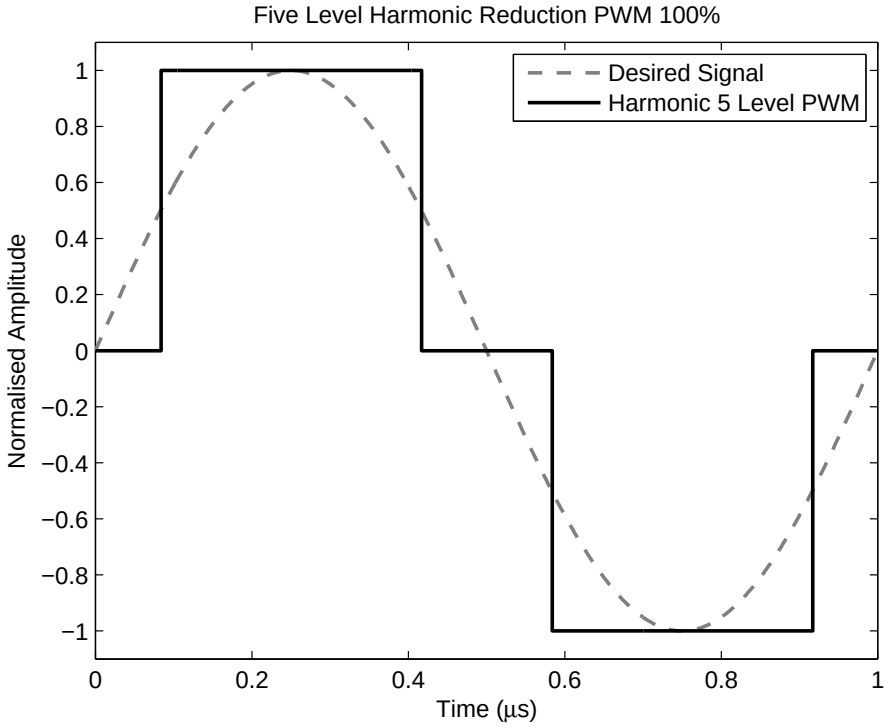

Figure 7.32: HRPWM 100% Amplitude

7.7 Evaluation of HRPWM signals

7.7.1 Simulation

This section demonstrates both control of fundamental amplitude, and reduction of third harmonic. Comparison is made between the PWM method shown in Chapters 5 and 6, and the HRPWM method discussed in this chapter. Firstly, a 6-cycle, Gaussian-windowed, 3 MHz tone-burst is considered, as shown in Figure 7.33. Gaussian windowed signals are desirable in applications such as harmonic imaging, as propagation does not distort the envelope of the signal [168]. This desired waveform can be encoded to a PWM switched-mode signal, or a HRPWM switched mode signal respectively as shown in Figures 7.34 and 7.35. Both PWM and HRPWM sequences have been designed with a sampling frequency of 100 MHz.

Figures 7.36 and 7.37 show the spectral content of the PWM and HRPWM signals respectively. It can be seen that the spectral noise floor is between -35 dB and -40 dB. For the PWM case there is a large third harmonic at approximately-15 dB below the

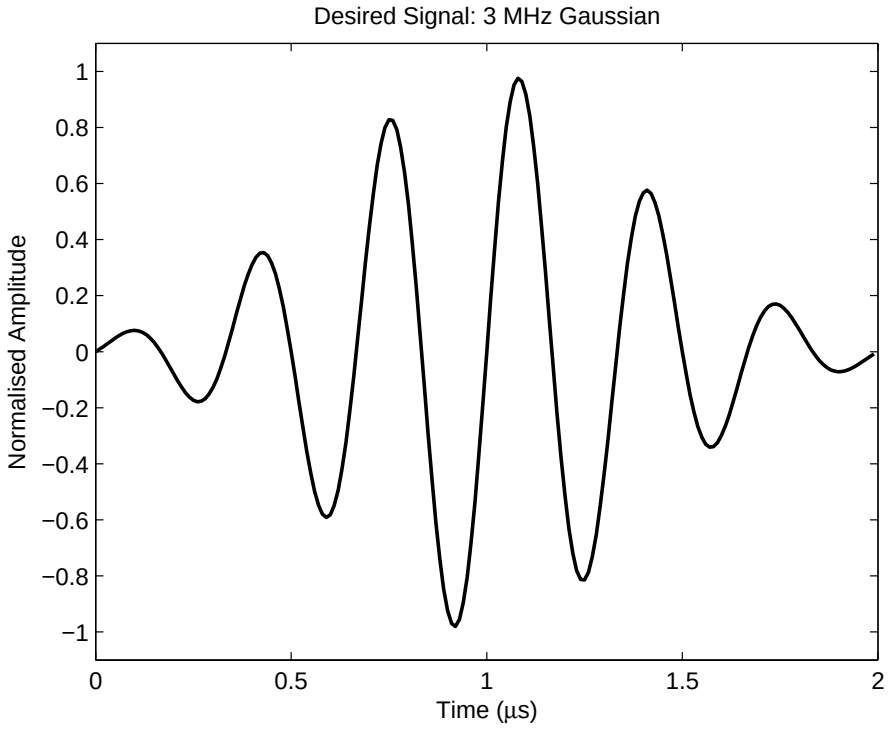

Figure 7.33: Desired 6-cycle Gaussian windowed tone-burst

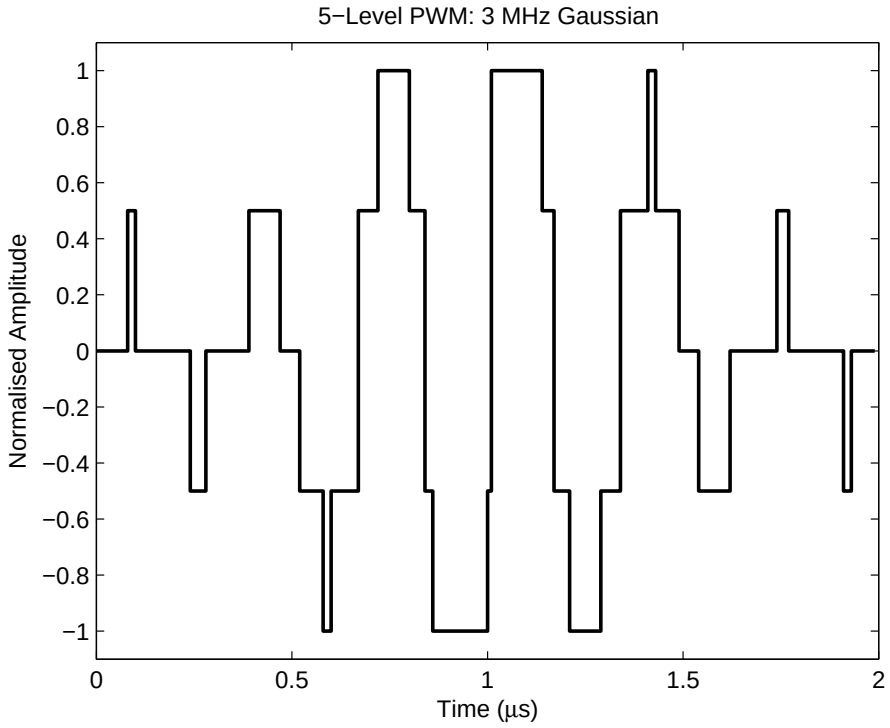

Figure 7.34: PWM encoded switched-mode signal 6-cycle, Gaussian-windowed tone-burst

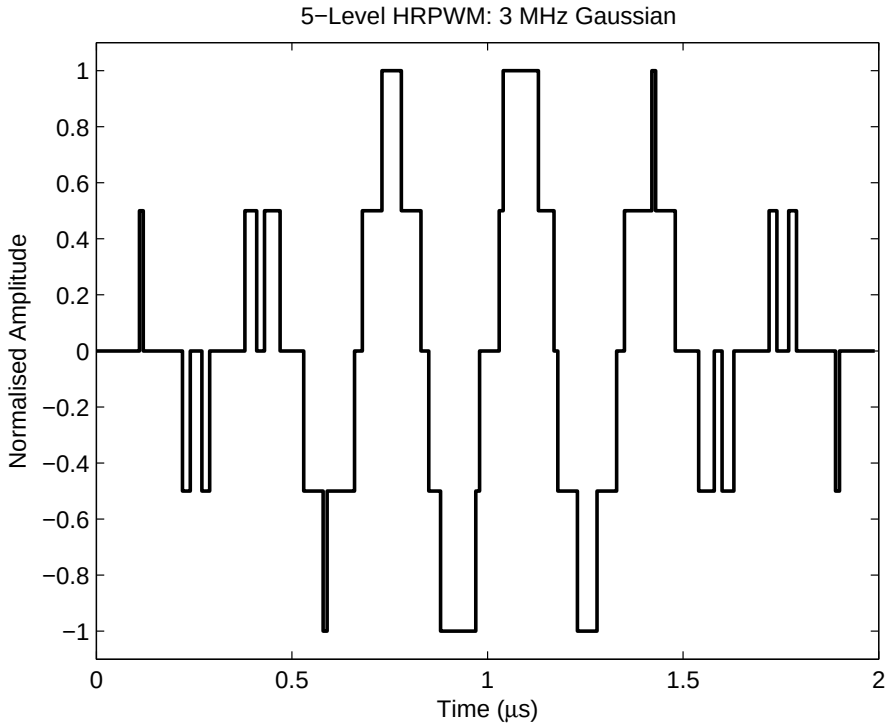

Figure 7.35: HRPWM encoded switched-mode signal 6-cycle, Gaussian-windowed tone-burst

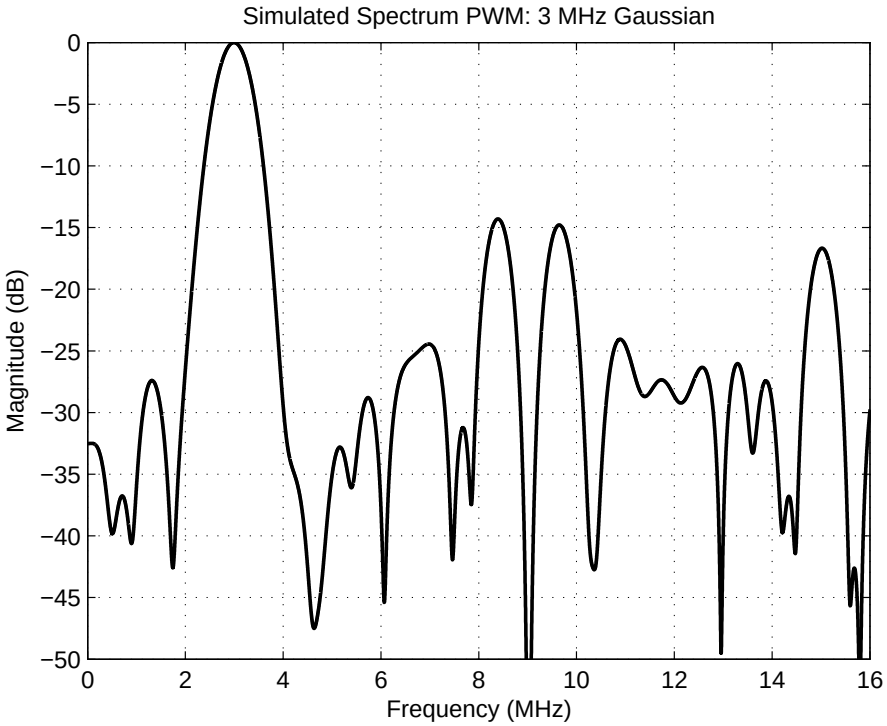

Figure 7.36: Spectrum of PWM encoded switched-mode signal 6-cycle, Gaussian-windowed tone-burst

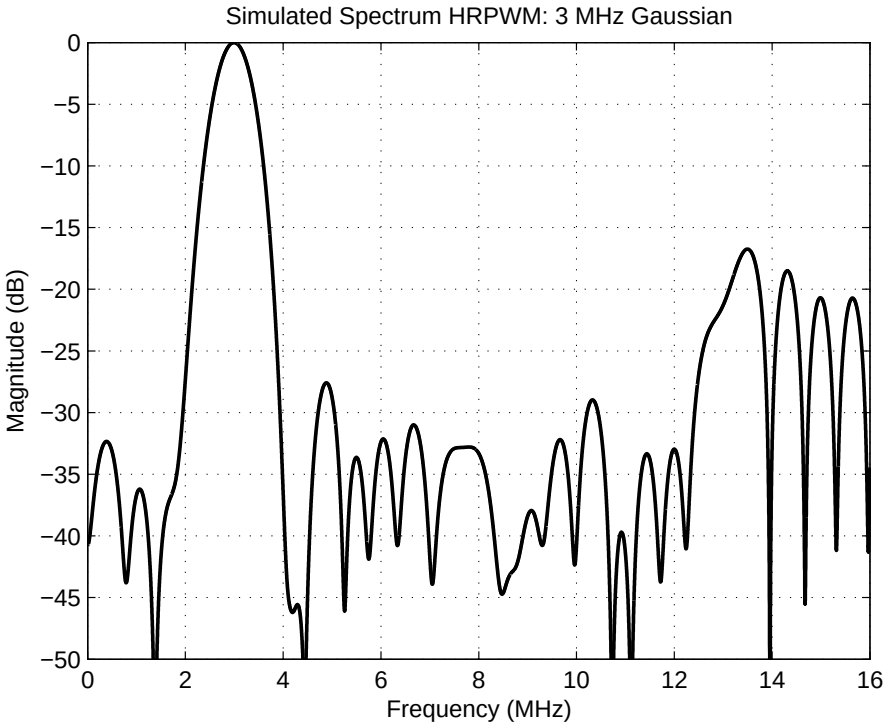

Figure 7.37: Spectrum of HRPWM encoded switched-mode signal 6-cycle, Gaussian-windowed tone-burst

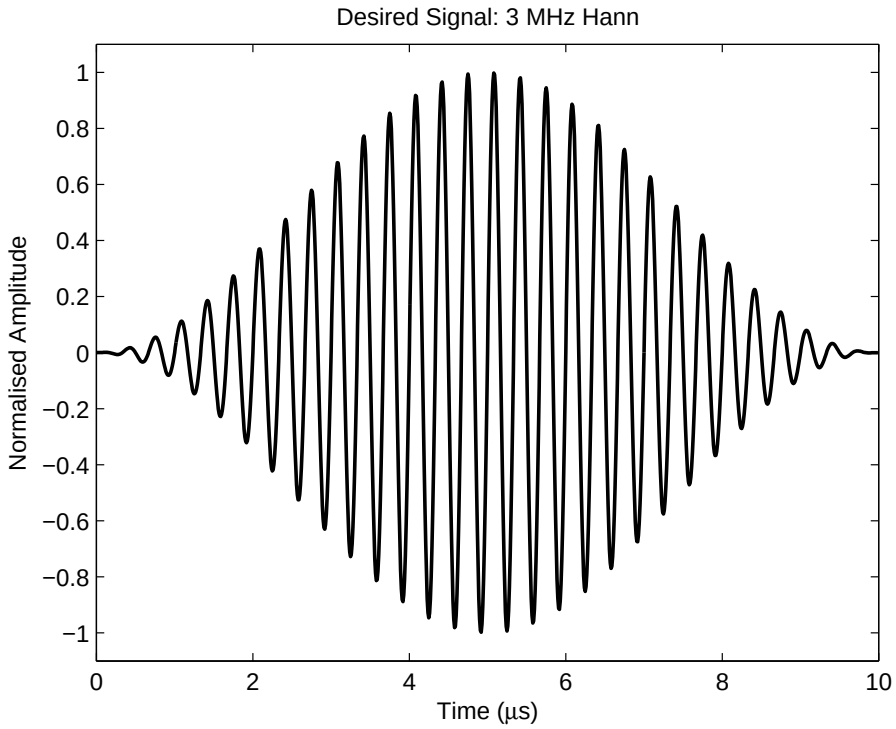

Figure 7.38: Desired 10 µs, Hann-windowed, 3 MHz tone-burst

fundamental. Whereas for the HRPWM case the third harmonic content is reduced to the same level as the spectral noise. This can also be seen in a second example. For this case, the desired signal is a 10 µs, Hann-windowed, 3 MHz tone-burst, as shown in Figure 7.38. PWM and HRPWM sequences are encoded at 100 MHz as shown in Figures 7.39 and 7.40 respectively. It can be seen that the spectrum of the PWM encoded signal in Figure 7.41 has a third harmonic component at a peak value of 15 dB below the fundamental, and above the spectral noise floor at 35 - 40 dB. For the HRPWM encoded case the third harmonic component is reduced to the same level as the spectral noise floor as shown in Figure 7.42.

A last example shows a 10 µs duration, hann-windowed, LFM chirp signal from 3 MHz to 4 MHz. Once again, PWM and HRPWM encoding can be applied to the desired signal using the respective carrier comparison methods. Encoded switched-mode signals are shown in Figures 7.44 and 7.45. Inspection of the harmonic content of each signal shows that the PWM case (Figure 7.46) has a peak value of third harmonic content, in the range 9-12 MHz, at -15 dB. In comparison with the HRPWM case in Figure 7.47, once again the third harmonic content is successfully reduced.

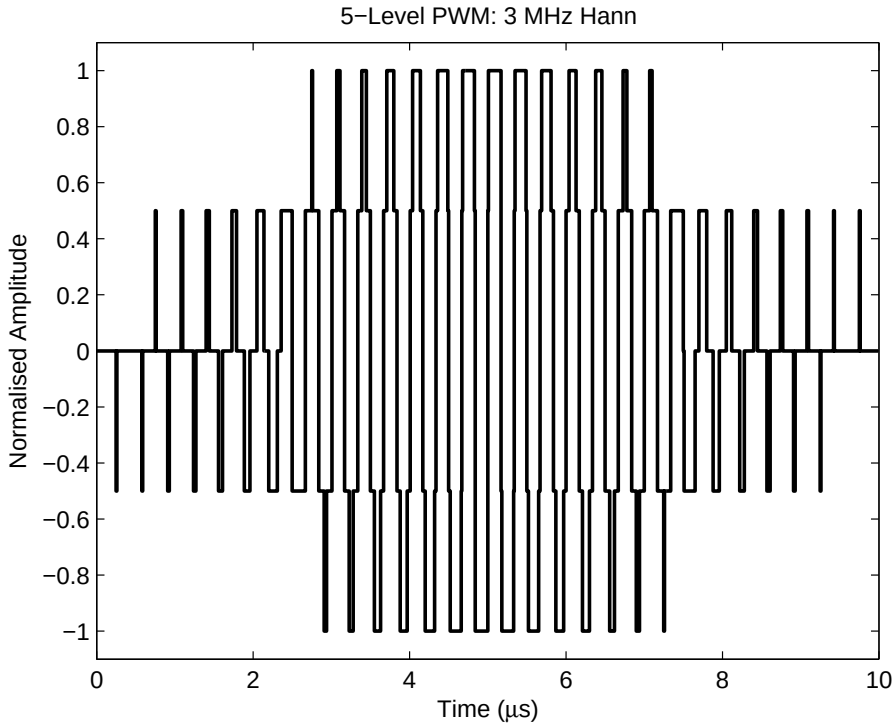

Figure 7.39: PWM encoded switched-mode signal 10 μs, Hann-windowed, 3 MHz tone burst

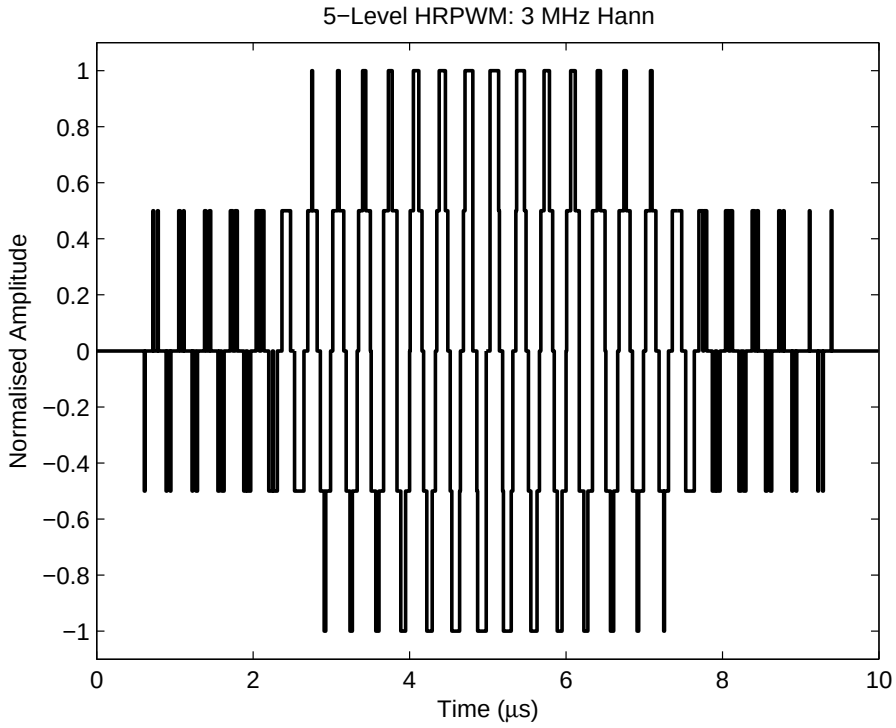

Figure 7.40: HRPWM encoded switched-mode signal 10 μs, Hann-windowed, 3 MHz tone burst

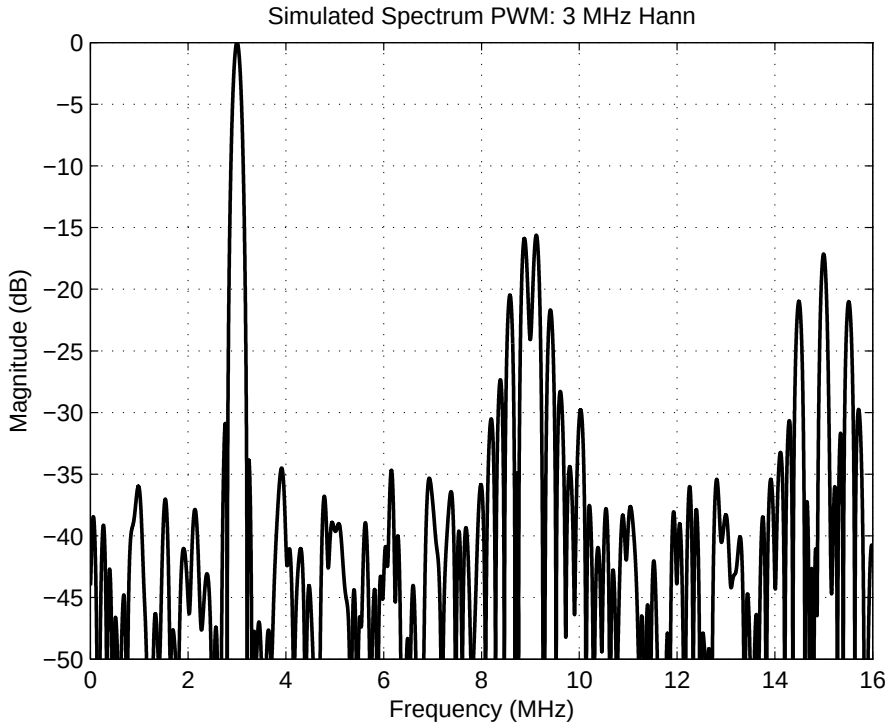

Figure 7.41: Spectrum of PWM encoded switched-mode signal 10 µs, Hann-windowed, 3 MHz tone burst

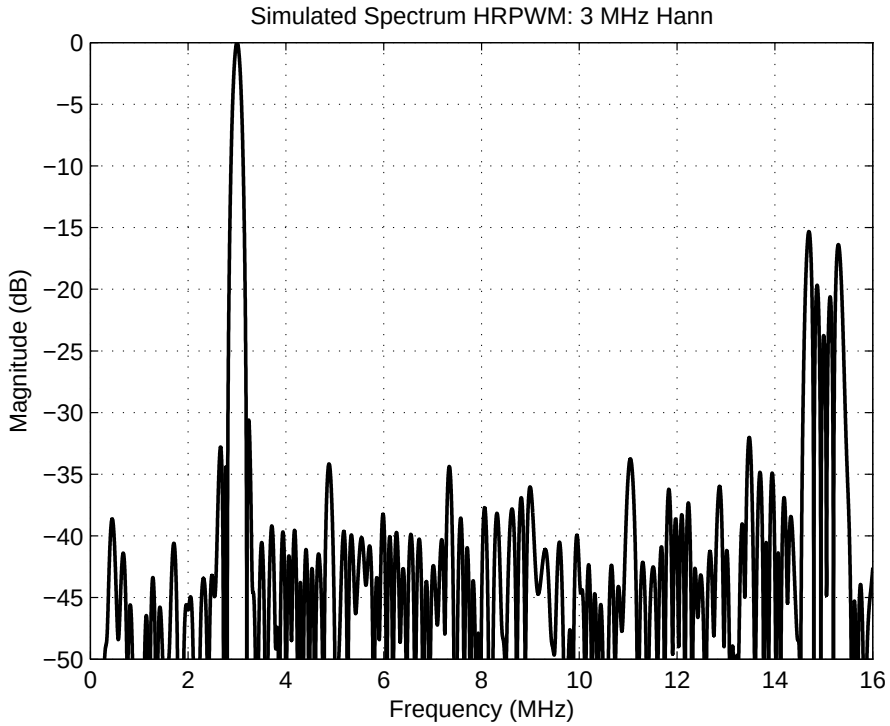

Figure 7.42: Spectrum of HRPWM encoded switched-mode signal 10 µs, Hann-windowed, 3 MHz tone burst

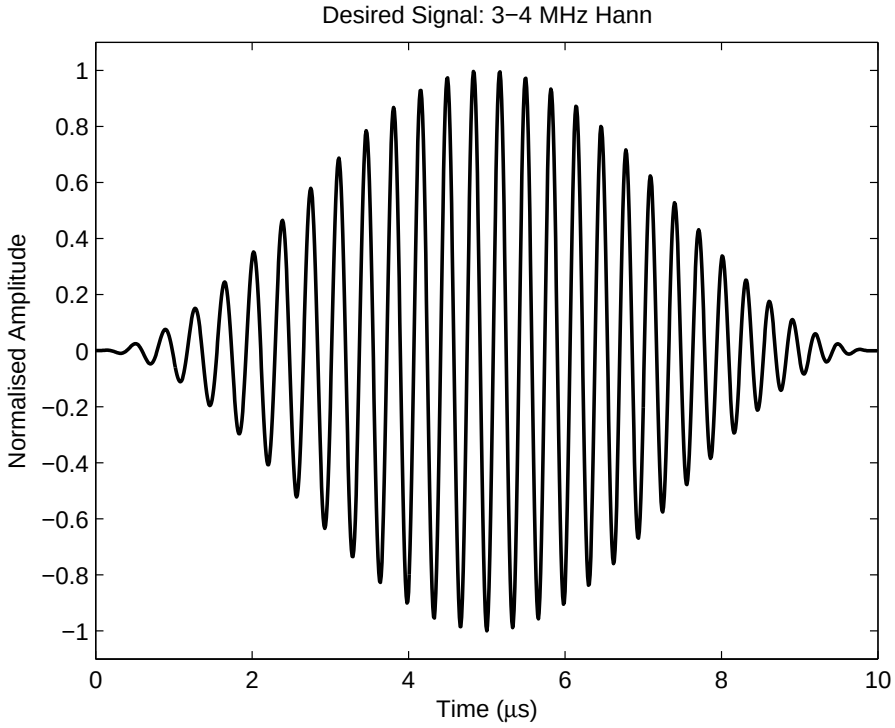

Figure 7.43: Desired 10 µs, Hann-windowed, 3-4 MHz LFM chirp

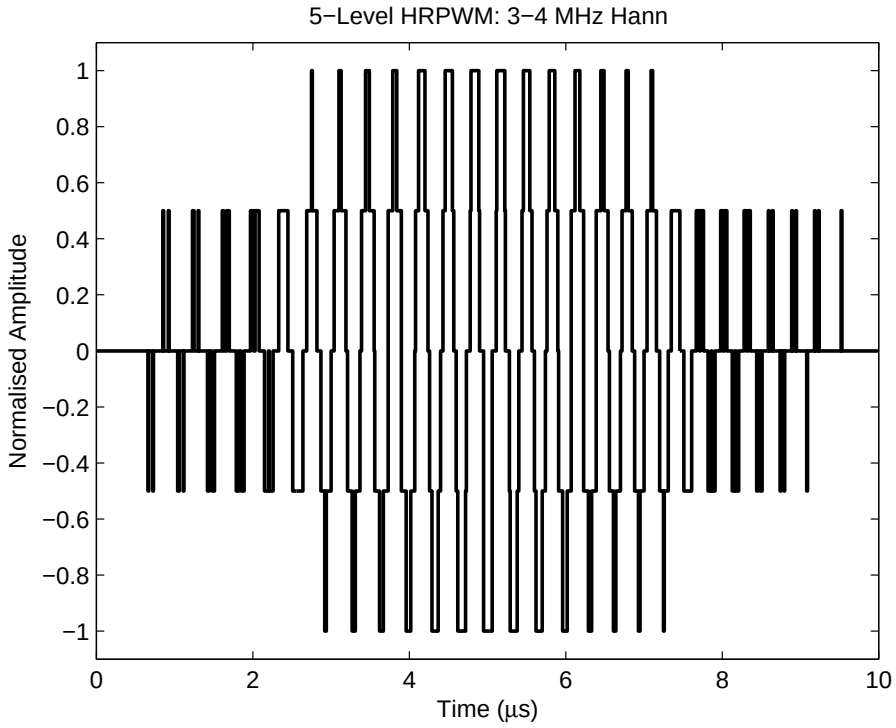

Figure 7.44: PWM encoded switched-mode signal 10 µs, Hann-windowed, 3-4 MHz LFM chirp

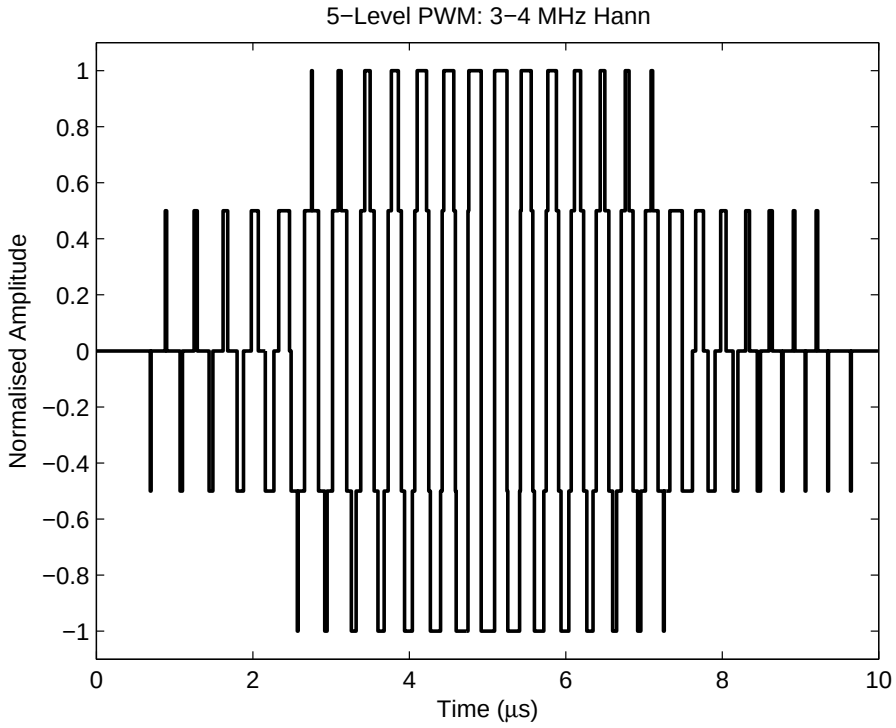

Figure 7.45: HRPWM encoded switched-mode signal 10 µs, Hann-windowed, 3-4 MHz LFM chirp

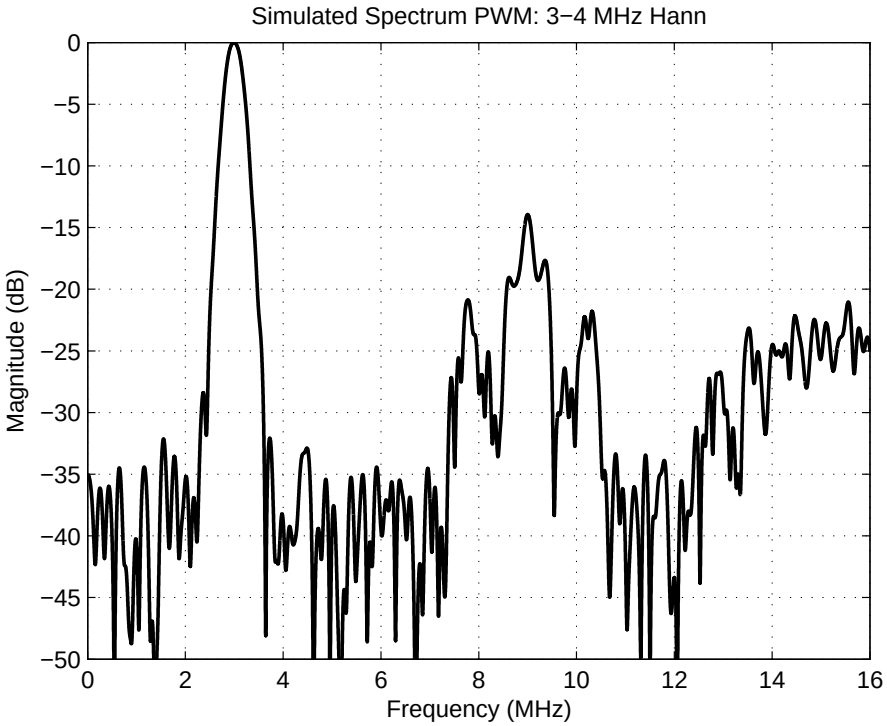

Figure 7.46: Spectrum of PWM encoded switched-mode signal 10 µs, Hann-windowed, 3-4 MHz LFM chirp

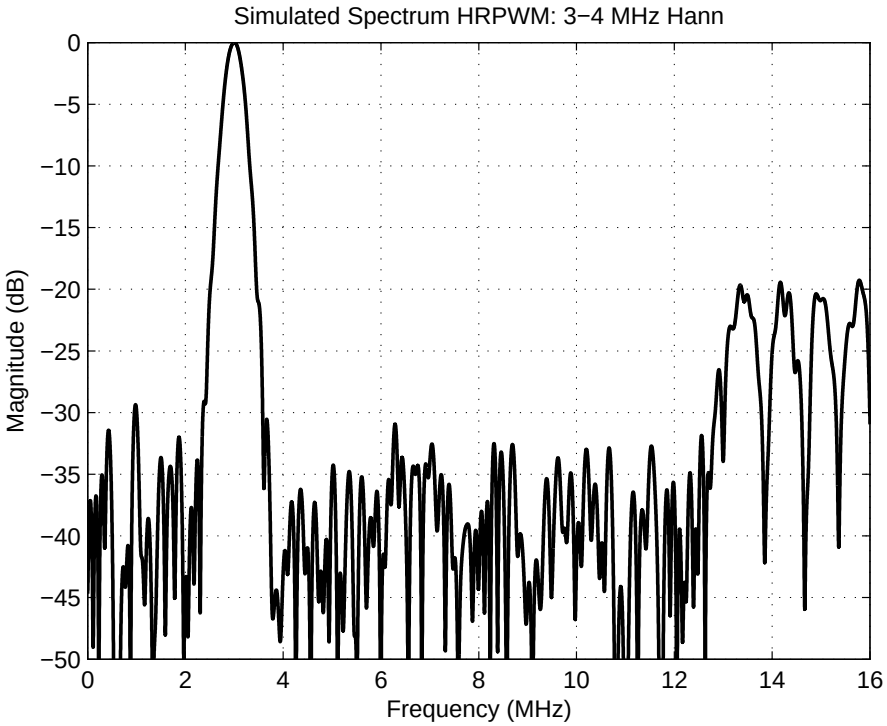

Figure 7.47: Spectrum of HRPWM encoded switched-mode signal 10 µs, Hann-windowed, 3-4 MHz LFM chirp

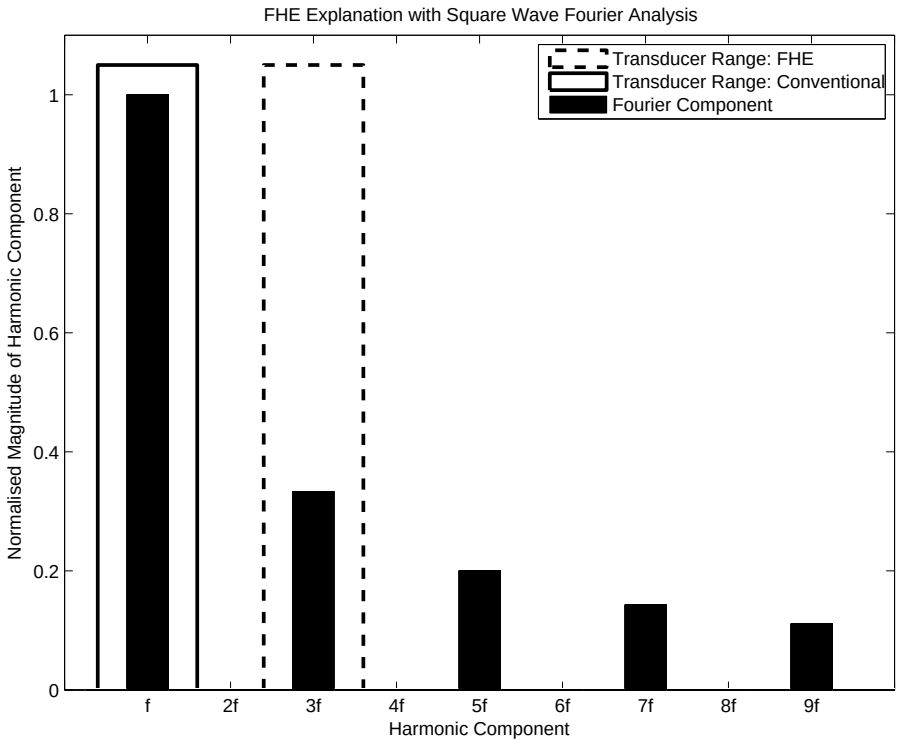

Figure 7.48: Fractional harmonic excitation method using third harmonic

7.7.2 Experimental

Experimentally showing the effect of increased or decreased third harmonic requires the use of a very wide bandwidth transducer, such as a CMUT. Previous research however has shown that a transducer will respond to an excitation harmonic matched to the centre frequency or bandwidth [6]. [6] demonstrated how switching frequencies could be used to excite transducers at higher frequencies, for both tone and coded imaging. In [6] a fractional, harmonic excitation was used, the basis of which is shown in Figure 7.48, where the excitation signal deliberately contains a large third harmonic, and the fundamental frequency is designed at a fraction $(1/3)$ of the desired fundamental. It is the third harmonic that is then transmitted with most amplitude by the transducer.

In the absence of a very wide bandwidth transducer, a strategy similar to [6] has been used to further demonstrate a reduction in third harmonic content. A difference between the work described in this section, and with [6] is that in this case, it is desired to reduce the level of third harmonic transmitted, as opposed to attempting to utilise it effectively. Excitation signals were designed with a fundamental frequency of $1/3$ of the transducer's

peak frequency. This ensured that third harmonic content was at the peak of the bandwidth, and would not be suppressed by the 'roll off' of the transducer's bandwidth at higher frequencies. The transducer used was the Prosonic L3-8 array transducer used throughout this thesis (shown in Figure 4.76 and described in Table 4.6), and experimental signals were obtained using a 1 mm needle hydrophone (shown in Figure 5.13) aligned with the face of the transducer as described in previous chapters. Successful harmonic reduction should see a lower level of output from the transducer with matched input signals.

Figures 7.49 and 7.50 show transducer-loaded switched-mode signals of PWM and HRPWM, as generated by the UARP, encoded for a 10 μs, 1.6 MHz, Hann windowed tone burst. Averaging of 100 measurements was used to reduce noise. As the HRPWM sacrifices maximum amplitude, for harmonic control, switching levels were adjusted so that equal pressure was output by each technique before evaluating for harmonic reduction. It is noticeable from Figures 7.49 and 7.50 the effect of rise and fall time from the MOSFET devices at the start and end of the sequences (low desired amplitude). This shows that the MOSFET cannot switch as quickly as the minimum 'on' period determined by the sampling frequency (10 ns) and therefore cannot rise to full amplitude before switching off again. This effect was also seen in the pulse shaping examples in Chapter 5 when moving from the low level to high level switching, with a slight distorting due to non-ideal switching.

Figure 7.51 shows an FFT of the transducer-loaded excitation signals shown in Figures 7.49 and 7.50. Notice the peak frequency is at 1.6 MHz, with the PWM signals containing a third harmonic component at -17 dB, and the HRPWM signals showing third harmonic content at -27 dB (10 dB difference).

Figures 7.52 and 7.53 show the simulated and experimental pressure waveforms for the PWM case. To complement these, Figures 7.54 and 7.55 show the simulated and experimentally obtained pressure waveforms respectively. To simulate pressure waveforms radiated from the transducer, a linear time-invariant model is assumed. Pressure waveforms can then be simulated by convolving the PWM sequence with the transducer's impulse response as described in (5.37). It can be seen, especially for the PWM case, that

simulation predicts the response of the transducer particularly accurately. Overall there is a reduction in third harmonic content, as can be seen in the FFT of the experimentally obtained pressure waveforms shown in Figure 7.56. of greater than 10 dB.

A second example shows an LFM signal (10 µs, 1.1 - 2.1 MHz, Hann window) encoded with PWM and HRPWM methods. Transducer-loaded excitation signals can be seen in Figures 7.57 to 7.58. FFT analysis shows a reduction in third harmonic, however this reduction is not as prevalent towards the higher end of the third harmonic bandwidth ($>$ 6 MHz). This is a result of the HRPWM carrier requiring greater carrier oversampling for optimal results.

Simulated and experimental pressure waveforms (Figures 7.60, 7.61 and Figures 7.62, 7.63) show an expected reduction in third harmonic content. The FFT of the experimentally obtained signals (Figure 7.64) shows improved harmonic reduction in the low and middle parts of the third harmonic bandwidth, with nearly 10 dB difference between the two signals between 4.5 to 5 MHz.

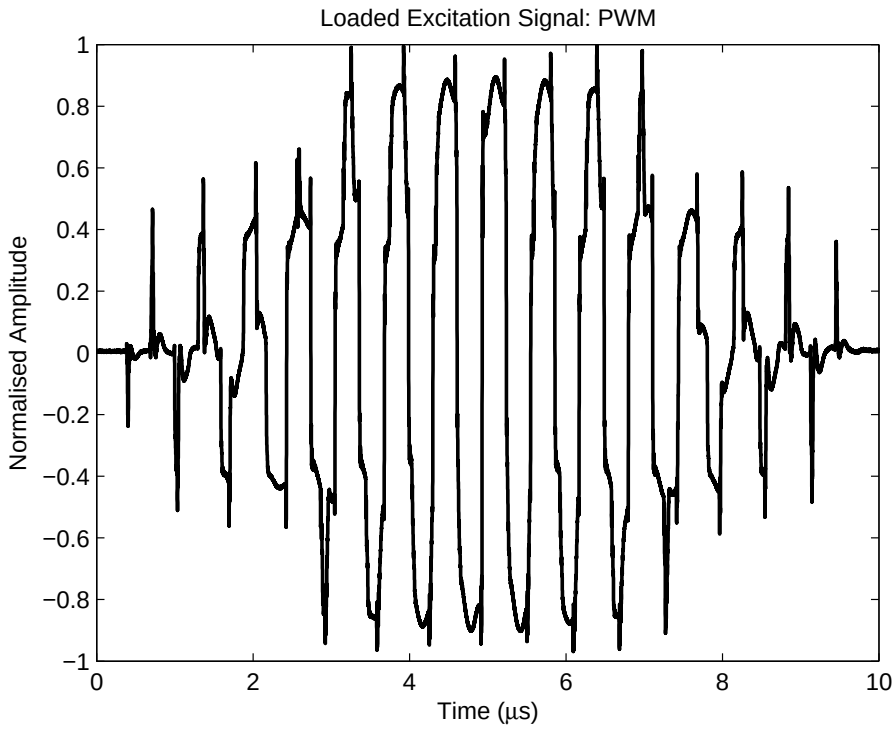

Figure 7.49: Transducer-loaded PWM electrical signal for 10 µs, 1.6 MHz, Hann-windowed tone-burst (100 measurements averaged)

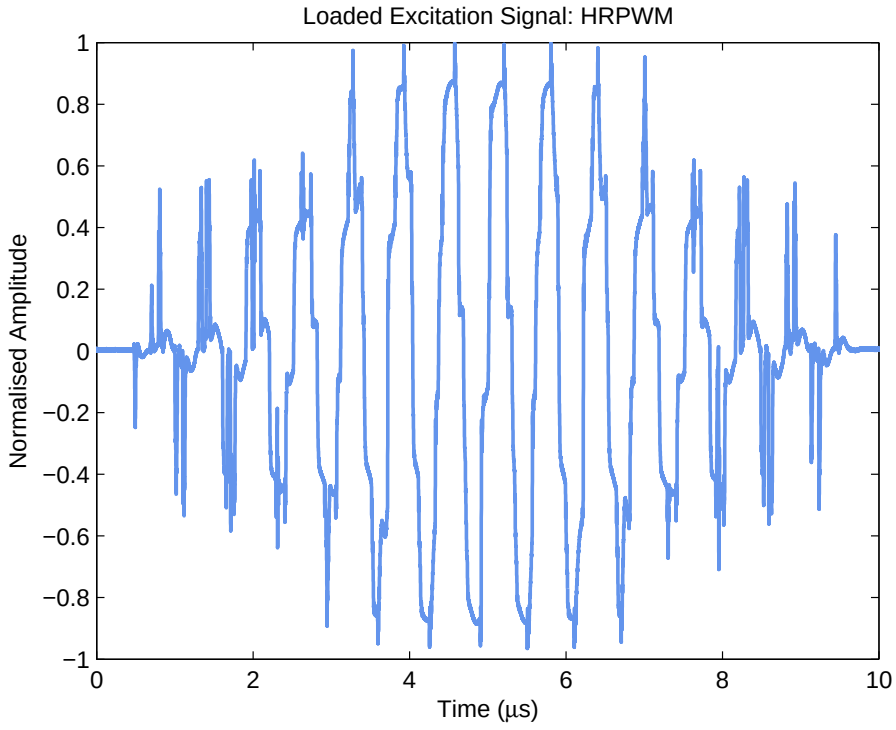

Figure 7.50: Transducer-loaded HRPWM electrical signal for 10 µs, 1.6 MHz, Hann-windowed tone-burst (100 measurements averaged)

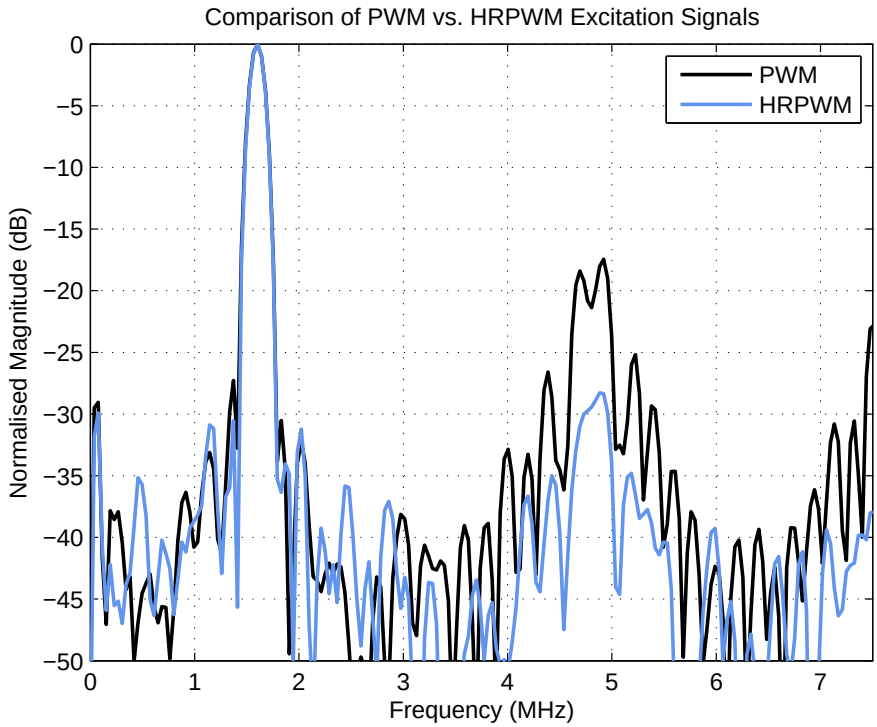

Figure 7.51: FFT of transducer-loaded electrical PWM and HRPWM drive signals showing reduction in third harmonic content (100 measurements averaged)

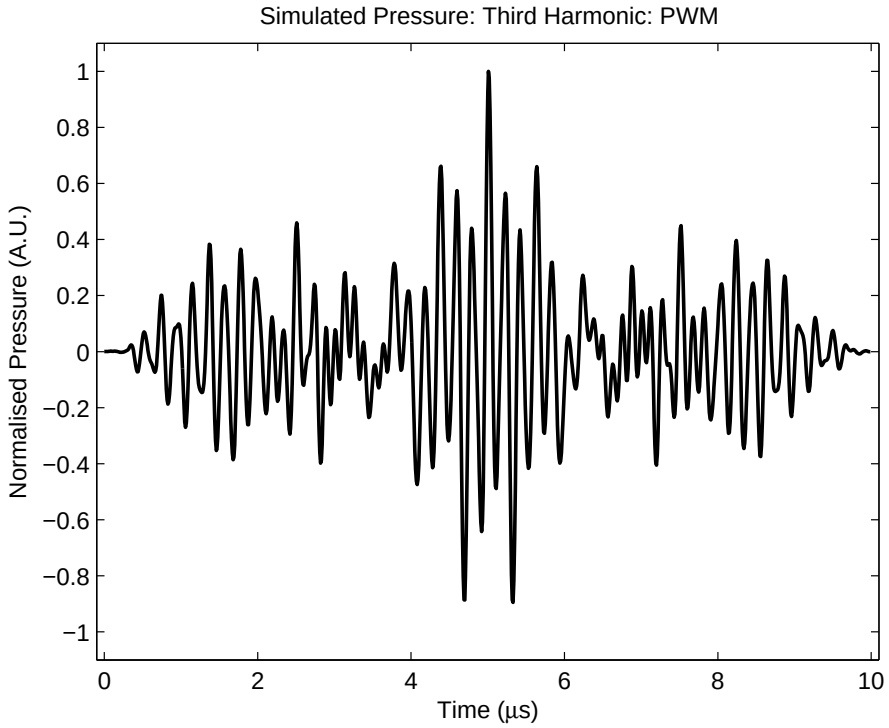

Figure 7.52: Simulated pressure for 10 µs, 1.6 MHz, Hann-windowed tone-burst PWM signal through transducer with centre frequency 5 MHz (third harmonic matched to centre frequency)

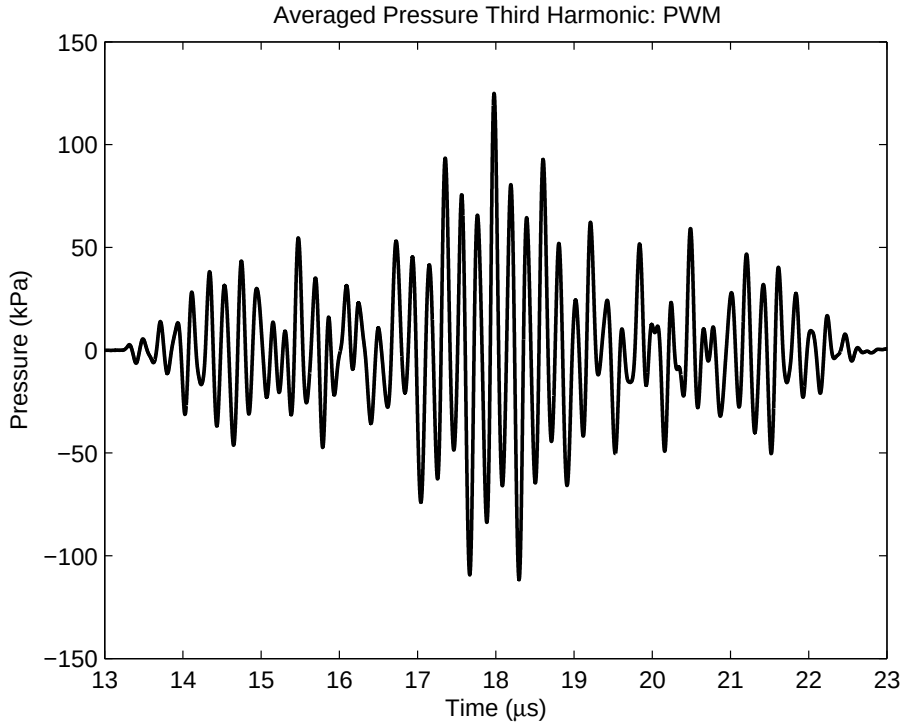

Figure 7.53: Pressure in water from a 10 µs, 1.6 MHz, Hann-windowed, PWM signal through an array transducer (100 measurements averaged)

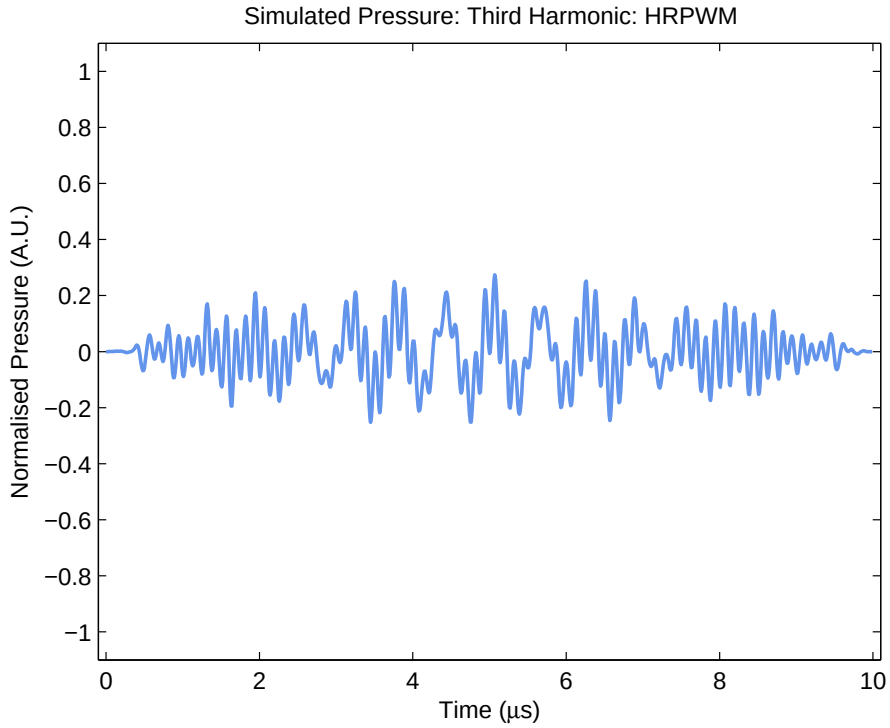

Figure 7.54: Simulated pressure for 10 µs, 1.6 MHz, Hann-windowed tone-burst HRPWM signal through transducer with centre frequency 5 MHz (third harmonic matched to centre frequency)

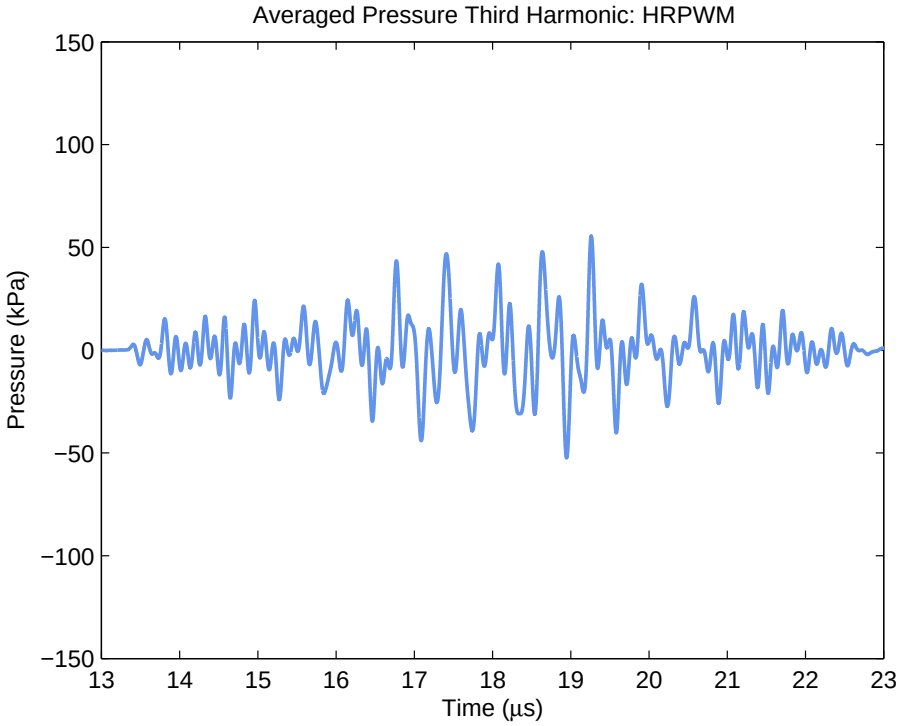

Figure 7.55: Pressure in water from a 10 µs, 1.6 MHz, Hann-windowed, HRPWM signal through an array transducer (100 measurements averaged)

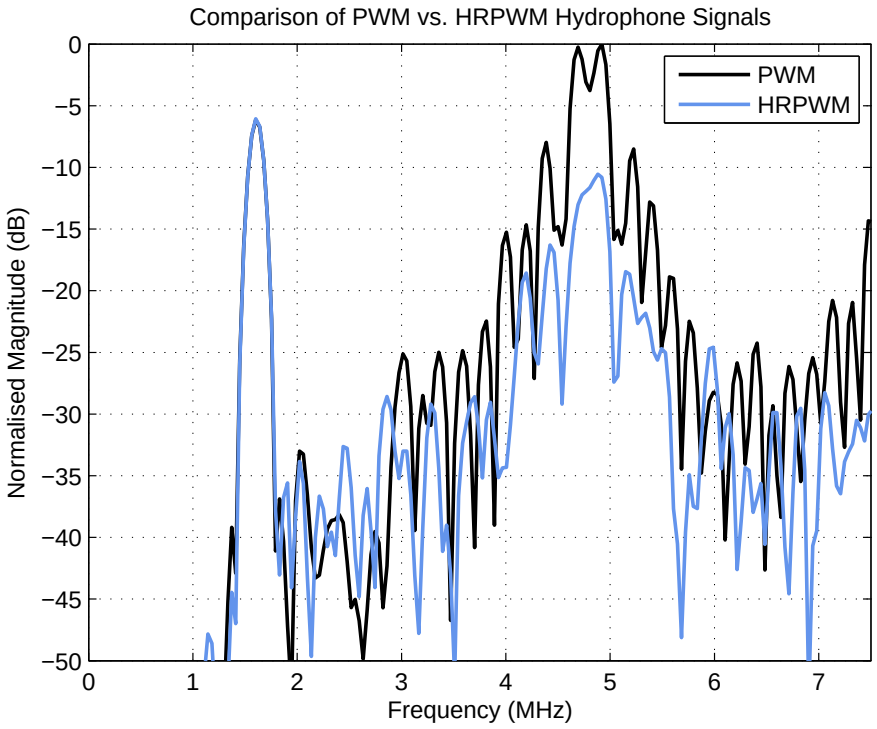

Figure 7.56: FFT of pressure measurements with PWM and HRPWM tone-burst drive signals showing reduction in third harmonic content (100 measurements averaged)

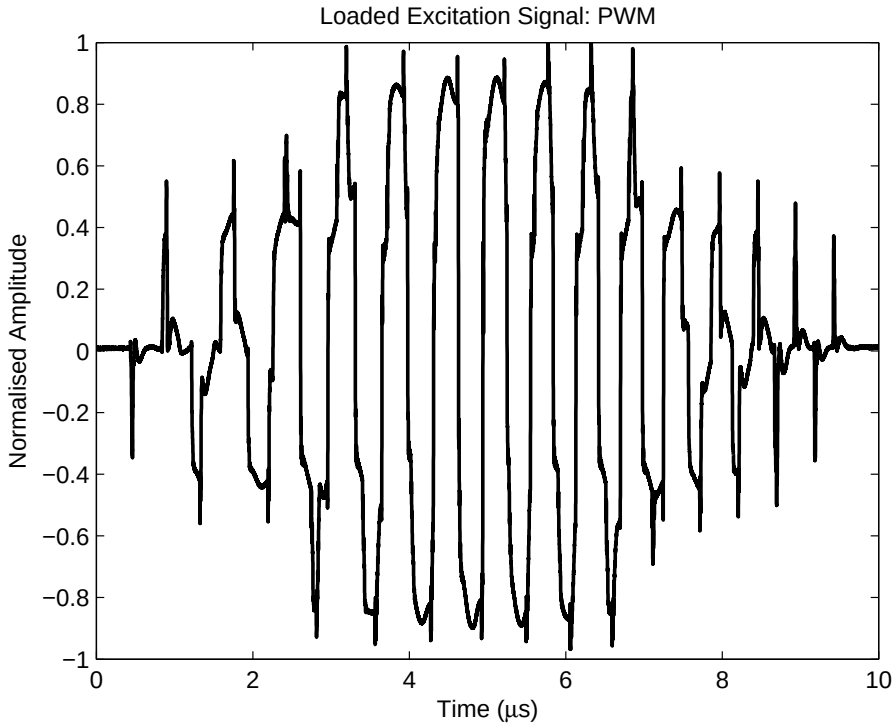

Figure 7.57: Transducer loaded PWM electrical signal for 10 µs, 1.1 to 2.1 MHz, Hann-windowed chirp (100 measurements averaged)

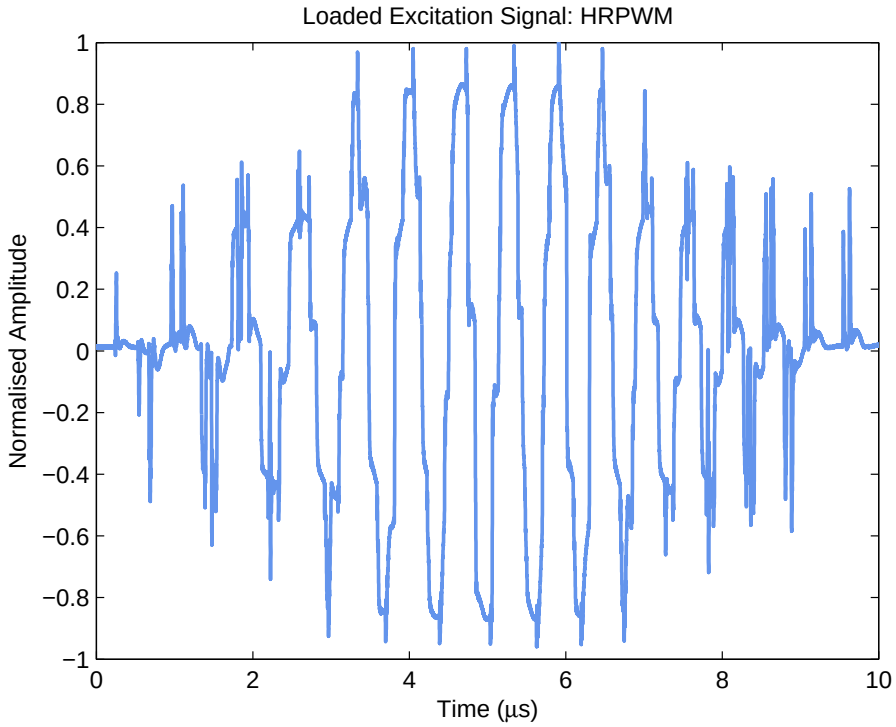

Figure 7.58: Transducer loaded HRPWM electrical signal for 10 µs, 1.1 to 2.1 MHz, Hann-windowed chirp (100 measurements averaged)

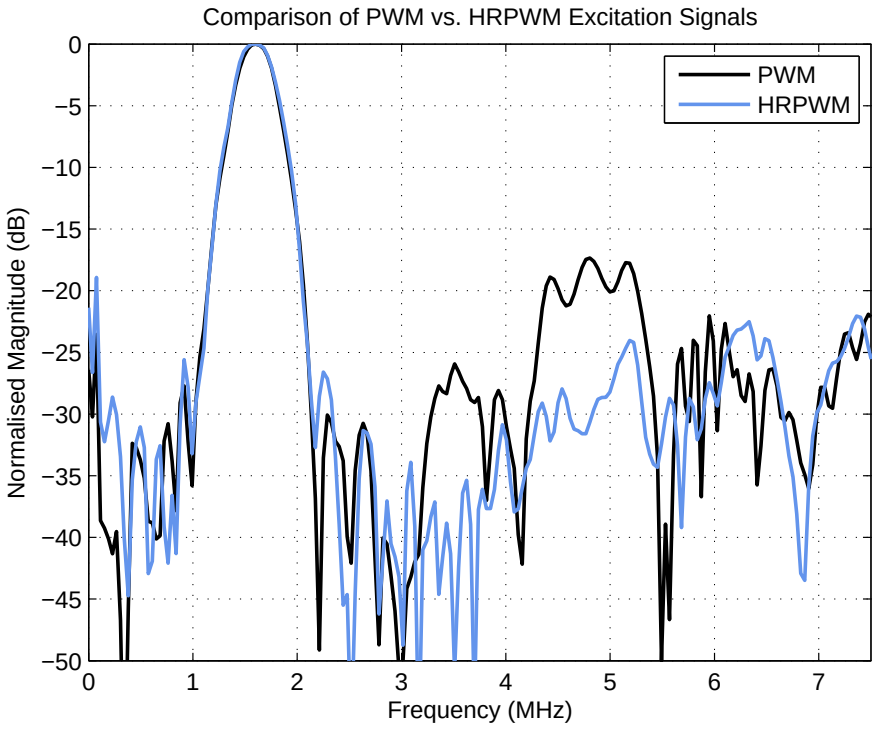

Figure 7.59: FFT of transducer-loaded electrical PWM and HRPWM chirp drive signals showing reduction in third harmonic content (100 measurements averaged)

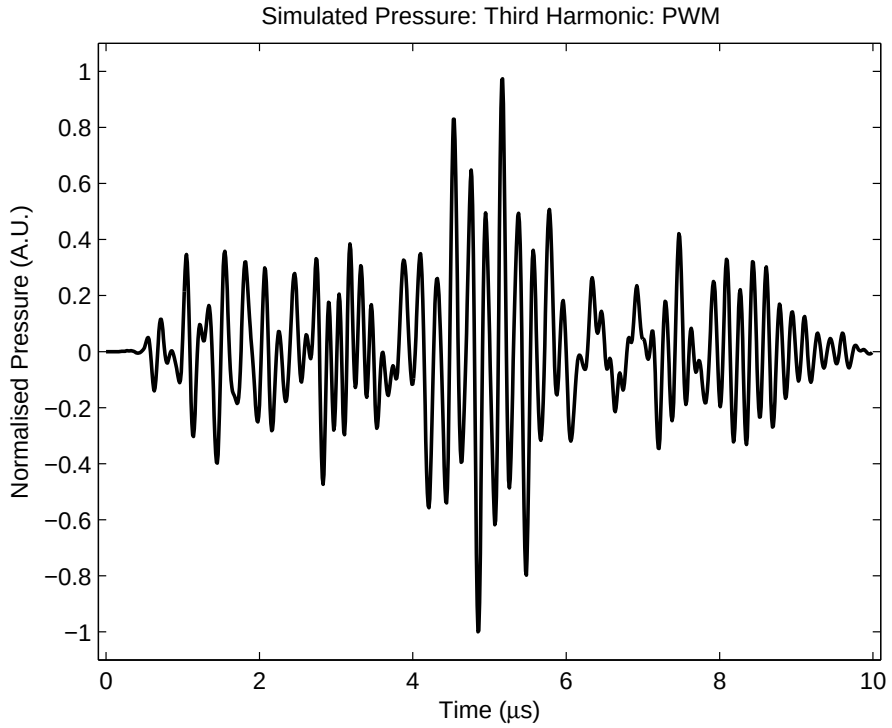

Figure 7.60: Simulated pressure for 10 μs, 1.1 to 2.1 MHz, Hann-windowed chirp PWM signal through transducer with centre frequency 5 MHz (third harmonic matched to centre frequency)

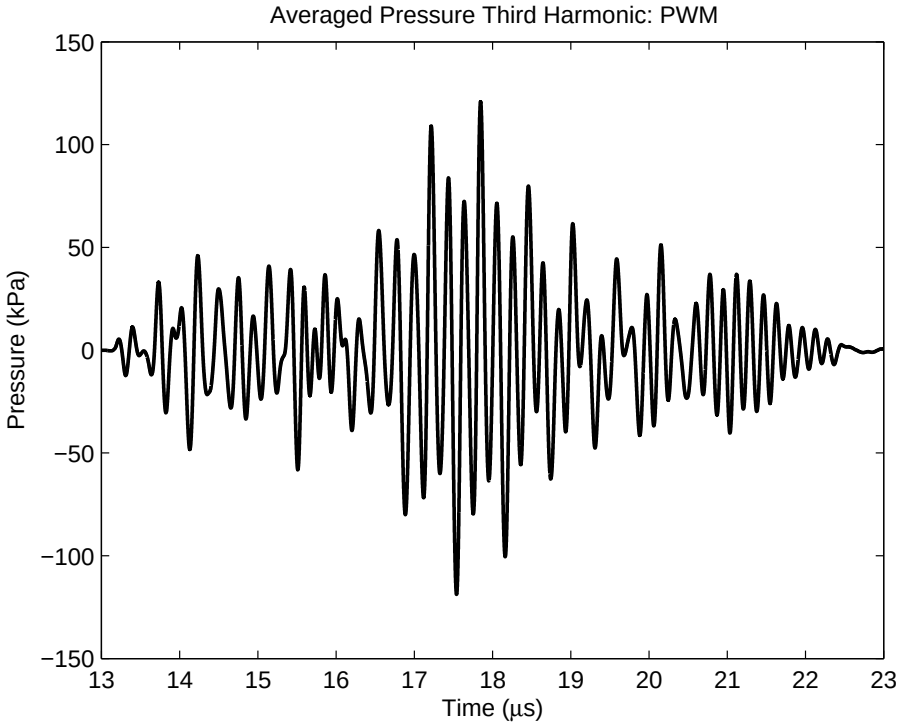

Figure 7.61: Pressure in water from the 10 μs, 1.1 to 2.1 MHz, Hann-windowed, PWM signal through an array transducer (100 measurements averaged)

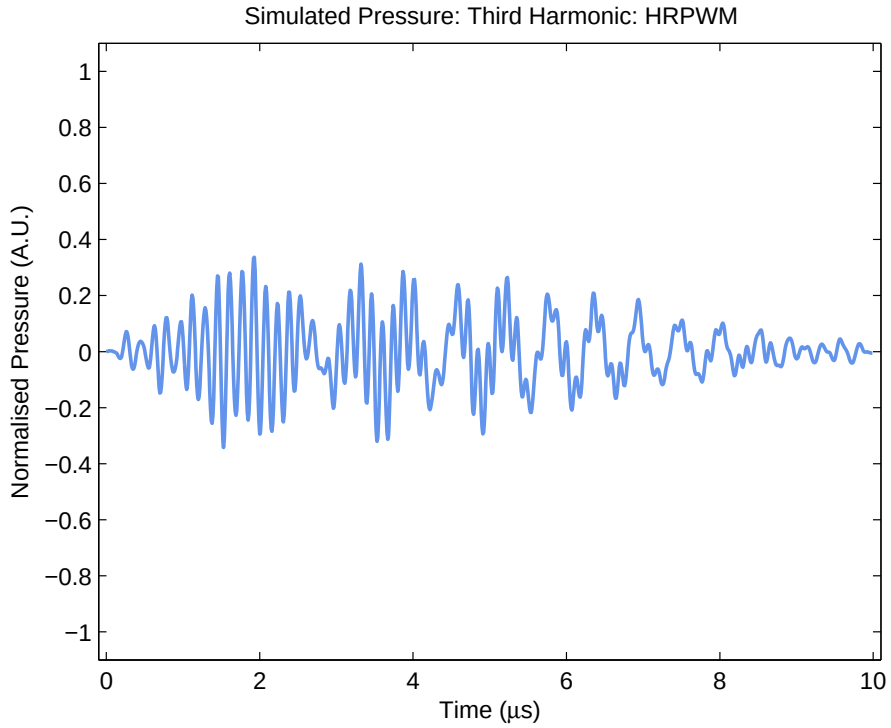

Figure 7.62: Simulated pressure for 10 µs, 1.1 to 2.1 MHz, Hann-windowed chirp HRPWM signal through transducer with centre frequency 5 MHz (third harmonic matched to centre frequency)

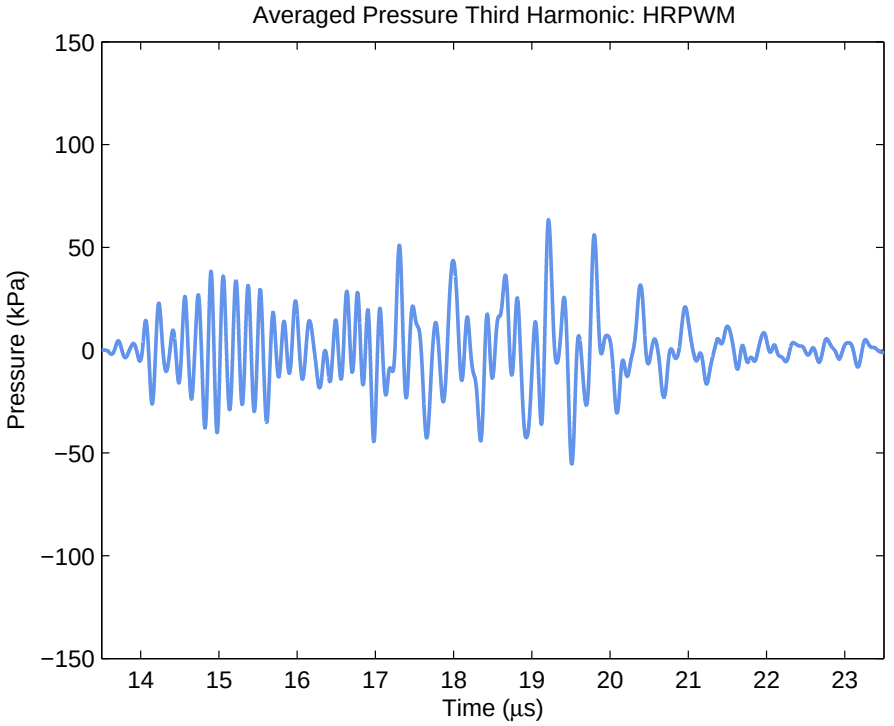

Figure 7.63: Pressure in water from the 10 µs, 1.1 to 2.1 MHz, Hann-windowed, HRPWM signal through an array transducer (100 measurements averaged)

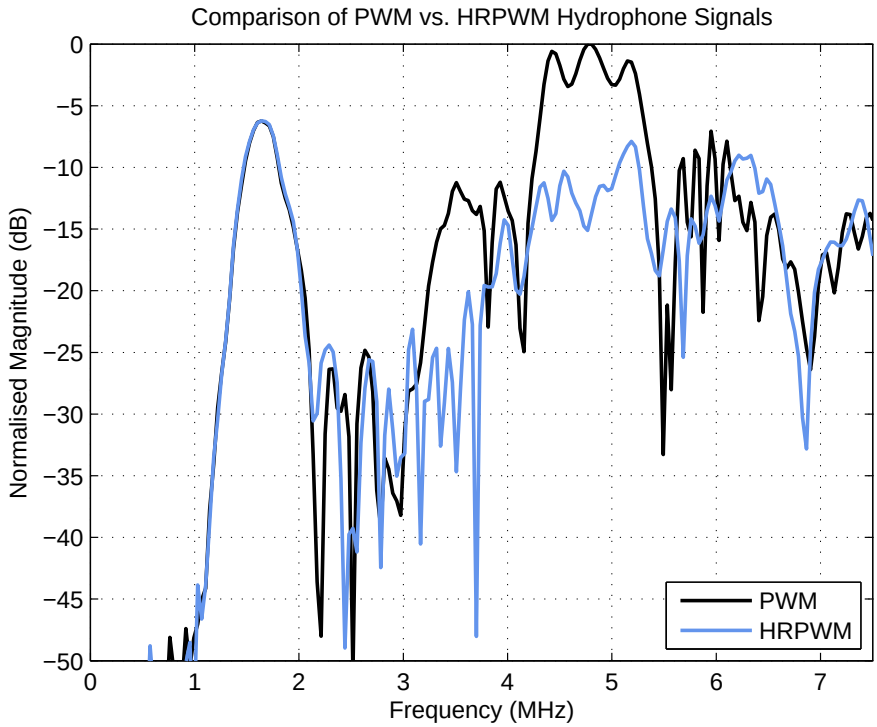

Figure 7.64: FFT of pressure measurements with PWM and HRPWM chirp drive signals showing reduction in third harmonic content (100 measurements averaged)

7.8 Discussion

A comparison can be made between the proposed pulse-width modulation method and existing literature, as follows. Due to the symmetry of a switched-mode bipolar waveform its spectral content is mostly comprised of odd-order components (1,3,5...) as can be seen with Fourier analysis. Tang and Clement [13] discussed a SHE method of reducing the third harmonic in ultrasound switched-mode signals. This method used a single switching angle of $\delta = \pi/6$ to separate positive and negative switching legs by $\pi/3$ thus reducing all $3n$ harmonics. This work was extended further by Cowell in [53], [5] and [7] to suppress multiple odd-order harmonics using multi-level signals. Note that in all these cases pulses were encoded for harmonic content, and not for amplitude control. A patent by Dodd *et al.* described PWM signals for ultrasound imaging with reduced harmonic response [169]. In [169] suppression of harmonic content and control of amplitude was described by using switched mode signals of a variety of forms. Most notably the ability to modulate for shaped pulses, and reduce the second harmonic to -60 dB. The work in this chapter differs from [169] as pulses are encoded to reduce even order harmonics, and the largest odd order harmonic, whilst also encoding for amplitude control and is applicable to tone-burst or coded excitations.

Encoding of the HRPWM sequences is achieved using a carrier comparison method as discussed in Chapters 5 and 6. This carrier comparison encoding relies on digital generation of a carrier waveform. As a consequence the carrier is itself a sampled version of an ideal waveform. Fundamental switching frequency assists with this, as it reduces the overall sampling frequency. To further explain, in conventional PWM, with multiple pulses per cycle, the carrier frequency operates at approximately 10 times the fundamental [13]. In digital carrier generation, this requires a greater oversampling factor to accommodate the carrier frequency at $10f$. Chapter 5 discussed a limitation of PWM generation due to the effect of poor carrier sampling. The HRPWM encoding is more sensitive to this, especially as low sampling rates reduce the number of widths available, thus causing slight deviation from the path of least third harmonic. To prevent this, an estimation of greater than 50 times oversampling is proposed. In combination, it is desirable that the

MOSFETs used at the front end can ideally switch as quickly as possible, and at least have typical rise and fall times less than 15 ns for diagnostic frequencies.

7.9 Conclusions

This Chapter has described a harmonic reduction encoding scheme for multi-level switched-mode tone-burst and LFM coded waveforms. Firstly, a motivation for the need to reduce low order, high magnitude harmonics was discussed including an explanation of newer wide bandwidth transducer technologies. Secondly, an overview of selective harmonic elimination strategies was given. These techniques can reduce harmonic content, but are restrictive in terms of pulse shaping. A new HRPWM carrier-comparison method, based on the methods shown in the previous chapters was derived. The HRPWM method simultaneously encodes two switching angles and is noticeable for its reduction in lower level pulse width with an increase in desired output amplitude. This is a non-intuitive step. In the absence of very high bandwidth transducers such as CMUT devices, the efficacy of the HRPWM encoding has been simulated, and demonstrated using a novel fractional harmonic excitation method.

Wide bandwidth CMUTs lend themselves to integration with switched-mode output stages, due to their nature of fabrication, and use in array transducers. For applications such as harmonic imaging, it is desirable to reduce the level of excitation harmonic, so that any received harmonic is fully due to propagation in the medium. The HRPWM sequences are capable of reducing third harmonic content to the level of the spectral noise floor in simulation, and when applied to real MOSFETs are capable of replicating this behaviour. As with any switched-mode encoding scheme, its performance is directly proportional to the specification of the MOSFETs used, in terms of switching frequency, rise and fall times, and propagation delay. Also discussed is the ratio of fundamental frequency to sampling frequency, with a ratio of > 50 essential for proper representation of switching angles derived by the ‘path of least third harmonic’.

Chapter 8

Research Summary and Further Work

8.1 Introduction

This thesis has discussed methods of optimising the nature of the transmitted ultrasound field and pressure signals. The topics discussed in this thesis are mostly incorporated within a bespoke hardware research platform that has been developed as a technology to control multi-element array transducers. Work surrounding or supported by this thesis has culminated in a total of four journal papers, eleven conference proceedings and two UK patent applications to date. A detailed summary of the research can be given as follows.

8.2 Summary of Research

8.2.1 Research Platform Development

Array devices have been the adopted transducer technology for several years. In order to drive such devices requires a system with multiple channels, ideally enough to match the number of transducer elements. In order to research a wide range of techniques using array transducers, it is essential for the multi-channel system to be flexible. In the first stage of this research, an enabling technology, the University of Leeds UARP was developed alongside various other group members [53], [54], [55], [58], [57], [56], [170], [171], [172]. The main contribution from the author to the UARP project was the design and de-

velopment of an eight-channel switched-mode transmitter board with accompanying software. Other contributions by the author include: the design of auxiliary boards, sequencing and control software, and technical support during collaborative projects. The UARP has served as an enabling technology for many other research students and projects, and has provided both opportunity for collaboration, and opportunity for research into system design, examples of which have been provided in this thesis.

8.2.2 Transmit Beamformer Architecture with Embedded PLLs

A major advantage of array transducers is the ability to electronically steer or focus a pressure beam to a desired location. This increases sensitivity at a particular location in imaging, or can be used to direct energy towards a desired target for therapeutic applications. In order to achieve this it is necessary to have a transmit beamformer architecture that can provide inter-channel delays according to beamforming principles. Poor realisation of steering and focusing delays results in unwanted deposition of energy in the form of discrete phase or time quantization lobes, or a general increase in sidelobe level. These features occur due to correlated (periodic) or uncorrelated (random) phase or time error. Another potential source of error can be introduced by system components such as the transducer, or non-ideal propagation in the medium. Such errors can cause undesirable beam patterns or reduced sensitivity in imaging. To correct these errors in transmit requires a beamformer that can provide accurate and variable inter-channel delays. This has been implemented within the UARP using embedded phase-locked loop components within commercial FPGAs. Switched-mode signals for a particular channel are delayed using a coarse delay (integer multiples of the system clock period) and fine delay (PLL phase shift) to generate accurate delay profiles or provide adjustment to compensate for minor error.

8.2.3 Power Control Method for Switched-Mode Circuitry using Fundamental Mode PWM

Switched-mode circuits have been known to be convenient and cost effective excitation methods for array transducers, and are often deployed in commercial clinical and NDT systems due to their ability to quickly switch high voltages. Such components generate square-wave or stepped 'pseudo-tones', that are approximations of sinusoidal signals. For a research setting, the majority of literature describes the use of DAC and analogue power amplifier technology as an excitation method, as this is known to provide arbitrary waveform capability. Such solutions are inherently large and expensive however due to the requirement for cooling and heat-sinks.

This research has challenged the perceived limitations of switched-mode signals, and has proposed a fundamental-mode, carrier-comparison, pulse-width modulation strategy to provide more flexible amplitude control. Pulse widths are assigned in accordance with the expected response from a transducer to a square-wave excitation. The method differs from 'conventional' PWM used in Class D amplifiers due to the use of a rectified trigonometric carrier as opposed to a more conventional triangular carrier. Using the proposed method, arbitrary shaped sequences for ultrasonic applications can now be encoded using PWM.

8.2.4 Extension of Pulse Width Modulation Strategy for Coded Linear Frequency Modulated Signals

DACs and analogue power amplifiers are also widely used to produce frequency modulated or 'coded' excitations. These excitations can increase the SNR of weak signals by detection of a particular feature, and then compression of the coded pulse. The technique is enhanced by using a tapered excitation signal which gradually rises in amplitude at the start and ends of the pulse according to a particular window function such as a Hann or Hamming function. Tapered frequency modulated signals can easily be generated using a DAC and analogue power amplifier, however recent literature has described

a limitation of switched-mode signals in generating such signals. This research takes the previous pulse-width modulation strategy and extends it for generation of tapered coded waveforms using switched-mode circuits.

8.2.5 Extension of Pulse Width Modulation Strategy for Coded Linear Frequency Modulated Signals

A further criticism of the use of switched-mode signals is the nature of harmonic content. For newer wide-bandwidth transducer technologies such as CMUTs, and for techniques such as coded imaging that rely on spectral integrity, reducing the level of harmonics within the switched-mode signals is desirable. Also desirable is the requirement for amplitude control during coded harmonic imaging. The largest harmonic present in a bipolar switched-mode signal is predominantly the third harmonic. This research has developed a novel method of encoding pulse-width modulation sequences that reduce the level of third harmonic whilst maintaining amplitude control. The method can be seen as incorporating pressure control for linear frequency modulated signals and also selective harmonic elimination strategies. A particularly noticeable feature of the method after encoding is a non-intuitive increase and decrease in pulse width for increasing desired amplitude.

8.3 Ideas for Further Work

8.3.1 Embedded IP Core Development

PWM signals are currently generated off-line and uploaded to the UARP. A more desirable solution is to generate encoded waveforms ‘on-the-fly’ based on a set of instruction signals. A future direction for the work is the development of an embedded IP core designed using the carrier-comparison method and implemented within digital logic. Such a core would allow integration of the method within portable devices without requiring a PC.

8.3.2 Integration with CMUT devices

Wide-bandwidth CMUT devices have been cited as the next-generation transducer technology. Wider bandwidth devices permit improvement to harmonic and coded harmonic imaging. The third harmonic content within a switched-mode signal will be transmitted through a wide bandwidth CMUT device, causing distortion in the waveform and interference in signal processing. The HRPWM has been shown to suppress this harmonic whilst maintaining the use of switched-mode components. CMUTs are also suited to fabrication alongside high-voltage MOSFET devices, due to the method of manufacture. Future direction for the research could investigate the integration and test of the HRPWM with CMUT arrays.

References

[1] P. R. Smith, D. M. J. Cowell, B. Raiton, C. V. Ky, T. Pham, B. Q. Bui, and S. Freear, "A PLL-based phased array method to minimize phase quantization errors and reduce phasing-lobes," in *Ultrasonics Symposium (IUS), 2010 IEEE*, pp. 1837 –1840, Oct. 2010.

[2] P. R. Smith, D. M. J. Cowell, B. Raiton, C. V. Ky, and S. Freear, "Ultrasound array transmitter architecture with high timing resolution using embedded phase-locked loops," *Ultrasonics, Ferroelectrics and Frequency Control, IEEE Transactions on*, vol. 59, pp. 40 –49, January 2012,

[3] P. R. Smith, S. Harput, D. M. J. Cowell, J. McLaughlan, and S. Freear, "Predistorted amplitude modulated (PDAM) chirps for transducer compensation in harmonic imaging." Ultrasonics Symposium (IUS), 2012 IEEE, In Press.

[4] P. R. Smith, D. M. J. Cowell, and S. Freear, "Width-modulated square-wave pulses for ultrasound applications." In Review.

[5] D. M. J. Cowell, P. R. Smith, and S. Freear., "Harmonic cancellation in switched mode linear frequency modulated (LFM) excitation of ultrasound arrays," in *Ultrasonics Symposium (IUS), 2011 IEEE International*, pp. 454–457, 2011.

[6] P. R. Smith, D. M. J. Cowell, and S. Freear, "A fractional harmonic excitation (FHE) method for high frequency array imaging." Ultrasonics Symposium (IUS), 2012 IEEE, In Press.

[7] D. M. J. Cowell, P. R. Smith, and S. Freear, "Phase inversion based selective harmonic elimination (PI-SHE) in multi-level switched mode tone and frequency modulated excitation." In Press.

[8] P. Curie, J. Curie, "Dveloppement par pression de l'lectricit plaire dans les cristaux hermidres faces inclines," *Compt Rend*, vol. 91, p. 294, 1880,

[9] B. Haider, "Power drive circuits for diagnostic medical ultrasound," in *Procedeedings of the 18th Internation Symposium on Power Semiconductor Devices & ICS*, International Symposium on Power Semiconductor Devices and ICs, pp. XXXIII–XL, IEEE; Pels, IEEE, 2006. 18th International Symposium on Power Semiconductor Devices and ICs, Univ Naples Feder II, Naples, Italy, Jun 04-08, 2006.

[10] P. Levesque and M. Sawan, "Real-time hand-held ultrasound medical-imaging device based on a new digital quadrature demodulation processor," *Ultrasonics, Ferroelectrics and Frequency Control, IEEE Transactions on*, vol. 56, no. 8, pp. 1654–1665, 2009,

[11] C.-C. Huang, P.-Y. Lee, P.-Y. Chen, and T.-Y. Liu, "Design and implementation of a smartphone-based portable ultrasound pulsed-wave doppler device for blood flow measurement," *Ultrasonics, Ferroelectrics and Frequency Control, IEEE Transactions on*, vol. 59, pp. 182 –188, January 2012,

[12] G.-D. Kim, C. Yoon, S.-B. Kye, Y. Lee, J. Kang, Y. Yoo, and T. kyong Song, "A single FPGA-based portable ultrasound imaging system for point-of-care applications," *Ultrasonics, Ferroelectrics and Frequency Control, IEEE Transactions on*, vol. 59, pp. 1386 –1394, July 2012,

[13] S. C. Tang and G. Clement, "A harmonic cancellation technique for an ultrasound transducer excited by a switched-mode power converter," *Ultrasonics, Ferroelectrics and Frequency Control, IEEE Transactions on*, vol. 55, pp. 359 –367, February 2008,

[14] W. Qiu, Y. Yu, F. K. Tsang, and L. Sun, "A multifunctional, reconfigurable pulse generator for high-frequency ultrasound imaging," *Ultrasonics, Ferroelectrics and Frequency Control, IEEE Transactions on*, vol. 59, pp. 1558 –1567, July 2012,

[15] B. Raiton, J. R. McLaughlan, S. Harput, P. R. Smith, D. M. J. Cowell, and S. Freear, "The capture of flowing microbubbles with an ultrasonic tap using acoustic radiation force," *Applied Physics Letters*, vol. 101, no. 4, p. 044102, 2012,

[16] B. Raiton, J. McLaughlan, P. R. Smith, D. M. J. Cowell, S. Harput, and S. Freear, "Counter flow microbubble channeling using acoustic radiation force funnel," in *Ultrasonics Symposium (IUS), 2011 IEEE International*, pp. 2432–2435, 2011.

[17] S. S. Qureshi, P. R. Smith, D. M. J. Cowell, K. M. Rajpoot, and S. Freear, "A compact, parameterized, real-time beamformer, benchmarked for ultrasound imaging." Ultrasonics Symposium (IUS), 2012 IEEE, In Press.

[18] C. A. Winckler, P. R. Smith, D. M. J. Cowell, O. Olagunju, and S. Freear, "The design of a high speed receiver system for an ultrasound array research platform." Ultrasonics Symposium (IUS), 2012 IEEE, In Press.

[19] B. Raiton, J. McLaughlan, S. Harput, P. R. Smith, and D. M. J. Cowell, "Non-invasive cavitation nuclei trap for histotripsy." Ultrasonics Symposium (IUS), 2012 IEEE, In Press.

[20] J. McLaughlan, P. R. Smith, N. Ingram, L. Coletta, S. Evans, and S. Freear, "Chirp excitation of polydisperse microbubble populations for increasing sonoporation efficiency." Ultrasonics Symposium (IUS), 2012 IEEE, In Press.

[21] O. Olagunju, D. M. J. Cowell, P. R. Smith, and S. Freear, "Randomized excitation - a novel ultrasound array excitation scheme." Ultrasonics Symposium (IUS), 2012 IEEE, In Press.

[22] S. Harput, J. McLaughlan, P. R. Smith, D. M. J. Cowell, S. D. Evans, and S. Freear, "Separating the second harmonic response of tissue and microbubbles using bispectral analysis." Ultrasonics Symposium (IUS), 2012 IEEE, In Press.

[23] G. Bambi, T. Morganti, S. Ricci, E. Boni, F. Guidi, C. Palombo, and P. Tortoli, "A novel ultrasound instrument for investigation of arterial mechanics," *Ultrasonics*, vol. 42, no. 19, pp. 731 – 737, 2004, Proceedings of Ultrasonics International 2003.

[24] S. Ricci, E. Boni, F. Guidi, T. Morganti, and P. Tortoli, "A programmable real-time system for development and test of new ultrasound investigation methods," *Ultrasonics, Ferroelectrics and Frequency Control, IEEE Transactions on*, vol. 53, pp. 1813 –1819, October 2006,

[25] S. Ricci, L. Bassi, A. Dallai, E. Boni, and P. Tortoli, "A dual transducer ultrasound system for quantitative doppler measurements," in *Industrial Electronics, 2007. ISIE 2007. IEEE International Symposium on*, pp. 2718–2723, 2007.

[26] L. Sun, W. Richard, J. Cannata, C. Feng, J. Johnson, J. Yen, and K. Shung, "A high-frame rate high-frequency ultrasonic system for cardiac imaging in mice," *Ultrasonics, Ferroelectrics and Frequency Control, IEEE Transactions on*, vol. 54, no. 8, pp. 1648–1655, 2007,

[27] W. Qiu, Y. Yu, H. Chabok, C. Liu, F. K. Tsang, Q. Zhou, K. Shung, H. Zheng, and L. Sun, "A flexible annular-array imaging platform for micro-ultrasound," *Ultrasonics, Ferroelectrics and Frequency Control, IEEE Transactions on*, vol. 60, no. 1, pp. 178–186, 2013,

[28] L. Bassi, E. Boni, A. Dallai, F. Guidi, S. Ricci, and P. Tortoli, "ULA-OP: A novel ultrasound advanced open platform for experimental research," in *Ultrasonics Symposium, 2007. IEEE*, pp. 632–635, 2007.

[29] L. Bassi, E. Boni, A. Cellai, A. Dallai, F. Guidi, S. Ricci, and P. Tortoli, "A novel digital ultrasound system for experimental research activities," in *Digital System Design Architectures, Methods and Tools, 2008. DSD '08. 11th EuroMicro Conference on*, pp. 413–417, 2008.

[30] P. Tortoli, L. Bassi, E. Boni, A. Dallai, F. Guidi, and S. Ricci, "ULA-OP: An advanced open platform for ultrasound research," *Ultrasonics, Ferroelectrics and Frequency Control, IEEE Transactions on*, vol. 56, pp. 2207 –2216, Oct 2009,

[31] S. Ricci, L. Bassi, E. Boni, A. Dallai, and P. Tortoli, "Multichannel FPGA-based arbitrary waveform generator for medical ultrasound," *Electronics Letters*, vol. 43, no. 24, pp. 1335–1336, 2007,

[32] M. Lewandowski, Z. Klimonda, P. Karwat, M. Seklewski, A. Nowicki, L. Bassi, and P. Tortoli, "Comparison of different schemes of synthetic transmit aperture using an ultrasound advanced open platform (ULA-OP)," in *Ultrasonics Symposium (IUS), 2010 IEEE*, pp. 1988–1991, 2010.

[33] J. Cowe, J. Gittins, and D. H. Evans, "Improving performance of pulse compression in a Doppler ultrasound system using amplitude modulated chirps and Wiener filtering," *Ultrasound in Medicine & Biology*, vol. 34, pp. 326–333, Feb 2008,

[34] A. Dallai, E. Boni, L. Bassi, A. Cellai, F. Guidi, S. Ricci, and P. Tortoli, "A novel DSP-based ultrasound research platform for development and test of new imaging and doppler methods," in *Education and Research Conference (EDERC), 2010 4th European*, pp. 19–22, 2010.

[35] E. Boni, L. Bassi, A. Dallai, F. Guidi, A. Ramalli, S. Ricci, J. Housden, and P. Tortoli, "A reconfigurable and programmable FPGA-based system for nonstandard ultrasound methods," *Ultrasonics, Ferroelectrics and Frequency Control, IEEE Transactions on*, vol. 59, no. 7, pp. 1378–1385, 2012,

[36] E. Boni, L. Bassi, A. Dallai, F. Guidi, A. Ramalli, S. Ricci, and P. Tortoli, "Implementation of non standard methods with the ultrasound advanced open platform (ULA-OP)," in *Ultrasonics Symposium (IUS), 2011 IEEE International*, pp. 466–469, 2011.

[37] C. Hu, X. chen Xu, J. Cannata, J. Yen, and K. Shung, "Development of a real-time, high-frequency ultrasound digital beamformer for high-frequency linear array transducers," *Ultrasonics, Ferroelectrics and Frequency Control, IEEE Transactions on*, vol. 53, no. 2, pp. 317–323, 2006,

[38] C. Hu, K. Snook, P.-J. Cao, and K. Shung, "High-frequency ultrasound annular array imaging. part ii: digital beamformer design and imaging," *Ultrasonics, Ferroelectrics and Frequency Control, IEEE Transactions on*, vol. 53, no. 2, pp. 309–316, 2006,

[39] X. Xu, J. Yen, and K. Shung, "A low-cost bipolar pulse generator for high-frequency ultrasound applications," *Ultrasonics, Ferroelectrics and Frequency Control, IEEE Transactions on*, vol. 54, pp. 443 –447, February 2007,

[40] J. Chang, J. Yen, and K. Shung, "A novel envelope detector for high-frame rate, high-frequency ultrasound imaging," *Ultrasonics, Ferroelectrics and Frequency Control, IEEE Transactions on*, vol. 54, no. 9, pp. 1792–1801, 2007,

[41] L. Zhang, X. Xu, C. Hu, L. Sun, J. Yen, J. Cannata, and K. Shung, "A high-frequency, high frame rate duplex ultrasound linear array imaging system for small animal imaging," *Ultrasonics, Ferroelectrics and Frequency Control, IEEE Transactions on*, vol. 57, no. 7, pp. 1548–1557, 2010,

[42] C. Hu, Q. Zhou, and K. Shung, "Design and implementation of high frequency ultrasound pulsed-wave doppler using FPGA," *Ultrasonics, Ferroelectrics and Frequency Control, IEEE Transactions on*, vol. 55, no. 9, pp. 2109–2111, 2008,

[43] J. Park, C. Hu, and K. Shung, "Stand-alone front-end system for high- frequency, high-frame-rate coded excitation ultrasonic imaging," *Ultrasonics, Ferroelectrics and Frequency Control, IEEE Transactions on*, vol. 58, no. 12, pp. 2620–2630, 2011,

[44] J. Park, C. Hu, X. Li, Q. Zhou, and K. Shung, "Wideband linear power amplifier for high-frequency ultrasonic coded excitation imaging," *Ultrasonics, Ferroelectrics and Frequency Control, IEEE Transactions on*, vol. 59, no. 4, pp. 825–832, 2012,

[45] J. Jensen, O. Holm, J. Jensen, H. Bendsen, H. Pedersen, K. Salomonsen, J. Hansen, and S. Nikolov, "Experimental ultrasound system for real-time synthetic imaging," in *Ultrasonics Symposium, 1999. Proceedings. 1999 IEEE*, vol. 2, pp. 1595–1599 vol.2, 1999.

[46] J. Jensen, O. Holm, L. Jerisen, H. Bendsen, S. Nikolov, B. Tomov, P. Munk, M. Hansen, K. Salomonsen, J. Hansen, K. Gormsen, H. Pedersen, and K. Gammelmark, "Ultrasound research scanner for real-time synthetic aperture data acquisition," *Ultrasonics, Ferroelectrics and Frequency Control, IEEE Transactions on*, vol. 52, pp. 881 –891, May 2005,

[47] J.-y. Lu, J. Cheng, and W. Jing, "High frame rate imaging system for limited diffraction array beam imaging with square-wave aperture weightings high frame rate imaging system for limited diffraction array beam imaging with square-wave aperture weightings," *Ultrasonics, Ferroelectrics and Frequency Control, IEEE Transactions on*, vol. 53, no. 10, pp. 1796–1812, 2006,

[48] M. Hemmsen, S. Nikolov, M. Pedersen, M. Pihl, M. Enevoldsen, J. Hansen, and J. Jensen, "Implementation of a versatile research data acquisition system using a commercially available medical ultrasound scanner," *Ultrasonics, Ferroelectrics and Frequency Control, IEEE Transactions on*, vol. 59, no. 7, pp. 1487–1499, 2011,

[49] V. Shamdasani, U. Bae, S. Sikdar, Y. M. Yoo, K. Karadayi, R. Managuli, and Y. Kim, "Research interface on a programmable ultrasound scanner," *Ultrasonics*, vol. 48, no. 3, pp. 159 – 168, 2008,

[50] T. Wilson, J. Zagzebski, T. Varghese, Q. Chen, and M. Rao, "The ultrasonix 500RP: A commercial ultrasound research interface," *Ultrasonics, Ferroelectrics and Frequency Control, IEEE Transactions on*, vol. 53, no. 10, pp. 1772–1782, 2006,

[51] M. Ashfaq, S. Brunke, J. Dahl, H. Ermert, C. Hansen, and M. Insana, "An ultrasound research interface for a clinical system," *Ultrasonics, Ferroelectrics and Frequency Control, IEEE Transactions on*, vol. 53, no. 10, pp. 1759–1771, 2006,

[52] D. M. J. Cowell and S. Freear, "Quinary excitation method for pulse compression ultrasound measurements," *Ultrasonics*, vol. 48, no. 2, pp. 98–108, 2008,

[53] D. M. J. Cowell, *Optimised Coded Ultrasound Techniques for Process Measurement*. PhD thesis, School of Electronic and Electrical Engineering, University of Leeds, Leeds, 2008.

[54] O. Anwar, "Ultrasonic array resarch platform - data acquisition," Master's thesis, School of Electronic and Electrical Engineering, University of Leeds, Leeds, 2009.

[55] P. Thompson, "Ultrasonic array research platform 8 channel high speed receiver board and system integration," Master's thesis, School of Electronic and Electrical Engineering, University of Leeds, Leeds, 2010.

[56] C. V. Ky, "Ultrasonic array research platform (UARP) the main controller & transmitters," Master's thesis, School of Electronic and Electrical Engineering, University of Leeds, Leeds, 2010.

[57] T. H. Pham, "Ultrasonic array research platform (UARP) the receiver side," Master's thesis, School of Electronic and Electrical Engineering, University of Leeds, Leeds, 2010.

[58] B. Q. Bui, "Ultrasonic array research platform (UARP) system integrated," Master's thesis, School of Electronic and Electrical Engineering, University of Leeds, Leeds, 2010.

[59] B. Raiton, J. McLaughlan, S. Harput, D. M. J. Cowell, and S. Freear, "Apparatus and method for manipulating entrained particles p138728gb," 2012.

[60] D. A. Peterson and R. N. Phelps, "Multiple level transmitter and method of transmitting, US 6939300B2," Sep. 6 2005.

[61] K. Kristoffersen and H. G. Torp, "Method and apparatus for generating a multilevel ultrasound pulse, US 7022074B2," Apr. 4 2006.

[62] T. Whittingham, "Medical diagnostic applications and sources.," *Progress in biophysics and molecular biology*, vol. 93, no. 1-3, p. 84, 2007,

[63] K. Shung and M. Zippuro, "Ultrasonic transducers and arrays," *Engineering in Medicine and Biology Magazine, IEEE*, vol. 15, no. 6, pp. 20–30, 1996,

[64] S. O. Kasap, *Principles of Electronic Materials and Devices 2nd Edition*. McGraw Hill Publishing Company, 2002.

[65] G. Shirane and K. Suzuki, "Crystal structure of pb (zr-ti) o_3," *Journal of the Physical Society of Japan*, vol. 7, no. 3, pp. 333–333, 1952,

[66] B. Jaffe, R. Roth, and S. Marzullo, "Piezoelectric properties of lead zirconate-lead titanate solid-solution ceramics," *Journal of Applied Physics Letters*, vol. 25, no. 6, pp. 809–810, 1954,

[67] J. Hunt, M. Arditi, and F. Foster, "Ultrasound transducers for pulse-echo medical imaging," *Biomedical Engineering, IEEE Transactions on*, vol. BME-30, no. 8, pp. 453–481, 1983,

[68] T. L. Szabo, *Diagnostic Ultrasound Imaging: Inside Out*. Elsevier Academic Press, 2004.

[69] R. S. C. Cobbold, *Foundations of Biomedical Ultrasound*. Oxford University Press, 2007.

[70] H. Kawai, "The piezoelectricity of poly (vinylidene fluoride)," *Japanese Journal of Applied Physics*, vol. 8, no. 7, pp. 975–976, 1969,

[71] F. Foster, K. A. Harasiewicz, and M. Sherar, "A history of medical and biological imaging with polyvinylidene fluoride (PVDF) transducers," *Ultrasonics, Ferroelectrics and Frequency Control, IEEE Transactions on*, vol. 47, no. 6, pp. 1363–1371, 2000,

[72] W. P. Mason, *Electromechanical Transducers and Wave Filters*. Van Nostrand, 1942.

[73] M. Redwood, "Transient performance of a piezoelectric transducer," *The Journal of the Acoustical Society of America*, vol. 33, p. 527, 1961,

[74] R. Krimholtz, D. Leedom, and G. Matthaei, "New equivalent circuits for elementary piezoelectric transducers," *Electronics Letters*, vol. 6, no. 13, pp. 398–399, 1970,

[75] W. M. Leach, "Controlled-source analogous circuits and SPICE models for piezoelectric transducers," *Ultrasonics, Ferroelectrics and Frequency Control, IEEE Transactions on*, vol. 41, no. 1, pp. 60–66, 1994,

[76] G. S. Kino, *Acoustic waves: devices, imaging, and analog signal processing*, vol. 107. Prentice-Hall Englewood Cliffs, NJ, 1987.

[77] K. R. Erikson, "Tone-burst testing of pulse-echo transducers," *Sonics and Ultrasonics, IEEE Transactions on*, vol. 26, no. 1, pp. 7–13, 1979,

[78] J. Okyere and A. Cousin, "The design of a high voltage SCR pulse generator for ultrasonic pulse echo applications," *Ultrasonics*, vol. 17, no. 2, pp. 81–84, 1979,

[79] P. Mattila and L. M, "FET pulse-generator for ultrasonic pulse echo applications," *Ultrasonics*, vol. 19, no. 5, pp. 235–236, 1981,

[80] R. Martin, "Variable pulse width piezoelectric ultrasonic transducer driver," *NDT international*, vol. 17, no. 4, pp. 209–213, 1984,

[81] G. Hayward and M. Jackson, "A study of electronic switching devices for the characterisation of ultrasonic probe assemblies," in *1983 Ultrasonics Symposium*, pp. 752–756, IEEE, 1983.

[82] H. W. Persson, "Electric excitation of ultrasound transducers for short pulse generation," *Ultrasound in Medicine & Biology*, vol. 7, no. 3, pp. 285 – 291, 1981,

[83] M. Certo, D. Dotti, and P. Vidali, "A programmable pulse generator for piezoelectric multielement transducers," *Ultrasonics*, vol. 22, no. 4, pp. 163–166, 1984,

[84] J. Johnston, "Generating analogue FM pulses using a 1 bit digital technique," *Communications, Radar and Signal Processing, IEE Proceedings*, vol. 131, no. 4, pp. 349–356, 1984,

[85] M. O'Donnell, "Coded excitation system for improving the penetration of real-time phased-array imaging systems," *Ultrasonics, Ferroelectrics and Frequency Control, IEEE Transactions on*, vol. 39, pp. 341 –351, May 1992,

[86] M. Pollakowski and H. Ermert, "Chirp signal matching and signal power optimization in pulse-echo mode ultrasonic nondestructive testing," *Ultrasonics, Ferroelectrics and Frequency Control, IEEE Transactions on*, vol. 41, pp. 655 –659, Sep. 1994,

[87] T. Suzuki, H. Ikeda, H. Yoshida, and S. Shinohara, "Megasonic transducer drive utilizing MOSFET DC-to-RF inverter with output power of 600 W at 1 Mhz," *Industrial Electronics, IEEE Transactions on*, vol. 46, pp. 1159 –1173, Dec 1999,

[88] K. Agbossou, J.-L. Dion, S. Carignan, M. Abdelkrim, and A. Cheriti, "Class D amplifier for a power piezoelectric load," *Ultrasonics, Ferroelectrics and Frequency Control, IEEE Transactions on*, vol. 47, pp. 1036 –1041, Jul 2000,

[89] J. Brown and G. Lockwood, "Low-cost, high-performance pulse generator for ultrasound imaging," *Ultrasonics, Ferroelectrics and Frequency Control, IEEE Transactions on*, vol. 49, pp. 848 –851, June 2002,

[90] M. Urban, C. Chalek, R. Kinnick, T. Kinter, B. Haider, J. Greenleaf, K. Thomenius, and M. Fatemi, "Implementation of vibro-acoustography on a clinical ultrasound system," *Ultrasonics, Ferroelectrics and Frequency Control, IEEE Transactions on*, vol. 58, pp. 1169 –1181, June 2011,

[91] R. G. Wodnicki, "Reconfigurable array with multi-level transmitters, US 0264171A1," Oct. 30 2008.

[92] Z. Gao and P. Gui, "A look-up-table digital predistortion technique for high-voltage power amplifiers in ultrasonic applications," *Ultrasonics, Ferroelectrics and Frequency Control, IEEE Transactions on*, vol. 59, pp. 1550 –1557, July 2012,

[93] B. Cordell, *Designing audio power amplifiers*. McGraw-Hill, 2011.

[94] E. Gaalaas, "Class d audio amplifiers: What, why, and how," *Analog Dialogue*, vol. 40, no. 6, pp. 1–7, 2006,

[95] P. Horowitz, W. Hill, and T. C. Hayes, *The art of electronics*, vol. 2. Cambridge university press Cambridge, 1989.

[96] M. I. Circuits, *MAX4810/MAX4811/MAX4812 Dual, Unipolar/Bipolar, High-Voltage Digital Pulsers Datasheet*, 2008.

[97] M. Eaton, B. Bardsley, R. Melen, and J. Meindl, "Effects of coarse phase quantization in ultrasound scanners," in *1978 Ultrasonics Symposium*, pp. 784 – 788, 1978.

[98] B. W. Drinkwater and P. D. Wilcox, "Ultrasonic arrays for non-destructive evaluation: A review," *NDT & E International*, vol. 39, no. 7, pp. 525 – 541, 2006,

[99] B. A. Angelsen, H. Torp, S. Holm, K. Kristoffersen, and T. Whittingham, "Which transducer array is best?," *European journal of ultrasound*, vol. 2, no. 2, pp. 151–164, 1995,

[100] S. Holm and K. Kristoffersen, "Analysis of worst-case phase quantization sidelobes in focused beamforming," *Ultrasonics, Ferroelectrics and Frequency Control, IEEE Transactions on*, vol. 39, no. 5, pp. 593 –599, 1992,

[101] S. Wooh and Y. Shi, "Influence of phased array element size on beam steering behavior," *Ultrasonics*, vol. 36, no. 6, pp. 737 – 749, 1998,

[102] S. Wooh and Y. Shi, "Optimum beam steering of linear phased arrays," *Wave Motion*, vol. 29, no. 3, pp. 245 – 265, 1999,

[103] L. Azar, Y. Shi, and S. C. Wooh, "Beam focusing behavior of linear phased arrays," *NDT & E International*, vol. 33, pp. 189 – 198, 2000,

[104] O. T. Von Ramm and S. W. Smith, "Beam steering with linear arrays," *Biomedical Engineering, IEEE Transactions on*, vol. 30, no. 8, pp. 438 –452, 1983,

[105] M. I. Skolnik, *Radar Handbook 2nd Edition*. McGraw Hill Publishing Company, 1990.

[106] D. Duxbury, J. Russell, and M. Lowe, "The effect of variation in phased array element performance for non-destructive evaluation (nde)," *Ultrasonics*, vol. 53, no. 6, pp. 1065 – 1078, 2012,

[107] J. Zhang, B. W. Drinkwater, and P. D. Wilcox, "Effects of array transducer inconsistencies on total focusing method imaging performance," *NDT & E International*, vol. 44, no. 4, pp. 361 – 368, 2011,

[108] S. Smith, G. Trahey, and O. Von Ramm, "Phased array ultrasound imaging through planar tissue layers," *Ultrasound in medicine & biology*, vol. 12, no. 3, pp. 229–243, 1986,

[109] W. Beaver, "Phase error effects in phased array beam steering," in *Ultrasonics Symposium, 1977*, pp. 264 – 267, 1977.

[110] P. Magnin, O. von Ramm, and F. Thurstone, "Delay quantization error in phased array images," *Sonics and Ultrasonics, IEEE Transactions on*, vol. 28, no. 5, pp. 305 – 310, 1981,

[111] P. 't Hoen, "Influence of component errors on the directivity function of pulsed, ultrasonographic linear arrays," *Ultrasonics*, vol. 21, no. 6, pp. 275–279, 1983,

[112] K. N. Bates, "Tolerance analysis for phased arrays," in *Acoustical Imaging* (K. Wang, ed.), vol. 9 of *Acoustical Imaging*, pp. 239–262, Springer US, 1980.

[113] H. Wang, E. Ebbini, and C. Cain, "Effect of phase errors on field patterns generated by an ultrasound phased-array hyperthermia applicator," *Ultrasonics, Ferroelectrics and Frequency Control, IEEE Transactions on*, vol. 38, pp. 521 –531, Sep 1991,

[114] D. Peterson and G. Kino, "Real-time digital image reconstruction: A description of imaging hardware and an analysis of quantization errors," *Sonics and Ultrasonics, IEEE Transactions on*, vol. 31, no. 4, pp. 337 – 351, 1984,

[115] S. Freeman, M. Quick, M. Morin, R. Anderson, C. Desilets, T. Linnenbrink, and M. O'Donnell, "Delta-sigma oversampled ultrasound beamformer with dynamic delays," *Ultrasonics, Ferroelectrics and Frequency Control, IEEE Transactions on*, vol. 46, no. 2, pp. 320 –332, 1999,

[116] O. Oralkan, A. S. Ergun, J. A. Johnson, M. Karaman, U. Demirci, K. Kaviani, T. H. Lee, and B. T. Khuri-Yakub, "Capacitive micromachined ultrasonic transducers: Next-generation arrays for acoustic imaging?," *Ultrasonics, Ferroelectrics and Frequency Control, IEEE Transactions on*, vol. 49, no. 11, pp. 1596–1610, 2002,

[117] C. Lancée, J. Vissers, S. Mientki, C. Ligtvoet, and N. Bom, "Influence of phase errors on beam-steered phased arrays," *Ultrasonics*, vol. 25, no. 3, pp. 154–159, 1987,

[118] J. Jensen and N. Svendsen, "Calculation of pressure fields from arbitrarily shaped, apodized, and excited ultrasound transducers," *Ultrasonics, Ferroelectrics and Frequency Control, IEEE Transactions on*, vol. 39, pp. 262 –267, Mar 1992,

[119] J. A. Jensen, "FIELD: A program for simulating ultrasound systems," in *10th Noric Baltic Conference on Biomedical Imaging, Vol. 4, Supplement 1, Part 1:351–353*, pp. 351–353, 1996.

[120] C.-H. Hu, X.-C. Xu, J. Cannata, J. Yen, and K. Shung, "Development of a real-time, high-frequency ultrasound digital beamformer for high-frequency linear array transducers," *Ultrasonics, Ferroelectrics and Frequency Control, IEEE Transactions on*, vol. 53, pp. 317 –323, Feb. 2006,

[121] A. Lovejoy, P. Pedrick, A. Doran, T. A. Delchar, J. A. Mills, and A. Stamm, "A novel 8-bit ultrasound phased-array controller for hyperthermia applications," *Ultrasonics*, vol. 33, no. 1, pp. 69 – 73, 1995,

[122] J. V. Hatfield and K. S. Chai, "A beam-forming transmit ASIC for driving ultrasonic arrays," *Sensors and Actuators A: Physical*, vol. 92, no. 1-3, pp. 273 – 279, 2001,

[123] Altera, "Phase-Locked Loop (ALTPLL) Megafunction User Guide." pdf, Nov 2009.

[124] Altera, "Chapter 5, Cyclone III Device Handbook, Volume 1." pdf, Dec 2009.

[125] K. Kurbjan and C. Ribbing, "XAPP879 PLL Dynamic Reconfiguration." pdf, May 2010.

[126] A. H. Aitkenhead, J. A. Mills, and A. J. Wilson, "An analysis of the origin of differences between measured andsimulated fields produced by a 15-element ultrasound phased array," *Ultrasound in Medicine & Biology*, vol. 36, no. 3, pp. 410 – 418, 2010,

[127] G. Athanasopoulos, S. Carey, and J. Hatfield, "Circuit design and simulation of a transmit beamforming asic for high-frequency ultrasonic imaging systems," *Ultrasonics, Ferroelectrics and Frequency Control, IEEE Transactions on*, vol. 58, pp. 1320 –1331, July 2011,

[128] L. Franquelo, J. Rodriguez, J. Leon, S. Kouro, R. Portillo, and M. Prats, "The age of multilevel converters arrives," *Industrial Electronics Magazine, IEEE*, vol. 2, pp. 28 –39, June 2008,

[129] B. D. Bedford and R. G. Hoft, *Principles of Inverter Circuits*. John Wiley & Sons, Inc., 1964.

[130] S.-W. Huang and P.-C. Li, "Arbitrary waveform coded excitation using bipolar square wave pulsers in medical ultrasound," *Ultrasonics, Ferroelectrics and Frequency Control, IEEE Transactions on*, vol. 53, pp. 106 –116, Jan. 2006,

[131] D. Holmes and T. Lipo, *Pulse Width Modulation for Power Converters: Principles and Practice*. Wiley-IEEE Press, 2003.

[132] B. H. Haider, "Imaging system with transmit apodization using pulse width variation, US 6135963," Oct. 24 2000.

[133] B. McGrath and D. Holmes, "Multicarrier pwm strategies for multilevel inverters," *Industrial Electronics, IEEE Transactions on*, vol. 49, pp. 858 – 867, Aug 2002,

[134] V. Behar and D. Adam, "Parameter optimization of pulse compression in ultrasound imaging systems with coded excitation," *Ultrasonics*, vol. 42, no. 10, pp. 1101 – 1109, 2004,

[135] P. 't Hoen, "Aperture apodization to reduce the off-axis intensity of the pulsed-mode directivity function of linear arrays," *Ultrasonics*, vol. 20, no. 5, pp. 231–236, 1982,

[136] G. Cincotti, G. Cardone, P. Gori, and M. Pappalardo, "Efficient transmit beamforming in pulse-echo ultrasonic imaging," *Ultrasonics, Ferroelectrics and Frequency Control, IEEE Transactions on*, vol. 46, pp. 1450 –1458, Nov 1999,

[137] Y. Takeuchi, "An investigation of a spread energy method for medical ultrasound systems: Part one: Theory and investigation," *Ultrasonics*, vol. 17, no. 4, pp. 175 – 182, 1979,

[138] Y. Takeuchi, "Chirped excitation for¡-100 dB time sidelobe echo sounding," in *Ultrasonics Symposium, 1995. Proceedings., 1995 IEEE*, vol. 2, pp. 1309–1314, IEEE, 1995.

[139] T. Misaridis and J. Jensen, "Use of modulated excitation signals in medical ultrasound. part i: basic concepts and expected benefits," *Ultrasonics, Ferroelectrics and Frequency Control, IEEE Transactions on*, vol. 52, pp. 177 –191, Feb. 2005,

[140] Misaridis, T. and Jensen, J.A., "Use of modulated excitation signals in medical ultrasound. part ii: design and performance for medical imaging applications," *Ultrasonics, Ferroelectrics and Frequency Control, IEEE Transactions on*, vol. 52, pp. 192 –207, Feb. 2005,

[141] T. Misaridis and J. Jensen, "Use of modulated excitation signals in medical ultrasound. part iii: high frame rate imaging," *Ultrasonics, Ferroelectrics and Frequency Control, IEEE Transactions on*, vol. 52, pp. 208 –219, Feb. 2005,

[142] F. Harris, "On the use of windows for harmonic analysis with the discrete fourier transform," *Proceedings of the IEEE*, vol. 66, pp. 51 – 83, Jan. 1978,

[143] A. Nuttall, "Some windows with very good sidelobe behavior," *Acoustics, Speech and Signal Processing, IEEE Transactions on*, vol. 29, pp. 84 – 91, Feb 1981,

[144] J. Adams, "A new optimal window," *Signal Processing, IEEE Transactions on*, vol. 39, pp. 1753 –1769, Aug 1991,

[145] C. E. Cook and M. Bernfeld, *Radar signals: An introduction to theory and application*. New York: Academic Press, 1967.

[146] D. M. J. Cowell and S. Freear, "Separation of overlapping linear frequency modulated (LFM) signals using the fractional fourier transform," *Ultrasonics, Ferroelectrics and Frequency Control, IEEE Transactions on*, vol. 57, pp. 2324 –2333, Oct. 2010,

[147] J. Jensen, "Simulation of advanced ultrasound systems using field ii," in *Biomedical Imaging: Nano to Macro, 2004. IEEE International Symposium on*, pp. 636 – 639 Vol. 1, 2004.

[148] N. Rao, "Investigation of a pulse compression technique for medical ultrasound: a simulation study," *Medical and Biological Engineering and Computing*, vol. 32, no. 2, pp. 181–188, 1994,

[149] M. L. Oelze, "Bandwidth and resolution enhancement through pulse compression," *Ultrasonics, Ferroelectrics and Frequency Control, IEEE Transactions on*, vol. 54, pp. 768–781, Apr 2007,

[150] J. McLaughlan, N. Ingram, P. R. Smith, S. Harput, D. Cowell, P. L. Coletta, S. Evans, and S. Freear, "Increasing the sonoporation efficiency of targeted polydisperse microbubble populations using chirp excitation." In Review.

[151] B. Zoran, L. Yao, and P. L. V. Behren, "Coded excitation imaging for use with biploar unipolar and other waveforms, US 7094204b2," Aug. 22 2006.

[152] C.-C. Shen and P.-C. Li, "Harmonic leakage and image quality degradation in tissue harmonic imaging," *Ultrasonics, Ferroelectrics and Frequency Control, IEEE Transactions on*, vol. 48, pp. 728 –736, May 2001,

[153] B. Ward, A. Baker, and V. Humphrey, "Nonlinear propagation applied to the improvement of resolution in diagnostic medical ultrasound," *Journal of the Acoustical Society of America*, vol. 101, pp. 143–154, Jan 1997,

[154] A. Bouakaz, B. J. Krenning, W. B. Vletter, F. J. ten Cate, and N. D. Jong, "Contrast superharmonic imaging: A feasibility study," *Ultrasound in Medicine & Biology*, vol. 29, no. 4, pp. 547 – 553, 2003,

[155] J. Thomas and D. Rubin, "Tissue harmonic imaging: Why does it work?," *Journal of the American Society of Echocardiography*, vol. 11, pp. 803–808, Aug 1998,

[156] F. Tranquart, N. Grenier, V. Eder, and L. Pourcelot, "Clinical use of ultrasound tissue harmonic imaging," *Ultrasound in medicine & biology*, vol. 25, no. 6, pp. 889–894, 1999,

[157] G. Matte, P. Van Neer, M. Danilouchkine, J. Huijssen, M. Verweij, and N. De Jong, "Optimization of a phased-array transducer for multiple harmonic imaging in medical applications: frequency and topology," *Ultrasonics, Ferroelectrics and Frequency Control, IEEE Transactions on*, vol. 58, pp. 533 –546, March 2011,

[158] J. Rasmussen, Y. Du, and J. Jensen, "Third harmonic imaging using pulse inversion," in *Ultrasonics Symposium (IUS), 2011 IEEE International*, pp. 2269–2272, 2011.

[159] P. L. M. J. Van Neer, G. Matte, M. Danilouchkine, C. Prins, F. Van Den Adel, and N. de Jong, "Super-harmonic imaging: development of an interleaved phased-array transducer," *Ultrasonics, Ferroelectrics and Frequency Control, IEEE Transactions on*, vol. 57, no. 2, pp. 455–468, 2010,

[160] J. Borsboom, C. T. Chin, A. Bouakaz, M. Versluis, and N. de Jong, "Harmonic chirp imaging method for ultrasound contrast agent," *Ultrasonics, Ferroelectrics and Frequency Control, IEEE Transactions on*, vol. 52, pp. 241 –249, Feb. 2005,

[161] I. Akiyama, S. Saito, and A. Ohya, "Development of an ultra-broadband ultrasonic imaging system: prototype mechanical sector device," *Journal of Medical Ultrasonics*, vol. 33, no. 2, pp. 71–76, 2006,

[162] J. Johnson, Ö. Oralkan, U. Demirci, S. Ergun, M. Karaman, and P. Khuri-Yakub, "Medical imaging using capacitive micromachined ultrasonic transducer arrays," *Ultrasonics*, vol. 40, no. 1, pp. 471–476, 2002,

[163] İ. Çiçek, A. Bozkurt, and M. Karaman, "Design of a front-end integrated circuit for 3D acoustic imaging using 2D CMUT arrays," *Ultrasonics, Ferroelectrics and Frequency Control, IEEE Transactions on*, vol. 52, no. 12, pp. 2235–2241, 2005,

[164] I. O. Wygant, X. Zhuang, D. T. Yeh, O. Oralkan, A. S. Ergun, M. Karaman, and B. T. Khuri-Yakub, "Integration of 2D CMUT arrays with front-end electronics for volumetric ultrasound imaging," *Ultrasonics, Ferroelectrics and Frequency Control, IEEE Transactions on*, vol. 55, no. 2, pp. 327–342, 2008,

[165] B. T. Khuri-Yakub and mer Oralkan, "Capacitive micromachined ultrasonic transducers for medical imaging and therapy," *Journal of Micromechanics and Microengineering*, vol. 21, no. 5, p. 054004, 2011,

[166] L. L. Wong, A. I. Chen, A. S. Logan, and J. T. Yeow, "An FPGA-based ultrasound imaging system using capacitive micromachined ultrasonic transducers," *Ultrasonics, Ferroelectrics and Frequency Control, IEEE Transactions on*, vol. 59, no. 7, pp. 1513–1520, 2012,

[167] M. Arif, D. M. J. Cowell, and S. Freear, "Pulse compression of harmonic chirp signals using the fractional fourier transform," *Ultrasound in Medicine & Biology*, vol. 36, no. 6, pp. 949 – 956, 2010,

[168] L. Ferrari and J. P. Jones, "The propagation of gaussian modulated pulses in dissipative and/or dispersive media such as tissue," *Ultrasound in medicine & biology*, vol. 11, no. 2, pp. 299–305, 1985,

[169] S. S. Dodd, S. L. Carp, D. M. Hedburg, S. H. Maslak, B. S. Ramamurthy, and D. E. Need, "Ultrasonic imaging method and apparatus for generating pulse width modulated waveforms with reduced harmonic response, US 5833614," Nov. 10 1998.

[170] P. R. Smith, "Ultrasonic array research platform (UARP) transmitter board development," Master's thesis, School of Electronic and Electrical Engineering, University of Leeds, Leeds, 2009.

[171] C. A. Winckler, "The design of a high speed receiver board for the ultrasound array research platform," Master's thesis, School of Electronic and Electrical Engineering, University of Leeds, Leeds, 2012.

[172] S. S. Qureshi, "Ultrasound beamforming: FPGA implementation and dynamic focusing," Master's thesis, School of Electrical Engineering and Computer Science, National University of Sciences and Technology (NUST), 2012.